

*Review*

# Sulfurized Polyacrylonitrile for Rechargeable Batteries: A Comprehensive Review

Mufeng Wei 

Department of Chemistry, University of California Berkeley, Berkeley, CA 94720, USA; mufeng\_wei@berkeley.edu; Tel.: +1-510-993-6623

## Abstract

This paper presents a comprehensive review of research on sulfurized polyacrylonitrile (SPAN) for rechargeable batteries which was firstly reported by Jiulin Wang in July 2002. Spanning over two decades (2002–2025), this review cites over 600 publications, covering various aspects of SPAN-based battery systems. These include SPAN chemical structure, structural evolution during synthesis, redox reaction mechanism, synthetic conditions, cathode, electrolyte, binder, current collector, separator, anode, SPAN as additive, SPAN as anode, and high-energy SPAN cathodes. As this field continues to advance rapidly and garners significant interest, this review aims to provide researchers with a thorough and in-depth overview of the progress made over the past 23 years. Additionally, it highlights emerging trends and outlines future directions for SPAN research and its practical applications in energy storage technologies.

**Keywords:** sulfurized polyacrylonitrile; Li || SPAN batteries; Li-S batteries; cathodes; anodes; electrolytes; binders; separators; current collectors

## 1. Introduction

Metal–sulfur batteries (MSBs, M: Li, Na, K, Mg, Al, etc.) are widely regarded as a promising alternative for energy storage, offering the potential for high energy density and cost-effectiveness [1,2]. Sulfur, the key active material in MSBs, boasts an impressive theoretical specific capacity of 1675 mAh g<sup>-1</sup>, achieved through a 16-electron transfer redox reaction of crown-shaped sulfur (S<sub>8</sub>). This enables lithium–sulfur batteries (LSBs) to achieve an exceptionally high theoretical energy density of up to 2600 Wh kg<sup>-1</sup>, significantly exceeding those of currently commercially available lithium-ion batteries (LIBs) [3]. Sulfur is also naturally abundant, economically viable, environmentally benign, and free from supply chain constraints [4]. In addition to lithium–metal anodes, other metallic anodes—such as sodium (Na), potassium (K), magnesium (Mg), and aluminum (Al)—have also been explored for use in MSBs. These alternatives may offer promising solutions to challenges associated with lithium, including its limited availability and rising cost. These attributes position MSBs as compelling candidates to address the growing demand for extended-range electric vehicles (EVs) and to meet the need for affordable, large-scale energy storage solutions.

Conventional MSBs typically consist of a C/S composite cathode made from a composite of elemental sulfur, conductive additives, and binders, paired with a metallic anode. Taking LSBs for an example, during discharge, S<sub>8</sub> undergoes a “two-stage” reduction process, first converting to soluble lithium polysulfide species Li<sub>2</sub>S<sub>n</sub> (4 ≤ n ≤ 8), which are then further reduced to insoluble Li<sub>2</sub>S<sub>2</sub> or Li<sub>2</sub>S [5]. This process involves a “solid–liquid–solid”



Academic Editor: Torsten Brezesinski

Received: 4 July 2025

Revised: 24 July 2025

Accepted: 25 July 2025

Published: 1 August 2025

**Citation:** Wei, M. Sulfurized Polyacrylonitrile for Rechargeable Batteries: A Comprehensive Review. *Batteries* **2025**, *11*, 290. <https://doi.org/10.3390/batteries11080290>

**Copyright:** © 2025 by the author. Licensee MDPI, Basel, Switzerland. This article is an open access article distributed under the terms and conditions of the Creative Commons Attribution (CC BY) license (<https://creativecommons.org/licenses/by/4.0/>).

transition and is characterized by a dual-voltage plateau (ca. 2.4 V and 2.1 V) in the discharge profile. The charging process essentially reverses these steps. Although traditional LSBs hold the promise of high theoretical energy density and low cost, several intrinsic drawbacks have hindered their practical implementation [6]. Firstly, the poor electrical and ionic conductivity of elemental sulfur,  $\text{Li}_2\text{S}_2$ , and  $\text{Li}_2\text{S}$  results in sluggish reaction kinetics and low utilization of the active materials. Secondly, the sulfur cathode undergoes significant volume changes during cycling due to the density difference between elemental sulfur ( $2.03 \text{ g cm}^{-3}$ ) and the discharge product  $\text{Li}_2\text{S}$  ( $1.66 \text{ g cm}^{-3}$ ) [7]. These substantial volume changes can cause the pulverization of active materials and disintegration of the electrode. Thirdly, the long-chain polysulfide intermediates  $\text{Li}_2\text{S}_n$  ( $4 \leq n \leq 8$ ) are soluble in conventional ether-based electrolytes [8]. Under the influence of concentration and electric field gradients, these intermediates shuttle between the cathode and anode, a phenomenon known as the “shuttle effect”. This leads to the loss of active materials, anode deterioration, internal energy inefficiencies, and rapid capacity decay. These issues collectively hinder the performance of traditional MSBs.

To overcome the challenges of conventional MSBs, sulfurized polyacrylonitrile (SPAN) has emerged as a promising cathode material, gaining significant research attention since its initial reports by Wang et al. during 2002 and 2004 [9–11]. Unlike traditional C/S composites, SPAN features sulfur covalently bonded to a conductive polymer backbone in short-chain configurations ( $-\text{S}_n-$ , where  $2 \leq n \leq 4$ ), ensuring atomic-level dispersion [5]. The polypyrrole conductive framework in SPAN exhibits significantly higher electrical conductivity ( $10^{-5}$  to  $10^{-7} \text{ S cm}^{-1}$ ) compared to insulating elemental sulfur ( $10^{-30} \text{ S cm}^{-1}$ ). A key advantage of SPAN is its “solid–solid” conversion mechanism during cycling, eliminating the issues associated with the solid–liquid–solid transition seen in C/S composites. This unique behavior grants SPAN several advantages: (1) compatibility with carbonate-based electrolytes, unlike C/S composites [12]; (2) minimal “shuttle effect”, enabling high sulfur utilization and superior cycling stability; and (3) improved performance under lean electrolyte conditions due to the absence of liquid-phase conversion process. However, SPAN still faces limitations that hinder its practical application: (1) low sulfur (typically 35–50 wt%, with up to ~56 wt%); (2) substantial volume expansion during cycling; (3) sluggish reaction kinetics; and (4) irreversible capacity loss in the first cycle. Despite these challenges, Metal || SPAN batteries hold great potential to outperform conventional LIBs, offering a theoretical energy density exceeding  $1000 \text{ Wh kg}^{-1}$  (based on cathode + metallic lithium anode mass) compared to  $\sim 800 \text{ Wh kg}^{-1}$  for Li || NMC batteries, while leveraging low-cost raw materials [3]. Continued advancements in Metal || SPAN batteries could position them as a viable high-energy, cost-effective alternative to conventional LIBs.

In this paper, the author presents a comprehensive review of all peer-reviewed research studies (available in the Scopus database and Google Scholar) on SPAN and its applications in rechargeable batteries from 2002 to 2025. This review begins with outlining the methodology for literature collection and analyzing the key research trends over the past two decades. Subsequently, it provides a systematic and in-depth discussion on the following critical aspects: synthesis, characterization and mechanism studies, cathode design, electrolytes, solid-state batteries, binders, current collectors, separators, anodes, cell configurations, and theoretical studies. By consolidating two decades of research, this review not only summarizes the advancements in SPAN research but also identifies key challenges and proposes possible future research directions to accelerate the development of high-energy, long-lasting, and commercially viable SPAN-based batteries.

## 2. Dataset Construction and Research Progress

The methodology for compiling the comprehensive dataset of SPAN-related studies is detailed in the Supporting Information and graphically summarized in Figures 1 and S1. This dataset encompasses all peer-reviewed literature on SPAN-based rechargeable batteries from its first report in 2002 through 6 May 2025. As of the latest update, the database includes 437 original research articles and 160 non-original publications (reviews, perspectives, etc.). The dataset is kept and maintained periodically in the author's GitHub repository [13]. Figure 1 illustrates the evolving research trends, revealing a notable surge in SPAN-related studies beginning in 2018, with sustained growth through 2022. Since 2021, annual publication rates have stabilized at approximately 50–60 original research papers per year, reflecting sustained interest in SPAN as a promising cathode material. This review systematically examines every peer-reviewed study on SPAN-based batteries published between 2002 and 2025, ensuring a thorough analysis of the field's progression. By mapping historical developments, we identify key milestones, emerging trends, and future opportunities to advance SPAN technology toward commercialization.

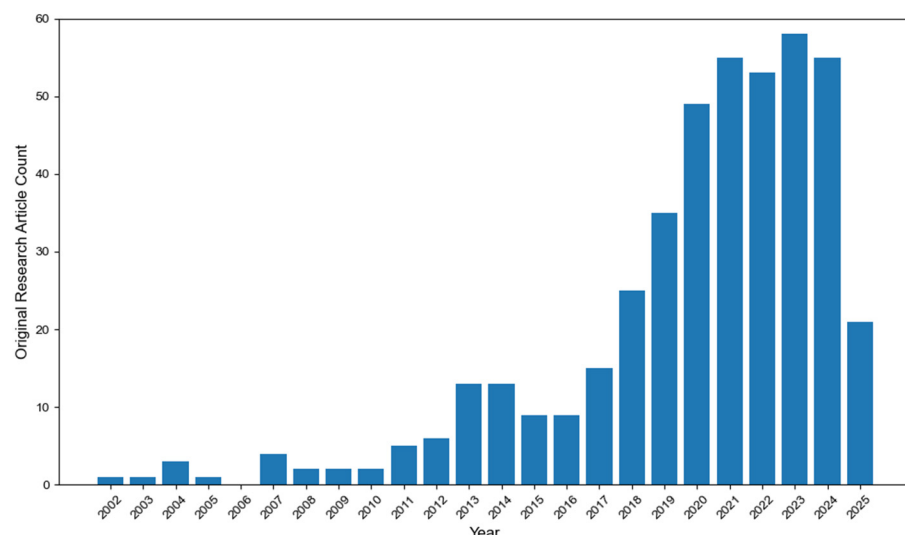


**Figure 1.** Number of publications of original research articles on SPAN for rechargeable batteries from 2002 to 6 May 2025.

## 3. Chemical Structure

Since the groundbreaking work by Wang et al. [9], numerous studies have explored the possible chemical structure of SPAN. In their initial studies published in 2002 and 2003 [9,10], Wang et al. synthesized SPAN by heating a mixture of polyacrylonitrile (PAN) and sulfur at 280–300 °C for 6 h under argon, followed by comprehensive characterization. Elemental analysis (EA) reveals a composition of 53.41 wt% S, 10.73 wt% N, 30.92 wt% C, and 0.89 wt% H. Solid-state <sup>13</sup>C nuclear magnetic resonance (NMR) spectra indicate the formation of double bonds due to the cyclization of -CN groups, while Fourier transform infrared (FT-IR) and Raman spectroscopy rules out C-S bond formation. X-ray photoelectron spectroscopy (XPS) confirms the presence of elemental sulfur. Based on these findings, the authors proposed that PAN undergoes dehydrogenation and cyclization during vulcanization, resulting in a conjugated polypyridine skeleton encapsulating elemental nano sulfur (Figure 2a).

In 2004, Yu et al. proposed, for the first time, that sulfur is covalently incorporated into the backbone as -C-S-S-C- linkages in SPAN synthesized temperatures ranging from 250 to 800 °C [14] (Figure 2b). Elemental sulfur was detected in SPAN synthesized at 250 °C but diminished with increasing temperature and nearly disappeared above 450 °C.

Fanous et al. employed time-of-flight secondary ion mass spectrometry (TOF-SIMS) in 2011 to investigate the sulfur bonding modes in SPAN [15]. Fragments such as CNS ( $\text{CNS}^-$ ,  $\text{C}_3\text{NS}^-$ ,  $\text{C}_5\text{NS}^-$ ), CS ( $\text{C}_2\text{S}^-$ ),  $\text{S}_x$  ( $\text{S}_2^-$ ,  $\text{S}_3^-$ ) were detected while no SN fragments were observed, suggesting sulfur binds exclusively to carbon (not nitrogen) and oligosulfide structures exist. The strong  $\text{CNS}^-$  signal indicated that sulfur primarily bonds to carbon adjacent to nitrogen. XPS and FT-IR spectra further excluded the presence of elemental  $\text{S}_8$ , leading to a revised SPAN structural model (Figure 2c). In a follow-up study (2012), Fanous et al. demonstrated that higher synthesis temperatures reduce sulfur content and enhance graphitization of the polymer backbone, improving rate capability and cycling stability [16].

Doan et al. investigated the binding mechanism of sulfur and PAN in the SPAN composite by heating PAN-sulfur mixtures at 300 °C for 0.5–4 h [17]. They concluded that  $\text{S}_8$  was embedded between heterocyclic rings of dehydrogenated PAN, which was similar to the structure proposed by Wang et al. [9]. Zhang et al. (2014) consolidated prior findings with their own data, proposing a structure where short  $-\text{S}_x-$  chains covalently attach to cyclized, partially dehydrogenated PAN backbones [18] (Figure 2d). Wei et al. (2015) further suggested that sulfur existed as  $\text{S}_3/\text{S}_2$  units bonded to pyridinic-N-containing carbon backbones, retaining this configuration throughout redox processes [19] (Figure 2e).

In 2018, Wang et al. employed solid-state NMR, electron paramagnetic resonance (EPR), EA, and simulations to deduce a repeating  $\text{C}_3\text{N}_1\text{S}_1$  unit in SPAN, with PAN chains linked by  $-\text{S}_2-$  bridges [20] (Figure 2f). Jin et al. proposed a similar structure but with  $-\text{S}_x-$  ( $2 \leq x \leq 4$ ) bridging adjacent polypyridine rings [21] (Figure 2g).

The existence of N-S bonds in the SPAN structure was firstly evidenced and proposed by Weret et al. in 2020 [22] (Figure 2h). From the high-resolution cross-polarization/magic angle spinning (CP-MAS)  $^{15}\text{N}$  solid-state NMR, XPS, and FT-IR spectra, they identified N-S and N=C-S bonds, which contribute to the high initial discharge capacity. Huang et al. (2021) provided new via CP-MAS solid-state NMR, XPS, and density functional theory (DFT) calculations [23], proposing a vicinal pyridinic/pyrrolic nitrogen structure that attracts  $\text{S}_2$  during synthesis and facilitates N-S bond formation (Figure 2i). In a subsequent study, Huang et al. proposed an energetically favorable  $-\text{N}-\text{S}_x-\text{N}-$  ( $x < 4$ ) configuration on the SPAN backbone, supported by Raman spectroscopy and computational results [24].

Theoretical studies have further elucidated SPAN's structure. Zhu et al. used DFT to identify stable motifs in PAN and SPAN [25]. It is found that backbone structures with multiple stair-like configurations are energetically favored for PAN. For PAN, stair-like backbone configurations are energetically favored, while SPAN stabilizes S=C double bonds at kink/edge sites and sulfur bridges between backbones. S-N bonds were found to be unstable, and larger  $\text{S}_n$  rings (reducing internal stress) are more stable than smaller ones.

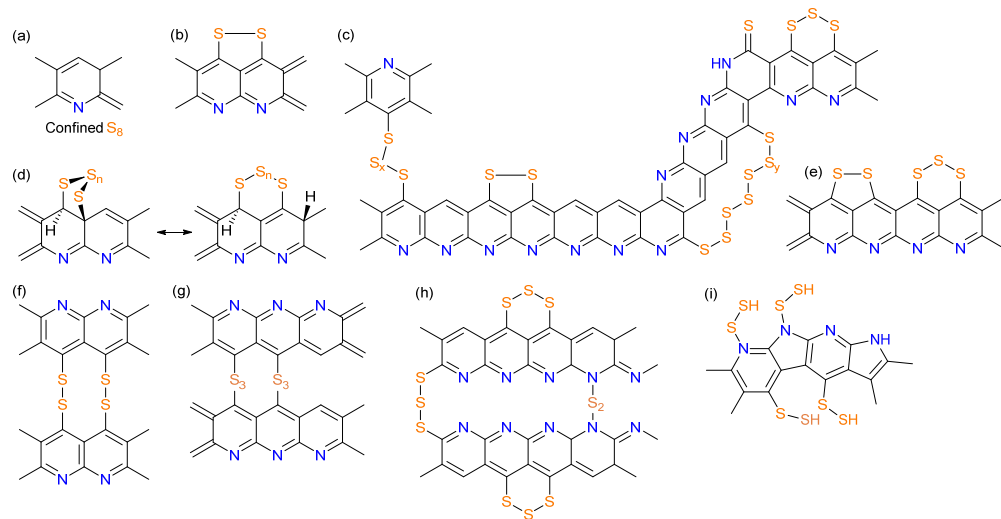


**Figure 2.** Proposed chemical structures of SPAN in previous papers by (a) Wang et al., reproduced with permission [9]. Copyright © 2002, Wiley-VCH; (b) Yu et al., reproduced with permission [14]. Copyright © 2004, Elsevier; (c) Fanous et al., reproduced with permission [15]. Copyright © 2011, American Chemical Society; (d) Resonated structures proposed by Zhang et al., reproduced with permission [18]. Copyright © 2014, MDPI; (e) Wei et al., reproduced with permission [19]. Copyright © 2015, American Chemical Society; (f) Wang et al. reproduced with permission [20]. Copyright © 2018, American Chemical Society; (g) Jin et al., reproduced with permission [21]. Copyright © 2018, Elsevier; (h) Weret et al., reproduced with permission [22]. Copyright © 2020, Elsevier; (i) Huang et al., reproduced with permission [23]. Copyright © 2021, American Chemical Society.

#### 4. Structural Evolution During Synthesis

SPAN is typically synthesized by heating a mixture of PAN and sulfur at elevated temperatures for an extended duration under an inert atmosphere [5,26]. The structural evolution from PAN to SPAN, along with the associated chemical transformations, has been extensively investigated. Key findings are summarized below.

In their pioneering 2002 study, Wang et al. proposed that sulfur acts as an effective dehydrogenating agent, removing hydrogen from PAN to produce H<sub>2</sub>S during heat treatment [9] (Figure 3a). Simultaneously, the -CN groups undergo cyclization, forming a conjugated heterocyclic chain. He et al. (2008) later employed thermogravimetry (TG) and differential scanning calorimetry (DSC) to analyze PAN and sulfur mixtures heated to 600 °C [27]. Their DSC data revealed exothermic peaks near 320 °C for sulfur/PAN ratios below 3.5:1, transitioning to endothermic peaks at ratios above 4:1, suggesting a critical reaction threshold at this temperature.

In 2020, Weret et al. proposed a mechanistic pathway for SPAN synthesis based on spectroscopic evidence [22] (Figure 3b). They hypothesized that thermally initiated ring-opening of S<sub>8</sub> generates polysulfane diradicals, which subsequently attack nitrile carbons, initiating heterocycle formation and sulfur incorporation into the PAN backbone.

A more detailed thermodynamic analysis was provided by Xie et al. in 2025, who utilized X-ray absorption spectroscopy (XAS) to probe bonding interactions during SPAN synthesis with element-specific resolution (C, N, S) [28] (Figure 3c). During the synthetic process, the formation of C=S bonds begins at around 180 °C, where sulfur bonds to the carbon adjacent to the nitrogen in the matrix. In 180–220 °C, PAN cyclization occurs, but not significantly. Major reactions, including cyclization of PAN and the formation of C-S bonds occur predominantly between 220 and 270 °C. Sulfur tends to bond with the  $\gamma$ -site of the six-membered ring and connect two carbon rings with C-S<sub>x</sub>-C bonds. Above 250 °C, pyrrolic rings and graphitic structures start to form. At 300 °C, the average length of x of

sulfur chains in C-S<sub>x</sub>-C is approximately 3.33. This work underscores the utility of XAS in elucidating reaction pathways for organic cathode materials and provides a foundation for optimizing SPAN's electrochemical cyclability.

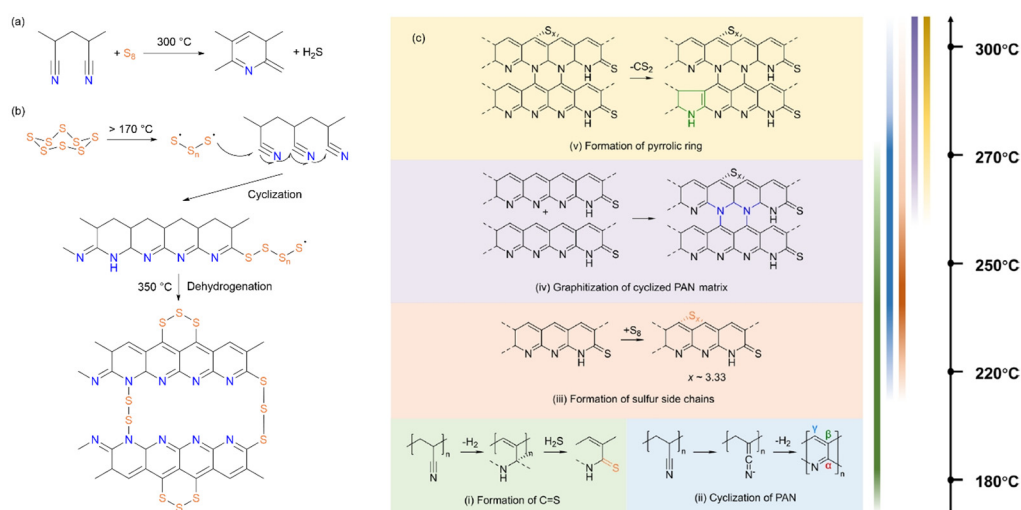


**Figure 3.** The proposed structural evolution mechanisms of the synthesis of SPAN by (a) Wang et al., reproduced with permission [9]. Copyright © 2002, Wiley–VCH; (b) Weret et al., reproduced with permission [22]. Copyright © 2020, Elsevier; (c) Xie et al., reproduced with permission [28]. Copyright © 2025, American Chemical Society.

## 5. Electrochemical Properties

Extensive research into the electrochemical behavior of SPAN cathodes has revealed several consistent characteristics as understanding of its chemical structure has advanced. These include high initial discharge capacity with accompanying voltage hysteresis, a “solid–solid” conversion mechanism during charge/discharge processes, significant volume expansion during cycling, relatively stable cycling performance, compatibility across a wide temperature range, and sluggish reaction kinetics. These properties have been systematically investigated through numerous studies.

Initially, Wang et al. assembled Li || SPAN batteries with polyvinylidenefluoride-hexafluoropropylene (PVDF-HFE) gel electrolyte system containing 1 M LiPF<sub>6</sub> in ethylene carbonate (EC) and dimethyl carbonate (DMC) (1:1, *v/v*) [9–11]. The Li || SPAN batteries delivered an initial discharge capacity of 850 mAh g<sup>−1</sup>SPAN and retained above 600 mAh g<sup>−1</sup>SPAN after 50 cycles. This corresponded to approximately 90% sulfur utilization, with Li<sub>2</sub>S identified as the discharge product through subsequent analysis. Cyclic voltammetry studies revealed two closely spaced reduction peaks centered around 1.85 V versus Li<sup>+</sup>/Li during discharge, and a single oxidation peak at approximately 2.27 V during charge.

Further investigations by He et al. between 2007 and 2009 provided additional insights into the charge/discharge characteristics of SPAN cathodes [29–31]. Their work established important operational limits, showing that while SPAN cathodes suffer irreversible degradation when charged above 4.0 V, they maintain excellent reversibility even when deeply discharged to 0 V. The temperature resilience of SPAN was clearly demonstrated through capacity measurements of 854 mAh g<sup>−1</sup>SPAN at 60 °C and 632 mAh g<sup>−1</sup>SPAN at –20 °C. In addition, these studies first documented the substantial volume changes occurring during cycling, revealing a 22% increase in cathode thickness during discharge associated with Li<sup>+</sup> insertion and accompanying structural rearrangements.

The importance of electrode engineering parameters on electrochemical properties of SPAN has been thoroughly examined in multiple studies. Wang et al. demonstrated in 2010 that compaction pressure significantly affects electrochemical behavior, with optimal performance achieved at 8 MPa and notable degradation occurring at higher pressures of 24 MPa due to pore structure collapse and reduced ionic accessibility [32]. Niesen et al. systematically investigated the relationship between electrode density and electrochemical performance of SPAN cathodes [33]. The results show that while calendaring reduced the electrical resistance, compressing the electrodes to densities higher than  $1.05 \text{ g cm}^{-3}$  led to a reduction in rate capability due to the loss of active reaction sites and a poor wettability of the electrode. Moschner et al. further advanced this understanding by characterizing the springback phenomenon in compressed SPAN electrodes and its detrimental effects on long-term cycling stability [34]. Their comprehensive analysis combining experimental and simulation approaches identified maintenance of homogeneous electronic networks as critical for sustained performance, suggesting several optimization strategies including improved binder systems and incorporation of advanced conductive additives such as carbon nanotubes or graphene.

The kinetic limitations and interfacial phenomena of SPAN cathodes were elucidated through detailed electrochemical impedance spectroscopy (EIS) studies by Wang et al. in 2011 [35]. Their work tracking impedance evolution at various states of charge revealed dynamic changes in both interfacial impedance ( $R_{sf}$ ) and charge transfer resistance ( $R_{ct}$ ) during cycling, with values increasing during delithiation and decreasing during lithiation. Notably, the  $\text{Li}^+$  diffusion coefficient was found to reach its maximum value after the initial formation cycle, while both  $R_{sf}$  and  $R_{ct}$  decreased following the first complete lithiation, indicating improved electrode kinetics and reversibility after this activation process.

## 6. Redox Reaction Mechanism

The distinctive electrochemical behavior of sulfurized polyacrylonitrile (SPAN) has motivated comprehensive investigations into its redox reaction mechanism, with researchers employing increasingly sophisticated analytical techniques to unravel the complex structure-property relationships. The evolving understanding of this mechanism has progressed through several key stages of discovery.

Initial studies by Wang et al. established fundamental observations regarding SPAN's electrochemical behavior, noting both the remarkably high initial discharge capacity and the characteristic low voltage plateau [9–11]. Their proposed mechanism implicated strong electronic interactions between sulfur heteroatoms and nitrogen centers within the polypyridine framework, suggesting that the energetic requirements for sulfur dissociation contributed to the observed discharge potential. This work first proposed the structural modifications occurring during the initial cycle, particularly the change of nitrogen environments that accounted for subsequent more positive discharge potentials in electrochemical behavior.

Yu et al. advanced this understanding by proposing a multi-origin capacity contribution model [14] (Figure 4a): (1) conventional sulfur redox chemistry involving embedded nano-sized elemental sulfur, (2) cleavage and reformation of S-S linkages within the polymer matrix, and (3) Faradaic processes associated with lithium intercalation/deintercalation in the layered structure. This mechanism explained SPAN's exceptional capacity while accounting for its unique voltage profile.

Subsequently, Fanous et al. conducted electrolyte studies and found that the Li||SPAN cells prepared from LiTFSI in 1,3-dioxolane (DOL) and dimethoxyethane (DME) displayed a shoulder peak in the discharge profile, indicating the formation of elemental sulfur [15]. They proposed that in ether-based electrolytes, the sulfur of the polysulfides that was not bound to carbon but to the sulfur was first released from the backbone and further reduced to Li<sub>2</sub>S. In addition, the authors proposed that the polymer backbone contributes to an additional ~100 mAh g<sup>-1</sup><sub>cathode</sub> to the capacity only in the first discharge cycle. Complementary investigations into the electroactivity of the SPAN backbone within expanded charge–discharge windows by Wang et al. revealed an ultra-high lithium storage capacity at low potentials (0–1 V vs. Li<sup>+</sup>/Li) corresponding to four-electron transfer per C<sub>3</sub>NH unit [36]. The reversible capacity of SPAN could reach 1750 mAh g<sup>-1</sup><sub>sulfur</sub> in the charge–discharge range of 0–3 V. This finding was further elucidated by Jiang et al. who employed several *in situ* characterization techniques to study the over-lithiation process in SPAN via *in situ* Raman spectroscopy and *in situ* electrochemical atomic force microscopy (EC-AFM) [37]. It is revealed that the S-S/C-S bonds gradually break during the initial over-lithiation stage and C-Li bonds generate.

The origin of the voltage hysteresis and the initial irreversible capacity was systematically investigated by Zhang et al., who identified two primary contributors [18]: (1) interfacial resistance at SPAN-conductive carbon particle boundaries and (2) irreversible reduction in short conjugated carbon bonds. Their proposed “solid–solid” conversion mechanism, involving direct transformation between SPAN and Li<sub>2</sub>S without soluble lithium polysulfides (LiPSs) intermediates, provided a coherent explanation for the minimal shuttle effect and outstanding cycle life out SPAN cathodes (Figure 4b). Several researchers investigated the electrolyte-dependent behavior of the formation of LiPSs during the redox process. Wei et al. proposed that Li<sub>2</sub>S was the only discharge product in carbonated-based electrolytes, while LiPSs could form and shuttle in ether-based electrolytes [19]. Dominko et al. analyzed the electrochemical behavior of the SPAN cathode by *in operando* UV-Vis spectroscopy and 4-electrode Swagelok setup cell setup [38]. No LiPSs or elemental sulfur was observed during the redox process in the sulfolane electrolyte. Warneke et al. reported no long chain polysulfides were observed during discharge for the SPAN cathode in carbonate and ether mixed electrolytes [39].

Wang et al. confirmed the presence of the thiyl radical after the cleavage of the S-S bond in the first cycle through the characterization of <sup>7</sup>Li solid-state NMR, EPR, and simulations [20]. Their comprehensive characterization revealed that Li<sup>+</sup> participate in reversible binding interactions with anionic sites localized on both sulfur and nitrogen atoms, which was fundamentally responsible for SPAN’s exceptional cycle life and rate performance characteristics (Figure 4c). Complementing these findings, Jin et al. conducted detailed investigations of SPAN’s lithium storage mechanism using solid-state NMR and XPS [21] (Figure 4d). During the electrochemical process, other than the conventional sulfur redox reactions, C=N and C=C groups also react with lithium to form Li-C-N-Li and Li-C-C-Li groups and afford additional capacity. After the first charge, a portion of these lithiated carbon species remain permanently reduced. This partial irreversibility was correlated with the observed first-cycle capacity loss in SPAN electrodes.

Building upon the identification of N-S and N=C-S bonds in SPAN’s structure alongside S-S and C-S bonds, Weret et al. proposed a comprehensive SPAN redox mechanism [22] (Figure 4e). During the first discharge, electrochemical cleavage of the covalent bonds results in the irreversible formation of Li-C and Li-N bonds, contributing the high initial discharge capacity. The electron-donating effect of Li-C and Li-N species increases the electron density of the conjugated structure and benefits the decrease in the voltage hysteresis after the second cycle. Huang et al. further elucidated the critical role of N-S

bonds in mediating the “solid–solid” transformation, identifying a stepwise process where N-S<sub>x</sub>-N and C-S<sub>3</sub>-C linkages cleave to form N/C-Sy-Li, N/C-Li, and Li<sub>2</sub>S species [24] (Figure 4f). Their studies revealed that during full lithiation, Li<sub>2</sub>S preferentially aligns along nitrogen-rich edges of the SPAN matrix through Li-N interactions. While N/C-S bond reformation occurs during charging, the re-establishment of bridge-type N-S<sub>x</sub>-N and C-S<sub>3</sub>-C configurations is energetically disfavored, leading instead to stabilized thiy radical formation within the conjugated system. Kappler et al. provided comparative evidence for nitrogen’s essential role through studies of nitrogen-free sulfurized poly(vinylacetylene) (SPVac) [40], conclusively demonstrating that the nitrogen-rich aromatic backbone in SPAN is prerequisite for achieving both high sulfur utilization and reversible binding.

In 2023, Wang et al. studied the structural transformation in SPAN during the first cycle and proposed a post-thermal treatment strategy to reduce the first cycle irreversible capacity loss [41] (Figure 4g). The authors believed that the loss of nonaromatic functional groups such as C-S, C=S, and N-H was responsible for the irreversible capacity loss during the first cycle and conductive carbon was found to actively participate in the conversion of SPAN intermediates to the discharge products. Therefore, the authors developed a post-thermal treatment by annealing SPAN at 350 °C for 24 h to reduce the nonaromatic groups. As a result, SPAN with post-treatment exhibited nearly identical reversible capacity of 520 mAh g<sup>-1</sup> SPAN as the pristine SPAN while reducing the first-cycle irreversible capacity loss from 225 to ~100 mAh g<sup>-1</sup> SPAN.

Advanced characterization by Tan et al. using synchrotron-based pair distribution function (PDF) and soft X-ray absorption spectroscopy (sXAS) provided atomic-scale insights into cycling-induced interphasial changes in SPAN [42] (Figure 4h). PDF analysis of pristine SPAN identified C-S bonds and S-S dimers connecting pyridine networks, while discharged states showed S-S cleavage and -S-Li formation. During the first discharge, the S-S dimer is replaced by short sulfur chains (-S-S-S-), accompanied by the breaking of nonaromatic C-S and C=S bonds which supplies the sulfur needed in forming short sulfur chains. The short sulfur chains are actively involved in the following reversible cycling. The study further demonstrated electrolyte-dependent interphase formation, with localized high concentration electrolyte (LHCE: 1.8 M LiFSI in diethyl ether (DEE)/bis-(2,2,2-trifluorosulfonyl)imide (BTFE)) producing stable FSI<sup>-</sup>-derived interphases, while DOL/DME led to unstable cathode-electrolyte interfaces (CEI) and polysulfide dissolution. In Xie et al.’s work, they identified the role of the bonding interactions of SPAN, including S-S, C-S, and C=S bonds, in the electrochemical reactions by tracking the evolution of XAS features of intermediate states [28] (Figure 4i).

Pereira et al. investigated the redox mechanism of SPAN in LiNO<sub>3</sub>-containing ether electrolytes by a combination of post-mortem analysis with XPS and in-operando FT-IR study [43]. The in-operando FT-IR spectra reveal that C-S bonds reform during cycling despite breaking in the initial cycle in ether electrolytes with concentrated LiNO<sub>3</sub>. However, this reformation does not occur in ether electrolytes without LiNO<sub>3</sub>. Additionally, soluble polysulfide species exist in both systems during the first discharge but only persist in ether electrolytes without LiNO<sub>3</sub>. XPS analysis reveals the formation of a stable LiF-rich CEI in ether electrolytes with concentrated LiNO<sub>3</sub>. Based on the results, the authors proposed that a quasi-solid–solid conversion of sulfur occurred in electrolytes with sulfur enabled by a robust CEI coupled with C-S bond reformation during cycling.

Hu et al. studied the molecular structure and electrochemical reaction mechanism of SPAN by various techniques including *in situ* Raman, *ex situ* XPS, and EPR [44] (Figure 4j). As it is consistent with several previous studies, the authors proposed that the reversible capacity came from the reversible S-S and C-S bond cleavage and reformation; and the initial irreversible capacity came from the irreversible reaction between C=N and Li<sup>+</sup>. The residual Li<sup>+</sup> on the carbon matrix enhances the conductivity of the SPAN skeleton and results in the reduction in voltage hysteresis after the second cycle. The authors proposed a novel insight, where a conjugate aromatic structure with radical was formed after the C-S bond cleavage. And during the charge process, sulfur prioritizes to combine with the C radical on the aromatic ring, resulting in elimination of polysulfides generation over long cycles. Liu et al. investigated the role of the polymer backbone of SPAN from multiple aspects, including electrochemistry, spectroscopy, microscopy, and theoretical calculations [45]. The results revealed four critical backbone functions: (1) sulfur anchoring sites, (2) conductive π-network with narrowed HOMO-LUMO gap by sulfur-doping, (3) irreversible Li<sup>+</sup> binding affecting first-cycle efficiency, and (4) pyridinic nitrogen-mediated Li<sub>2</sub>S stabilization.

The redox mechanism of Na||SPAN batteries was studied by Kappler et al. in 2023 [46]. They reported a high-performance Na||SPAN battery with a simple commercially available carbonated-based electrolyte and investigated the SPAN redox chemistry. The *in situ* EIS and XAS at different depths of charge and discharge revealed that the formation of Na<sub>2</sub>S<sub>2</sub> or Na<sub>2</sub>S occurs abruptly close to the lower voltage cut-off, not gradually over discharge as that in Li||SPAN batteries.

Computational studies have been dedicated to investigating the redox reaction mechanism of SPAN and significantly advanced its understanding. In 2017, Zhu et al. employed DFT calculation to study the interactions between Li<sup>+</sup> and SPAN with sulfur chain lengths varying from one to eight and proposed a hypothetical mechanism for the charge–discharge process [47]. Their study revealed that in both discharging and charging process, Li<sup>+</sup> preferentially coordinates with N atoms. In addition, spatially separating a dissociated S<sub>n</sub>Li fragment from the backbone is difficult, which provides a plausible explanation for the minimal polysulfides shuttling problem in SPAN cathodes. Based on these findings, the authors proposed a mechanism for the discharging process: First, a Li<sup>+</sup> approaches the SPAN backbone where the Li<sup>+</sup> simultaneously coordinates with the free end of the S-chain and the N atoms on the backbone. Then, a second Li<sup>+</sup> attacks the end of the backbone attached to the S-chain, cleaving the S-chain, and leaving behind a single S or a S<sub>2</sub> unit attached to the backbone and forming Li<sub>2</sub>S<sub>y</sub> intermediate. The detached Li<sub>2</sub>S<sub>y</sub> can be further reduced to Li<sub>2</sub>S or reattach at another location on the backbone. In 2022, Bertolini et al. investigated the discharge process of SPAN via ab initio molecular dynamics [48]. The simulation suggests that Li<sup>+</sup> tends to coordinate with the nitrogen in the polymer backbone at low lithiation degree. As the lithiation progresses, Li<sup>+</sup> coordinates with sulfur, indicating that the nitrogen plays an important role in capturing PSs.

Beltran et al. used ab initio molecular dynamics to study the electrochemical lithiation processes in a multi-layer graphene nanosheet-based sulfur–carbon composite model embedded in DOL solvent [49]. Their calculation showed that a strong C-S interaction, which is evidenced in SPAN composites, not only contributes to eliminate the sulfur dissociation into the solvent but also leads to an “all in-solid-state” sulfur reduction pathway, skipping the formation of long-chain LiPSs. In another one of their studies, they addressed and explained the lithiation of SPAN via first-principles computational approaches [50]. Their model indicated that during the lithiation process above 1.0 V vs. Li/Li<sup>+</sup>, the Li<sup>+</sup>/electrons first reduce sulfur in intermediate positions that are not interacting with the graphitized backbone directly and then attack sulfur atoms engaged in C-S bonding, leading to the C-S

cleavage. Below 1.0 V, the reduction in the graphitized backbone dominates via C-Li and N-Li interactions, which accounts for the irreversible capacity loss observed in the first two discharge cycles. The effect of electrochemical lithiation on the SPAN mechanical integrity was investigated by Beltran et al. via uniaxial tensile loading tests using molecular dynamics with the ReaxFF potential [51]. Volume expansion, Young's modulus, yield strength, and ultimate tensile strength with increasing lithium contents were evaluated. The results showed that the SPAN lithiation leads to a volume expansion which barely changes with a higher graphitization degree, increase YM modulus, and decreased ductility.

Bertolini et al. made significant contributions to understanding the dynamic behavior of uncoordinated carbon ( $C_{uc}$ ) on the SPAN backbone through a series of computational studies. It was revealed that  $C_{uc}$  is able to not only capture a polysulfide (PS) from the electrolyte but also decompose and bind to the solvent and/or remove lithium from the PS [52]. In 2022, Bertolini et al. further investigated the role of  $C_{uc}$  in the SPAN backbone using DFT [53,54]. The simulation suggested that  $C_{uc}$  can be thermodynamically created due to lithiation. Furthermore,  $C_{uc}$  can react with the solvent on the polymer backbone through different mechanisms which are affected by the interaction between the solvent and  $C_{uc}$ . These findings provided insights into how SPAN's structure governs lithiation of sulfur chains and revealed previously unrecognized reaction pathways between electrolytes and host materials containing a  $C_{uc}$ . Further investigations by Bertolini et al. using ab initio molecular dynamics simulations elucidated overpotential-driven side reactions during charging [55]. The simulation indicated that under high-potential conditions, electron-deficient polymer backbones become susceptible to nucleophilic attack by hydrogen atoms from electrolyte solvents, with preferential reaction sites at sulfur chains and nitrogen centers in SPAN. These parasitic reactions were shown to progressively degrade battery performance through both active material consumption and interface destabilization.

Recently, Simanjuntak et al. advanced the theoretical understanding of SPAN electrodes through a novel continuum model [56]. The discharge mechanism of SPAN and the impact of different parameters and processes on cell behavior were investigated (Figure 4k). The simulations identified current collector-cathode interface resistance as the dominant factor underlying large overpotentials at elevated current densities, rather than bulk electrolyte transport limitations. For cell designs targeting high energy densities, the simulation demonstrated that the morphology and microstructure of the SPAN cathode is crucial.

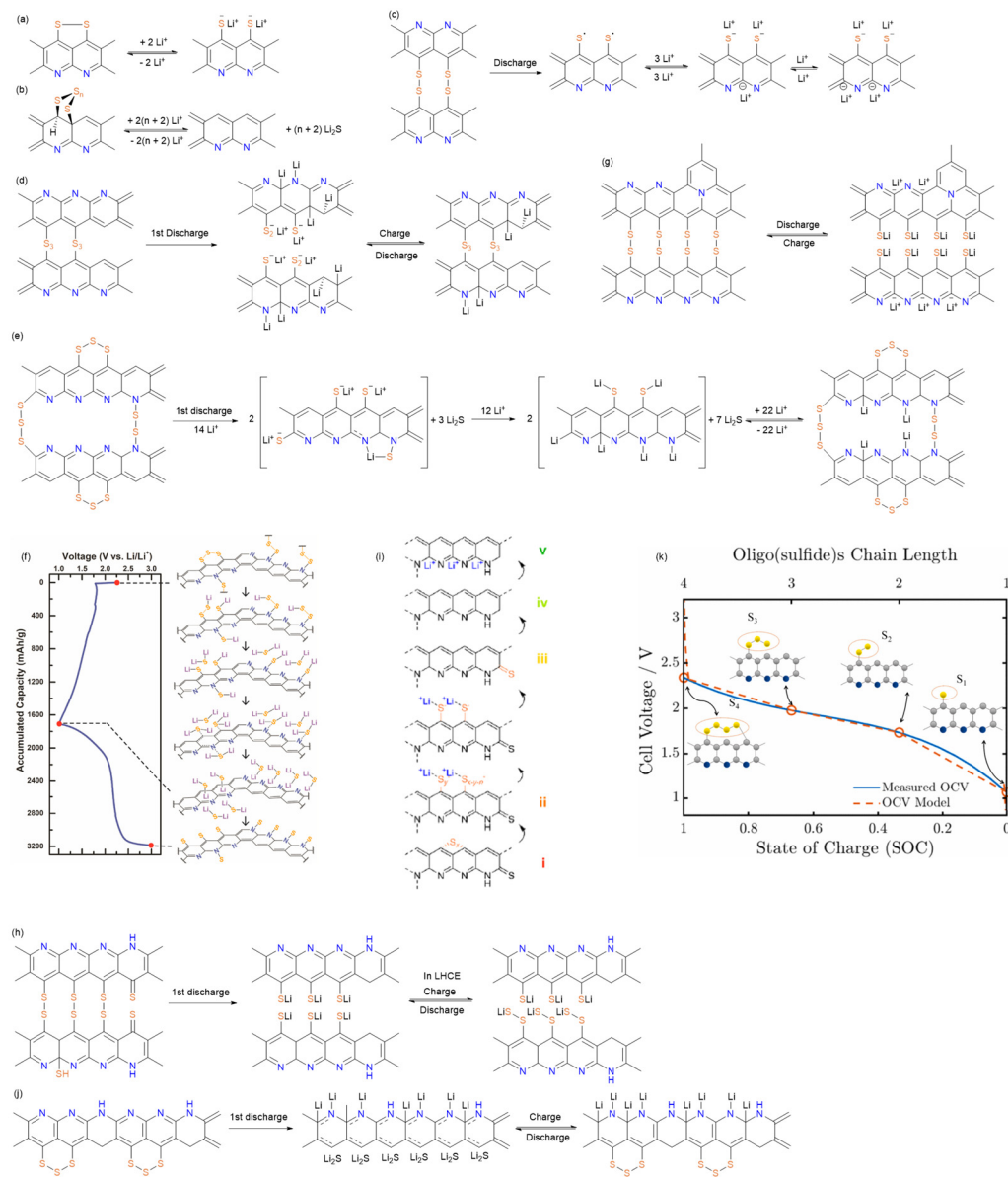
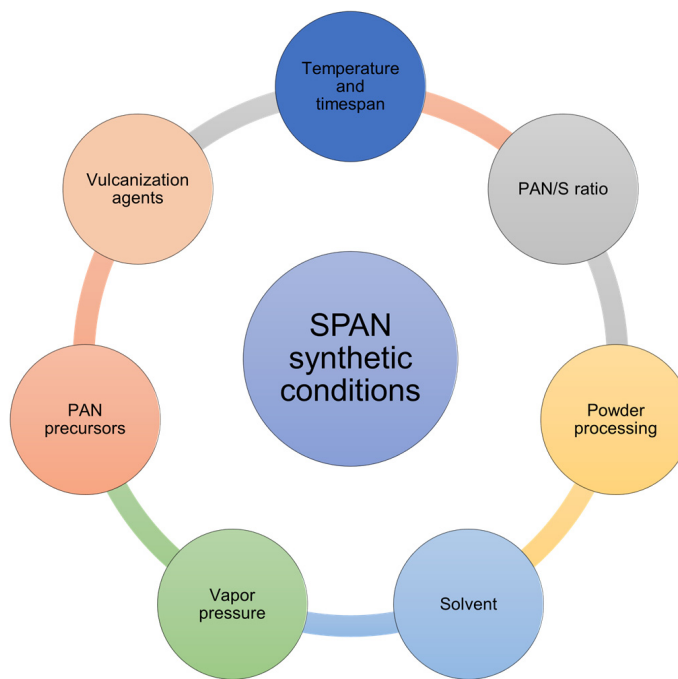


**Figure 4.** The proposed redox reaction mechanisms of SPAN by (a) Yu et al., reproduced with permission [14]. Copyright © 2004, Elsevier; (b) Zhang et al., reproduced with permission [18]. Copyright © 2014, MDPI; (c) Wang et al., reproduced with permission [20]. Copyright © 2018, American Chemical Society; (d) Jin et al., reproduced with permission [21]. Copyright © 2018, Elsevier; (e) Weret et al., reproduced with permission [22]. Copyright © 2020, Elsevier; (f) Huang et al., reproduced with permission [24]. Copyright © 2021, Elsevier; (g) Wang et al., reproduced with permission [41]. Copyright © 2023, American Chemical Society; (h) Tan et al., reproduced with permission [42]. Copyright © 2023, American Chemical Society; (i) Xie et al., reproduced with permission [28]. Copyright © 2025, American Chemical Society; (j) Hu et al., reproduced with permission [44]. Copyright © 2024, Elsevier; (k) Simanjuntak et al., reproduced with permission [56]. Copyright © 2024, Elsevier.

## 7. SPAN Synthetic Conditions

The chemical structure and the properties of SPAN are dependent on synthetic conditions. Various synthetic parameters including temperature, timespan, PAN/S ratio, powder processing, solvent, vapor pressure, PAN precursors, and vulcanization agents have been investigated by researchers to understand the correlation between the chemical

structure and the property of SPAN and to optimize the synthetic procedure (Scheme 1). A comprehensive discussion is provided below.



**Scheme 1.** Schematic diagram of SPAN synthetic conditions.

### 7.1. Temperature and Timespan

The synthesis temperature critically determines SPAN's structural and electrochemical properties, with most studies identifying 300–450 °C as the optimal range for achieving high-performance materials [5,6,26]. The performance of SPAN synthesized at different temperatures is summarized in Table 1. Initially, Wang et al. synthesized SPAN by heating the mixture of polyacrylonitrile (PAN) and sulfur at 280–300 °C for 6 h under argon [9–11], yielding SPAN with 53.41 wt% of sulfur. The Li | SPAN battery exhibited an initial discharge capacity of 850 mAh g<sup>-1</sup><sub>SPAN</sub> and retained above 600 mAh g<sup>-1</sup><sub>SPAN</sub> at 0.3 mA cm<sup>-2</sup> after 50 cycles.

**Table 1.** Summary of cycling performance of SPAN synthesized at different temperatures.

| Cathode  | Synthetic Temperature (°C) | Cathode Loading             | Initial Discharge Capacity         | Cycles | Final Discharge Capacity    | Capacity Retention | Rate/Current Density    | Ref. |
|----------|----------------------------|-----------------------------|------------------------------------|--------|-----------------------------|--------------------|-------------------------|------|
| CSM-300  | 300                        | 4.5 mg <sub>composite</sub> | 510 mAh g <sup>-1</sup><br>(2nd)   | 50     | 470 mAh g <sup>-1</sup>     | 92.2%              | 0.2 mA cm <sup>-2</sup> | [57] |
| CSM-350  | 350                        | 4.5 mg <sub>composite</sub> | 570 mAh g <sup>-1</sup><br>(2nd)   | 50     | 490 mAh g <sup>-1</sup>     | 86.0%              | 0.2 mA cm <sup>-2</sup> | [57] |
| CSM-450  | 450                        | 4.5 mg <sub>composite</sub> | 520 mAh g <sup>-1</sup><br>(2nd)   | 50/380 | 503/470 mAh g <sup>-1</sup> | 96.7%/90.4%        | 0.2 mA cm <sup>-2</sup> | [57] |
| CSM-550  | 550                        | 4.5 mg <sub>composite</sub> | 315 mAh g <sup>-1</sup><br>(2nd)   | 50     | 375 mAh g <sup>-1</sup>     | 119.0%             | 0.2 mA cm <sup>-2</sup> | [57] |
| CSM-650  | 650                        | 4.5 mg <sub>composite</sub> | 245 mAh g <sup>-1</sup><br>(2nd)   | 50     | 290 mAh g <sup>-1</sup>     | 118.4%             | 0.2 mA cm <sup>-2</sup> | [57] |
| CSM-800  | 800                        | 4.5 mg <sub>composite</sub> | 115 mAh g <sup>-1</sup><br>(2nd)   | 50     | 130 mAh g <sup>-1</sup>     | 113.0%             | 0.2 mA cm <sup>-2</sup> | [57] |
| SPAN-300 | 300                        | N/A                         | 702.4 mAh g <sup>-1</sup><br>(2nd) | 50     | 552.7 mAh g <sup>-1</sup>   | 78.7%              | 100 mA g <sup>-1</sup>  | [58] |
| SPAN-350 | 350                        | N/A                         | 801.5 mAh g <sup>-1</sup><br>(2nd) | 50     | 795.4 mAh g <sup>-1</sup>   | 98.1%              | 100 mA g <sup>-1</sup>  | [58] |
| SPAN-400 | 400                        | N/A                         | 650.6 mAh g <sup>-1</sup><br>(2nd) | 50     | 559.6 mAh g <sup>-1</sup>   | 86.1%              | 100 mA g <sup>-1</sup>  | [58] |

**Table 1.** Cont.

| Cathode   | Synthetic Temperature (°C) | Cathode Loading                            | Initial Discharge Capacity     | Cycles | Final Discharge Capacity | Capacity Retention | Rate/Current Density   | Ref. |
|-----------|----------------------------|--|--------------------------------|--------|--------------------------|--------------------|------------------------|------|
| SPAN-300  | 300                        | 2 mg <sub>composite</sub> cm <sup>-2</sup> | 1195 mAh g <sup>-1</sup> (3nd) | 100    | 239 mAh g <sup>-1</sup>  | 20.0%              | C/10                   | [59] |
| SPAN-350  | 350                        | 2 mg <sub>composite</sub> cm <sup>-2</sup> | 696 mAh g <sup>-1</sup> (3nd)  | 100    | 675 mAh g <sup>-1</sup>  | 97.0%              | C/10                   | [59] |
| PAN/S-250 | 250                        | N/A  | 751 mAh g <sup>-1</sup>        | 50     | 467 mAh g <sup>-1</sup>  | 62.2%              | 100 mA g <sup>-1</sup> | [60] |
| PAN/S-300 | 300                        | N/A  | 723 mAh g <sup>-1</sup>        | 50     | 505 mAh g <sup>-1</sup>  | 69.8%              | 100 mA g <sup>-1</sup> | [60] |
| PAN/S-350 | 350                        | N/A  | 725 mAh g <sup>-1</sup>        | 50     | 506 mAh g <sup>-1</sup>  | 69.8%              | 100 mA g <sup>-1</sup> | [60] |
| PAN/S-400 | 400                        | N/A  | 810 mAh g <sup>-1</sup>        | 50     | 579 mAh g <sup>-1</sup>  | 71.5%              | 100 mA g <sup>-1</sup> | [60] |
| PAN/S-450 | 450                        | N/A  | 586 mAh g <sup>-1</sup>        | 50     | 412 mAh g <sup>-1</sup>  | 70.3%              | 100 mA g <sup>-1</sup> | [60] |

Yu et al.'s systematic investigation demonstrated that SPAN synthesized at 450 °C exhibited exceptional cyclability (90.4% capacity retention after 380 cycles) [57]. Wang et al. synthesized SPAN at 300, 350, and 400 °C and compared the electrochemical performances [58] (Figure 5a). They identified the optimal temperature for the SPAN synthesis as 350 °C, with which the Li||SPAN battery delivered a reversible capacity of about 795 mAh g<sup>-1</sup> SPAN and a capacity retention of 98.1% after 50 cycles based on the 2nd discharge capacity. These findings were corroborated by Langrud et al., who showed complete sulfurization at 350 °C/3 h enabled 97% capacity retention over 100 cycles [59]. Fanous et al. also studied the influence of the synthesis temperature on the chemical structure and electrochemical performance of SPAN [16]. Higher synthesis temperature leads to lower sulfur content and higher degree of graphitization of the polymer backbone in SPAN, eventually resulting in higher rate capability and cycle stability. They concluded that SPAN prepared at temperatures > 450 °C showed a structural degradation, rendering 390–460 °C the optimal temperature range for synthesis. There observations were confirmed by Pan et al., who identified 300–400 °C for 12 h reaction time as producing SPAN with optimal electrochemical performance [60].

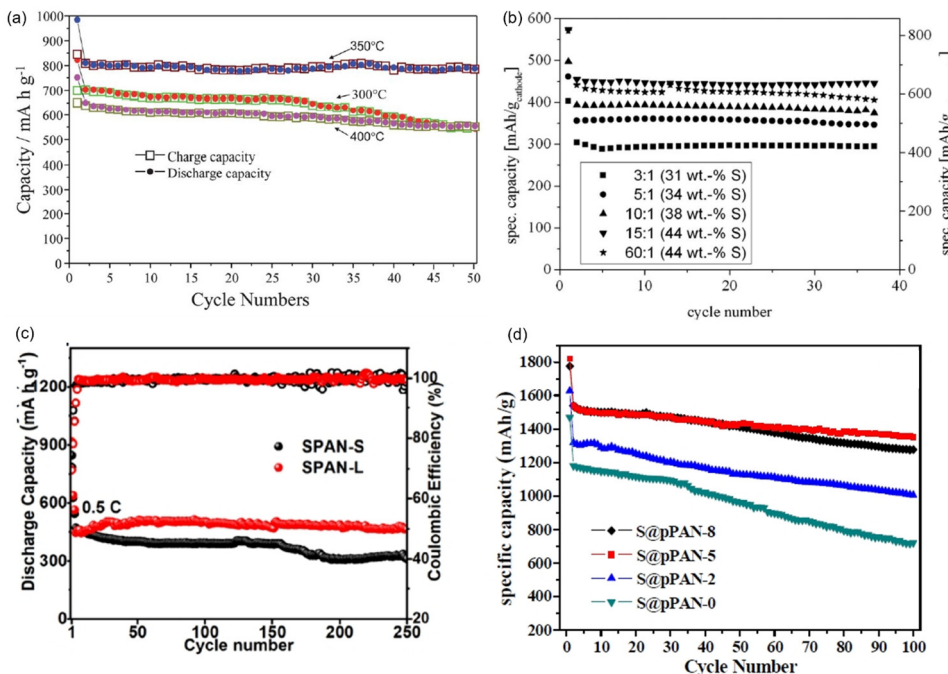


**Figure 5.** The cycling performance of SPAN cathodes prepared via different synthetic conditions. (a) Cycling performance of SPAN cathodes prepared at different temperatures (red: 300 °C; blue: 350 °C;

purple: 400 °C). Reproduced with permission [58]. Copyright © 2012, Royal Society of Chemistry; (b) Cycling performance of SPAN cathodes with different sulfur content. Reproduced with permission. Copyright © 2013, IOP Publishing, Ltd.; (c) Long-term cycling performance of SPAN cathodes prepared via conventional solid-phase synthesis (SPAN-S) and liquid-phase cyclization method (SPAN-L). Reproduced with permission [61]. Copyright © 2024, American Chemical Society; (d) Cycling performance of SPAN cathodes prepared at different vapor pressures. The number x in S@pPAN-x is the vapor pressure during the synthesis of SPAN. Reproduced with permission [62]. Copyright © 2016, Royal Society of Chemistry.

Jerez et al. reported a novel two-stage synthesis process for SPAN [63], involving initial heating at 150 °C to melt elemental sulfur followed by 300 °C treatment for complete vulcanization of PAN. The yielded SPAN composite contains 38.3% of sulfur. The assembled Li || SPAN battery delivered high capacity and stable cycling performance, with above 1000 mAh g<sup>-1</sup> sulfur after 150 cycles at 0.1 C.

While reaction time has a relatively smaller effect on the chemical and electrochemical properties of SPAN, a critical timespan of around 3–6 h is required for most SPAN synthesis to ensure the complete transformation of the PAN matrix and the covalent binding between sulfur and PAN [6]. The performance of SPAN synthesized at different timespan is summarized in Table 2. Doan et al.'s investigation of heating duration (0.5–4 h at 300 °C) determined 56 wt% as the upper limit for sulfur content while maintaining good cycle performance [17]. Lower temperatures generally require longer reaction times to achieve complete vulcanization as demonstrated by Pan et al. [60].

**Table 2.** Summary of cycling performance of SPAN synthesized at different timespan.

| Cathode  | Timespan (h) | Cathode Loading | Initial Discharge Capacity | Cycles | Final Discharge Capacity | Capacity Retention | Rate/Current Density   | Ref. |
|----------|--------------|-----------------|----------------------------|--------|--------------------------|--------------------|------------------------|------|
| PAN/S-6  | 6            | N/A             | 789 mAh g <sup>-1</sup>    | 50     | 607 mAh g <sup>-1</sup>  | 76.9%              | 100 mA g <sup>-1</sup> | [60] |
| PAN/S-12 | 12           | N/A             | 836 mAh g <sup>-1</sup>    | 50     | 648 mAh g <sup>-1</sup>  | 77.5%              | 100 mA g <sup>-1</sup> | [60] |
| PAN/S-18 | 18           | N/A             | 840 mAh g <sup>-1</sup>    | 50     | 612 mAh g <sup>-1</sup>  | 72.9%              | 100 mA g <sup>-1</sup> | [60] |

These collective findings reveal several fundamental structure-property relationships. The 300–350 °C range optimizes sulfur incorporation (50–55 wt%) while preserving the conjugated polymer structure, whereas 350–450 °C promotes enhanced graphitization that improves electronic conductivity at the expense of reduced sulfur content. Temperatures below 300 °C result in incomplete sulfurization and poor cycling performance, while exceeding 450 °C causes excessive carbonization and electrochemical activity degradation. These temperature-dependent behaviors originate from complex interplay between sulfur bonding configuration evolution (S-S versus C-S), backbone conjugation length, nitrogen environment preservation, and domain size/crystallinity development. The preponderance of evidence indicates that 350–450 °C for 3–6 h represents the optimal synthesis window, effectively balancing sulfur content, structural integrity, and electrochemical performance in SPAN materials.

## 7.2. PAN to Sulfur Ratio

The available binding sites for sulfur on the PAN matrix is limited, which restricts the final sulfur content in the SPAN (typically ranges from 30 to 56 wt%), and consequently affects the energy density of the SPAN cathode. The ratio of PAN and sulfur in the starting materials directly impacts the sulfur content in the SPAN. The performance of SPAN synthesized with different PAN/S ratio is summarized in Table 3. Fanous et al. conducted a comprehensive study examining SPAN synthesized at 550 °C with PAN/S ratio varying

from 1/3 to 1/60 [64] (Figure 5b). Their work demonstrated that while increasing sulfur content in the precursor mixture generally enhances sulfur incorporation, a saturation point exists beyond which additional sulfur does not increase the final sulfur content. Specifically, both 1:15 and 1:60 PAN/S ratios yielded SPAN with identical sulfur content of 44 wt%. Complementary research by Pan et al. explored PAN/S ratio ranging from 1/1 to 1/2, producing SPAN with sulfur content between 37.5 and 56.7 wt% [60]. The authors concluded that SPAN synthesized from PAN/S ratio of 1/1.5 delivered the optimal electrochemical performance.

**Table 3.** Summary of cycling performance of SPAN synthesized with different PAN/S ratio.

| Cathode     | PAN/S Ratio | Cathode Loading                 | Initial Discharge Capacity | Cycles | Final Discharge Capacity          | Capacity Retention | Rate/Current Density   | Ref. |
|-------------|-------------|---------------------------------|----------------------------|--------|-----------------------------------|--------------------|------------------------|------|
| SPAN_3:1    | 1:3         | 5 mg composite cm <sup>-2</sup> | N/A                        | 40     | 429 mAh g <sup>-1</sup> composite | ~100%              | C/10                   | [65] |
| SPAN_5:1    | 1:5         | 5 mg composite cm <sup>-2</sup> | N/A                        | 40     | 514 mAh g <sup>-1</sup> composite | ~100%              | C/10                   | [65] |
| SPAN_10:1   | 1:10        | 5 mg composite cm <sup>-2</sup> | N/A                        | 40     | 557 mAh g <sup>-1</sup> composite | ~100%              | C/10                   | [65] |
| SPAN_15:1   | 1:15        | 5 mg composite cm <sup>-2</sup> | N/A                        | 40     | 629 mAh g <sup>-1</sup> composite | ~100%              | C/10                   | [65] |
| SPAN_60:1   | 1:60        | 5 mg composite cm <sup>-2</sup> | N/A                        | 40     | 614 mAh g <sup>-1</sup> composite | ~100%              | C/10                   | [65] |
| PAN/S-1:1.5 | 1:1.5       | N/A                             | 856 mAh g <sup>-1</sup>    | 50     | 678 mAh g <sup>-1</sup>           | 79.2%              | 100 mA g <sup>-1</sup> | [60] |
| PAN/S-1:1.8 | 1:1.8       | N/A                             | 843 mAh g <sup>-1</sup>    | 50     | 523 mAh g <sup>-1</sup>           | 62.0%              | 100 mA g <sup>-1</sup> | [60] |
| PAN/S-1:2   | 1:2         | N/A                             | 819 mAh g <sup>-1</sup>    | 50     | 525 mAh g <sup>-1</sup>           | 64.1%              | 100 mA g <sup>-1</sup> | [60] |

### 7.3. Powder Processing

The preparation of SPAN typically involves mechanical processing of PAN and sulfur powder mixtures prior to thermal treatment. Conventional methods employ high-energy ball milling to achieve homogeneous mixing. In 2014, Konarov et al. used manual mixing followed by heat treatment at 300 °C (SPAN-m) [66]. Compared to SPAN prepared by high-energy ball milling mixing (SPAN-b), the authors claimed that manual mixing was less time and energy consuming and could avoid the breakage of PAN chains. Morphological results suggested the presence of protected uniform nanoscopic particles in SPAN-m, which exhibits better capacity retention and rate capability than SPAN-b. Further optimization of mechanical processing was investigated by Cho et al., who examined the effects of ball milling time on pre-heated PAN/S mixtures [65]. They found that pre-heated PAN/S mixtures with 5 h ball milling time yielded SPAN cathodes with the best electrochemical properties.

### 7.4. Solvent

While conventional SPAN synthesis typically employs dry powder mixtures of PAN and sulfur, alternative solvent-based methods have emerged as promising routes to enhance material homogeneity and electrochemical performance. These "wet" synthesis strategies enable molecular-level control over sulfur distribution and polymerization reactions.

In 2016, Du et al. pioneered an innovative solvent-mediated approach using dimethyl sulfoxide (DMSO) as the reaction medium [67]. Their method involved direct reaction of PAN with sulfur in DMSO solution followed by thermal treatment at 500 °C. This liquid-phase process achieved unprecedented uniformity in sulfur distribution throughout the polymer matrix, as confirmed by spectroscopic and microscopic characterization. The

resulting SPAN cathode exhibited exceptional electrochemical performance, delivering a reversible capacity of  $1304 \text{ mAh g}^{-1}$  sulfur maintained over 100 cycles at 0.5 C. More recently, Shi et al. developed a liquid-phase cyclization method employing  $\text{SOCl}_2$  as both solvent and sulfur source [61]. This two-step process first converts PAN to cyclized PAN (cPAN-L) at a relatively low temperature of  $130^\circ\text{C}$ , followed by thermal treatment at  $300^\circ\text{C}$  to produce SPAN-L. The reaction temperature is significantly lowered for the preparation of cPAN-L precursor, thereby inhibiting side reactions, and improving the structural regularity in SPAN-L. Conventional SPAN (SPAN-S) synthesized via solid-phase reaction was also prepared and tested. As a result, the  $\text{Li} \parallel \text{SPAN-L}$  battery delivered a reversible capacity of  $607.4 \text{ mAh g}^{-1}$  after 100 cycles at 0.1 C, corresponding to a capacity retention of 89.4% (Figure 5c), whereas the  $\text{Li} \parallel \text{SPAN-S}$  battery only retained 64.1% of the capacity.

### 7.5. Vapor Pressure

The vapor pressure conditions during SPAN synthesis have emerged as a critical parameter influencing both the material's chemical structure and electrochemical performance. While most preparations occur under ambient pressure or in open systems, controlled vapor pressure environments can significantly enhance the resulting material properties. The performance of SPAN synthesized at different vapor pressure is summarized in Table 4.

**Table 4.** Summary of cycling performance of SPAN synthesized at different vapor pressure.

| Cathode  | Vapor Pressure | Cathode Loading                   | Initial Discharge Capacity             | Cycles | Final Discharge Capacity         | Capacity Retention | Rate/Current Density    | Ref. |
|----------|----------------|-----------------------------------|--|--------|----------------------------------|--------------------|-------------------------|------|
| S@pPAN-0 | open           | 1.9 mg composite $\text{cm}^{-2}$ | $1176 \text{ mAh g}^{-1}$ sulfur (2nd) | 100    | $721 \text{ mAh g}^{-1}$ sulfur  | 61.3%              | $200 \text{ mA g}^{-1}$ | [64] |
| S@pPAN-2 | 2 MPa          | 1.9 mg composite $\text{cm}^{-2}$ | $1320 \text{ mAh g}^{-1}$ sulfur (2nd) | 100    | $1007 \text{ mAh g}^{-1}$ sulfur | 76.3%              | $200 \text{ mA g}^{-1}$ | [64] |
| S@pPAN-5 | 5 MPa          | 1.9 mg composite $\text{cm}^{-2}$ | $1542 \text{ mAh g}^{-1}$ sulfur (2nd) | 100    | $1357 \text{ mAh g}^{-1}$ sulfur | 88.0%              | $200 \text{ mA g}^{-1}$ | [64] |
| S@pPAN-8 | 8 MPa          | 1.9 mg composite $\text{cm}^{-2}$ | $1538 \text{ mAh g}^{-1}$ sulfur (2nd) | 100    | $1277 \text{ mAh g}^{-1}$ sulfur | 83.0%              | $200 \text{ mA g}^{-1}$ | [64] |
| SPAN     | Open system    | N/A                               | $1295 \text{ mAh g}^{-1}$ sulfur       | 200    | $1253 \text{ mAh g}^{-1}$ sulfur | 96.8%              | C/3                     | [68] |
| SPAN     | Closed system  | N/A                               | $1301 \text{ mAh g}^{-1}$ sulfur       | 200    | $1170 \text{ mAh g}^{-1}$ sulfur | 89.9%              | C/3                     | [68] |

In 2016, Liu et al. conducted systematic investigations in 2016 by synthesizing SPAN under precisely controlled vapor pressures of 0, 2, 5, and 8 MPa [62]. Their comprehensive characterization revealed that SPAN prepared at 5 MPa (SPAN-5MPa) exhibited the highest degree of graphitization, indicating formation of an optimal conductive molecular architecture. As a result, SPAN-5MPa delivered an optimal electrochemical performance, with about  $1542 \text{ mAh g}^{-1}$  sulfur in the second cycle, and a capacity retention of 88% after 100 cycles at  $200 \text{ mA g}^{-1}$  (Figure 5d). Pan et al. demonstrated that vapor pressure manipulation through reactor volume adjustment in sealed hydrothermal systems could improve SPAN's cycle stability [60]. Their findings suggested that moderate pressure increases promote more complete vulcanization reactions while preserving the polymer backbone's structural integrity. In 2024, Sarode et al. reported a novel synthesis method for SPAN with high sulfur content (53.62%) by heating PAN, sulfur, and  $\text{CoCl}_2$  mixture at elevated temperature in an alumina ceramic boat closed with an alumina plate [68]. The synthesis

method resulted in an 18% increase in sulfur incorporation, compared to the traditional open-system synthetic method.

### 7.6. PAN Precursors

The selection and characteristics of PAN precursors play a pivotal role in determining the structural and electrochemical properties of SPAN. While most studies employ commercial PAN homopolymers (average  $M_w \approx 150,000 \text{ g mol}^{-1}$ ), emerging research demonstrates that precursor molecular engineering can significantly impact SPAN performance.

Innovative synthetic strategies have explored direct polymerization of acrylonitrile (AN) monomers in the presence of sulfur. Zhu et al. developed a suspension polymerization method combining AN and elemental sulfur, yielding SPAN with  $400 \text{ mAh g}^{-1}$  reversible capacity over 30 cycles at 0.1 C [69]. Zhang et al. reported an *in situ* polymerization of acrylonitrile with nano-sulfur particles followed by vulcanization as a synthetic route to prepare SPAN [70]. The Li || SPAN battery demonstrated enhanced reversibility, with a second-cycle discharge capacity of  $1177 \text{ mAh g}^{-1}$  sulfur and retained about 100% after 100 cycles at 0.5 C.

The molecular weight of the PAN precursors influences directly on the chemical composition and the properties of SPAN. Pu et al. identified distribution of the molecular weight and purity of the PAN precursor as critical factors affecting the electrochemical performance of the SPAN [71]. Lei et al. demonstrated that higher molecular weight PAN (555 kDa) yields SPAN with 55 wt% sulfur content and outstanding cycling stability ( $710 \text{ mAh g}^{-1}$  SPAN after 200 cycles at 1 C) [72] (Figure 6a). Later, Liu et al. and Wang et al. also employed the “high-molecular-weight PAN precursor” strategy to synthesize SPAN with high sulfur content [73,74]. Liu et al. incorporated high molecular weight PAN (360 kDa) with reduced graphene oxide (rGO), creating bamboo-structured SPAN fibers with 53 wt% sulfur content. Wang et al. achieved breakthrough performance using ultra-high molecular weight PAN (1000 kDa), obtaining 54.5 wt% sulfur content and exceptional rate capability ( $695 \text{ mAh g}^{-1}$  SPAN at 5 C).

The chemical composition of PAN precursors plays an important role in the chemical and electrochemical properties of SPAN. According to Yi et al.’s report [75] and several reports on the carbon fiber industry [76,77], it is a common practice to introduce copolymeric monomers, such as itaconic acid, methacrylate, acrylic acid, or acrylamide, into the PAN polymerization system to improve the mechanical properties of the carbon fiber which is a product of PAN. Yi et al. found that the introduction of even a small amount of a second monomer into the PAN structure could lead to a significantly worse electrochemical performance of the resulting SPAN (Figure 6b). Much earlier than Yi et al.’s work, Wei et al. successfully developed a SPAN/MWCNT composite as cathode materials by ball-milling S, PAN, and MWCNT followed by pyrolysis at  $300^\circ\text{C}$  in  $\text{N}_2$  atmosphere in 2011 [78]. Instead of using homopolymer PAN, they used copolymer PAN composed of 92 wt% acrylonitrile and 8 wt% of methylacrylate, which is extensively used in textile industry and thus cheaper and more available, for the synthesis of SPAN and SPAN/MWCNT. The Li || SPAN/MWCNT battery delivered a capacity retention rate of 96.5% after 100 cycles at 0.5 C and exhibited excellent rate capability up to 7 C.

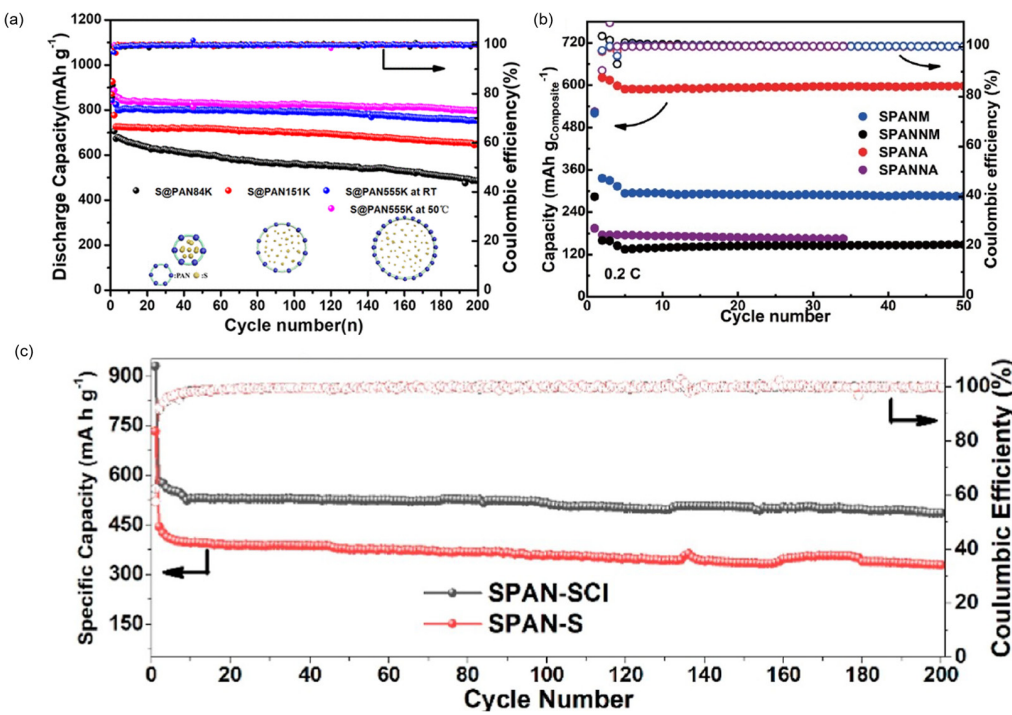


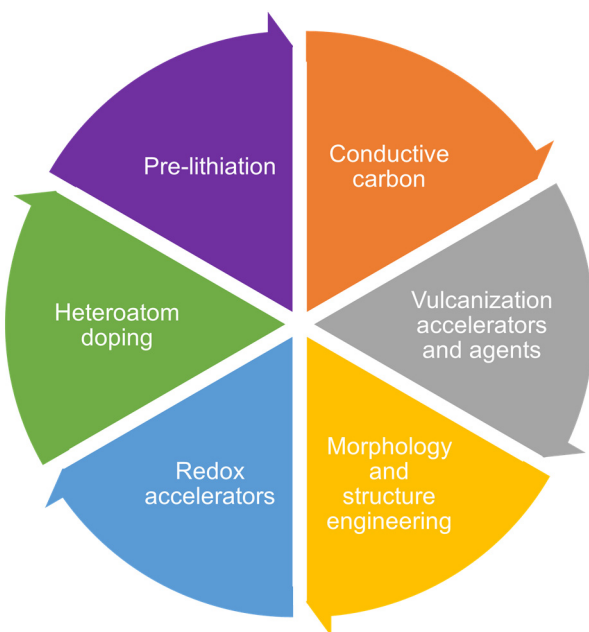
**Figure 6.** The cycling performance of SPAN cathodes prepared via different synthetic conditions. (a) Cycling performance of SPAN of different molecular weights (where the number following S@PAN indicates its molecular weight). Reproduced with permission [72]. Copyright © 2020, American Chemical Society; (b) Cycling performance of SPAN with different PAN precursors. Blue: SPANM (Macklin PAN precursor, early product); black: SPANNM (Macklin PAN precursor, recent product); red: SPANA (Sigma-Aldrich PAN precursor, early product); purple: SPANNA (Sigma-Aldrich PAN precursor, recent product). Reproduced with permission [75]. Copyright © 2024, Springer Nature; (c) Cycling performance of SPAN cathodes prepared from different vulcanization agents ( $S_2Cl_2$ : SPAN-SCI; sulfur: SPAN-S). Reproduced with permission [79]. Copyright © 2022, American Chemical Society.

### 7.7. Vulcanization Agents

Vulcanization agents other than elemental sulfur have been proposed to lower the vulcanization temperature and optimize the SPAN structure. In 2022, Shi et al. reported a highly efficient vulcanization agent,  $S_2Cl_2$ , for the SPAN synthesis with low reaction temperature [79]. It was found that  $S_2Cl_2$  could promote PAN cyclization, reduce the cyclization reaction temperature, and prevent the loss of nitrogen atoms and the agglomeration of SPAN primary particles at elevated temperatures. As a result, SPAN prepared using  $S_2Cl_2$  has a more regular structure and smaller particle size, and the Li<sup>+</sup> | SPAN battery delivered better electrochemical performance, with a second and 200th discharge capacity of 580 and 487 mAh g<sup>-1</sup> at 0.1 A g<sup>-1</sup>, respectively, corresponding to a capacity retention of 84% (Figure 6c).

## 8. Cathode Modification

Researchers have developed many effective strategies for SPAN cathode modification to improve the electrochemical performance. These strategies could be categorized into six primary research directions: conductive carbon additives, vulcanization accelerators, morphology and structure engineering, redox accelerators, heteroatoms doping, and pre-lithiation of SPAN (Scheme 2). The details are presented below.



**Scheme 2.** Schematic diagram of cathode modifications.

### 8.1. Conductive Carbon Additives

The intrinsically low electrical conductivity of SPAN represents a fundamental limitation that researchers have addressed through strategic incorporation of various carbon-based conductive additives. These materials form percolating networks that dramatically improve charge transport while maintaining the advantageous properties of SPAN. The most extensively studied carbon additives include carbon nanotubes (CNTs), graphene, porous carbon, graphite, carbon fibers, dense carbons, and their derivatives. In this section, research works that feature the modification of the SPAN cathode with conductive carbon additives will be discussed.

#### 8.1.1. Carbon Nanotubes

Carbon nanotubes (CNTs) have emerged as a transformative conductive additive for SPAN cathodes, leveraging their exceptional electrical conductivity, high aspect ratio, and mechanical flexibility to overcome the intrinsic conductivity limitations of SPAN materials [80,81]. The integration of CNTs into SPAN cathodes has been achieved through several innovative approaches, each offering distinct advantages in terms of electrochemical performance and structural stability. The performance of SPAN cathode with CNTs additives is summarized in Table 5.

In 2011, Yin et al. developed a novel SPAN@MWCNTs core–shell composite by the *in situ* co-polymerization of AN and itaconic acid (IA) on the surface of MWCNTs followed by vulcanization [82]. This approach enabled homogeneous CNT distribution throughout the SPAN matrix, establishing continuous conductive networks that significantly enhanced both cycle life and rate capability compared to conventional SPAN cathodes. Parallel work by Wei and Kim demonstrated that mechanical ball-milling of PAN, sulfur, and MWCNTs followed by pyrolysis could produce composite cathodes with similarly improved cyclability and rate performance [78,83].

CNTs have been extensively used in the construction of freestanding SPAN electrodes. In 2019, Razaq et al. reported a freestanding thin-film SPAN/CNTs cathode fabricated via electrospinning method by co-spinning sulfur, PAN, and CNTs followed by vulcanization [84] (Figure 7a). The pre-added sulfur creates a conductive pathway in the nanofiber structure upon vaporization. The interconnected CNTs network also provide a conductive

pathway for fast  $\text{Li}^+$  diffusion and electronic charge transfer. As a result, the freestanding SPAN/CNTs cathode delivered a high initial discharge capacity of  $1610 \text{ mAh g}^{-1}$  sulfur at  $0.2 \text{ C}$  and cycle stability of  $1106 \text{ mAh g}^{-1}$  sulfur for over 500 cycles at  $1 \text{ C}$ . In later works, Razzaq et al. reported a freestanding and fibrous  $\text{CoS}_2/\text{SPAN}/\text{CNTs}$  composite cathode [85] and  $\text{Co}_{10}/\text{SPAN}/\text{CNTs}$  composite cathode [86]. While CNTs dramatically enhance the fiber conductivity and generate mesoscopic porosity for charge and mass transport, the atomically dispersed Co effectively enhances the electronic conductivity and facilitates the redox kinetics of SPAN. The as-assembled  $\text{Li} \parallel \text{CoS}_2/\text{SPAN}/\text{CNTs}$  pouch cell with a high cathode areal capacity ( $8.1 \text{ mAh cm}^{-2}$ ) delivered a reversible discharge capacity of  $1322 \text{ mAh g}^{-1}$  sulfur after 17 cycles. And the  $\text{Li} \parallel \text{Co}_{10}/\text{SPAN}/\text{CNTs}$  coin cell delivered an initial capacity of  $1252 \text{ mAh g}^{-1}$  sulfur and retained  $1020 \text{ mAh g}^{-1}$  sulfur after 1500 cycles at  $1 \text{ C}$ .

**Table 5.** Summary of cycling performance of SPAN cathode with CNTs additives.

| Cathode                     | Cathode Loading  | Initial Discharge Capacity               | Cycles | Final Discharge Capacity           | Capacity Retention | Rate/Current Density    | Ref. |
|-----------------------------|--|--|--------|------------------------------------|--------------------|-------------------------|------|
| pPAN-S@MWCNT                | N/A  | $697 \text{ mAh g}^{-1}$ composite (2nd) | 50     | $592 \text{ mAh g}^{-1}$ composite | 85.0%              | C/10                    | [82] |
| SPAN/MWCNT                  | $4 \text{ mg}_{\text{composite}} \text{ cm}^{-2}$            | N/A                                      | 100    | N/A                                | 96.5%              | C/2                     | [78] |
| SPAN/C                      | N/A  | $500 \text{ mAh g}^{-1}$                 | 100    | $400 \text{ mAh g}^{-1}$           | 80.0%              | 1 C                     | [83] |
| SPAN-CNT20                  | $0.9\text{--}1.1 \text{ mg}_{\text{sulfur}} \text{ cm}^{-2}$ | N/A                                      | 500    | $1106 \text{ mAh g}^{-1}$ sulfur   | N/A                | 1 C                     | [84] |
| $\text{CoS}_2$ -SPAN-CNT    | $2.4 \text{ mg}_{\text{sulfur}} \text{ cm}^{-2}$             | $1799 \text{ mAh g}^{-1}$                | 100    | $1240 \text{ mAh g}^{-1}$          | 68.9%              | 0.2 C                   | [85] |
| $\text{Co}_{10}$ -SPAN-CNT  | $1 \text{ mg}_{\text{sulfur}} \text{ cm}^{-2}$               | $1252 \text{ mAh g}^{-1}$ sulfur         | 1500   | $1020 \text{ mAh g}^{-1}$ sulfur   | 81.5%              | 1 C                     | [86] |
| SPAN/CNT-12                 | $2 \text{ mg}_{\text{sulfur}} \text{ cm}^{-2}$               | N/A                                      | 1000   | $1180 \text{ mAh g}^{-1}$ sulfur   | ~100%              | 0.2 C                   | [87] |
| SPAN/CNT-500                | N/A  | $1814 \text{ mAh g}^{-1}$                | 200    | $1280 \text{ mAh g}^{-1}$          | 70.6%              | $400 \text{ mA g}^{-1}$ | [88] |
| CNT <sub>1</sub> @SPAN      | $5 \text{ mg}_{\text{sulfur}} \text{ cm}^{-2}$               | N/A                                      | 50     | $1079.1 \text{ mAh g}^{-1}$        | N/A                | 0.1 C                   | [89] |
| ICIHP-SPAN                  | N/A  | $614.8 \text{ mAh g}^{-1}$               | 500    | $500 \text{ mAh g}^{-1}$           | 81.3%              | 5 C                     | [90] |
| PDA@SPAN                    | $7.16 \text{ mg}_{\text{composite}} \text{ cm}^{-2}$         | N/A                                      | 160    | N/A                                | 87.18%             | 0.1 C                   | [91] |
| SPAN/MWCNTs-NH <sub>2</sub> | N/A  |  | 400    | $594.8 \text{ mAh g}^{-1}$         | 90.0%              | 1 C                     | [92] |

Further innovations in freestanding SPAN/CNTs electrode design have focused on improving electrolyte compatibility and charge transport. Wang et al. developed a freestanding fibrous SPAN/CNTs cathode compatible with both ether and carbonate electrolytes [87]. The interwoven SPAN/CNTs network not only accelerates charge transfer but also supplies fast  $\text{Li}^+$  transport channels. The SPAN/CNTs cathode delivered a reversible capacity of  $1180 \text{ mAh g}^{-1}$  sulfur with no capacity decay over 1000 cycles at  $800 \text{ mA g}^{-1}$  in ether electrolytes, demonstrating its potential for practical applications. Li et al. also reported a flexible and freestanding SPAN/CNTs nanofibrous cathode prepared via electrospinning followed by the vulcanization process [88]. The SPAN/CNTs nanofiber prepared at  $500 \text{ }^\circ\text{C}$  showed a low charge transfer resistance and the optimal cell performance, delivering reversible capacity of  $1280 \text{ mAh g}^{-1}$  over 200 cycles at  $400 \text{ mA g}^{-1}$ , corresponding to a capacity decay rate of 0.02% per cycle (Figure 7b).

Recent advances have focused on three-dimensional porous architectures to support high active material loadings. Hu et al. reported a high-loading three-dimensional hollow CNT@SPAN freestanding cathode fabricated by a one-step phase inversion method followed by vulcanization [89]. The 3D porous framework facilitates fast transport of ions and electrons, accommodates volume expansion during cycling, and mitigates the shuttle effect (Figure 7c). In addition, it was revealed that during the first discharge process,

the lithium ions occupy the carbon skeleton irreversibly, enhancing the conductivity of the composite. As a result, the  $\text{Li} \parallel \text{CNT}@\text{SPAN}$  battery with a high cathode loading (sulfur loading =  $7.5 \text{ mg cm}^{-2}$ ) exhibited  $10.21 \text{ mAh cm}^{-2}$  and delivered stable cycling for over 30 cycles at  $0.1 \text{ C}$ . In 2024, Shao et al. reported a self-supporting CNT-interpenetrating hierarchically porous SPAN (CIHP-SPAN) electrode prepared via a facile phase separation method [90]. The unique porous CIHP-SPAN cathode exhibits exceptional electron and ion conductivity. With a  $\text{V}_2\text{O}_5$ -anchored carbon fiber as the interlayer, the  $\text{Li} \parallel \text{CIHP-SPAN}$  battery delivered an initial capacity of  $614.8 \text{ mAh g}^{-1}$  sulfur and retained  $500 \text{ mAh g}^{-1}$  sulfur after 500 cycles at  $5 \text{ C}$ . Inspired by mussel and cobweb, Zuo et al. reported a high-loading SPAN cathode (PDA@SPAN/SWCNTs) enabled by the combination of polydopamine (PDA) coating and a bimodal SWCNTs slurry dispersed in polyvinylpyrrolidone (PVP) [91]. The cobweb-structured SWCNTs networks and the interactions between PDA and PVP not only improve the electrode integrity but also promote charge transport. In addition, the dynamic N-H...O hydrogen bond effectively prevents the electrode from cracking even under a high active material ratio of 95%. As a result, the  $\text{Li} \parallel \text{PDA}@\text{SPAN}/\text{SWCNTs}$  battery with a high active material loading ( $7.16 \text{ mg cm}^{-2}$ ,  $5.16 \text{ mAh cm}^{-2}$ ) retained 92.0% and 87.2% of capacity in 80 and 160 cycles at  $0.1 \text{ C}$ , respectively. Furthermore, the  $\text{Li} \parallel \text{PDA}@\text{SPAN}$  battery with an ultra-high active material loading ( $16.24 \text{ mg cm}^{-2}$ ) and lean electrolyte ( $E/\text{SPAN} = 4.8$ ) exhibited stable cycling over 60 cycles at  $0.1 \text{ C}$ .

The dispersity and chemical properties of CNTs can be altered by the chemical functionalization. Liu et al. investigated the dispersion behavior of functionalized MWCNTs within a PAN matrix and subsequently elucidated their impacts on electrochemical performance via computational and experimental studies [92]. It was found that aminated MWCNTs (MWCNTs-NH<sub>2</sub>), which possess lower mixing free energy and the closest Hansen solubility parameters to PAN, exhibit the optimal dispersion characteristics. Consequently, the  $\text{Li} \parallel \text{SPAN}/\text{MWCNTs-NH}_2$  battery delivered initial discharge capacities of 907.4 and  $842.4 \text{ mAh g}^{-1}$  and retained 92.4% and 90.0% after 200 and 400 cycles at  $0.2$  and  $1.0 \text{ C}$ , respectively (Figure 7d).

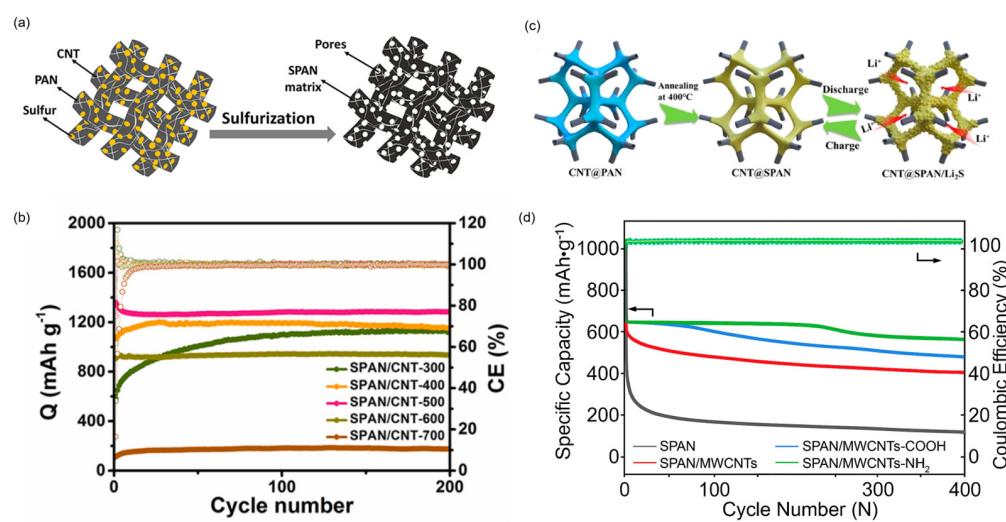


**Figure 7.** SPAN cathodes composed with CNTs. (a) Synthesis of the freestanding thin-film SPAN/CNTs cathode. Reproduced with permission [84]. Copyright © 2019, Elsevier; (b) Cycling performance of SPAN/CNT composite cathodes prepared at different temperatures. The number followed by the “–” sign is the temperature at which the SPAN/CNT is prepared. Reproduced with permission [88]. Copyright © 2021, Elsevier; (c) Schematic representation of the synthesis and

charge/discharge behavior of CNT@SPAN cathode. Reproduced with permission [89]. Copyright © 2023, American Chemical Society. (d) Cycling performance of different SPAN/MWCNT composites. Reproduced with permission [92]. Copyright © 2023, American Chemical Society.

### 8.1.2. Graphene

Graphene is a two-dimensional carbon material with a single layer of carbon atoms in a honey-comb lattice [93]. Graphene has been used as a carbon additive in the SPAN cathode. The performance of SPAN cathode with graphene additives is summarized in Table 6.

**Table 6.** Summary of cycling performance of SPAN cathode with graphene additives.

| Cathode              | Cathode Loading                                  | Initial Discharge Capacity                      | Cycles | Final Discharge Capacity          | Capacity Retention | Rate/Current Density | Ref.  |
|----------------------|--|---|--------|-----------------------------------|--------------------|----------------------|-------|
| pPAN-S/GNS 4%        | N/A  | 1500 mAh g <sup>-1</sup> sulfur                 | 100    | 1200 mAh g <sup>-1</sup> sulfur   | 80%                | C/10                 | [94]  |
| pPAN-S/mGO-S         | 1–2 mg <sub>composite</sub> cm <sup>-2</sup>     | 900 mAh g <sup>-1</sup> composite               | 50     | 650 mAh g <sup>-1</sup> composite | N/A                | C/10                 | [95]  |
| S/PAN/Graphene       | 3.5 mg <sub>composite</sub> cm <sup>-2</sup>     | 612 mAh g <sup>-1</sup> (2nd cycle)             | 100    | N/A                               | 77%                | C/10                 | [96]  |
| pPAN-S@GNS           | 2 mg <sub>composite</sub> cm <sup>-2</sup>       | 681.2 mAh g <sup>-1</sup> composite (2nd cycle) | 300    | N/A                               | 88.8%              | 0.2 C                | [97]  |
| S/DPAN/rGO           | N/A  | g <sup>-1</sup> sulfur (2nd cycle)              | 100    | N/A                               | 92%                | 0.2 C                | [98]  |
| PAN/S/GO             | 2.4 mg <sub>sulfur</sub> cm <sup>-2</sup>        | 1402 mAh g <sup>-1</sup> sulfur                 | 50     | 1096 mAh g <sup>-1</sup> sulfur   | N/A                | 0.2 C                | [99]  |
| 3DHG/PS2             | 15.2 mg <sub>composite</sub> cm <sup>-2</sup>    | N/A   | 1500   | 581.6 mAh g <sup>-1</sup> sulfur  | 81.5%              | 2 C                  | [100] |
| 2D-SPAN/G            | 10 mg <sub>sulfur</sub> cm <sup>-2</sup>         | N/A   | 300    | N/A                               | 79.0%              | 0.25 C               | [101] |
| SFPAN-g-rGO (2000:1) | 1.2–1.6 mg <sub>composite</sub> cm <sup>-2</sup> | 1303 mAh g <sup>-1</sup> (after activation)     | 800    | 1129 mAh g <sup>-1</sup>          | N/A                | 1 C                  | [73]  |
| SPAN/RGO             | 8.0 mg <sub>composite</sub> cm <sup>-2</sup>     | N/A   | 60     | 670.2 mAh g <sup>-1</sup>         | N/A                | 0.1 C                | [102] |

In 2012, Yin et al. reported the preparation of SPAN/graphene nanosheet (GNS) composite via in situ polymerization of AN at the presence of graphene oxide, followed by reduction by hydrazine hydrate and pyrolysis with sulfur [94]. The resulting composite cathode with 4 wt% graphene demonstrated significantly improved cycle life and rate capacity (Figure 8a). In the same year, the same group reported a dual-mode SPAN/mildly reduced graphene oxide nanosheets composite as cathode materials [95]. In this composite, sulfur is both covalently bonded with the PAN matrix and non-covalently dispersed in the mildly reduced graphene oxide nanosheets, achieving a high sulfur content of 65.1 wt%. The composite cathode exhibited about 900 mAh g<sup>-1</sup> composite discharge capacity and 650 mAh g<sup>-1</sup> composite reversible capacity for 50 cycles. Zhang et al. prepared a SPAN/graphene composite via ball milling of PAN, sulfur, and graphene, followed by heat treatment at 350 °C [96]. The cell displayed stable cycling across various current densities between 0.5 and 4 C, demonstrating improved electrochemical properties. Li et al. synthesized graphene oxide (GO) via a modified Hummer's method and fabricated SPAN/GO composite with a simple physical blending method [103].

With further studies of graphene for SPAN cathodes, different preparation methods have been employed to tailor SPAN/graphene composite with different morphologies and chemical structures. Wang et al. reported a microspherical-structured SPAN/GNS composite cathode prepared via spray drying PAN nanoparticles and GNS, followed by vulcanization [97] (Figure 8b). Scanning electron microscopy (SEM) and TEM revealed that

PAN nanoparticles are uniformly and loosely wrapped by GNS. The SPAN/GNS composite cathode exhibited a high reversible capacity of  $681.2 \text{ mAh g}^{-1}$  composite in the second cycle and retained 88.8% capacity after 300 cycles at 0.2 C.

Konarov et al. developed a SPAN/rGO composite prepared through self-assembling modification of rGO on SPAN, enhancing the electric conductivity of the composite to  $\sim 10^{-4} \text{ S cm}^{-1}$  [98]. This SPAN/rGO cathode exhibited an initial discharge capacity of  $1490 \text{ mAh g}^{-1}$  sulfur and retained 92% capacity after 100 cycles at 0.2 C (Figure 8c). Similarly, Krishnaveni et al. fabricated a SPAN/GO composite via solution processing [99]. Morphological study showed that SPAN is wrapped by highly conductive wrinkled layers of GO which not only suppress the shuttling issue but also help accommodating volume changes during cycling. The resulting Li || SPAN battery delivered an initial discharge capacity of  $1402 \text{ mAh g}^{-1}$  sulfur and retained  $1096 \text{ mAh g}^{-1}$  sulfur after 50 cycles at 0.1 C.

For high-mass-loading SPAN cathodes, Wang et al. designed a three-dimensional holey graphene/SPAN (SPAN/3DHG) composite [100]. The 3D holey graphene framework ensures fast electron and ion transport within the thick electrode and affords space to mitigate the volume expansion during cycling. The as-assembled Li || SPAN/3DHG battery with a cathode loading of  $15.2 \text{ mg cm}^{-2}$  delivered  $581.6 \text{ mAh g}^{-1}$  sulfur after 1500 cycles at 2 C, corresponding to a capacity retention of 81.5%. A compact and high-mass-loading two-dimensional SPAN/graphene (2D-SPAN/G) cathode was prepared via a high-pressure pelletization method by Kim et al. [101] (Figure 8d). The graphene nanosheets function as a robust and conductive scaffold, encapsulating SPAN nanoparticles, providing structural integrity, and enabling high utilization of sulfur. The Li || 2D-SPAN/G battery with a high areal capacity of  $11 \text{ mAh cm}^{-2}$  exhibited a capacity retention of 79.0% after 300 cycles at  $4 \text{ mA cm}^{-2}$ . In addition, the Li || 2D-SPAN/G pouch cell with an area capacity of  $6 \text{ mAh cm}^{-2}$  retained 69.1% capacity after 150 cycles at  $4 \text{ mA cm}^{-2}$ .

Liu et al. developed a bamboo-shaped SPAN/rGO composite with SPAN as the bamboo stalk and rGO as the bamboo joint [73]. The SPAN/rGO composite is fabricated by the free radical polymerization of AN in the presence of rGO followed by electrospinning and vulcanization. In 2025, Lu et al. reported a freestanding SPAN/rGO cathode with nacre-like architecture fabricated by high-speed dispersion and coating [102]. The graphene nanosheets provide a conductive framework and the dense layered structure effectively alleviates the volume expansion during cycling. As a result, the Li || SPAN/rGO batteries with high SPAN loadings of  $8.0$  and  $10.0 \text{ mg cm}^{-2}$  delivered  $670.2$  and  $525.5 \text{ mAh g}^{-1}$  after 60 cycles at 0.1 C, respectively.

### 8.1.3. Porous Carbon

Porous carbon is one of the most representative carbon materials which possesses pores of various sizes [104]. Porous carbons such as acetylene black (AB), Ketjen black (KB), Super P, etc., and their derivatives have been used as a conductive additive for the SPAN electrodes in many works. This subsection focuses on studies featuring the use of porous carbon in SPAN cathodes are discussed. The performance of SPAN cathode with porous carbon additives is summarized in Table 7.

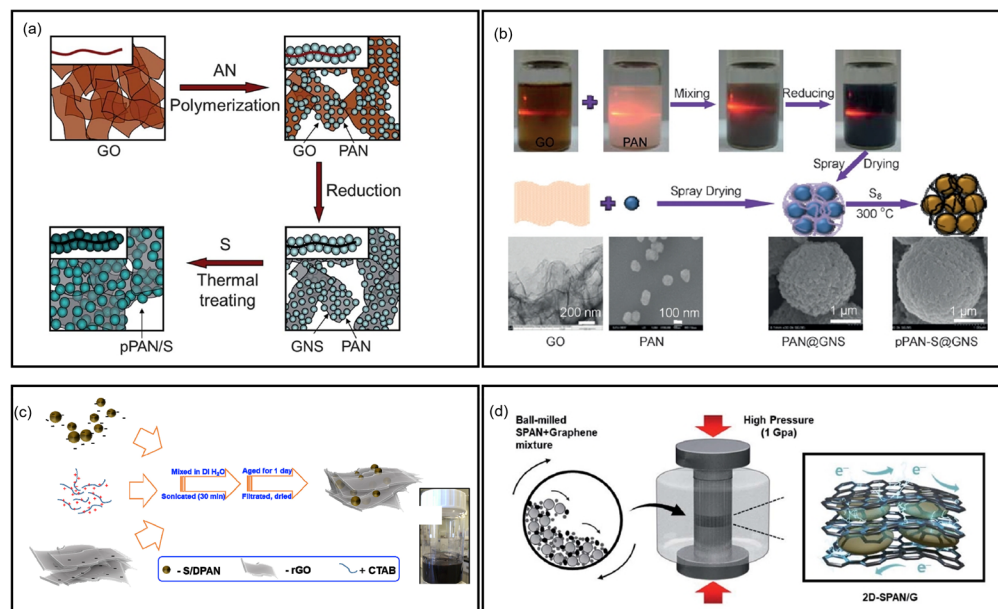


**Figure 8.** SPAN cathodes composed with graphenes. (a) Schematic illustration of the in situ polymerization and synthesis of SPAN/graphene composites. Reproduced with permission [94]. Copyright © 2012, Royal Society of Chemistry; (b) Schematic illustration of the synthetic process of SPAN/graphene composite via spray drying and heat treatment. Reproduced with permission [97]. Copyright © 2014, Wiley—VCH; (c) Schematic illustration of rGO attachment to SPAN by self-assembly. Reproduced with permission [98]. Copyright © 2017, Elsevier; (d) Schematic illustration of the fabrication of 2D-SPAN/G. Reproduced with permission [101]. Copyright © 2022, Royal Society of Chemistry.

**Table 7.** Summary of cycling performance of SPAN cathode with porous carbon additives.

| Cathode                | Cathode Loading                                    | Initial Discharge Capacity                    | Cycles | Final Discharge Capacity            | Capacity Retention | Rate/Current Density    | Ref.  |
|------------------------|--|---|--------|-------------------------------------|--------------------|-------------------------|-------|
| PAN-S/C                | N/A  | N/A   | 50     | 658.8 mAh g <sup>-1</sup> SPAN      | 95%                | C/10                    | [105] |
| pPAN-KB/S              | 4.4 mg <sub>sulfur</sub> cm <sup>-2</sup>          | N/A   | 50     | 513 mAh g <sup>-1</sup> sulfur      | N/A                | C/2                     | [106] |
| SPAN@D-KB              | 2 mg <sub>composite</sub> cm <sup>-2</sup>         | N/A   | 350    | 653 mAh g <sup>-1</sup> composite   | N/A                | 0.2 C                   | [107] |
| pPAN <sup>1</sup> @C/S | 0.6–0.8 mg <sub>sulfur</sub> cm <sup>-2</sup>      | 1269 mAh g <sup>-1</sup> sulfur               | N/A    | N/A                                 | N/A                | 0.5 C                   | [108] |
| S/MCPs-PAN-52          | 1 mg <sub>sulfur</sub> cm <sup>-2</sup>            | 789.7 mAh g <sup>-1</sup> composite           | 200    | 666.2 mAh g <sup>-1</sup> composite | N/A                | 160 mA g <sup>-1</sup>  | [109] |
| S/rSP@SPAN             | 0.79–0.81 mg <sub>composite</sub> cm <sup>-2</sup> | 1500 mAh g <sup>-1</sup> sulfur (2nd cycle)   | 100    | 1251 mAh g <sup>-1</sup> sulfur     | N/A                | 0.1 C                   | [110] |
| PANC@BP/PAN/S          | N/A  | 700 mAh g <sup>-1</sup> composite (2nd cycle) | 400    | 612 mAh g <sup>-1</sup> composite   | 87.6%              | 100 mA g <sup>-1</sup>  | [111] |
| PBD622-400             | 2.5–6.7 mg <sub>composite</sub> cm <sup>-2</sup>   | 1431 mAh g <sup>-1</sup> sulfur               | 150    | 806 mAh g <sup>-1</sup> sulfur      | N/A                | 1050 mA g <sup>-1</sup> | [112] |

In 2013, Wen et al. reported the preparation of SPAN/porous carbon composite by the heat diffusion method, where porous carbon was synthesized from pyrolyzed phenol resin by hydrothermal reaction [105]. The SPAN/porous carbon composite cathode retained  $658.8 \text{ mAh g}^{-1}$  SPAN after 50 cycles at 0.1 C, 95% of the second cycle charging capacity.

A dual-mode SPAN/KB composite was developed by Sohn et al. where sulfur was both covalently bonded to the SPAN matrix and noncovalently dispersed in the composite [106]. In 2024, Xu et al. engineered defective Ketjen Black (D-KB) as the matrix of

SPAN by a dissolution-precipitation process to construct the internal conductive network of SPAN (SPAN@D-KB) [107]. Compared to pristine KB, D-KB has the advantages of high active site density and high specific surface area ( $1446.3\text{ m}^2\text{ g}^{-1}$ ), therefore the conductivity and reaction kinetics of the obtained SPAN@D-KB is improved. The  $\text{Li} \parallel \text{SPAN@D-KB}$  battery delivered a reversible discharge capacity of  $700\text{ mAh g}^{-1}$  composite and retained  $653\text{ mAh g}^{-1}$  composite after 350 cycles at  $0.2\text{ C}$  (Figure 9a).

Chang et al. reported an interconnected core–shell pyrolyzed polyacrylonitrile@sulfur/carbon nanocomposites for LSBs [108], in which the conductive porous carbon structure acted as nanoreactors and restricted the polysulfides dissolution. The composite cathode delivered an initial capacity of  $1269\text{ mAh g}^{-1}$  sulfur at  $0.5\text{ C}$ . Zhang et al. developed novel microporous carbon polyhedrons (MCPs) encapsulated PAN nanofibers for fabricating sulfur composite cathodes [109] (Figure 9b). The S/MCPs-PAN composite was prepared by electrospinning MCPs and PAN followed by co-heating MCPs-PAN with sulfur. The MCPs provide a sufficient sulfur loading area and PAN offers the structure stability and a conductive path. Consequently, the S/MCPs-PAN cathode with 52 wt% sulfur content delivered an initial discharge capacity of  $789.7\text{ mAh g}^{-1}$  composite and  $666.2\text{ mAh g}^{-1}$  composite after 200 cycles at  $160\text{ mA g}^{-1}$  current density. Kuo et al. reported a SPAN wrapped porous carbon-sulfur composite (S/rSP@SPAN) as cathode materials for LSBs [110] (Figure 9c). S/rSP@SPAN was synthesized using a dissolution-reprecipitation method followed by the thermal treatment. The dissolution-reprecipitation process augments the surface area of the composite which provides high sulfur loading area, improved active materials-electrolytes contact, and high conductivity. The resulting  $\text{Li} \parallel \text{S/rSP@SPAN}$  battery delivered an excellent rate performance with  $492\text{ mAh g}^{-1}$  sulfur at  $10\text{ C}$  and stable cycling with  $1251\text{ mAh g}^{-1}$  sulfur over 100 cycles at  $0.1\text{ C}$ . A new  $\text{Li}^+$ -conductive porous carbon (PANC@BP) for SPAN electrodes was proposed by Zhang et al. [111]. PANC@BP was prepared by coating Black Pearls 2000 with 10% PAN pyrolysis carbon. It was demonstrated that PANC@BP could inhibit the polysulfides dissolution during cycling. The  $\text{Li} \parallel \text{PANC@BP-SPAN}$  battery delivered a second cycle discharge capacity of about  $700\text{ mAh g}^{-1}$  composite and maintained  $661\text{ mAh g}^{-1}$  composite after 300 cycles at  $100\text{ mA g}^{-1}$ . A novel composite material, SPAN confined in macro-porous carbon (MaPC), was firstly reported as the cathode material to improve the cycle stability of  $\text{Li} \parallel \text{SPAN}$  batteries [112]. MaPC provides an interconnected electron conductive network and the space to accommodate active materials. The  $\text{Li} \parallel \text{SPAN}$  coin cell delivered a discharge capacity of  $806\text{ mAh g}^{-1}$  sulfur after 150 cycles at  $1050\text{ mA g}^{-1}$ . A  $0.8\text{ Ah Li} \parallel \text{SPAN}$  pouch cell with high cathode loading of  $10\text{ mg composite cm}^{-2}$  and lean electrolyte ( $3\text{ mL Ah}^{-1}$ ) maintained stable cycling for 25 cycles at  $0.5\text{ C}$ .

#### 8.1.4. Graphite

Graphite (Gr), a naturally occurring crystalline carbon allotrope, is the most commercially successful anode material for LIBs due to its excellent conductivity and structural stability [113]. Its role has expanded to SPAN cathodes as a conductive additive.

In 2021, Zhang et al. demonstrated the effectiveness of KS6 graphite in SPAN cathodes [114]. The SPAN composite containing 10 wt% KS6 exhibited exceptional electrochemical performance, delivering an initial discharge capacity of  $1700\text{ mAh g}^{-1}$  sulfur and maintaining  $1050\text{ mAh g}^{-1}$  sulfur after 50 cycles at  $100\text{ mA g}^{-1}$ . This highlights graphite's potential not only as an anode material but also as a versatile conductive agent for high-performance SPAN-based cathodes.

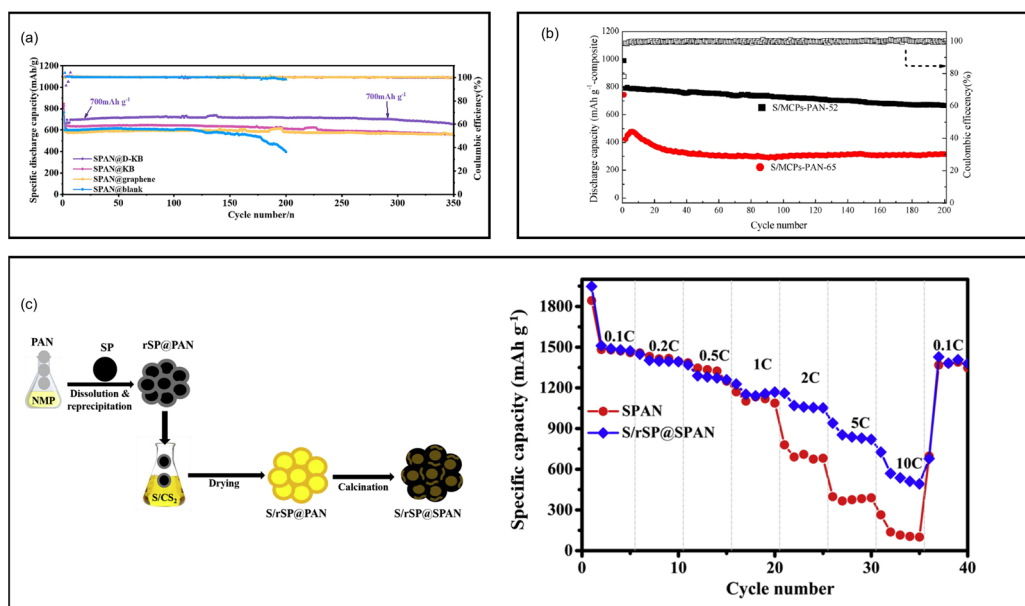


**Figure 9.** SPAN cathodes composed with porous carbon. (a) Cycling performance of SPAN@D–KB, SPAN@KB, SPAN@graphene, and SPAN@blank. Reproduced with permission [107]. Copyright © 2024, Elsevier; (b) Cycling performance of the S/MCPs–PAN composite. Reproduced with permission [109]. Copyright © 2017, American Chemical Society; (c) Schematic illustration of the synthetic procedure of S/rSP@SPAN and rate capabilities of the S/rSP@SPAN and the reference SPAN cathode. Reproduced with permission [110]. Copyright © 2019, Elsevier.

#### 8.1.5. Carbon Fibers

Carbon fibers have emerged as promising conductive frameworks for SPAN cathodes, offering both ionic conductive pathways and enhanced electrochemical performance. In 2019, Liu et al. reported a freestanding porous SPAN/vapor grown carbon fiber composite (VGCF) as cathode materials for Li||SPAN batteries [115] (Figure 10a). SPAN/VGCF was prepared by electrospinning PAN, polystyrene (PS), and VGCF suspension followed by vulcanization. During vulcanization, PS decomposed to create parallel channels in the fibers, enabling rapid ion transfer and complete utilization of the active materials. As a result, the freestanding SPAN/VGCF cathode demonstrated excellent cycling stability and rate performance, delivering 903 mAh g<sup>-1</sup> sulfur after 150 cycles at 1 C and 600 mAh g<sup>-1</sup> sulfur after 300 cycles at 2 C.

Han et al. reported a high-mass-loading Se<sub>0.05</sub>S<sub>0.95</sub>PAN cathode with a layered reinforce concrete structure (LRCS) by integrating an ice-template method with incorporated carbon fibers (CFs) [116] (Figure 10b). The LRCS enables aligned through-channel structure and intertwined conductive network, leading to fast electron and ion transport and enhanced electrode integrity. Consequently, the Li||Se<sub>0.05</sub>S<sub>0.95</sub>PAN battery with a high cathode mass loading (20.2 mg cm<sup>-2</sup>), low E/S ratio of 2, and limited Li (N/P = 2.7) delivered an areal capacity of 10 mAh cm<sup>-2</sup> and a capacity retention of 80.8% after 140 cycles at 1 mA cm<sup>-2</sup>. A 40 mAh Li||Se<sub>0.05</sub>S<sub>0.95</sub>PAN pouch cell (cathode loading of 20.2 mg cm<sup>-2</sup>, N/P = 2.7, E/S = 2) showed stable cycling over 15 cycles with slight capacity decay.

#### 8.1.6. Dense Carbon

Recent advances in SPAN composites have explored dense carbon architectures to enhance electrode density and conductivity. In 2022, Jo et al. reported a novel SPAN/dense carbon composite material (CS-DPAN) prepared by adding terephthalic acid (TPA) to the conventional SPAN synthesis [117]. CS-DPAN is composed of dense carbon and SPAN, resulting in higher tap density ( $\approx$ 1.02 g cm<sup>-3</sup>), conductivity, and surface area than the

conventional SPAN. As a result, the Na<sup>+</sup> | CS-DPAN battery delivers an initial discharge capacity of 1628 mAh g<sup>-1</sup> sulfur and retained 77% after 300 cycles at 0.5 C.

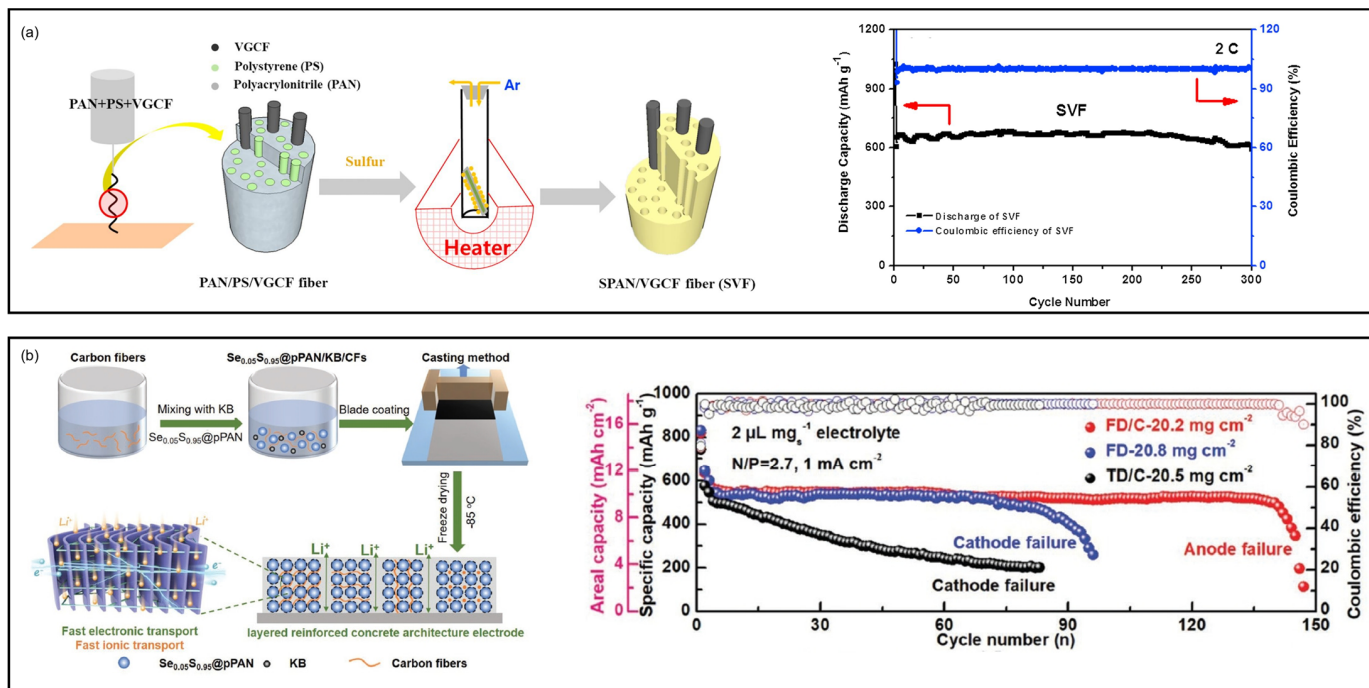


**Figure 10.** SPAN cathodes composed with carbons. **(a)** Schematic illustration of the fabrication steps for the SVF composite and cycling performance of SVF. Reproduced with permission [115]. Copyright © 2019, Elsevier; **(b)** Schematic illustration of the electrode fabrication process via lyophilization and incorporating carbon fibers and cycling performance of thick SPAN electrodes. Reproduced with permission [116]. Copyright © 2021, John Wiley and Sons.

### 8.2. Vulcanization Accelerators and Vulcanization Agents

The energy density of SPAN cathodes is intrinsically limited by their sulfur content. To address this, researchers have adapted vulcanization accelerators (VAs) from rubber industry practices, where these additives are known to promote crosslinking and improve material properties [118]. Typical VAs include thiocarbamates, thiazoles, sulfenamides, thiuram disulfides, etc. When incorporated into SPAN synthesis, these compounds not only increase sulfur incorporation but also enhance the electrochemical performance of the resulting cathodes. The performance of SPAN cathode with different VA additives is summarized in Table 8.

**Table 8.** Summary of cycling performance of SPAN cathode with different VA additives.

| Cathode   | Cathode Loading              | Initial Discharge Capacity                    | Cycles | Final Discharge Capacity          | Capacity Retention | Rate/Current Density | Ref.  |
|---|------------------------------|---|--------|-----------------------------------|--------------------|----------------------|-------|
| PAN-S-VA  | N/A                          | 494 mAh g <sup>-1</sup> composite (2nd cycle) | 200    | 477 mAh g <sup>-1</sup> composite | 95%                | 0.25 C               | [119] |
| S@PAN-DG  | 5 mg SPAN cm <sup>-2</sup>   | N/A   | 100    | 815 mAh g <sup>-1</sup> composite | 91.5%              | 0.25 C               | [120] |
| SPAN-DG   | 5 mg SPAN cm <sup>-2</sup>   | 730 mAh g <sup>-1</sup> composite (2nd cycle) | 500    | 620 mAh g <sup>-1</sup> composite | 84.93%             | 1 C                  | [121] |
| SPAN-1  | 2 mg sulfur cm <sup>-2</sup> | N/A   | 2000   | 857 mAh g <sup>-1</sup>           | N/A                | 5 A g <sup>-1</sup>  | [122] |
| Se <sub>0.05</sub> S <sub>0.95</sub> PAN-TiI <sub>1</sub> | 2 mg cm <sup>-2</sup>        | N/A   | 1000   | N/A                               | 89.4%              | 2 C                  | [123] |
| SPAN-1.5%HBO  | N/A                          | 853 mAh g <sup>-1</sup>                       | 100    | 577 mAh g <sup>-1</sup>           | N/A                | 1 C                  | [124] |

The pioneering work by Chen et al. in 2015 first demonstrated the effectiveness of this approach by employing 2-mercaptobenzothiazoles (MBT) as a VA [119]. Through a process involving ball milling with PAN and sulfur followed by thermal treatment at 280 °C, they achieved an 8 wt% increase in sulfur content and a corresponding 120 mAh g<sup>-1</sup> improvement in discharge capacity compared to conventional SPAN. This breakthrough prompted further systematic investigations into VA effects. Wang et al. conducted a comparative study on the effect of different VAs on the electrochemical performance of SPAN cathodes [120] (Figure 11a). Diphenyl guanidine (DG), zinc N-ethyl-N-phenyldithiocarbamate (ZDB), tetrathylthiuruam disulfide (TD), MBT, 2,2-dithiobis(benzothiazole) (DBB), and ethlenethiourea (ET) were selected and tested. Among these, the low-speed DG can effectively expand the space of the crosslinking of PAN chain and provide more vacancies and time for the sulfurization, resulting in an improvement of sulfur content in SPAN by 14 wt% and a remarkable discharge capacity of 897 mAh g<sup>-1</sup> composite at 0.1 C. The beneficial effect of DG and MBT on the electrochemical performance of SPAN is also confirmed in other works [74,121,122].

Recent advances have further refined this approach. In 2023, Wu et al. reported a triallyl isocyanurate (TI) incorporated Se<sub>0.05</sub>S<sub>0.95</sub>PAN fibrous composite (Se<sub>0.05</sub>S<sub>0.95</sub>PAN-TI11) prepared via electrospinning and vulcanization as the cathode materials for Li/Na||SPAN batteries [123]. TI as a commonly used polymer crosslinker and vulcanization accelerator could boost the S and Se content (54.2%) in the composite. The fibrous Se<sub>0.05</sub>S<sub>0.95</sub>PAN-TI11 structure allows for fast electron and ion transport and effectively mitigates the shuttle effect. Consequently, the Li||Se<sub>0.05</sub>S<sub>0.95</sub>PAN-TI11 and Na||Se<sub>0.05</sub>S<sub>0.95</sub>PAN-TI11 cells exhibited capacity retention rates of 89.4% and 74.3% after 1000 and 300 cycles at 2 C and 0.5 C, respectively. Remarkably, under practical conditions (S&Se loading = 5.5 mg cm<sup>-2</sup>, E/S&Se = 5 µL mg<sup>-1</sup>), the Li||Se<sub>0.05</sub>S<sub>0.95</sub>PAN-TI11 cell delivered a capacity retention of 84% after 200 cycles at 0.1 C. Boric acid (HBO) has been reported to retard the cyclization of PAN during carbon fiber manufacturing [125,126]. Zhang et al. introduced a small amount of HBO the precursor materials of SPAN by ball milling before heat treatment to delay the cyclization of PAN and increase the sulfur content of SPAN [124] (Figure 11b). The as-synthesized SPAN (SPAN-HBO) exhibits a high sulfur content of 54.24 wt%. As a result, the Li||SPAN-HBO battery delivers an initial discharge capacity of 881 mAh g<sup>-1</sup> and retains 734 mAh g<sup>-1</sup> after 100 cycles at 0.1 C.

### 8.3. Morphology and Structure Engineering

The electrochemical performance of SPAN-based batteries is critically dependent on both the intrinsic morphology of SPAN materials and the engineered architecture of the cathode. Conventional SPAN synthesized through direct heat treatment of PAN and sulfur typically forms amorphous particulate structures. However, strategic morphological engineering has enabled the development of advanced SPAN configurations with enhanced electrochemical properties.

The electrospinning technology has been widely employed to obtain fibrous SPAN, which possesses fast channels for ion transport and electron migration [127]. Li et al. investigated the effects of diameter of SPAN fibers on the sulfur content and the electrochemical performance [128] (Figure 12a). PAN fibers with various diameters were fabricated by electrospinning and were transformed into SPAN fibers by vulcanization. It is found that the smaller the fiber diameter, the higher the sulfur content, the larger the surface area, and the better the electrochemical performance in SPAN. The SPAN fibers derived from a PAN precursor with 0.5 µm diameter contains 47 wt% sulfur, delivers an initial discharge capacity of 1284 mAh g<sup>-1</sup> sulfur, and retains 92% of the capacity after 200 cycles at 0.2 C. The benefits of fibrous SPAN architectures were further demonstrated by Hwang et al.,

who developed electrospun SPAN nanofibers for room-temperature Na<sup>+</sup> | SPAN batteries [129]. The electrospun SPAN cathode exhibited excellent cycling performance such that 70% (153 mAh g<sup>-1</sup><sub>total</sub>) of the capacity (219 mAh g<sup>-1</sup><sub>total</sub>) in the fifth cycle was retained after 500 cycles. An ultrathin two-dimensional SPAN nanosheet cathode was developed by Wang et al. via a salt-templating method, which afforded a large contact area with the electrolyte and shortened the transport paths of electrons and ions during the redox reaction [130] (Figure 12b).

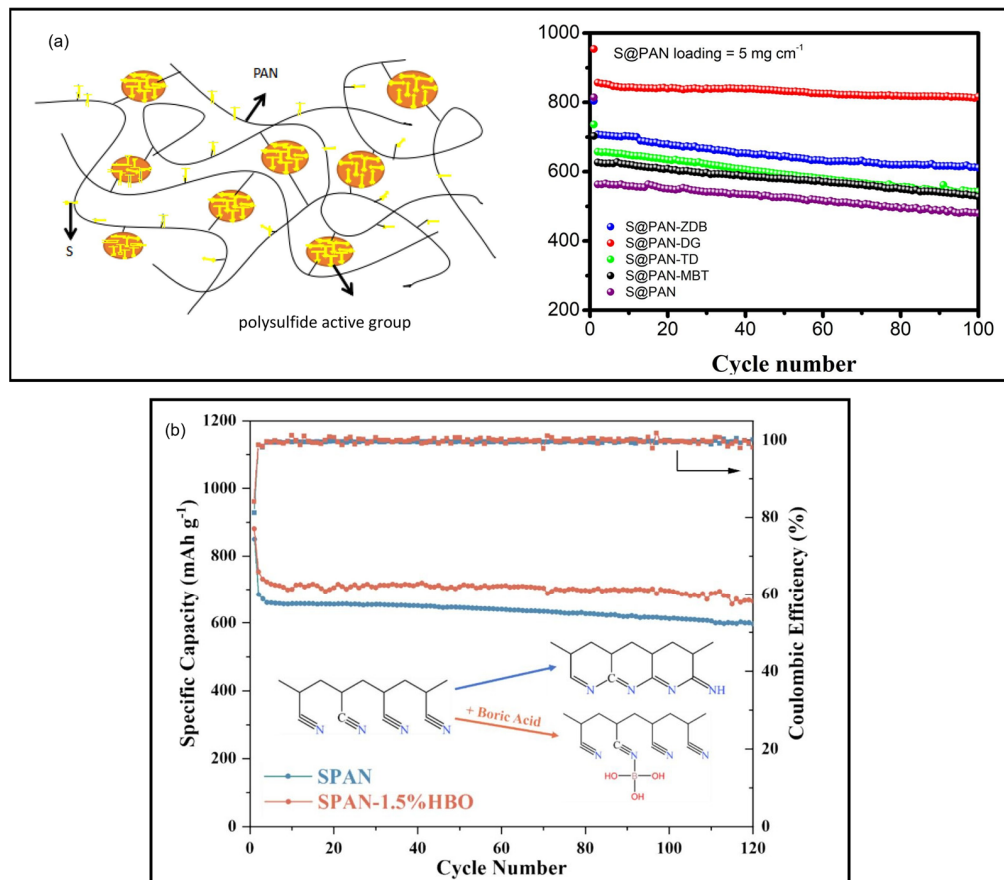


**Figure 11.** SPAN cathodes with different vulcanization accelerators. (a) Schematic illustration of SPAN co-vulcanized by vulcanization accelerators and cycling performance of SPAN–VA composites. Reproduced with permission [120]. Copyright © 2020, Elsevier; (b) Schematic illustration of the SPAN vulcanization process and cycling performance of SPAN and SPAN–1.5%HBO. Reproduced with permission [124]. Copyright © 2024, Elsevier.

The strategic use of sacrificial templates has enabled the development of porous SPAN architectures with superior electrochemical properties compared to conventional particulate structures. This approach creates precisely controlled cavities within both fibrous and bulk SPAN materials, significantly enhancing their performance characteristics. In 2017, Frey et al. firstly reported a fibrous SPAN composite prepared from a simple reaction of PAN/poly(methyl methacrylate) PMMA nonwoven fibers with sulfur at 550 °C [131]. The elimination of PMMA under high temperature produces cylindrical macropores in SPAN which help form electronic conductive networks. Consequently, the Li<sup>+</sup> | SPAN battery delivered an initial capacity of 1672 mAh g<sup>-1</sup><sub>sulfur</sub>, better rate performance than the normal SPAN cathode, and excellent cycle stabilities over 1000 cycles at C-rates alternating between 0.5 and 8 C. A highly ordered mesoporous SPAN composite (MSPAN) was developed by Liu et al. [132] (Figure 12c). MSPAN was synthesized via in situ polymerization of acrylonitrile in an SBA-15 template followed by etching with HF and heat treatment

with sulfur. The MSPAN exhibited ordered mesoporous structure which enhances the wettability, accessibility, and absorption of electrolytes. It facilitated rapid ion transfer and high specific surface area ( $423.8 \text{ m}^2 \text{ g}^{-1}$ ) which could disperse the current density through the electrode while achieving high utilization of the active materials. The MSPAN cathode delivered superior cycling and rate performance, with a reversible capacity of  $755 \text{ mAh g}^{-1}$  after 200 cycles at 1 C and  $610 \text{ mAh g}^{-1}$  after 900 cycles at 2 C. In several other works, PMMA [133,134], PS [115,135,136], polyethylene oxide [137] (PEO), and sodium bicarbonate [138] were used as the sacrificial precursors to construct SPAN cathode with rapid ionic and electronic channels. The performance of SPAN synthesized with different sacrificial templates is summarized in Table 9.

**Table 9.** Summary of cycling performance of SPAN synthesized with different sacrificial templates.

| Cathode               | Template           | Cathode Loading                                     | Initial Discharge Capacity                | Cycles | Final Discharge Capacity                  | Capacity Retention | Rate/Current Density   | Ref.  |
|-----------------------|--------------------|---|---|--------|---|--------------------|------------------------|-------|
| fibrous SPAN          | PMMA               | $0.672 \text{ mg}_{\text{sulfur}} \text{ cm}^{-2}$  | $1672 \text{ mAh g}^{-1}_{\text{sulfur}}$ | N/A    | N/A                                       | N/A                | 0.5 C                  | [131] |
| MSPAN                 | SBA-15             | $2.45 \text{ mg cm}^{-2}$                           | N/A                                       | 900    | $610 \text{ mAh g}^{-1}$                  | N/A                | 2 C                    | [132] |
| Porous PAN/S          | PMMA               | N/A   | $1620 \text{ mAh g}^{-1}_{\text{sulfur}}$ | 500    | $794 \text{ mAh g}^{-1}_{\text{sulfur}}$  | N/A                | 2 C                    | [134] |
| pPAN-SeS <sub>2</sub> | PS                 | $2 \text{ mg}_{\text{composite}} \text{ cm}^{-2}$   | $871 \text{ mAh g}^{-1}$                  | 2000   | $633 \text{ mAh g}^{-1}$                  | N/A                | $4 \text{ A g}^{-1}$   | [135] |
| MSPAN-2               | PS                 | $1 \text{ mg}_{\text{composite}} \text{ cm}^{-2}$   | $523 \text{ mAh g}^{-1}$                  | 100    | $437 \text{ mAh g}^{-1}$                  | N/A                | $0.1 \text{ A g}^{-1}$ | [136] |
| H-SPAN                | PEO                | $2.2 \text{ mg}_{\text{composite}} \text{ cm}^{-2}$ | N/A                                       | 300    | $1250 \text{ mAh g}^{-1}_{\text{sulfur}}$ | N/A                | 0.1 C                  | [137] |
| TPSPAN                | Sodium bicarbonate | N/A   | $962 \text{ mAh g}^{-1}$                  | 2000   | N/A                                       | 94.6%              | $2 \text{ A g}^{-1}$   | [138] |

The morphology of SPAN is also influenced by the morphology and the chemical composition of the PAN precursor, which results in different chemical, mechanical, and electrochemical properties. In 2019, Lebherz et al. synthesized monolithic PAN precursor via solvent-induced (SIPS) and thermally induced (TIPS) phase separation by addition-fragmentation chain transfer (RAFT) [139]. SPAN monoliths were subsequently synthesized with the monolithic PAN precursor and sulfur. Both PAN and SPAN monoliths showed a defined structure in SEM and high specific surface area up to  $225 \text{ m}^2 \text{ g}^{-1}$ . SIPS-derived SPAN monoliths exhibited high reversible capacity of  $900 \text{ mAh g}^{-1}_{\text{sulfur}}$  at 2 C and good cycle stability of less than 5% capacity decay after 200 cycles at 1 C. In 2023, He et al. reported a novel three-dimensional flower-shaped SPAN (SPAN-F) composite as the cathode material for Li || SPAN batteries to address the low sulfur content limitation and sluggish reaction kinetics challenge [140] (Figure 13a). SPAN-F was prepared via a simple free-radical polymerization of acrylonitrile in acetone followed by vulcanization. It appears as flower-shaped nanoparticles with a sulfur content of 52.8% and a specific surface area of  $33.8 \text{ m}^2 \text{ g}^{-1}$ , enabling high capacity and excellent reaction kinetics. The resulting Li || SPAN-F battery delivered a second cycle capacity of  $726 \text{ mAh g}^{-1}$  SPAN and retained  $673 \text{ mAh g}^{-1}$  SPAN after 500 cycles at 1 C, corresponding to a capacity decay rate of 0.015% per cycle. In addition, a Li || SPAN-F battery with high loading (SPAN-F loading =  $8.6 \text{ mg cm}^{-2}$ ) and lean electrolyte ( $E/\text{SPAN-F} = 5.0 \mu\text{L mg}^{-1}$ ) exhibited  $647 \text{ mAh g}^{-1}$  SPAN over 50 cycles at 0.2 C.

Further advancements came from Lei et al.'s crosslinking strategies. In 2021, Lei et al. reported a cross-linking strategy to address the low sulfur content issue with SPAN materials by using cross-linked PAN precursors with porous structure and high specific area [141] (Figure 13b). The as-prepared cross-linked SPAN renders an effective sulfur content up to 53.63 wt%. As a result, the Li || SPAN battery delivered an initial discharge

capacity of  $829 \text{ mAh g}^{-1}$  composite and retained  $744 \text{ mAh g}^{-1}$  composite after 200 cycles at 0.2 C. Later, Lei et al. reported another crosslinked PAN (CPAN) as the precursor for SPAN synthesis, resulting in a SPAN material with high sulfur content up to 55 wt% [142]. CPAN was prepared via the free radical polymerization of acrylonitrile with divinylbenzene as the crosslinking agent. It possesses high specific surface area of  $312.47 \text{ m}^2 \text{ g}^{-1}$ , offering additional space to accommodate more sulfur during vulcanization. Consequently, the  $\text{Li}||\text{SPAN}$  battery delivered a high initial discharge capacity of  $838 \text{ mAh g}^{-1}$  composite and exhibited stable cycling over 100 cycles at 0.2 C.

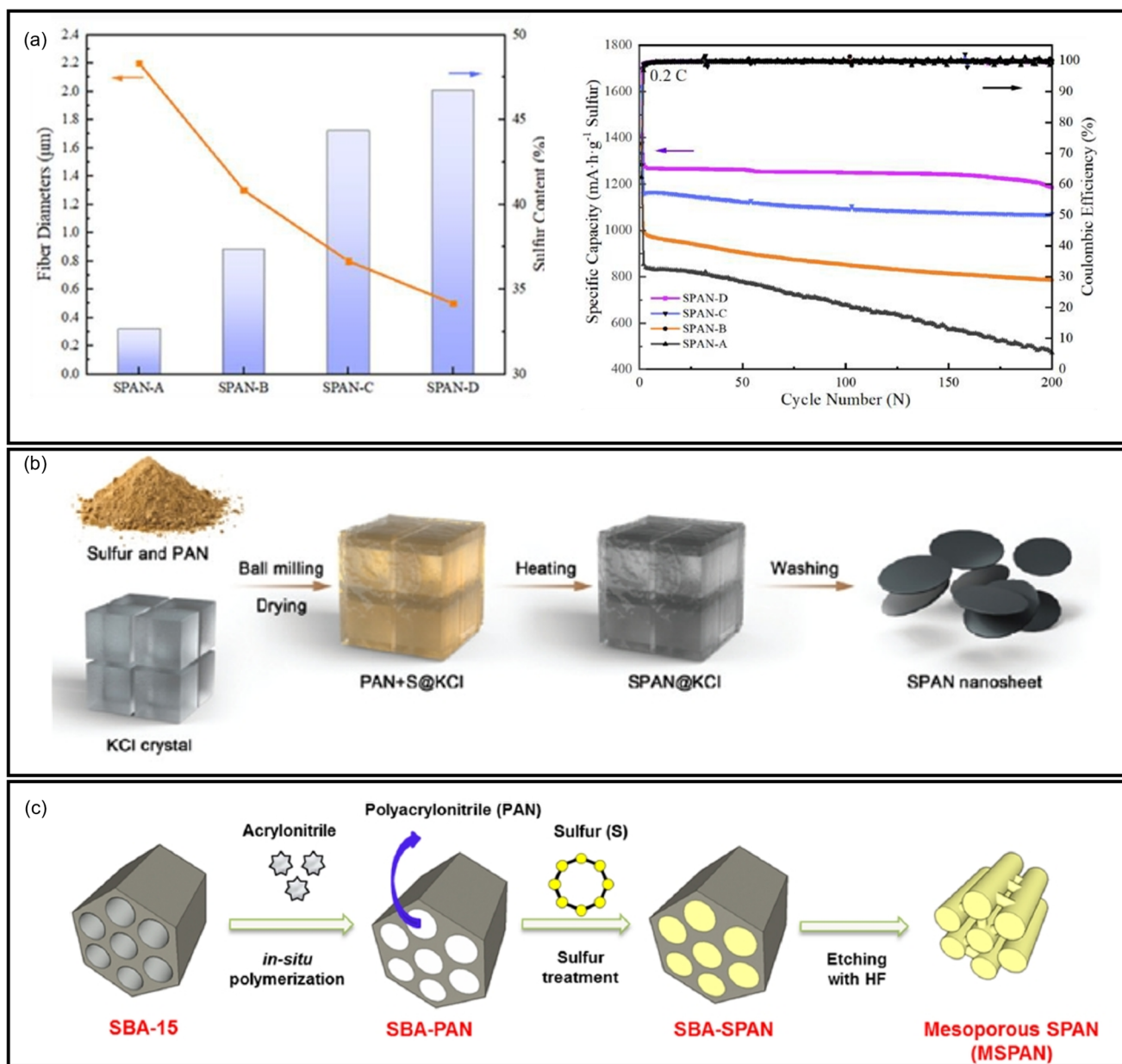


**Figure 12.** (a) left: fiber diameter graph; right: cycling performance of SPAN fibers with different diameters. Reproduced with permission [128]. Copyright © 2023, American Chemical Society; (b) Schematic illustration of the synthesis of SPAN nanosheets. Reproduced with permission [130]. Copyright © 2021, Royal Society of Chemistry; (c) Schematic illustration of the sequential fabrication steps for MSPAN. Reproduced with permission. Copyright © 2017, American Chemical Society.

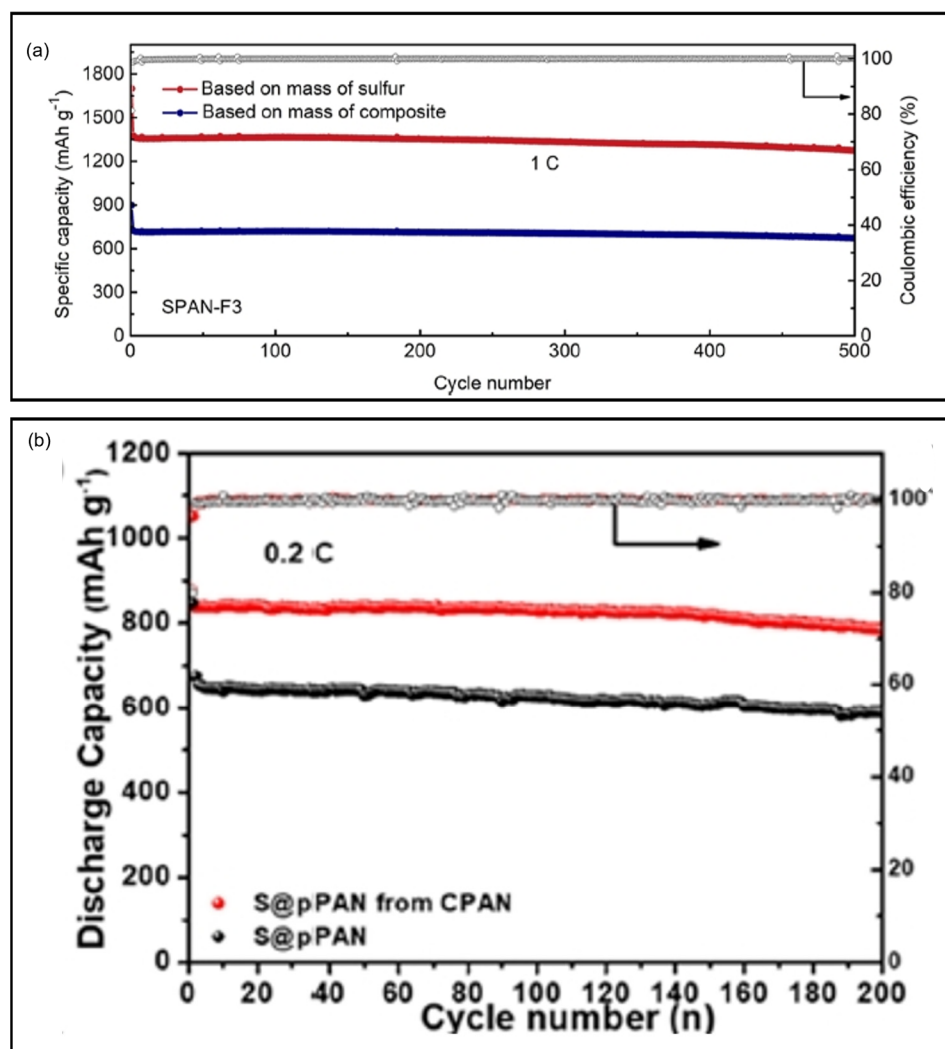


**Figure 13.** (a) Cycling performance of SPAN–F3. Reproduced with permission [140]. Copyright © 2023, American Chemical Society; (b) Cycling performance of SPAN from CPAN and the reference SPAN cathode. Reproduced with permission [141]. Copyright © 2021, American Chemical Society.

The conventional slurry casting method remains the predominant manufacturing approach for SPAN cathodes, involving the homogeneous dispersion of active materials, binders, and conductive additives in solvents followed by deposition onto current collectors. Moschner et al. investigated the processability of the SPAN in a water-based process route [143]. The authors analyzed the processing behavior of SPAN under various slurry mixing conditions using different tip speeds. All SPAN slurries showed good processability during slurry mixing, coating, and drying. The test results revealed that higher shear stress introduced by higher mixing tip speeds lead to increased internal resistances of the cells, resulting in worse electrochemical performance. And the decreasing carbon black percolation at higher tip speeds is related to the increased electrical resistance. These findings underscore the importance of optimized processing conditions, with the authors concluding that properly manufactured SPAN cathodes exhibit excellent compatibility with ether-based electrolytes and demonstrate promising scalability for industrial production.

While slurry casting offers manufacturing simplicity, the inherent limitations of inactive components—including binders, conductive additives, and current collectors—impose significant penalties on energy density and cost. This has motivated substantial research into freestanding cathode architectures that eliminate these inactive materials. Electrospinning has emerged as a particularly versatile technique for fabricat-

ing freestanding nanofibrous SPAN cathodes. This approach typically involves the electrospinning of PAN solutions containing various functional additives, including CNTs [84–86,88,89,144–146], VGCF [115], 2-methylimidazole (MeIM) [85], Co(OAc)<sub>2</sub>·4H<sub>2</sub>O [86], GNS [147], Fe<sub>x</sub>Mn<sub>1-x</sub>S [147], Fe<sub>2</sub>O<sub>3</sub> [148], trithiocyanuric acid (TTCA) [149], polypyrrole (Ppy) nanotubes [150], PVP [90], PS [151], PEO [137], polyethylene glycol (PEG) [152], nothing [153,154], etc., and are mixed, dispersed in solvents, and electrospun to obtain freestanding SPAN composite cathodes with tunable properties.

Beyond electrospinning, researchers have developed multiple alternative strategies for constructing freestanding SPAN cathodes. Mentbayeva et al. reported a freestanding SPAN/MWCNT cathode prepared by the vacuum filtration of SPAN and MWCNT mixture suspensions [155] (Figure 14a). Wang et al. developed a three-dimensional holey graphene/SPAN (SPAN/3DHG) composite and directly compressed the SPAN/3DHG composite into a freestanding wafer electrode [100]. Kim et al. fabricated freestanding bulk-type SPAN disk cathodes from pressed sulfur and PAN powders using a simple heating process [156] (Figure 14b). The SPAN disks were used directly as the cathode and possessed interconnected pores which improved the Li<sup>+</sup> mobility. As a result, the Li||SPAN battery with a high cathode loading (16.37 mg cm<sup>-2</sup>, 8.5 mAh cm<sup>-2</sup>) delivered a high reversible discharge capacity of 517 mAh g<sup>-1</sup> electrode after the 10th cycle at 15 mA g<sup>-1</sup> electrode. Yang et al. reported a freestanding SPAN cathode (FS-SPAN) prepared via phase inversion and sulfurization of PAN [157]. Sabet et al. developed a freestanding 3D SPAN/carbonized delignified wood (CDW) cathode prepared via impregnating SPAN into a 3D carbon framework derived from carbonized delignified wood (CDW) for high-loading Li||SPAN batteries [158] (Figure 14c). Lu et al. reported a freestanding SPAN/RGO cathode with nacre-like architecture fabricated by high-speed dispersion and coating [102].

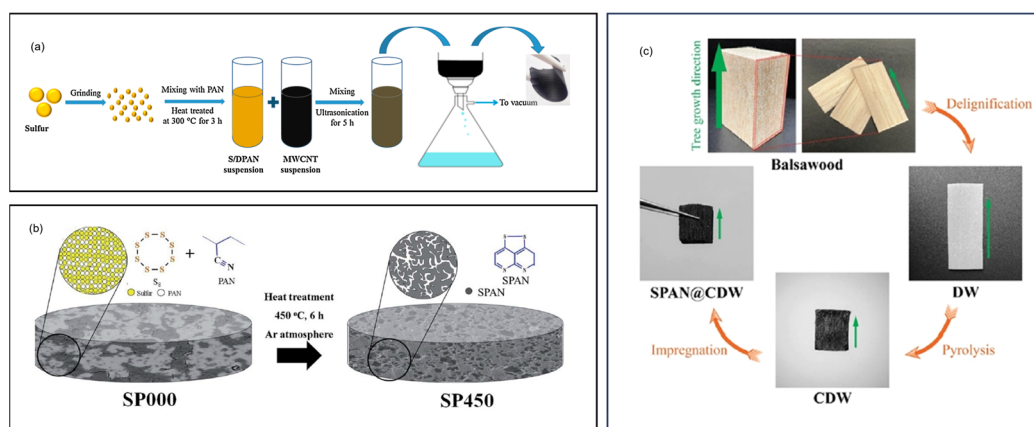


**Figure 14.** (a) Schematic illustration of preparation process for the freestanding SPAN/MWCNT composite cathode. Reproduced with permission [155]. Copyright © 2016, Elsevier; (b) Schematic illustration of the synthesis of SP450. Reproduced with permission [156]. Copyright © 2021, Royal Society of Chemistry; (c) Schematic illustration of the fabrication procedure for freestanding SPAN@CDW electrodes from natural wood. Reproduced with permission [158]. Copyright © 2023, American Chemical Society.

Recent advances in surface modification and interfacial engineering have significantly enhanced the performance and durability of SPAN-based cathodes. Strategic coating technologies have emerged as particularly effective approaches for improving both electrochemical performance and structural integrity. In 2017, Peng et al. developed a carbon-coated SPAN composite (C@SPAN) by electrospinning sulfur, PAN, and sucrose followed by heat treatment at 80 °C and 450 °C [159]. The unique core–shell structure

of C@SPAN demonstrated remarkable stability, delivering a high initial discharge capacity of  $1461 \text{ mAh g}^{-1}$  sulfur while maintaining 89% capacity after 200 cycles at 0.1 C. In 2022, Wang et al. reported a PDA-coated SPAN composite material (SPAN/PDA) for high-performance Na  $\parallel$  SPAN batteries [160]. PDA exclusively binds with SPAN and the pulutan-graft-sodium polyacrylic acid (PuA) binder through polar-polar interactions, forming a SPAN/PDA/PuA cathode with strong mechanical and interfacial strengths. In addition, various functional groups in the composite cathode effectively restrains the polysulfide dissolution. Consequently, the Na  $\parallel$  SPAN/PDA/PuA battery delivered a reversible capacity of  $1162 \text{ mAh g}^{-1}$  after 300 cycles at 1 C. In 2024, Zuo et al. developed a spray-drying method to produce micro-sized SPAN secondary particles (PC-SPAN) with composite coating comprising polydopamine (PDA), polyacrylic acid (PAA), and polyvinyl alcohol (PVA) [161] (Figure 15a). The abundant catecholamine, hydroxyl, and carboxyl groups not only construct strong adhesion to keep the electrode integrity, but also render built-ion ion passage. As a result, the Li  $\parallel$  PC-SPAN battery with a high areal capacity of  $13.3 \text{ mAh cm}^{-2}$  and lean electrolyte ( $E/\text{PC-SPAN} = 2.8 \mu\text{L mg}^{-1}$ ) in the second cycle retained 97.3% after 20 cycles at 0.1 C. A prototype Li  $\parallel$  PC-SPAN battery ( $530.2 \text{ Wh kg}^{-1}$ ) with a high areal capacity of  $19.1 \text{ mAh cm}^{-2}$ , extremely lean electrolyte ( $E/\text{PC-SPAN} = 0.93 \mu\text{L mg}^{-1}$ ), and limited Li ( $N/P = 1.66$ ) delivered stable cycling over 12 cycles.

The formation of a robust cathode-electrolyte interlayer (CEI) is the key for stable cycling of the SPAN batteries. LiNO<sub>3</sub> as an electrolyte additive is known for its beneficial effect of the facilitation of a high-quality CEI. In 2021, Holoubek et al. reported the integration of LiNO<sub>3</sub> as a solid additive to the SPAN cathode and employed DEE-based electrolytes to construct stable Li  $\parallel$  SPAN batteries with low cost [162] (Figure 15b). The sustained release of LiNO<sub>3</sub> into the electrolyte facilitates the formation of a stable CEI composed of SO<sub>4</sub>, S-O-F, and LiF species. As a result, the Li  $\parallel$  SPAN (2 wt% LiNO<sub>3</sub>) battery with an areal capacity of  $3.5 \text{ mAh cm}^{-2}$  delivered a reversible discharge capacity of  $360 \text{ mAh g}^{-1}$  after 100 cycles. Qin et al. reported a sulfur enriched silicon/SPAN composite (Si@SPANdC) as the cathode material for high-performance Li  $\parallel$  SPAN batteries [163]. The as-prepared Si@SPANdC cathode exhibited minimal volume expansion during cycling, improved reaction kinetics, and the formation of a robust CEI. As a result, the Li  $\parallel$  Si@SPANdC battery delivered a reversible capacity of  $699 \text{ mAh g}^{-1}$  after 200 cycles at  $0.2 \text{ A g}^{-1}$ .

#### 8.4. Redox Accelerators

Researchers have identified the sluggish redox kinetics of Li<sub>2</sub>S and SPAN as a key limitation in Li  $\parallel$  SPAN batteries. To address this, electrocatalysts have been employed to improve the redox kinetics of the SPAN and the overall conductivity of the SPAN cathode. These strategies are discussed below. The performance of SPAN cathode with different redox accelerators is summarized in Table 10.

Transitional metal sulfides have emerged as effective electrocatalyst additives for SPAN. In 2017, Liu et al. reported a NiS<sub>2</sub>-modified SPAN (NiS<sub>2</sub>-SPAN) prepared by co-heating the mixture of PAN, sulfur, and NiCO<sub>3</sub> [164]. NiS<sub>2</sub> has a conductivity of about  $55 \text{ S cm}^{-1}$  at room temperature and can accelerate the polysulfide reduction, enabling the NiS<sub>2</sub>-SPAN cathode to deliver a high reversible capacity of  $1533 \text{ mAh g}^{-1}$  sulfur after 100 cycles at  $0.2 \text{ A}$ .

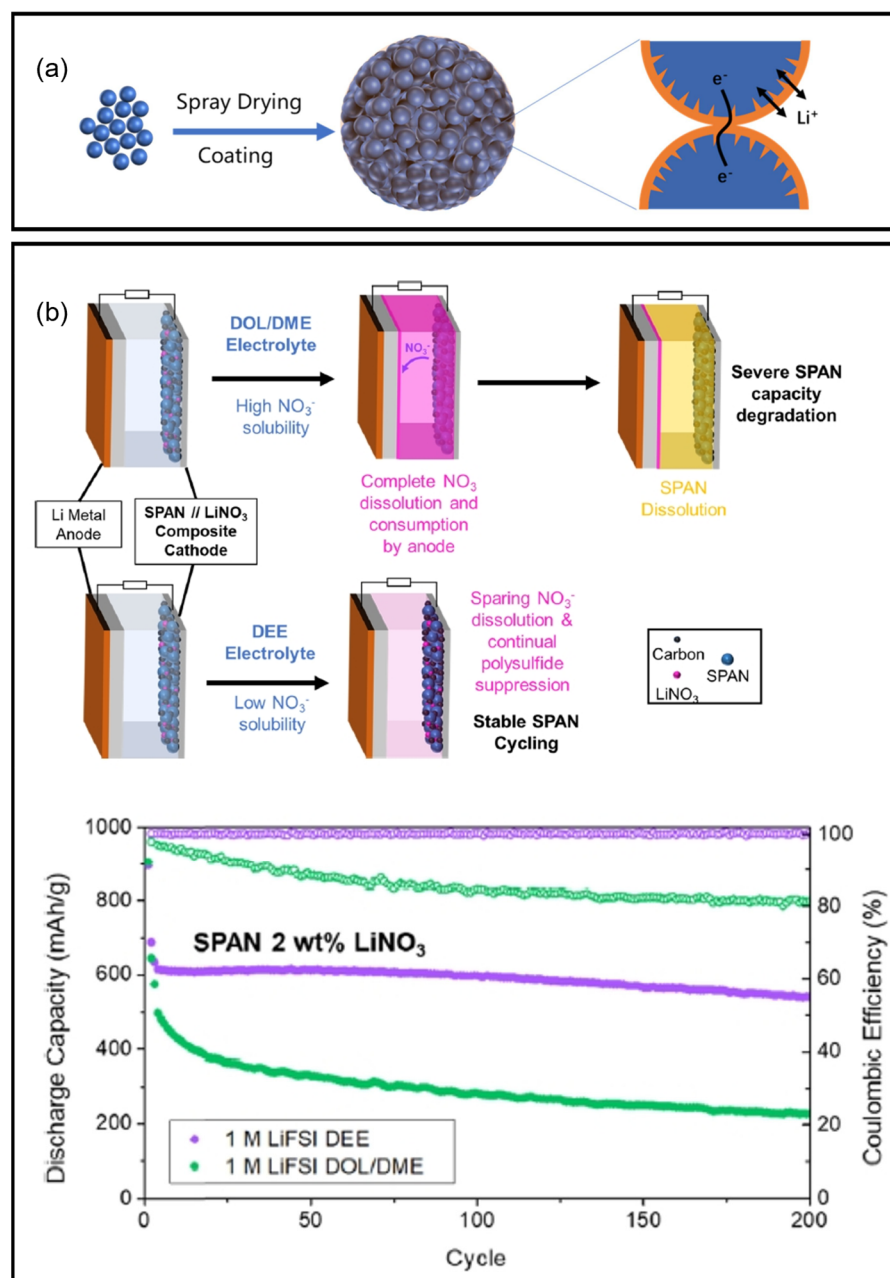


**Figure 15.** (a) Schematic illustration of the coating process through spray drying. Reproduced with permission [161]. Copyright © 2024, Elsevier; (b) Schematic illustration of the LiNO<sub>3</sub>/SPAN composite cathode and the impact of electrolyte composition on the cycling performance. Reproduced with permission [162]. Copyright © 2021, American Chemical Society.

Similarly, in Haridas et al.'s work, FeS was incorporated in the SPAN nanofiber matrix through electrospinning followed by vulcanization [165] (Figure 16a). FeS can enhance the conductivity of the SPAN matrix and facilitate the redox kinetics during the cycling process. As a result, the FeS@SPAN cathode retained 688.6 mAh g<sup>-1</sup> composite after 500 cycles at 1 A g<sup>-1</sup>. The electrocatalytic function of FeS was also demonstrated in Qin et al.'s study [122]. A SPAN/Fe<sub>1-x</sub>S/rGO composite was prepared via co-heating of PAN/FeCl<sub>3</sub>/GO nanofibers, sulfur, and 2-MBT at 300 °C for high-performance Li || SPAN batteries.

**Table 10.** Summary of cycling performance of SPAN with redox accelerators.

| Cathode                                     | Redox Accelerator                               | Cathode Loading                                     | Initial Discharge Capacity  | Cycles | Final Discharge Capacity                | Capacity Retention | Rate/Current Density   | Ref.  |
|---|---|---|---|--------|---|--------------------|------------------------|-------|
| NiS <sub>2</sub> -SPAN                      | NiS <sub>2</sub>                                | 1.15 mg <sub>sulfur</sub> cm <sup>-2</sup><br>1–1.2 | 1722 mAh g <sup>-1</sup> sulfur   | 100    | 1533 mAh g <sup>-1</sup> sulfur         | 89%                | 200 mA g <sup>-1</sup> | [162] |
| FeS@SPAN                                    | FeS   | mg composite cm <sup>-2</sup>                       | 844.5 mAh g <sup>-1</sup> composite   | 500    | 688.6 mAh g <sup>-1</sup> composite     | N/A                | 1 A g <sup>-1</sup>    | [163] |
| SPAN-1                                      | Fe <sub>1-x</sub> S                             | 2 mg <sub>sulfur</sub> cm <sup>-2</sup>             | N/A   | 2000   | 857 mAh g <sup>-1</sup>                 | N/A                | 5 A g <sup>-1</sup>    | [122] |
| CoS <sub>2</sub> -SPAN-CNT                  | CoS <sub>2</sub>                                | 2.4 mg <sub>sulfur</sub> cm <sup>-2</sup>           | 1799 mAh g <sup>-1</sup>  | 100    | 1240 mAh g <sup>-1</sup>                | 68.9%              | 0.2 C                  | [85]  |
| CoS <sub>2</sub> -SFPAN-3                   | CoS <sub>2</sub>                                | 1–1.4 mg <sub>sulfur</sub> cm <sup>-2</sup><br>1.67 | N/A   | 500    | 631 mAh g <sup>-1</sup>                 | N/A                | 1 C                    | [164] |
| CoSe <sub>2</sub> -10@SPAN                  | CoSe <sub>2</sub>                               | mg composite cm <sup>-2</sup>                       | ~800 mAh g <sup>-1</sup>  | 500    | 675 mAh g <sup>-1</sup>                 | 71.1%              | 1 A g <sup>-1</sup>    | [165] |
| Co <sub>10</sub> -SPAN-CNT                  | Co-N <sub>4</sub> S                             | 1 mg <sub>sulfur</sub> cm <sup>-2</sup>             | 1252 mAh g <sup>-1</sup> sulfur   | 1500   | 1020 mAh g <sup>-1</sup> sulfur         | 81.5%              | 1 C                    | [86]  |
| MoS <sub>2</sub> @SPAN                      | MoS <sub>2</sub>                                | 2 mg composite cm <sup>-2</sup>                     | N/A   | 500    | 264 mAh g <sup>-1</sup> composite       | N/A                | 2 A g <sup>-1</sup>    | [166] |
| FeMn@GN-SPAN                                | Fe <sub>x</sub> Mn <sub>1-x</sub> S             | 3 mg <sub>sulfur</sub> cm <sup>-2</sup>             | 967 mAh g <sup>-1</sup>   | 500    | 845 mAh g <sup>-1</sup>                 | N/A                | 0.3 C                  | [147] |
| WS <sub>2</sub> -SPAN                       | WS <sub>2</sub>                                 | N/A   | N/A   | 450    | 464 mAh g <sup>-1</sup>                 | N/A                | 0.5 A g <sup>-1</sup>  | [167] |
| WSSe-Se@PAN-2                               | WS <sub>x</sub> Se <sub>2-x</sub>               | N/A   | N/A   | 700    | 467 mAh g <sup>-1</sup>                 | N/A                | 2 A g <sup>-1</sup>    | [168] |
| BiSbS <sub>x</sub> @SPAN-450                | BiSbS <sub>x</sub>                              | N/A   | N/A   | 2000   | 472 mAh g <sup>-1</sup> composite       | N/A                | 1 A g <sup>-1</sup>    | [169] |
| SnS <sub>2</sub> @SPAN                      | SnS <sub>2</sub>                                | 0.5–1 mg cm <sup>-2</sup>                           | N/A   | 500    | 117.5 mAh g <sup>-1</sup>               | ~100%              | 4 A g <sup>-1</sup>    | [170] |
| SnS <sub>2</sub> -SPAN                      | SnS <sub>2</sub>                                | N/A   | N/A   | 700    | 218 mAh g <sup>-1</sup>                 | N/A                | 0.5 A g <sup>-1</sup>  | [171] |
| S/PAN/Mg <sub>0.6</sub> Ni <sub>0.4</sub> O | Mg <sub>0.6</sub> Ni <sub>0.4</sub> O           | 4 mg cm <sup>-2</sup>                               | 1545 mAh g <sup>-1</sup> sulfur   | 100    | 1223 mAh g <sup>-1</sup> sulfur         | N/A                | 0.1 C                  | [172] |
| S/PAN/SiO <sub>2</sub>                      | SiO <sub>2</sub>                                | 2.5 mg cm <sup>-2</sup>                             | N/A   | 100    | 1106 mAh g <sup>-1</sup>                | N/A                | 0.2 C                  | [173] |
| SPAN/Ti                                     | TiO <sub>2</sub>                                | 1 mg <sub>sulfur</sub> cm <sup>-2</sup>             | 1885 mAh g <sup>-1</sup> sulfur<br>1528 mAh g <sup>-1</sup> sulfur & oxides (5th cycle) | 200    | ~1600 mAh g <sup>-1</sup> sulfur        | N/A                | 0.5 C                  | [174] |
| SPAN/Ti-Y                                   | TiO <sub>2</sub> /Y <sub>2</sub> O <sub>3</sub> | 1 mg cm <sup>-2</sup>                               | g <sup>-1</sup> sulfur & oxides (5th cycle)   | 850    | 907 mAh g <sup>-1</sup> sulfur & oxides | N/A                | 3 C                    | [175] |
| FeNb@SPAN                                   | Fe <sub>x</sub> Nb <sub>y</sub> O               | 1 mg cm <sup>-2</sup>                               | N/A   | 80     | 201 mAh g <sup>-1</sup>                 | N/A                | 50 mA g <sup>-1</sup>  | [176] |

Razzaq et al. engineered a freestanding and fibrous CoS<sub>2</sub>-SPAN-CNT composite cathode fabricated by the in situ growth of ZIF-67 on the electrospun PAN-CNT-MeIM fibers followed by a vulcanization process [85]. The CoS<sub>2</sub> layer mitigated the volume expansion of the SPAN film and enhanced the electronic conductivity, facilitating the redox kinetics of the SPAN cathode. As a result, the as-assembled Li || SPAN pouch cell with an ultrahigh cathode areal capacity (8.1 mAh cm<sup>-2</sup>) delivered a reversible discharge capacity of 1322 mAh g<sup>-1</sup> sulfur after 17 cycles, demonstrating great potential for practical applications. Later, Li et al. reported a CoS<sub>2</sub>-SPAN composite cathode and Xu et al. reported a CoSe<sub>2</sub>-SPAN composite cathode for high-performance Li || SPAN batteries [166,167]. In another Razzaq et al.'s work, the atomically dispersed Co-N<sub>4</sub>S moieties in SPAN served as the catalytic center to expedite the reaction kinetics [86] (Figure 16b). Consequently, the Li || SPAN battery delivered an initial capacity of 1252 mAh g<sup>-1</sup> sulfur and retained 1020 mAh g<sup>-1</sup> sulfur after 1500 cycles at 1 C. MoS<sub>2</sub>@SPAN composite cathode was developed by Wang et al. in 2023, showing a second cycle capacity of 500 mAh g<sup>-1</sup> composite and retaining 264 mAh g<sup>-1</sup> composite after 500 cycles at 2 A g<sup>-1</sup>, corresponding to a capacity decay rate of 0.089% [168].

The synergistic electrocatalytic effect of transitional metal sulfides was investigated by Fang et al. in 2023 [177]. A nanofibrous FeCo/SPAN composite material was prepared

via electrospinning and heat treatment for high-performance Li<sup>+</sup>||SPAN batteries. Synchrotron X-ray absorption spectroscopy confirms the existence of Fe-S/Fe and Co-S bonds in FeCo/SPAN. The uniformly distributed Fe and Co efficiently accelerated the redox reactions of polysulfides. As a result, the Li<sup>+</sup>||FeCo/SPAN battery with high-concentration electrolytes exhibited the optimal electrochemical performance, with a specific capacity of 71.6% higher than that of batteries with 1 M LiTFSI electrolyte. Yuan et al. developed a freestanding nanofibrous SPAN composite prepared by embedding Fe<sub>x</sub>Mn<sub>1-x</sub>S nanoparticles into the conductive graphene nanosheet-doped SPAN fiber matrices [147]. The Fe<sub>x</sub>Mn<sub>1-x</sub>S nanoparticles possesses abundant electrochemically active sites to facilitate efficient electrocatalytic conversion of polysulfides.

WS<sub>2</sub> was reported as an effective electrocatalytic additive to composite with SPAN for Na<sup>+</sup>||WS<sub>2</sub>-SPAN batteries [169] (Figure 16c). DFT calculations revealed that the three-dimensional electrospun SPAN structure has fast kinetics for Na<sup>+</sup> and acted as a matrix for suppress the volume variation of WS<sub>2</sub> during cycling by introducing abundant S vacancies and in situ nitrogen doping, thereby endowing WS<sub>2</sub>-SPAN with stability in wide-temperature-range environments. As a result, the Na<sup>+</sup>||WS<sub>2</sub>-SPAN battery delivered a reversible capacity of 464 mAh g<sup>-1</sup> after 450 cycles at 0.5 A g<sup>-1</sup> and preserved reversible capacities of 354/190/129 mAh g<sup>-1</sup> after 1400/12,000/18,000 cycles at 2/5/10 A g<sup>-1</sup>, respectively. In addition, a K<sup>+</sup>||WS<sub>2</sub>-SPAN battery was assembled and delivered 362/278 mAh g<sup>-1</sup> after 100/3000 cycles at 0.1/1 A g<sup>-1</sup>, respectively.

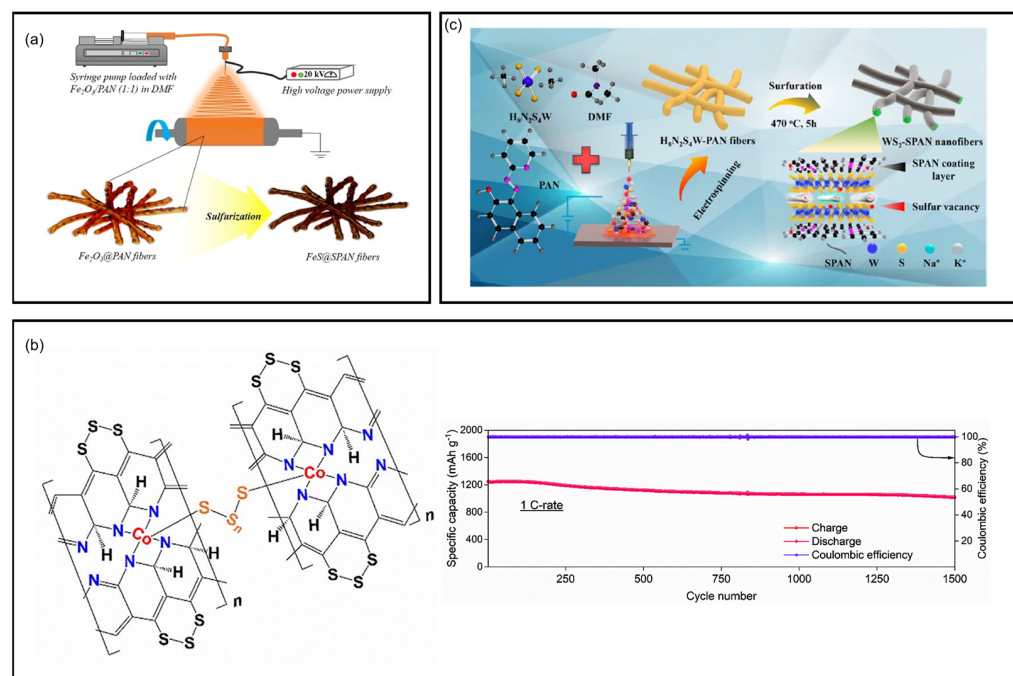


**Figure 16.** (a) Schematic illustration of the synthesis procedure for FeS@SPAN. Reproduced with permission [165]. Copyright © 2019, American Chemical Society; (b) Proposed crosslinking structure of Co<sub>10</sub>-SPAN-CNT and cycling performance of Co<sub>10</sub>-SPAN-CNT. Reproduced with permission [86]. Copyright © 2021, Elsevier; (c) Schematic illustration of the synthesis of WS<sub>2</sub>-SPAN nanofibers. Reproduced with permission [169]. Copyright © 2023, Royal Society of Chemistry.

Xiao et al. incorporated defect-rich WS<sub>x</sub>Se<sub>2-x</sub> nanocrystals in SePAN fibers (WSSe-SePAN) fabricated via a two-step electrospinning/annealing strategy [170]. The synergistic effect of Se-doping induced sulfur vacancies and the encapsulation of WS<sub>x</sub>Se<sub>2-x</sub> nanocrystals could expand the interlayer spacing, increase active sites, and accelerate Na<sup>+</sup>/K<sup>+</sup> diffusion kinetics. As a result, the Na<sup>+</sup>||WSSe-SePAN battery delivered a reversible capac-

ity of  $467 \text{ mAh g}^{-1}$  after 700 cycles at  $2 \text{ A g}^{-1}$ . When paired with a  $\text{Na}_3\text{V}_2(\text{PO}_4)_3$  cathode, the WSSe-SePAN ||  $\text{Na}_3\text{V}_2(\text{PO}_4)_3$  full cell delivered a reversible capacity of  $299 \text{ mAh g}^{-1}$  after 60 cycles at  $0.5 \text{ A g}^{-1}$ , corresponding to a capacity retention of 99.8%. In addition, it exhibited excellent electrochemical performance for potassium-ion batteries (PIBs), with a reversible capacity of  $139 \text{ mAh g}^{-1}$  after 1000 cycles at  $1 \text{ A g}^{-1}$ . A novel  $\text{BiSbS}_x$  nanocrystals embedded SPAN composite fibrous cathode ( $\text{BiSbS}_x@\text{SPAN}$ ) reported by Li et al. was prepared via electrospinning and annealing for  $\text{K}||\text{SPAN}$  batteries [171]. The unique structure afforded multiple binding sites and short diffusion paths for  $\text{K}^+$ , resulting in fast reaction kinetics. Consequently, the  $\text{K}||\text{BiSbS}_x@\text{SPAN}$  battery delivered a reversible capacity of  $472 \text{ mAh g}^{-1}$  composite after 2000 cycles at  $1 \text{ A g}^{-1}$ .  $\text{SnS}_2$  was introduced into SPAN fibers by Li, Tong, and Jiang et al. for  $\text{K}||\text{SPAN}$  batteries [172], and by Wang et al. for  $\text{Mg}||\text{SPAN}$  batteries [173].

Metal and non-metallic oxides have been widely explored as multifunctional additives for SPAN cathodes, offering electrocatalytic effects, polysulfides absorption, and even secondary electrochemically active component. In 2013, Zhang et al. pioneered the use of nanostructured  $\text{Mg}_{0.6}\text{Ni}_{0.4}\text{O}$  as an additive to the SPAN cathode to improve the morphology stability, chemical uniformity, and electrochemical performance [174]. The SPAN/ $\text{Mg}_{0.6}\text{Ni}_{0.4}\text{O}$  cathode achieved a reversible capacity of  $1223 \text{ mAh g}^{-1}$  sulfur and retained about 100% of capacity after 100 cycles at  $0.1 \text{ C}$ .

He et al. reported a novel lithium-ion full battery assembled with composite materials SPAN/ $\text{SiO}_2$  as the cathode and pre-lithiated graphite as the anode [175] (Figure 17a). The SPAN/ $\text{SiO}_2$  was synthesized by co-heating sulfur, PAN, and  $\text{SiO}_2$  at  $450^\circ\text{C}$ . The nano-sized  $\text{SiO}_2$  served as an effective polysulfide-trapping additive due to its ultra-high absorption ability. As a result, the pre-lithiated graphite || SPAN/ $\text{SiO}_2$  full battery delivered an initial capacity of  $804 \text{ mAh g}^{-1}$  and a reversible capacity of  $810 \text{ mAh g}^{-1}$  after 100 cycles at  $0.2 \text{ C}$ .

Jerez et al. synthesized SPAN/ $\text{TiO}_2$  composites by co-heating sulfur, PAN, and  $\text{TiO}_2$  [176].  $\text{TiO}_2$  served dual roles as a second capacity-contributing material and improving the overall reaction kinetics. The  $\text{Li}||\text{SPAN}/\text{TiO}_2$  battery delivered excellent cycling stability, retaining a capacity of  $672 \text{ mAh g}^{-1}$  sulfur after 1400 cycles at  $3.3 \text{ C}$ , and  $660 \text{ mAh g}^{-1}$  sulfur after 500 cycles at  $5 \text{ C}$ . The SPAN/ $\text{TiO}_2$  composite cathode was also tested in  $\text{Na}||\text{SPAN}/\text{TiO}_2$  batteries, demonstrating a stable cycling over 1000 cycles at  $0.2 \text{ C}$  with a capacity decay rate of 0.11% per cycle [178]. A ternary composite cathode composed of SPAN,  $\text{TiO}_2$ , and  $\text{Y}_2\text{O}_3$  was developed by Jerez et al. in 2023 [179] (Figure 17b).  $\text{TiO}_2$  and  $\text{Y}_2\text{O}_3$  effectively improved the reaction kinetics, inhibited the dissolution of polysulfides, and served as a capacity contributor during cycling. The  $\text{Li}||\text{SPAN}/\text{Ti-Y}$  battery achieved a fifth cycle capacity of  $1528 \text{ mAh g}^{-1}$  sulfur & oxides and retained  $907 \text{ mAh g}^{-1}$  sulfur & oxides after 850 cycles at  $3 \text{ C}$ .

Yuan et al. engineered electrospun SPAN nanofibers embedded with  $\text{Fe}_x\text{Nb}_y\text{O}$  nanoparticles ( $\text{FeNb}@SPAN$ ) for  $\text{K}||\text{SPAN}$  batteries [180]. The uniformly distributed  $\text{Fe}_3\text{O}_4$  and  $\text{Nb}_2\text{O}_5$  nanoparticles enhanced the sulfur kinetics and mitigated the polysulfides dissolution. The  $\text{K}||\text{FeNb}@SPAN$  battery delivered a reversible capacity of  $201 \text{ mAh g}^{-1}$  after 80 cycles at  $50 \text{ mA g}^{-1}$ .

### 8.5. Heteroatoms Doping

Heteroatoms doping/substitution is an effective strategy to enhance the conductivity of the SPAN cathode and accelerate the redox kinetics. In 2019, Ma et al. reported iodine-doped SPAN ( $\text{I}@SPAN$ ) for room-temperature  $\text{Na}||\text{SPAN}$  batteries and  $\text{K}||\text{SPAN}$  batteries in carbonate-based electrolytes [181].  $\text{I}@SPAN$  was synthesized by co-heating sulfur, PAN, and iodine in a sealed tube. Iodine-doping significantly enhanced the conductivity of the SPAN cathode. As a result, the  $\text{Na}||\text{I}@SPAN$  battery delivered an initial discharge

capacity of  $994 \text{ mAh g}^{-1}$  sulfur and maintained a reversible capacity of  $768 \text{ mAh g}^{-1}$  sulfur after 500 cycles at 0.5 C. As for the K || I@SPAN battery, it delivered an initial capacity of  $1448 \text{ mAh g}^{-1}$  sulfur and retained a reversible capacity of  $722 \text{ mAh g}^{-1}$  sulfur after 100 cycles at 0.1 C. Subsequent studies by Ma et al. [182] (Figure 18a) and Xue et al. [145] further confirmed the beneficial effects of iodine in enhancing cathode conductivity, optimizing the cathode-electrolyte interface, and improving reaction kinetics, collectively contributing to enhanced electrochemical performance.

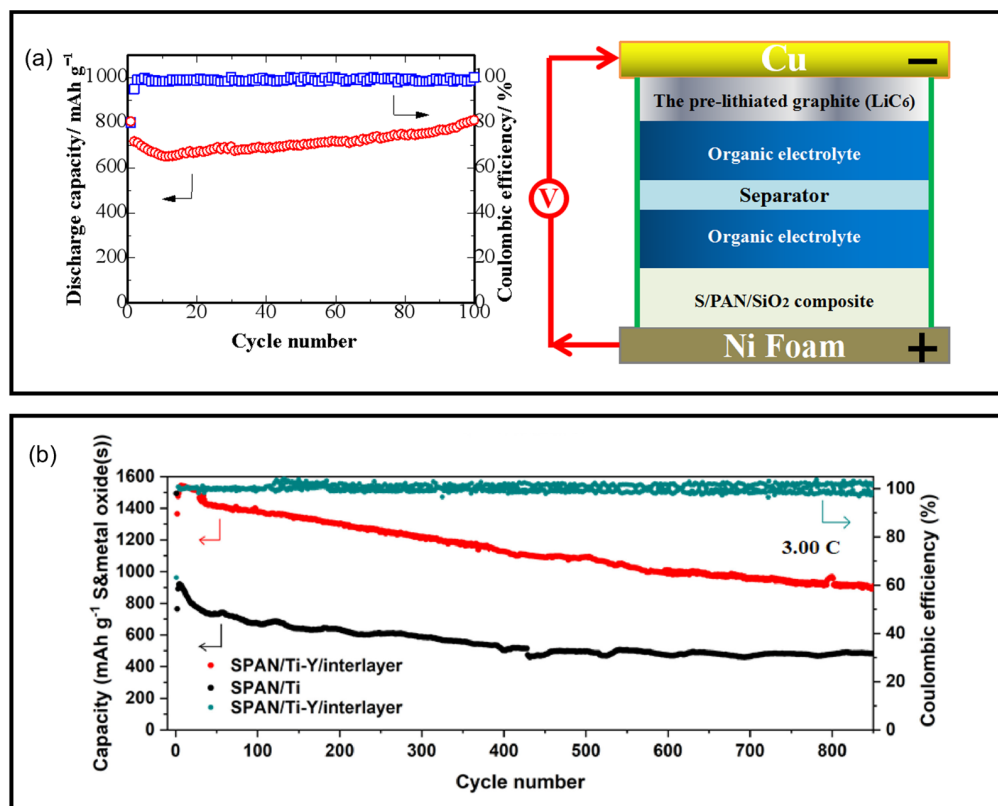


**Figure 17.** (a) Schematic illustration of the  $\text{LiC}_6 \parallel \text{SPAN}/\text{SiO}_2$  full cell and its cycling performance. Reproduced with permission [175]. Copyright © 2018, MDPI; (b) Cycling performance of SPAN/Ti–Y/interlayer and SPAN/Ti. Reproduced with permission [179]. Copyright © 2023, Elsevier.

In 2020, Ma et al. reported black phosphorus (BP) modified SPAN (BP-SPAN) cathode operated in ether electrolytes [183]. BP-SPAN was synthesized by co-heating sulfur, PAN, and black phosphorus at  $300^\circ\text{C}$ . Characterization revealed the presence of amorphous  $\text{P}_2\text{S}_{5+x}$  species in BP-SPAN, which play a crucial role in suppressing polysulfides shuttling and enhancing reaction kinetics of the cathode. With 2% of BP doping, the BP-SPAN cathode delivered a discharge capacity of  $1266 \text{ mAh g}^{-1}$  sulfur after 100 cycles at 0.1 C, corresponding to a capacity retention of 91.1%. Further advancing this approach, Wang et al. reported a SPAN/red phosphorus (SPAN/RP) composite prepared via a simple solution-phase method [184]. In this composite, RP was anchored to SPAN through the P-S bonding, enhancing the electrode conductivity and facilitating the formation of a uniform SEI on the electrode surface. The resulting  $\text{Li} \parallel \text{SPAN}/\text{RP}$  battery delivered an initial discharge capacity of  $1214 \text{ mAh g}^{-1}$  sulfur and retained  $860 \text{ mAh g}^{-1}$  sulfur after 200 cycles at 0.2 C. Baboukani et al. also reported a red phosphorus/SPAN (RP-SPAN) composite as the electrode materials for LIBs [185]. Expanding the application of SIBs, Hu et al. developed a red phosphorus/SPAN (P-SPAN) hybrid composite as potential electrode materials for

sodium-ion batteries [186] (Figure 18b). The Na||P-SPAN battery delivered a high capacity of over 1300 mAh g<sup>-1</sup> and capacity retention of 91% after 100 cycles at a current density of 520 mA g<sup>-1</sup>.

As homologous elements of sulfur, selenium (Se) and tellurium (Te) offer distinct advantages, including high electrical conductivity and improved redox kinetics [187]. In 2014, Wang et al. firstly reported a novel 1D CPAN/Se fiber cathode by heating the electrospun selenium and PAN fibers at 600 °C [188] (Figure 18c). The CPAN/Se cathode demonstrated superior cycling ability and rate performance, retaining about 600 mAh g<sup>-1</sup> SePAN for 500 cycles in Li||CPAN/Se batteries and 410 mAh g<sup>-1</sup> SePAN for 300 cycles in Na||CPAN/Se batteries. These findings were further corroborated by Guo et al., who also synthesized SePAN demonstrated its excellent electrochemical performance [189].

Despite these advantages, selenium's lower gravimetric capacity compared to sulfur has prompted strategies such as partial sulfur substitution or selenium doping to balance performance and capacity. In 2018, Li et al. reported a novel pPAN/SeS<sub>2</sub> composite with a multichannel structure, synthesized by electrospinning PAN/PS fibers followed co-heating with SeS<sub>2</sub> powder at 380 °C in a sealed glass vessel [135]. As a result, the Li||pPAN/SeS<sub>2</sub> battery delivered extraordinary cycling and rate performance, with 633 mAh g<sup>-1</sup> after 2000 cycles and a low decay rate of 0.014% per cycle at 4 A g<sup>-1</sup>. The Na||pPAN/SeS<sub>2</sub> battery delivered an initial discharge capacity of 1043 mAh g<sup>-1</sup> and 800 mAh g<sup>-1</sup> after 400 cycles at 1 A g<sup>-1</sup>. Zhu et al. developed S<sub>0.87</sub>Se<sub>0.13</sub>PAN composite materials by annealing the mixture of sulfur, selenium, and PAN at 400 °C [190]. The composite possesses good electrical conductivity due to the addition of selenium. The resulting Li||S<sub>0.87</sub>Se<sub>0.13</sub>PAN battery delivered a reversible capacity of 989 mAh g<sup>-1</sup> after 200 cycles at 0.3 A g<sup>-1</sup>, corresponding to a capacity retention rate of 95% compared to the second cycle.

Subsequent studies have expanded the scope of Se-doped SPAN cathodes, with contributions from Yajie Liu et al. (2017) [191], Chen et al. (2019) [192], Jiang et al. (2019) [193], Wenchao Zhang et al. (2019) [194], Yunyang Zhang et al. (2019) [195], Lihui Wang et al. (2019) [196], Pham et al. (2019) [197], Jia et al. (2020) [198,199], An et al. (2020) [200], Ziqi Zhang et al. (2020, 2022) [201,202], Jiang et al. (2020, 2021) [203–205], Wei Zhang et al. (2020) [206], Yu Liu et al. (2020) [207], Bin He et al. (2021) [208], Teng et al. (2022) [209], Kong et al. (2022) [210,211], Han et al. (2022) [216,212], Li et al. (2022) [213], Yiyi Wang et al. (2022, 2023) [214,215], Runhe He et al. (2022, 2023) [216,217], Wu et al. (2022, 2023) [123,218], Lihong Xu et al. (2023) [219], Zhiqiang Xu et al. (2023) [167], Yuan et al. (2023) [220], Yang et al. (2023) [221], Hao Liu et al. (2024, 2025) [151,222], Ting Ma et al. (2022, 2024) [223,224], Shaobo Ma et al. (2024) [225], Ke Wang et al. (2024) [226], and Xiao et al. (2024) [170].

Tellurium, as a eutectic accelerator, was firstly employed in SPAN cathodes by Li et al. and Wang et al. in 2019 [227–229]. In Li et al.'s studies, a Te<sub>0.04</sub>S<sub>0.96</sub>@pPAN composite was synthesized and demonstrated enhanced redox kinetics and minimized polysulfides dissolution (Figure 18d). The Te<sub>0.04</sub>S<sub>0.96</sub>@pPAN cathode exhibited good compatibility with both Li and Na anodes. Wang et al. synthesized a Te<sub>0.05</sub>S<sub>0.95</sub>PAN composite by co-heating Te<sub>x</sub>S<sub>1-x</sub> and PAN and the used the composite as the cathode materials for Li||SPAN batteries. Later, Zhang et al. (2020) [230], Yongbing Li et al. (2023) [231], Wang et al. (2024) [226], and Wu et al. (2024) [232] also developed Te-doped SPAN cathodes and demonstrated their enhanced electrochemical performance.

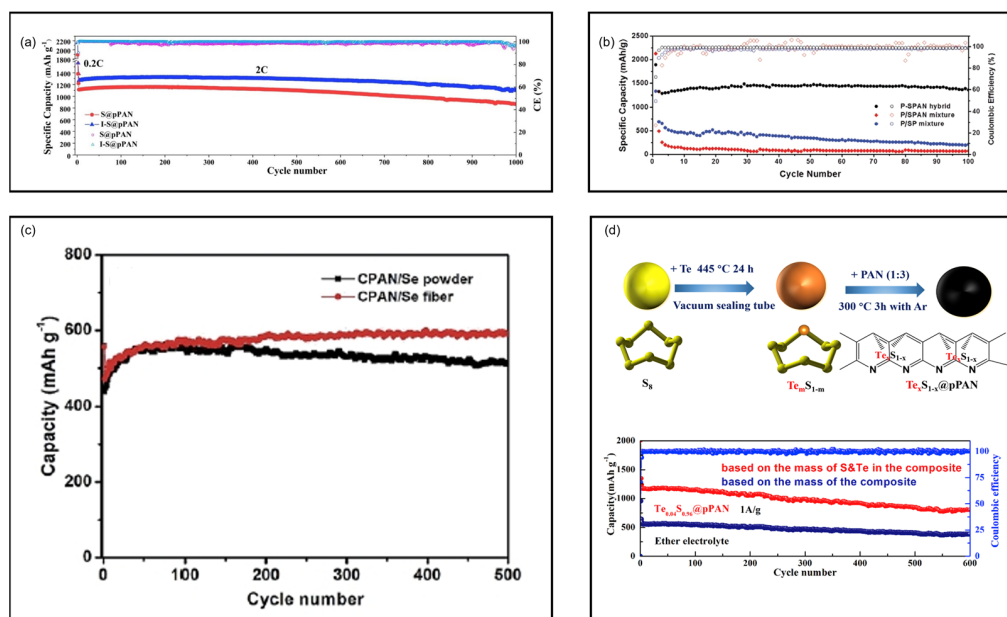


**Figure 18.** (a) The long-term cycling performance of I-S@pPAN. Reproduced with permission [182]. Copyright © 2021, Elsevier; (b) Cycling performance of P-SPAN hybrid, P/SPAN mixture, and P/SP mixture. Reproduced with permission [186]. Copyright © 2018, John Wiley and Sons; (c) Cycling performance of CPAN/Se fiber and powder electrodes. Reproduced with permission [188]. Copyright © 2014, Royal Society of Chemistry; (d) Schematic illustration of synthesis and proposed structure of  $\text{Te}_{0.04}\text{S}_{0.96}$ @pPAN and its cycling performance. Reproduced with permission [227]. Copyright © 2019, Elsevier.

### 8.6. Pre-Lithiation of SPAN

Li metal is considered as the optimal anode material for rechargeable Li batteries due to its high theoretical specific capacity ( $3860 \text{ mAh g}^{-1}$ ) and low reduction potential [233–235]. However, the practical application of Li metal anode is limited due to several severe issues, including the high reactivity of Li, the uncontrollable Li plating/stripping behavior, and the initial irreversible Li loss from the formation of solid-electrolyte interface (SEI) [236,237]. Unlike conventional cathodes such as lithium iron phosphate (LFP) or lithium nickel manganese cobalt oxide (NMC), no lithium exists in the pristine SPAN cathode and the traditional Li || SPAN batteries suffer from all the issues of lithium metal anode. To address these issues, pre-lithiation of the SPAN has emerged as an effective strategy. The following discussion will focus specifically on SPAN pre-lithiation approaches and their implications for battery performance.

#### 8.6.1. Half-Cell Electrochemical Method

The half-cell electrochemical method (HC-EM) involves assembling a Li || SPAN cell to electrochemically depositing Li into SPAN [238]. In 2009, He et al. pioneered the use of a pre-lithiated SPAN cathode and evaluated its electrochemical characteristics in a full-cell setup pairing with a graphite anode. In their work, SPAN was electrochemically pre-lithiated in a half-cell. The graphite || pre-lithiated SPAN cell could cycle stably at 0.1 C [239].

Jiang et al. reported a strategy to build a stable ultrathick lithium metal anode by overlithiating SPAN electrochemically [203] (Figure 19a). The resulting overlithiated SPAN showed uniform and dense morphology with an areal capacity up to  $30 \text{ mAh cm}^{-2}$  due to the formation of a robust  $\text{Li}_2\text{S}$ -rich hybrid SEI and a lithiophilic skeleton. When integrated into a Li-S battery with the overlithiated SPAN anode and the  $\text{Se}_{0.05}\text{S}_{0.95}$ PAN (areal

loading = 16 mAh cm<sup>-2</sup>) cathode, the battery exhibited excellent cycling stability at 1 mA cm<sup>-2</sup> under lean electrolyte (2.2  $\mu$ L mg<sup>-1</sup>s) and limited Li excess (N/P = 1.3). A 0.3 Ah Li-S pouch cell with sulfur loading of 8.7 mg cm<sup>-2</sup>, N/P of 1.5, and lean electrolyte of 3  $\mu$ L mg<sup>-1</sup>s was built and exhibited a capacity retention of 75% after 85 cycles at 0.5 mA cm<sup>-2</sup>.

In 2022, Ma et al. constructed an anode-free battery (Cu || LiSeSPAN) with electrochemically lithiated SeSPAN cathode [223]. It delivered an initial discharge capacity of 466 mAh g<sup>-1</sup> and retained 333 mAh g<sup>-1</sup> after 200 cycles at 2 mA cm<sup>-2</sup>, corresponding to a capacity retention of 71.5%. In 2024, Ma et al. reported a deep lithiation strategy for pPAN/SeS<sub>2</sub> cathode for high-performance anode-free SPAN batteries [224] (Figure 19b). The deep lithiation was achieved by deeply discharging the Li || pPAN/SeS<sub>2</sub> cells to a low potential of 0.28 V, where the Al current collector was also lithiated to form Li-Al alloy. Deep lithiation not only significantly boosts the lithium storage kinetics by accelerating lithium diffusion and improving electronic conductivity but also offers a stable lithiated pPAN/SeS<sub>2</sub> cathode for an anode-free cell system. An anode-free Cu || DL-pPAN/SeS<sub>2</sub> (areal mass loading = 7 mg cm<sup>-2</sup>) cell was fabricated and demonstrated superior cycling stability with a capacity retention of 90% after 45 cycles at 0.1 A g<sup>-1</sup>.

#### 8.6.2. Short-Circuit Electrochemical Method

The short-circuit electrochemical method (SC-EM) is achieved by the direct contact between Li metal and the SPAN electrode [238]. Unlike HC-EM, the complex assembly and disassembly of cells are avoided. However, SC-EM is considered more difficult to control and may pose safety risks due to excessive heat generation during the rapid pre-lithiation process.

Machida et al. investigated the electrochemical performance of pre-lithiated SPAN || Li<sub>4</sub>Ti<sub>5</sub>O<sub>12</sub> batteries treated with two lithiation strategies, HC-EM and SC-EM, respectively [240] (Figure 20). Both strategies enabled the SPAN || Li<sub>4</sub>Ti<sub>5</sub>O<sub>12</sub> batteries with excellent electrochemical properties and stable cycling.

In 2020, Shen et al. developed a simple in situ pre-lithiation approach for the SPAN cathode and graphite anode via direct contact with lithium metal foil in the presence of LP40 electrolyte (1 M LiPF<sub>6</sub> in EC/diethylene carbonate (DEC) (1/1, v/v)) [241]. The resulting Gr || Li<sub>2</sub>SPAN, LiGr || SPAN, and LiGr || Li<sub>2</sub>SPAN cells delivered initial capacities of about 1300, 1444, 1213 mAh g<sup>-1</sup> sulfur at 0.2 C, respectively, with stable cycling over 100 cycles. Wang et al. reported a facile mechanical kneading approach for the pre-lithiation of SPAN [242]. In this method, SPAN powder was spread between two pieces of Li foils and subjected to repeated folding and calendaring processes. When pairing with a LiCoO<sub>2</sub> cathode, the pre-lithiated SPAN || LiCoO<sub>2</sub> full cell exhibited a capacity retention of 96.5% after 100 cycles at 0.5 C, outperforming Li || LiCoO<sub>2</sub> cells. In 2024, Zhang et al. constructed Gr || LiSPAN and LiGr || SPAN pouch cells with graphite (Gr) and pre-lithiated SPAN or SPAN and pre-lithiated Gr, where the electrodes were in situ pre-lithiated by placing a thin Li foil on the electrodes during cell assembly [243]. Both cell configurations performed well, while the LiGr || SPAN pouch cell produced less heat than that of the Gr || LiSPAN pouch cell, making it a safer option for mass production.

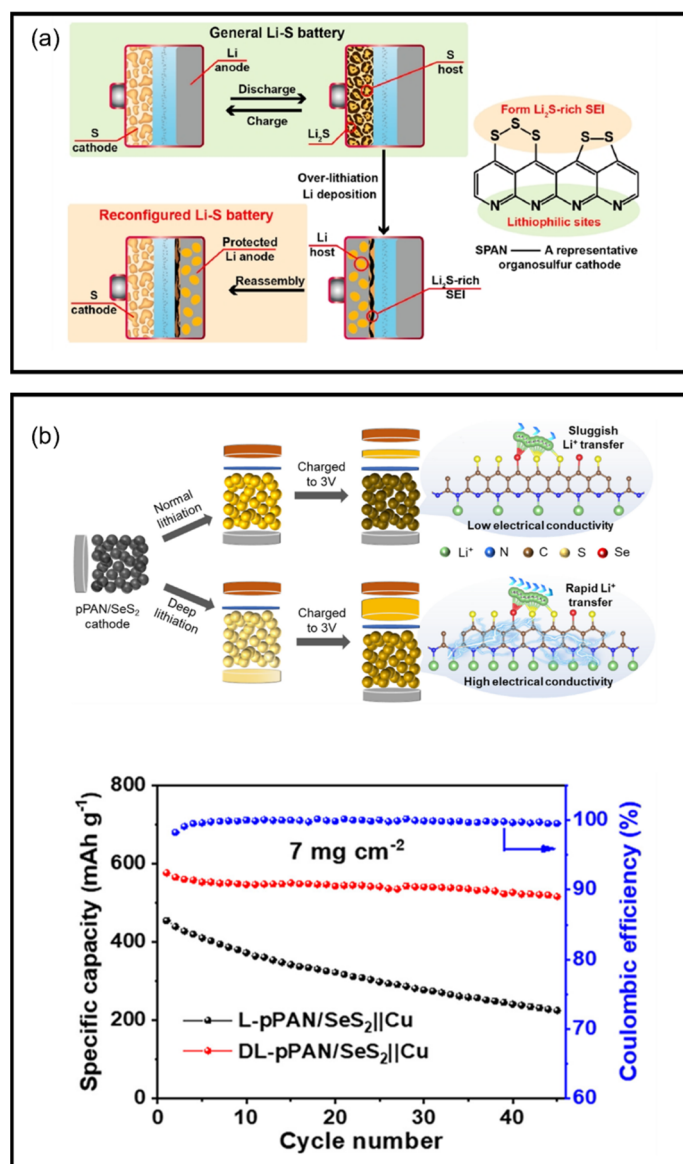


**Figure 19.** (a) Schematic illustration of the reconfiguration of a SPAN cathode by over-lithiation to produce a protected Li anode. Reproduced with permission [203]. Copyright © 2020, American Chemical Society; (b) Schematic illustration of normal lithiation and deep lithiation in pPAN/SeS<sub>2</sub> cathodes and their cycling performance in an anode–free cell configuration. Reproduced with permission [224]. Copyright © 2024, John Wiley and Sons.

#### 8.6.3. Chemical Method

The chemical pre-lithiation method for the SPAN electrode was first proposed by Shen et al. in 2019 [244]. Compared to other pre-lithiation methods, the chemical method is generally milder, more facile and scalable [238]. In Shen et al.'s study, they developed a facile chemical pre-lithiation strategy using lithium naphthalenide to fully lithiate SPAN into a Li<sub>2</sub>SPAN cathode and partially pre-lithiate nanosilicon into a Li<sub>x</sub>Si anode. The large initial irreversible capacity loss was prevented when the pre-lithiated Li<sub>2</sub>SPAN cathode was paired with the pre-lithiated Li<sub>x</sub>Si anode (Figure 21a). As a result, the Li<sub>x</sub>Si || Li<sub>2</sub>SPAN battery delivered a high specific energy of 710 Wh kg<sup>-1</sup>, high initial Coulombic efficiency (93.5%), and stable cyclability.

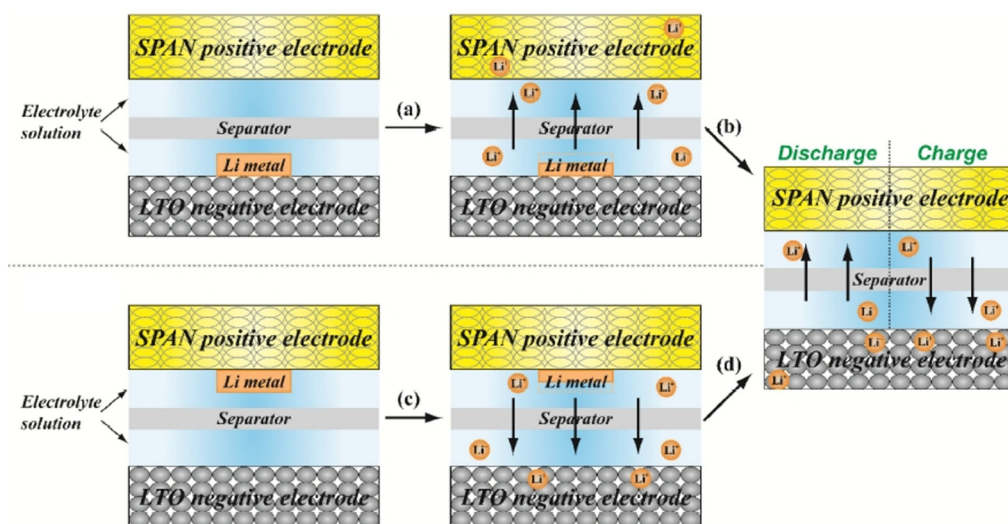


**Figure 20.** Schematic illustration of preparation and operation of SPAN ||  $\text{Li}_4\text{Ti}_5\text{O}_{12}$  cells by SC-EM. Reproduced with permission [240]. Copyright © 2022, The Electrochemical Society of Japan.

In 2022, Han et al. reported a high-areal-capacity Si-S full cell consisting of a pre-lithiated  $\text{SiO}$  anode and a thick pre-lithiated  $\text{Se}_{0.05}\text{S}_{0.95}\text{PAN}$  cathode [212]. The  $\text{SiO}$  anode and  $\text{Se}_{0.05}\text{S}_{0.95}\text{PAN}$  cathode were pre-lithiated chemically by Li-naphthalene and Li-4,4'-dimethylbiphenyl solution, respectively. The Si-S full cell featuring a high cathode loading ( $16 \text{ mg cm}^{-2}$ ), lean electrolyte ( $E/S = 2$ ), and limited lithium ( $N/P = 1.2$ ) delivered a high initial areal capacity of  $8.34 \text{ mAh cm}^{-2}$  and retained 52% after 80 cycles at  $0.5 \text{ mA cm}^{-2}$ .

Liu et al. reported a cathode lithiation strategy using  $\text{Li}_2\text{SPAN}$  as the lithium donor which was synthesized via chemical reaction between SPAN and Li-biphenyl complex solution [245] (Figure 21b). The  $\text{Li} \parallel \text{Li}_2\text{SPAN}$  cell shows an initial charge capacity of  $669 \text{ mAh g}^{-1}$ , indicating that all active lithium is released during the first charging process. The  $\text{Li}_2\text{SPAN}/\text{KB}$  in tetrahydrofuran (THF) slurry was loaded on the  $\text{LiFePO}_4$  electrode followed by compression to afford a pre-lithiated  $\text{LiFePO}_4/\text{Li}_2\text{SPAN}$  composite cathode. When paired with a silicon/graphite/carbon (Si/G/C) composite anode, the  $\text{Si/G/C} \parallel \text{LiFePO}_4/\text{Li}_2\text{SPAN}$  full cell delivered a reversible capacity of 123 and  $107 \text{ mAh g}^{-1}$  in the 1st and 10th cycle, which was 15.5% and 24.5% higher than the pristine  $\text{Si/G/C} \parallel \text{LiFePO}_4$  full cell, respectively. In addition, this work marked the first instance of chemical lithiation of SPAN in the powder form rather than as a pre-fabricated electrode.

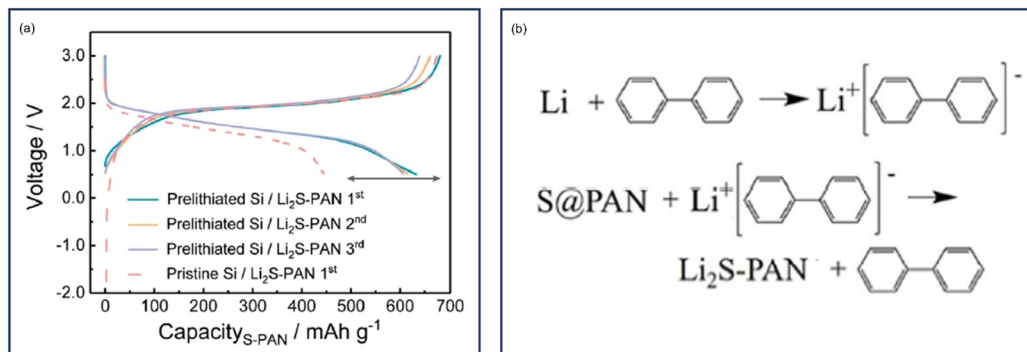


**Figure 21.** (a) Charge/discharge profiles of  $\text{Li}_x\text{Si} \parallel \text{Li}_2\text{SPAN}$  full cells. Reproduced with permission [244]. Copyright © 2019, American Chemical Society; (b) Synthetic reaction of Li-biphenyl and lithiation reaction of SPAN. Reproduced with permission. Copyright © 2021, American Chemical Society.

#### 8.6.4. Li-Containing Additives

The incorporation of Li-containing additive into the SPAN cathode represents another pre-lithiation strategy. In 2020, Lu et al. developed a novel Li/MgO/SPAN composite anode (LMS) for LSBs and LIBs [246] (Figure 22a). SPAN, Li powder, MgO, and CNTs were mixed in the glove box and pressed into anode disks. Upon annealing and electrolyte wetting, a “short circuit reaction” between Li and SPAN generated a hybrid framework rich in  $\text{Li}_2\text{S}$  and  $\text{Li}_3\text{N}$  which have been proved to be excellent SEI components. This in situ formed hybrid framework not only provided  $\text{Li}^+$  transport channels but also suppressed lithium dendrite growth. Consequently, the LMS || LiFePO<sub>4</sub> and LMS || SPAN full cells delivered stable cycle performance with capacity retention of 98.1% and 90.1% at 1 C, respectively.

A novel Li-S-PAN composite for LSBs was developed by Guo et al. in 2013 [247]. The Li-S-PAN composite was prepared by mixing  $\text{Li}_2\text{S}$  with PAN in a homogeneous solution, where PAN was lithiated and cross-linked by  $\text{Li}_2\text{S}$ , followed by carbonizing at elevated temperature to obtain an ideal Li-S-PAN composite. Multiple cathodic and anodic peaks between 1.5 and 3.5 V were observed during lithiation and de-lithiation process by CV.

In 2022, Wang et al. reported a novel silicon/carbon || SPAN/ $\text{Li}_3\text{N}$  full cell where the SPAN cathode was pre-loaded with  $\text{Li}_3\text{N}$  as the Li source [248] (Figure 22b). During the first charging,  $\text{Li}_3\text{N}$  decomposed via a nitrogen evolution reaction (NER), releasing  $\text{Li}^+$  into the silicon/carbon (Si/C) anode. ex situ EIS results indicated the decrease in resistance and improved reaction kinetics after the NER process. The Si/C || SPAN/ $\text{Li}_3\text{N}$  coin cell delivered a second cycle discharge capacity of  $1169.3 \text{ mAh g}^{-1}$  and retained 72% of the capacity after 100 cycles at  $500 \text{ mA g}^{-1}$ . In addition, the Si/C || SPAN/ $\text{Li}_3\text{N}$  pouch cell delivered an initial discharge capacity of 61.5 mAh and retained 40.7 mAh after 50 cycles at 3 mA, corresponding to a capacity retention of 67%.

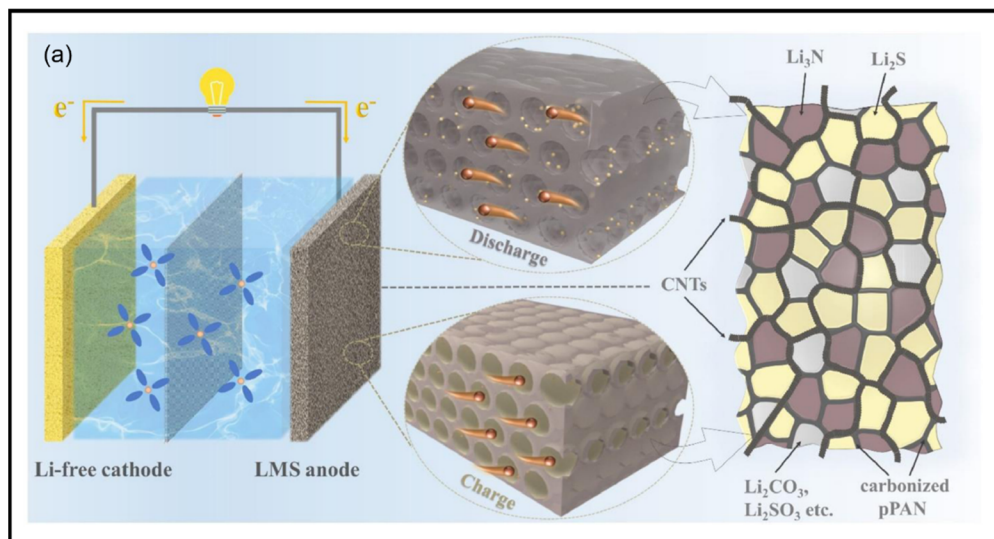


**Figure 22. Cont.**

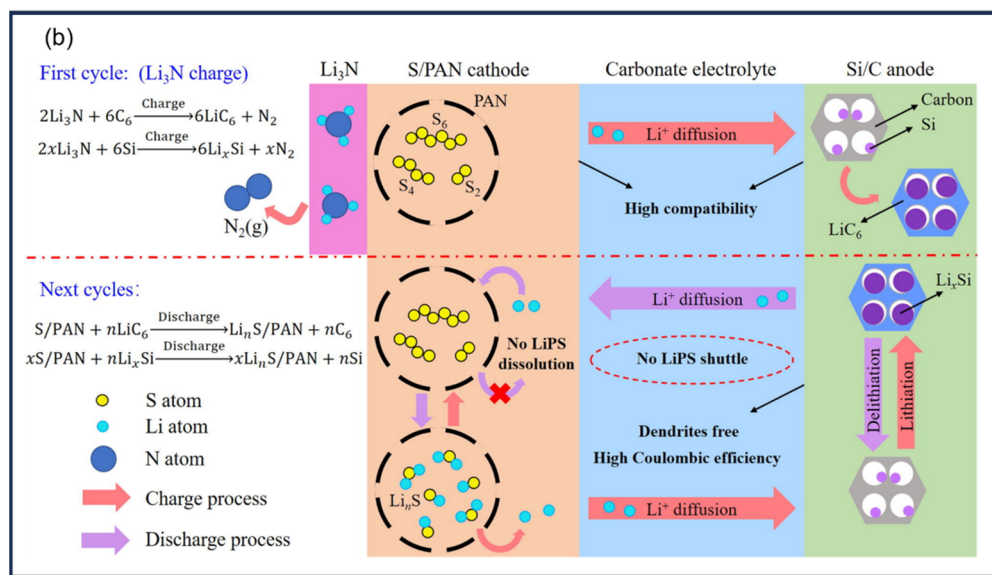


**Figure 22.** (a) Schematic illustration of behavior of Li in the LMS anode during plating/stripping process. Reproduced with permission [246]. Copyright © 2020, Elsevier; (b) Schematic illustration of the nitrogen evolution reaction process and the advantages of this battery system. Reproduced with permission [248]. Copyright © 2022, Elsevier.

## 9. Electrolytes

The development of compatible electrolytes for SPAN-based rechargeable batteries has been extensively reviewed in several publications [6,12,249–251] and remains an active area of research. This section discusses the studies that feature the development of electrolytes and is organized into the following categories: carbonate-based electrolytes, dilute ether-based electrolytes, high-concentration electrolytes (HCEs), localized high-concentration electrolytes (LHCEs), other liquid electrolytes, gel polymer electrolytes (GPEs), and solid-state electrolytes.

### 9.1. Carbonate-Based Electrolytes

In early SPAN studies focused on materials innovation, conventional carbonated-based electrolytes which have been widely used in Li-ion batteries were adopted for SPAN-based rechargeable batteries due to their chemical compatibility with the unique “solid–solid” conversion mechanism of SPAN [9–11,14]. These electrolytes typically consist of LiPF<sub>6</sub>, lithium bis(fluorosulfonyl)imide (LiFSI), or lithium bis(trifluoromethanesulfonyl)imide (LiTFSI) as the lithium salts, EC, dimethyl carbonate (DMC), DEC, ethyl methyl carbonate (EMC), or propylene carbonate (PC) as the solvents.

In 2012, Wang et al. conducted a comprehensive study on the charge/discharge characteristics of SPAN with different sulfur content using carbonate- and ether-based electrolytes [252]. The electrochemical performances of SPAN with 33.7 wt%, 42.0 wt%, and 46.3 wt% of sulfur content were tested in 1 M LiPF<sub>6</sub> in EC/DEC (1/1, v/v) and 1 M LiTFSI in DOL/DME (1/1, v/v), respectively. Their results demonstrated optimal electrochemical performance for SPAN with 42.0 wt% sulfur content. In addition, 1 M LiPF<sub>6</sub> in EC/DEC was a more suitable electrolyte than 1 M LiTFSI in DOL/DME for the SPAN cathode (Figure 23a). This observation was later explained by Zhang et al., who attributed the compatibility of Li||SPAN cells with carbonate-based electrolytes to the SPAN’s unique “solid–solid” redox reaction and the insolubility of sulfur species in carbonate solvents [18].

Further advancements in carbonate-based electrolyte optimization were reported by Warneke et al., who evaluated various linear carbonates (DMC, DEC, dipropyl carbonate

(DPC), and ethylene glycol bis(methyl carbonate) (EGBMC)) in the combination with FEC as electrolytes for Li || SPAN batteries [253]. Their study revealed an inverse correlation between the viscosity of these carbonates and the cell performance. Less viscous carbonates delivered high discharge capacities. As a result, 3 M LiTFSI in DMC/FEC (*v/v*, 2/1) endowed the battery with the best cycling performance and a reversible capacity of 991 mAh g<sup>-1</sup> sulfur after 600 cycles at 0.5 C.

Shen et al. reported that cyclic carbonates could help to sustain the “solid–solid” conversion mechanism for SPAN cathodes by forming a conformal polycarbonate-CEI which inhibited the polysulfides dissolution [254] (Figure 23b). In addition, cyclic carbonates also facilitate a stable Li deposition by inducing the formation of a bi-layered SEI with enhanced Li<sup>+</sup> transport and mechanical strength. A 100 mAh Li || SPAN pouch cell with limited lithium supply (N/P = 1.22) and 2 M LiFSI in EC as the electrolyte was built and delivered a capacity retention of 75% after 85 cycles at 1.038 mA cm<sup>-2</sup>. Highly concentrated carbonate-based electrolyte was studied by Wu et al. in 2014 [255]. They reported a novel carbonate-based desolvated gel electrolyte (DGE) for Li || SPAN batteries (Figure 23c). The DGE was prepared by adding LiPF<sub>6</sub> in EC/DMC until the solution become a gel, where the weight ratio of LiPF<sub>6</sub> to EC + DMC equaled to 0.72. With the high Li<sup>+</sup> to solvent ratio, Li<sup>+</sup> could be effectively desolvated, which was supported by IR spectra data and DFT calculations. DGE reduced the resistance of charge transfer at cathode/electrolyte interface and increased Li<sup>+</sup> transfer number, endowing Li || SPAN batteries with enhanced electrochemical performance.

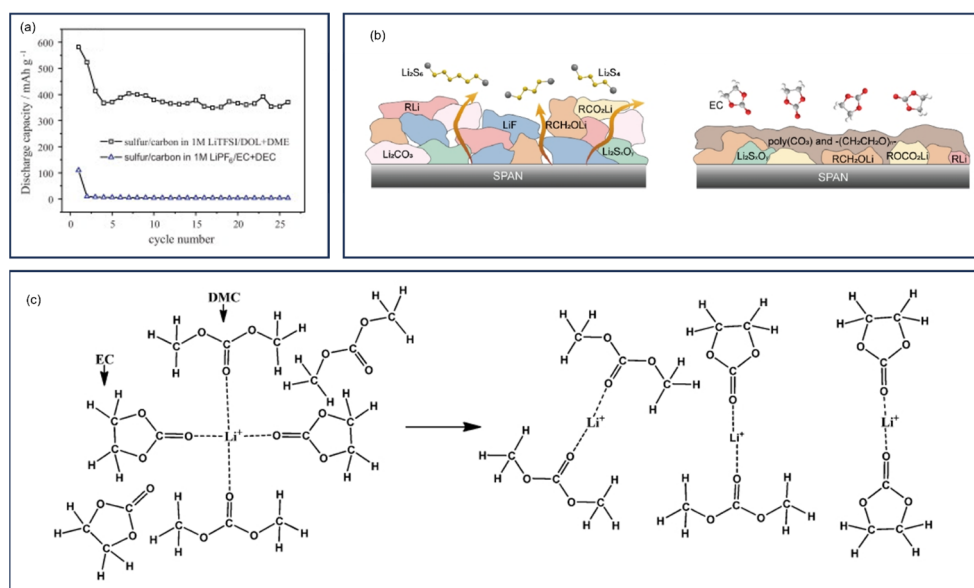


**Figure 23.** (a) Cycling performance of SPAN in 1 M LiTFSI in DOL/DME and 1 M LiPF<sub>6</sub> in EC/DEC electrolytes. Reproduced with permission [252]. Copyright © 2012, Elsevier; (b) Schematic illustration of the CEIs structure formed in 1 M LiFSI in DME (left) and 1 M LiFSI in DME/EC (right). Dark Grey: Li; yellow: S; light grey: C; red: O; white: H. Reproduced with permission [254]. Copyright © 2021, American Chemical Society; (c) Mechanism of the solvation effect of Li<sup>+</sup> in common carbonate electrolytes and desolvation of Li<sup>+</sup> in DGE. Reproduced with permission [255]. Copyright © 2014, American Chemical Society.

The effect of cyclic carbonates on the formation of SEI was investigated by Beltran et al. via ab initio molecular dynamics simulations [256]. The study revealed that linear solvents such as DOL and DMC remain stable with lithiated SPAN surface and are therefore unlikely to contribute to SEI formation. In contrast, cyclic carbonates such as EC and FEC are electrochemically active and undergo reductive decomposition on the lithiated

SPAN surface, forming a LiF-containing SEI. Additionally,  $\text{FSI}^-$  was found to be active and undergo a reductive defluorination path at the lithiated SPAN surface. However,  $\text{SO}_2\text{NSO}_2\text{F}^-$  and  $\text{SO}_2\text{NSO}_2^{2-}$  are stable against S-N cleavage, enabling LiFSI a potential suitable electrolyte salt candidate for  $\text{Li} \parallel \text{SPAN}$  batteries as it produces LiF without releasing  $\text{SO}_2$ . Further computational insights into the discharge behavior of  $\text{Li} \parallel \text{SPAN}$  batteries with carbonate-based electrolytes were provided by Klostermann et al. [257]. The results indicate that the discharge occurred in a stepwise reduction in the sulfur chain forming  $\text{Li}_2\text{S}$  in a “solid–solid” transition. The resulting  $\text{Li}_2\text{S}$  is stabilized by interactions with each other and with the nitrogen atoms on the polymer backbone.

The incorporation of functional additives has emerged as a promising strategy to engineer electrolyte properties in SPAN-based batteries. Particular attention has been directed toward addressing the inherent flammability of conventional organic electrolytes through the development of advanced flame-retardant additives, primarily focusing on phosphorus-containing compounds and fluorinated ethers. In 2013, Lin et al. reported using dimethyl methylphosphonate (DMMP) as a flame-retardant electrolyte additive to improve the thermal safety of  $\text{Li} \parallel \text{SPAN}$  batteries [258]. Subsequently, Wang et al. reported a flame-inhibiting electrolyte for  $\text{Li} \parallel \text{SPAN}$  batteries [259]. The addition of tris(2,2,2-trifluoroethyl) phosphite (TTFP), with a boiling point of 131 °C, to the  $\text{LiPF}_6$  in EC/DMC electrolyte, made the electrolyte non-flammable and modified the interfacial film generated on the SPAN cathode. Triphenyl phosphite (TPPi) as an electrolyte additive was demonstrated to improve the safety of  $\text{Li} \parallel \text{SPAN}$  batteries by Jia et al. [260]. Other than its flame-retardant properties, TPPi facilitated the formation of SEI and greatly reduced cell polarization. As a result, the  $\text{Li} \parallel \text{SPAN}$  battery with  $\text{LiPF}_6$  in EC/DMC containing 5 wt% TPPi delivered a capacity retention rate of 94.5% after 45 cycles at 0.5 C (Figure 24a). In 2018, Yang et al. developed a novel nonflammable electrolyte system consisting of 1 M lithium bis(oxalate) borate (LiBOB) in triethyl phosphate (TEP)/FEC (7/3, v/v) for  $\text{Li} \parallel \text{SPAN}$  batteries [261] (Figure 24b). The electrolyte is highly safe due to the flame-retardant property and thermal stability of TEP. The  $\text{Li} \parallel \text{SPAN}$  battery employing this novel electrolyte showed excellent electrochemical performance, delivering a capacity retention of 91.3% after 500 cycles at 1 C. Sodium trifluoromethanesulfonimide (NaTFSI) in trimethyl phosphate (TMP)/FEC was developed as a novel non-flammable electrolyte for room temperature  $\text{Na} \parallel \text{SPAN}$  batteries by Wu et al. [262].

The construction of a robust CEI and SEI, along with the inhibition of Li dendrite growth in carbonate-based electrolytes can benefit from the proper introduction of electrolyte additives or tailored electrolyte formulations. In 2015, Wu et al. introduced  $\text{Li}_2\text{SiO}_3$  particles into the  $\text{LiPF}_6$  in carbonate electrolytes during the cell assembly [263].  $\text{Li}_2\text{SiO}_3$  consumed the  $\text{PF}_5/\text{HF}$  species generated from the decomposition of the electrolytes, forming a passive protection layer on the cathode surface. The resulting  $\text{Li} \parallel \text{SPAN}$  battery with the  $\text{Li}_2\text{SiO}_3$  additive showed improved cyclability. Tris(trimethylsilyl) borate (TMSB) as an electrolyte additive was demonstrated as an effective facilitating agent for the construction of stable EEIs for  $\text{Li} \parallel \text{SPAN}$  batteries by Wang et al. [264] TMSB participated in the formation of stable interfaces with less impedance on both electrodes, thus improving cycling and rate performances. The  $\text{Li} \parallel \text{SPAN}$  battery with  $\text{LiPF}_6$  in EC/DMC containing 1% TMSB delivered a capacity retention of 81% after 150 cycles at 0.5 C, and a rate performance of above 1400  $\text{mAh g}^{-1}$  sulfur at 10 C.

To address Li dendrite formation, low Coulombic efficiency, and cathode instability, Xu et al. designed a novel electrolyte system comprising 1 M lithium oxalyldifluoroborate ( $\text{LiODFB}$ ) in EC/EMC/FEC (4.5/4.5/1, v/v/v) solvents for  $\text{Li} \parallel \text{SPAN}$  batteries [265]. LiODFB and FEC work synergistically to form a stable and compact SEI layer containing  $\text{Li}_2\text{CO}_3$ , LiF, and short chain organic compounds, mitigating side-reactions and accommo-

dating volume changes during cycling (Figure 24c). This electrolyte system demonstrated excellent compatibility with both Li anode and SPAN cathode, delivering a reversible capacity of about  $1400 \text{ mAh g}^{-1}$  sulfur and a capacity retention rate of 89% after 1000 cycles at 1 C. The beneficial effects of FEC has been further corroborated by subsequent by Kim et al. (2017) [266], Yang et al. (2018) [261,267], Chen et al. (2018) [268], Wu et al. (2019) [262], Shuai et al. (2019) [269], Cai et al. (2020) [270], Park et al. (2023) [271], highlighting its versatility in carbonated-based systems.

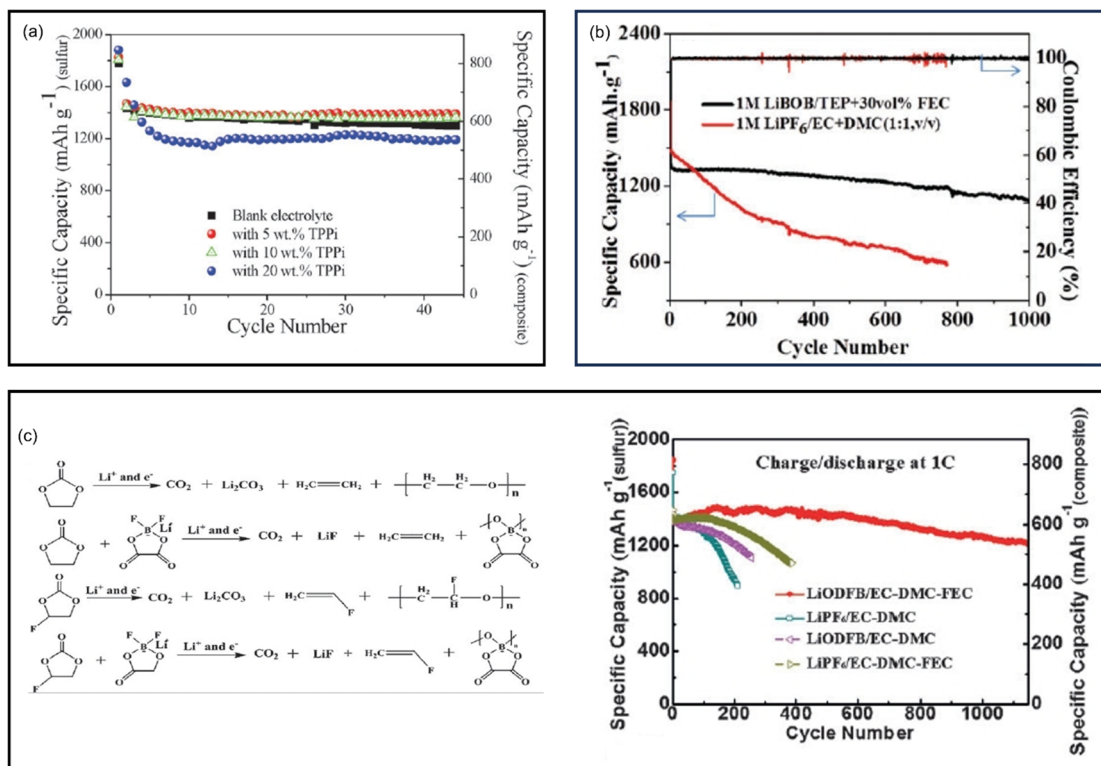


**Figure 24.** (a) Cycling performance of Li || SPAN cells with different concentrations of TPPi. Reproduced with permission [260]. Copyright © 2014, Royal Society of Chemistry; (b) Cycling performance of Li || SPAN cells in TEP–based electrolyte and standard carbonate electrolyte. Reproduced with permission [261]. Copyright © 2018, Royal Society of Chemistry; (c) left: Proposed formation mechanism of the protective film on the Li electrode; right: Cycling performance of Li || SPAN cells in different electrolytes. Reproduced with permission [265]. Copyright © 2016, John Wiley and Sons.

Dai et al. employed hexadecyl trimethylammonium chloride (CTAC) as a carbonated-based electrolyte additive for suppressing the Li dendrite growth in lithium metal batteries [272]. The CTAC surfactant aggregated around protuberances via electrostatic interactions and formed a nonpolar lithiophobic protect layer, driving the deposition of lithium ions to adjacent regions and prevent dendrite formation. Li || SPAN batteries were built with carbonate-based electrolytes with and without CTAC. Consequently, the Li || SPAN battery with CTAC showed better electrochemical performance, delivering high reversible capacity ( $962.8 \text{ mAh g}^{-1}$  sulfur at  $3.2 \text{ A g}^{-1}$ ) and long cycling life (up to 500 cycles).

LiBOB was explored as an electrolyte additive in EC/DMC/EMC to facilitate the in situ formation of a protective layer on the SPAN cathode surface by Jin et al. in 2019 [273]. The protective layer, composed of sulfides, inorganic  $\text{LiB}_x\text{O}_y$ , and limited amount of  $\text{ROCO}_2\text{Li}$  species, effectively mitigated the SPAN cathode from parasitic reactions with the electrolytes (Figure 25a). In 2023, Park et al. reported an electrolyte consisting of 0.8 M LiTFSI, 0.2 M lithium difluoro(oxalate)borate (LiDFOB), and 0.05 M LiPF<sub>6</sub> in EMC/FEC (3/1, v/v) solution for high-performance Li || SPAN batteries [271]. LiDFOB, with a low

LUMO energy level, facilitated boron compound formation which helped form a stable SEI on the anode. In addition, FEC facilitated the formation of a stable LiF-rich SEI on the anode. The small amount of LiPF<sub>6</sub> prevented Al corrosion by increasing the oxidation stability of the electrolyte due to its low HOMO energy level of LiPF<sub>6</sub>. Consequently, the Li || SPAN battery employing this electrolyte delivered a stable cycling with a capacity retention of 73.5% after 1000 cycles at 0.5 C.

A dual-additive strategy was employed by Li et al., introducing tris(trimethylsilyl) phosphite-vinylene carbonate (TMSP-VC) into the common carbonate-based electrolytes to enhance the electrochemical performance of Li || SPAN batteries [274]. During the charge/discharge process, TMSP was oxidized and scavenged HF derived from the electrolyte degradation, synergistically working with VC to form a protective and stable SEI layer with smaller impedance. The Li || SPAN battery with 1 wt% TMSP and 2 wt% VC in LiPF<sub>6</sub> + EC/DMC electrolyte exhibited a reversible capacity of 1243 mAh g<sup>-1</sup> sulfur over 800 cycles at 1 C, corresponding to a negligible capacity decay rate of 0.019% per cycle (Figure 25b). Dual additives of LiNO<sub>3</sub> and CsF in carbonate electrolytes were demonstrated to facilitate the formation of a stable inorganic-rich SEI on the Li metal anode by Zhao et al. in 2023 [275]. Due to the cation size effect, CsF improved the solubilization of LiNO<sub>3</sub> in carbonate solvents. The Li || SPAN batteries employing the electrolyte with the additives achieved better capacity retention than those of the batteries using the base electrolyte. In 2024, Guo et al. developed an EC-based electrolyte containing dual-additives (0.5 wt% 2-fluoropyridine (2-FP) and 0.5 wt% lithium difluorobis (oxalate) phosphate (LiDFBOP)) for Li || SPAN batteries [276]. 2-FP, with a low LUMO energy level, promoted the formation of a LiF-rich film on the electrode. Simultaneously, LiDFBOP facilitated the formation of a Li<sub>x</sub>PO<sub>y</sub>F<sub>z</sub>-rich electrolyte-electrode interface, compensating for the kinetic deterioration caused by the lower ionic conductive LiF (Figure 25c). Consequently, the Li || SPAN battery delivered a capacity retention of 97.5% after 200 cycles at 1 C and a superior rate performance with a capacity of 1128.1 mAh g<sup>-1</sup> at 5 C.

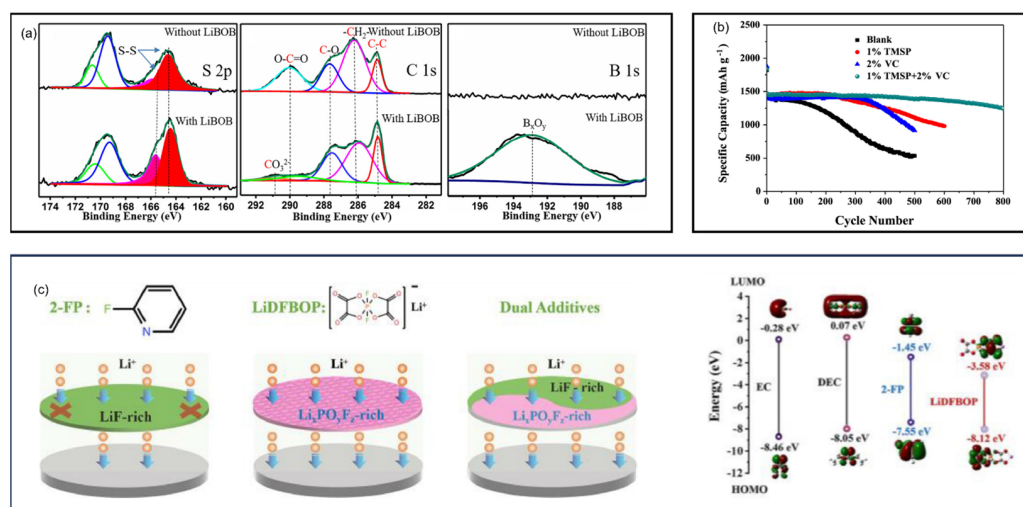


**Figure 25.** (a) S, C, and B XPS spectrum of SPAN electrodes after 100 cycles in electrolytes without and with 1 wt% LiBOB. Reproduced with permission [273]. Copyright © 2019, Elsevier; (b) Cycling performance of Li || SPAN cells with different additives. Reproduced with permission [274]. Copyright © 2018, Elsevier; (c) left: Proposed combined effect mechanism of dual additives in the formation of EEIs; right: LUMO and HOMO energies of EC, DEC, 2-FP, and LiDFBOP. Reproduced with permission [276]. Copyright © 2024, Elsevier.

Lebherz et al. reported the use of ionic dendrimers as conductive salts in carbonate-based electrolytes to mitigate polysulfides shuttling in Li || SPAN batteries [277]. The

best electrolyte system was obtained with an ionic dendrimer with a short side chain, possessing the lowest viscosity and highest conductivity. The as-assembled Li||SPAN battery delivered a discharge capacity of  $1150 \text{ mAh g}^{-1}$  sulfur at 0.5 C and  $780 \text{ mAh g}^{-1}$  sulfur at 1 C.

The correlation between cell performance and operating temperature in Li||SPAN batteries employing carbonate-based electrolytes was systematically investigated by Mayer et al. in 2018 [278]. Their study revealed that a rapid and irreversible cell degeneration occurs at temperatures exceeding  $38^\circ\text{C}$ , while reversible capacity loss is observed between  $-20^\circ\text{C}$  and  $0^\circ\text{C}$  with full recovery upon warming up to room temperature. Therefore, the authors conclude that Li||SPAN batteries can cycle reversibly between  $-20$  and  $38^\circ\text{C}$  in carbonate-based electrolytes.

By adopting electrolyte solvents with low melting point and high boiling point, SPAN batteries could operate under extended temperature range. Cai et al. reported a novel electrolyte comprising LiFSI in methyl propionate (MP)/FEC for low-temperature Li||SPAN batteries [270]. MP is a carboxylate ester with a low melting point ( $-87.5^\circ\text{C}$ ) and FEC is known for stabilizing the SEI. The Li||SPAN batteries employing this electrolyte system exhibited stable cycling and retain over 91% and 78% of their room temperature capacity at  $-20^\circ\text{C}$  and  $-40^\circ\text{C}$ , respectively. Further advancing this approach, Cai et al. later designed an all-fluorinated ester-based electrolyte comprising partially fluorinated carboxylate and carbonate esters (LiFSI in methyl 3,3,3-trifluoropropionate (MTFP)/FEC) for high areal loading Li||SPAN batteries operated under extreme temperatures [279]. The electrolyte combines temperature-resilient physicochemical properties with moderate ion-paired solvation, allowing facile desolvation and the formation of LiF-rich interphases. As a result, the Li||SPAN batteries with a high areal capacity ( $>3.5 \text{ mAh cm}^{-2}$ ) and thin Li metal anode (50  $\mu\text{m}$ ) delivered stable cycling at  $-40$ ,  $23$ , and  $50^\circ\text{C}$  (Figure 26a).

In 2021, Zhao et al. reported an innovative redox mediation strategy to accelerate the electron transfer process in Li||SPAN batteries [280] (Figure 26b). Specifically, a quinone-based redox mediator, 1,5-bis(2-(2-[2-methoxyethoxy]ethoxy)ethoxy)antra-9,10-quinon (BEAQ) was introduced to the carbonate-based or ether-based electrolytes as an additive. During cycling, oxidized BEAQ and reduced BEAQ actively assist the de-lithiation and lithiation of SPAN, facilitating the electrochemical process. Li||SPAN batteries with higher capacity, improved rate performance, and reduced polarization were achieved in both carbonate-based and ether-based electrolytes with BEAQ. Zhang et al. reported using phenyl diselenide (PDSe) as an electrolyte additive in both carbonate and ether-based electrolytes to enhance the reaction kinetics of the SPAN cathode, where the radical exchange in the solid–liquid interface forms dynamic S–Se bonds [281]. The S–Se bonds effectively accelerated the sulfur kinetics and reduced  $\text{Li}_2\text{S}$  deposition on the lithium metal anode, yielding improved battery performance. As a result, the Li||SPAN battery with the carbonate electrolyte delivered a discharge capacity of  $1135 \text{ mAh g}^{-1}$  sulfur after 100 cycles at 1 C.

Very recently, Chen et al. reported a novel external Li supply approach to provide extra  $\text{Li}^+$  to rejuvenate conventional Li-ion batteries after cycling [282] (Figure 27). Leveraging machine learning, an organic Li salt,  $\text{LiSO}_2\text{CF}_3$  was identified, synthesized, and used as an additive to the conventional carbonate-based electrolyte. During charging, the  $\text{SO}_2\text{CF}_3^-$  anion undergoes oxidative decomposition, releasing  $\text{SO}_2$  and  $\text{C}_2\text{F}_6/\text{CHF}_3$  gases and liberating active  $\text{Li}^+$ . As a proof of concept, a 30.5 Ah anode-less pouch cell with SPAN as the cathode and 61.0 Ah of active  $\text{Li}^+$  from  $\text{LiSO}_2\text{CF}_3$  was assembled and retained 80.1% of its capacity after 440 cycles at 0.5 C.

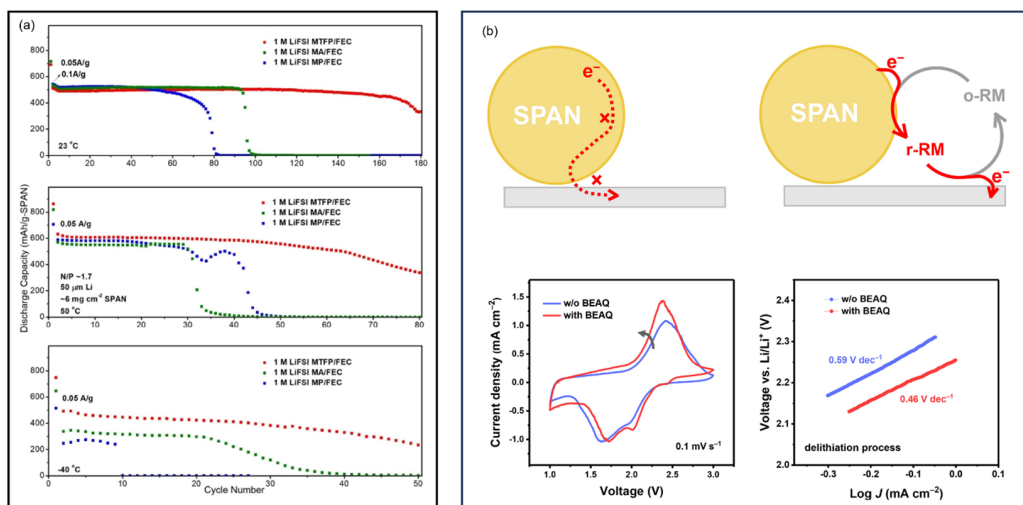


**Figure 26.** (a) Cycling performance of Li||SPAN cells in selected electrolytes at different temperatures. Reproduced with permission [279]. Copyright © 2023, John Wiley and Sons; (b) top: Schematic illustration of RM–assisted electron transfer pathway for SPAN electrode; bottom: CV curves and corresponding Tafel plots of Li||SPAN cells with and without BEAQ. Reproduced with permission [280]. Copyright © 2021, John Wiley and Sons.

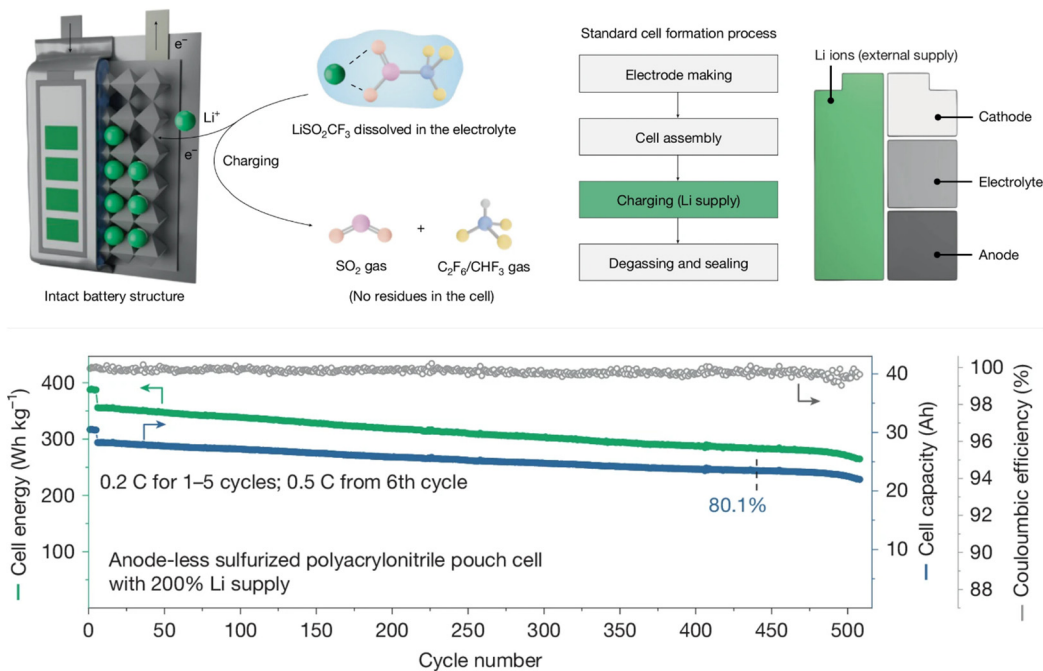


**Figure 27.** top: Schematic illustration of the charging process. LiSO<sub>2</sub>CF<sub>3</sub> is oxidized, resulting in the generation of SO<sub>2</sub>, C<sub>2</sub>F<sub>6</sub>, and CHF<sub>3</sub> gases. Consequently, an active Li<sup>+</sup> ion is donated to the cell and stored in the anode; bottom: Cycling performance of a 30.5 Ah anode-less SPAN pouch cell. Reproduced with permission [282]. Copyright © 2025, Springer Nature.

In Na||SPAN batteries, sodium salts are employed as the conductive salts in the electrolyte. The first report of a Na||SPAN batteries was reported by Wang et al. in 2007 [283], where 1 M NaClO<sub>4</sub> in EC/DMC was used as the electrolyte. The Na||SPAN battery was tested at room temperature, displaying an initial discharge capacity of 654.8 mAh g<sup>-1</sup><sub>SPAN</sub> and retaining a reversible specific discharge capacity of about 500 mAh g<sup>-1</sup><sub>SPAN</sub> in the following 18 cycles. Murugan et al. later reported a room temperature Na||SPAN battery with an electrolyte containing sodium tetrakis(hexafluoroisopropoxy) borate (Na[B(hfip)<sub>4</sub>])

in EC/DMC/FEC [284]. The hfp anion, being weakly coordinating, imparts high anodic stability, high ionic conductivity, and superior electrochemical performance in carbonate-based solvents. As a result, the Na || SPAN battery employing this electrolyte delivered an initial discharge capacity of  $1360 \text{ mAh g}^{-1}$  sulfur and retained  $1072 \text{ mAh g}^{-1}$  sulfur after 1000 cycles at 3 C, corresponding to a capacity decay rate of 0.021% per cycle. In 2021, Murgan et al. introduced a novel sodium salt, sodium bis(perfluoropinacol)borate (NaPPB), for room temperature Na || SPAN batteries [285]. NaPPB offers a wide redox window, high solubility, and good compatibility with Na || SPAN batteries. The Na || SPAN battery employing 1 M NaPPB in PC/FEC exhibited a discharge capacity of  $965 \text{ mAh g}^{-1}$  sulfur after 500 cycles at 2 C, corresponding to a capacity decay rate of 0.016% per cycle.

For K || SPAN batteries, KPF<sub>6</sub> is one of the mostly used salts in electrolytes. In 2018, Liu et al. assembled a room temperature K || SPAN battery operated in 0.8 M KPF<sub>6</sub> in EC/DEC (*v/v*, 1/1), yielding an initial discharge capacity of  $710 \text{ mAh g}^{-1}$  sulfur and 54% of capacity retention after 100 cycles at 0.5 C [286]. Lou et al. developed a hybrid Na-K || SPAN battery employing a sodium metal anode, a SPAN cathode, and a mixed electrolyte composed of NaPF<sub>6</sub> + KPF<sub>6</sub> in EC/DMC/EMC [287]. This Na-K || SPAN battery delivered a high reversible capacity of  $1405.5 \text{ mAh g}^{-1}$  sulfur after 100 cycles at 35 mA g<sup>-1</sup>.

## 9.2. Dilute Ether-Based Electrolytes

Compared to carbonate-based electrolytes, ether-based electrolytes generally exhibit better chemical compatibility with the Li metal anodes. However, studies have shown that dilute ether-based electrolytes lead to fast capacity decay in SPAN-based batteries due to the dissolution of polysulfides, making them an inferior option than the carbonate-based electrolytes [15,43,252].

Wu et al. studied the structural transformation of SPAN and the role of the cathode-electrolyte interface (CEI) in Li || SPAN batteries in different electrolytes via multiple characterization techniques [288] (Figure 28). Their findings revealed that in carbonated-based electrolytes, a robust CEI is formed while a porous dendrite Li morphology is observed on the Li anode. In contrast, in ether-based electrolytes, a weak CEI is formed on the cathode and a dense spherical morphology is observed on the Li anode. The authors designed an ether-based electrolyte with LiNO<sub>3</sub> additive and demonstrated its superior compatibility with Li || SPAN batteries.

To address the dendrite growth issue with Li metal anode, Miao et al. developed a novel dual-salt system composed of LiFSI and LiTFSI in DOL/DME for Li || SPAN batteries [289]. Compared to LiTFSI in DOL/DME and LiPF<sub>6</sub> in EC/DMC electrolytes, the dual-salt electrolyte system displayed improvement in Li crystal growth pattern and higher columbic efficiency. In addition, this electrolyte system showed good compatibility with Li || SPAN batteries. The roles of lithium salts and solvents in the electrolytes during the SPAN discharge process were studied via ab initio molecular dynamics by Kuai et al. in 2024 [290]. Through XPS and AIMD analyses, they demonstrated that LiFSI serves versatile roles during the electrochemical process: (1) as the primary source of the CEI, (2) being a charge carrier, and (3) as a mediator in the PSs generation process. In addition, the analysis of ab initio molecular dynamics trajectories during lithiation revealed that ether solvents, compared to carbonate solvents, provide stronger solvation and enhanced chemical stabilization for both salts and SPAN structures.

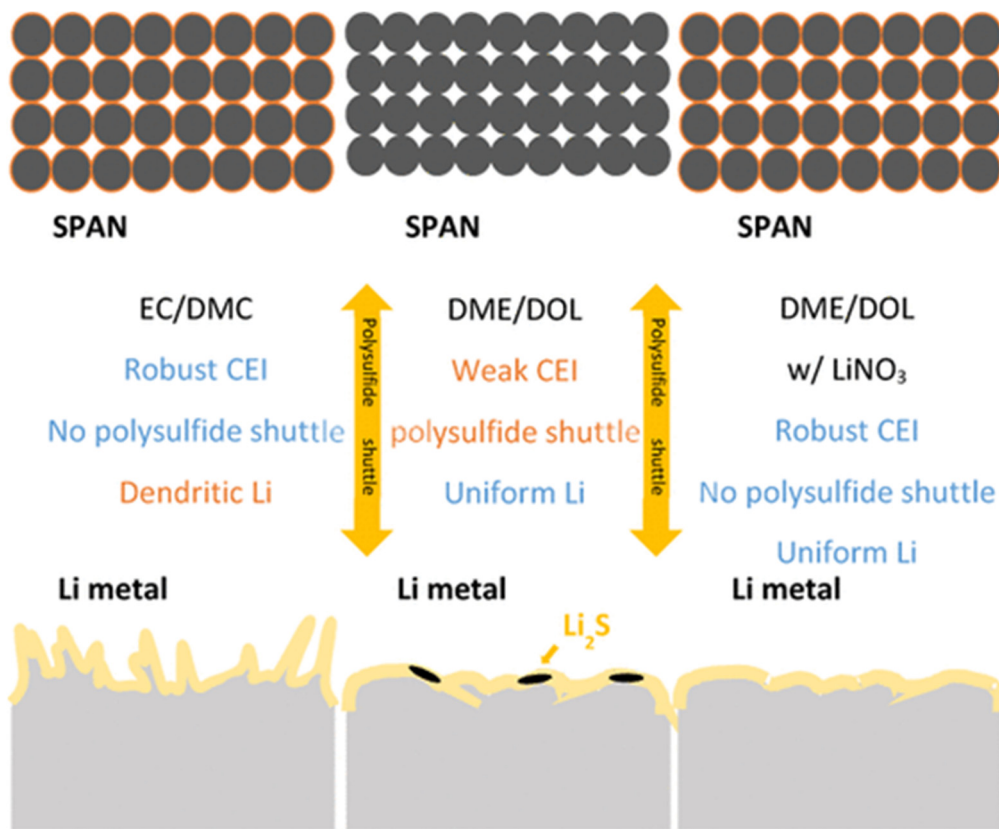


**Figure 28.** Schematic illustration of formation process of CEI for  $\text{Li} \parallel \text{SPAN}$  cells in different electrolytes. Reproduced with permission [288]. Copyright © 2021, American Chemical Society.

In 2019, Shuai et al. further optimized ether-based electrolytes by introducing FEC and  $\text{LiNO}_3$  as dual additives into  $\text{LiTFSI}/\text{DME}/\text{DOL}$  for  $\text{Li} \parallel \text{SPAN}$  batteries [291] (Figure 29a). FEC and  $\text{LiNO}_3$  synergistically regulated the solvation sheath of  $\text{Li}^+$  and facilitated the formation of a high-quality SEI and CEI composed of  $\text{LiF}$ ,  $\text{LiN}_x\text{O}_y$ , and  $\text{Li}_2\text{S}_x\text{O}_y$  on both the lithium metal anode and the SPAN cathode. As a result, the  $\text{Li} \parallel \text{SPAN}$  battery employing this electrolyte delivered a reversible capacity of  $670 \text{ mAh g}^{-1}$  SPAN and retained 75% of its capacity after 300 cycles at  $0.2 \text{ C}$  with  $4 \text{ mAh cm}^{-2}$  and  $7 \mu\text{L mg}^{-1}$  SPAN electrolyte. The beneficial effects of  $\text{NO}_3^-$  in ether-based electrolytes were also demonstrated by multiple studies by Kim et al. (2015) [292,293], Wu et al. (2021) [288] Jia et al. (2024) [294], and Luo et al. (2024) [295]. Chen et al. developed a mixed diisopropyl ether-based (mixed-DIPE) electrolyte composed of 1 M  $\text{LiTFSI}$  in DIPE/DOL/DME (2/1/1, *v/v*) with 5% EC additive to effectively protect the lithium metal anode in  $\text{Li} \parallel \text{SPAN}$  batteries [296]. The mixed-DIPE electrolyte facilitated the formation of a stable lithium-oxide-rich SEI layer on the lithium anode and suppressed the lithium dendrite growth, rendering significantly improved cycling stability. Consequently, the  $\text{Li} \parallel \text{SPAN}$  battery with an ultrathin lithium metal anode ( $50 \mu\text{m}$ ) contributed to a doubled life span of 156 cycles at  $0.5 \text{ C}$  compared with the routine electrolytes (Figure 29b). To mitigate the polysulfide dissolution issue associated with the dilute ether-based electrolytes, 4-aminobenzoic acid (4-ABA) as an additive was introduced into ether-based electrolytes by Zheng et al. [297]. 4-ABA contributes to the formation of a stable CEI which protects the SPAN cathode and minimizes the active material loss. As a result, the  $\text{Li} \parallel \text{SPAN}$  battery delivered a reversible capacity of  $1178.73 \text{ mAh g}^{-1}$  after 100 cycles at  $0.5 \text{ C}$ , corresponding to a capacity retention of 88.81%.

Li et al. reported a strategy to address the low initial Coulombic efficiency issue induced by the sluggish reaction kinetics in  $\text{Li} \parallel \text{SPAN}$  batteries by introducing a trace

amount of soluble  $\text{Li}_2\text{S}8$  as a redox mediator into the electrolyte [146]. During discharge, the  $\text{Li}_2\text{S}$  formed is oxidized by  $\text{Li}_2\text{S}8$ , facilitating the transformation of not only C-S and S-S bonds in SPAN but also elemental sulfur. This approach enabled the  $\text{Li} \parallel \text{SPAN}$  battery with a high initial CE of 82.9% at  $200 \text{ mA g}^{-1}$  and a discharge capacity of  $1170 \text{ mAh g}^{-1}$  sulfur after 400 cycles at  $1 \text{ A g}^{-1}$ . Wu et al. reported a dual-functional electrolyte additive,  $\text{Li}_2\text{Se}$ , as a sulfur redox mediator and a Li deposition regulator for  $\text{Li} \parallel \text{SPAN}$  batteries with dilute ether-based electrolytes [298]. For the SPAN cathode,  $\text{Li}_2\text{Se}$  could react with the S-S bonds of polysulfides to form more electrochemically active S-Se bonds with lower bond dissociation energy to accelerate the sulfur redox kinetics. For the Li metal anode,  $\text{Li}_2\text{Se}$  could promote  $\text{Li}^+$  transportation across the interface, achieve homogeneous  $\text{Li}^+$  flux, and suppress the Li dendrite growth (Figure 29c). The resulting  $\text{Li} \parallel \text{SPAN}$  battery delivered a discharge capacity of  $1187 \text{ mAh g}^{-1}$  after 100 cycles at  $0.5 \text{ C}$ , corresponding to a capacity retention of 80%.

Zhang et al. proposed a bifunctional electrolyte additive, 1,4-difluoroanthraquinone (DFAQ), which acts as both a lithium regulator and a sulfur redox mediator in ether-based electrolytes for  $\text{Li} \parallel \text{SPAN}$  batteries [299]. DFAQ facilitates the formation of a rigid and smooth LiF-rich SEI, enabling reversible Li plating/stripping and inhibiting Li dendrite growth. In addition, DFAQ serves as a redox mediator through a radical-mediated catalytic cycle to promote the conversion of LiPSs. As a result, the  $\text{Li} \parallel \text{SPAN}$  battery with a high areal loading ( $5.8 \text{ mg s cm}^{-2}$ ), lean electrolyte ( $E/S = 5$ ) exhibited a reversible capacity of  $1013.4 \text{ mAh g}^{-1}$  sulfur ( $5.9 \text{ mAh cm}^{-2}$ ) after 80 cycles at  $0.1 \text{ C}$  (Figure 29d).

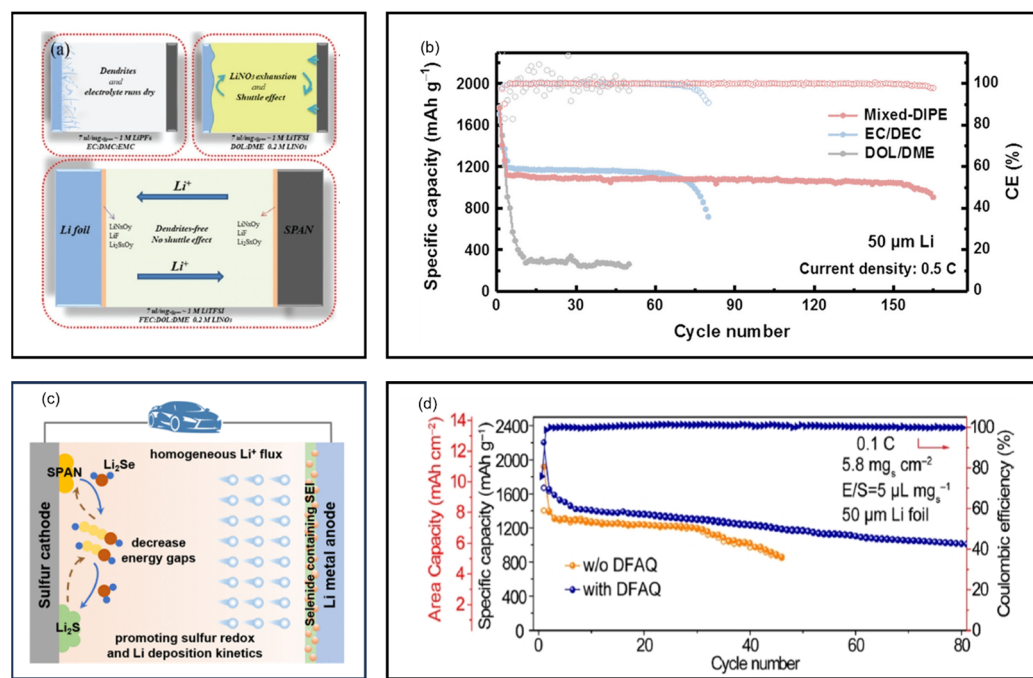


**Figure 29.** (a) Schematic illustration of full cells with different electrolytes. Reproduced with permission [291]. Copyright © 2019, Royal Society of Chemistry; (b) Cycling performance of  $\text{Li} \parallel \text{SPAN}$  cells with different electrolytes. Reproduced with permission [296]. Copyright © 2020, John Wiley and Sons; (c) Schematic illustration of the effects of  $\text{Li}_2\text{Se}$  mediator in  $\text{Li} \parallel \text{SPAN}$  cells. Reproduced with permission [298]. Copyright © 2023, American Chemical Society; (d) Cycling performance of  $\text{Li} \parallel \text{SPAN}$  cells with and without DFAQ. Reproduced with permission [299]. Copyright © 2022, American Chemical Society.

Iodine-nitrate ( $\text{I}_2\text{-LiNO}_3$ ) as dual additives introduced into the standard DOL/DME-based ether electrolyte for high-performance  $\text{Li} \parallel \text{SPAN}$  batteries were reported by Jia

et al. [294]. In this system,  $\text{NO}_3^-$  oxidizes  $\text{HI}$  to  $\text{I}_3^-/\text{IO}_3^-$  species to avoid  $\text{HI}$ -induced DOL-ring opening polymerization reactions. Meanwhile,  $\text{I}_3^-/\text{IO}_3^-$  species promote the reaction kinetics of the SPAN cathode by oxidizing the insulating  $\text{Li}_2\text{S}$  and reactivate dead Li on the anode by forming soluble  $\text{LiI}$ , releasing Li back to the battery cycling. As a result, the  $\text{Li} \parallel \text{SPAN}$  battery delivered a reversible capacity of  $1200 \text{ mAh g}^{-1}$  after 1000 cycles at  $1 \text{ A g}^{-1}$ , with a capacity retention of almost 100%.

The electrolyte solvation structure and the solvating power of solvent have been demonstrated to be critical for the reversible cycling of Li metal. Electrolytes with weakly solvating power exhibit lower desolvation energy and allow for uniform Li deposition morphology. In 2021, Holoubek et al. conducted a comparative study of 1 M LiFSI in weakly solvating DEE and 1 M LiFSI in DOL/DME for low temperature  $\text{Li} \parallel \text{SPAN}$  batteries [300] (Figure 30). The  $\text{Li} \parallel \text{SPAN}$  battery retained 76% capacity at  $-60^\circ\text{C}$  in the DEE electrolyte, in stark contrast to only 2.8% in the DOL/DME-based control. Further advancing this concept, Ma et al. developed a novel dimethoxymethane (DMM)-based electrolyte with weakly solvating power for LMBs [301]. Molecular dynamics (MD) simulations and spectral analysis revealed that weaker solvating solvents promote greater anion participation in  $\text{Li}^+$  solvation sheaths, enabling faster desolvation kinetics. The DMM-based electrolyte consequently yielded uniform Li deposition morphology and high plating/stripping efficiency across a broad temperature range ( $25^\circ\text{C}$  to  $-40^\circ\text{C}$ ) (Figure 31a). In addition, the  $\text{Li} \parallel \text{SPAN}$  battery demonstrated excellent low-temperature performance ( $-40^\circ\text{C}$ ), with a capacity retention of 63.8% after 120 cycles at  $0.1 \text{ C}$ . Subsequent studies have expanded the library of weakly solvating solvents for dilute ether-based electrolytes, including dipropyl ether (DPE) [211,302], dibutyl ether (DBE) [303,304], butyl methyl ether (BME) [305], n-hexane [306], 1,4-dioxane [307], dimethoxymethane (DMM) [307], and  $\text{Me}_2\text{O}$  [308].

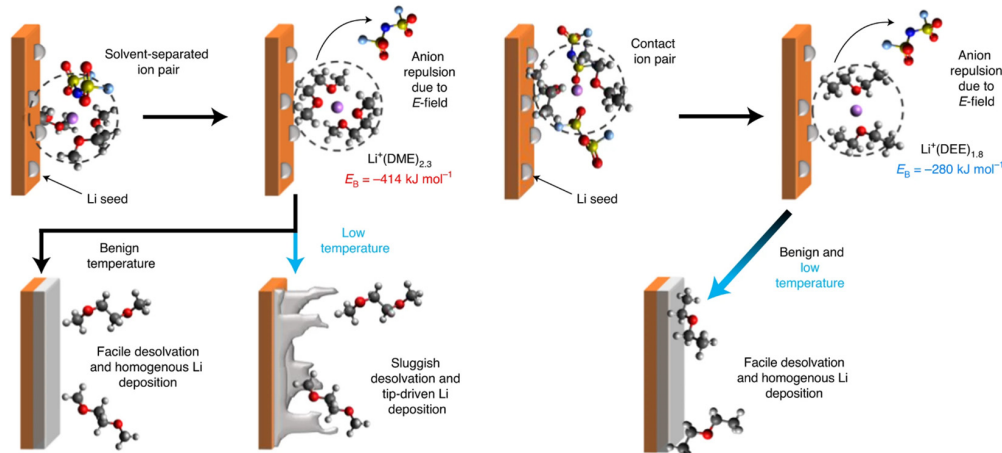


**Figure 30.** Proposed desolvation mechanism and  $\text{Li}^+$ /solvent binding energies obtained from quantum simulations in 1 M LiFSI DOL/DME (left) and 1 M LiFSI DEE (right). Reproduced with permission [300]. Copyright © 2021, Springer Nature.

A nontoxic and nonflammable ether electrolyte, dipropylene glycol dimethyl ether (DPGDME) for  $\text{Li} \parallel \text{SPAN}$  batteries was developed by Chen et al. in 2022 [309] (Figure 31b). DPGDME undergoes in situ electrochemical polymerization during cycling, forming a polyether-rich layer on the cathode which effectively mitigates interfacial side reactions and decreases the polarization. As a result, the  $\text{Li} \parallel \text{SPAN}$  battery delivered a remarkable capacity retention of 99.5% over 400 cycles at  $4 \text{ C}$ . A high-loading SPAN cathode ( $6.61 \text{ mAh cm}^{-2}$ ) achieved stable cycling over 50 cycles.

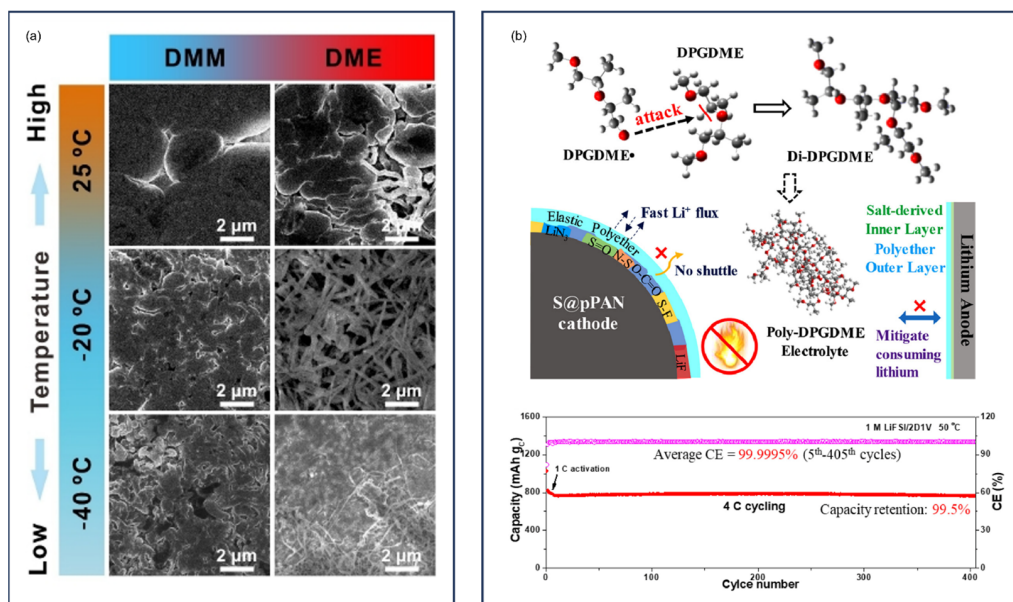


**Figure 31.** (a) Li deposition morphology under  $0.5 \text{ mA cm}^{-2}$  for  $0.5 \text{ h}$  in different electrolytes and temperatures. Reproduced with permission [301]. Copyright © 2022, John Wiley and Sons; (b) **top:** Schematic illustration of the polymerization of DPGDME and the superiority of Poly–DPGDME; **bottom:** Cycling performance of  $\text{Li} \parallel \text{SPAN}$  cells in the proposed electrolytes under  $50 \text{ }^\circ\text{C}$  at  $4 \text{ C}$ . Reproduced with permission [309]. Copyright © 2022, Elsevier.

Dilute ether-based electrolytes have been successfully extended to  $\text{Na} \parallel \text{SPAN}$  and  $\text{K} \parallel \text{SPAN}$  battery systems. In 2020, Zhou et al. developed an electrolyte engineering strategy to optimize the  $\text{Na}^+$  solvation structure for fast-charging Na-ion and Na-S batteries [310]. By adopting a compatible electrolyte ( $1 \text{ M NaPF}_6$  in DME), the sodium anode and copper current collector corrosion induced by anions was suppressed, achieving a  $\text{Na} \parallel \text{SPAN}$  battery with high Coulombic efficiency (CE) (>99%) and good capacity retention of 65.2% after 50 cycles at  $0.2 \text{ C}$ .

A tetraethylene glycol dimethyl ether (TEGDME)-based electrolyte with FEC as an additive for  $\text{Na} \parallel \text{SPAN}$  batteries was reported by Liu et al. [311]. The room temperature  $\text{Na} \parallel \text{SPAN}$  battery delivered a reversible capacity of  $587 \text{ mAh g}^{-1}$  after 200 cycles at  $0.2 \text{ A g}^{-1}$ , corresponding to a capacity decay rate of 0.23% per cycle. To suppress the Na dendrite growth,  $\text{BiI}_3$  was introduced as an additive in the glycol dimethyl ether-based electrolyte of  $\text{Na} \parallel \text{SPAN}$  battery [312].  $\text{BiI}_3$  could facilitate the formation of a thin and compact layer of Na-Bi alloy on the Na metal surface which protects Na from parasitic reactions. Theoretical and experimental results revealed that  $\text{BiI}_3$  results in a decrease in binding energy through the modulation of the solvation shell, while the in situ formed Na-Bi layer facilitates rapid and uniform Na plating, leading to a dendrite-free morphology. A mixed electrolyte strategy for  $\text{Na} \parallel \text{SPAN}$  batteries was proposed by Basel et al., where PC, DOL, DME, and diglyme (DIG) are mixed in different ratios to promote the formation of bilateral SEI [313]. The  $\text{Na} \parallel \text{SPAN}$  battery with  $0.8 \text{ M NaTFSI}$  in PC/DIG (1/1, v/v) exhibited a capacity retention of 74.6% after 100 cycles at  $0.1 \text{ C}$ .

Li et al. proposed a “salt-in-presalt” strategy to promote the formation of inorganic NaF-rich interphases on both the SPAN and Na electrodes [314]. Specifically, the electrolyte was prepared by dissolving NaFSI in a liquid precursor, N,N-dimethyltrifluoromethane-sulfonamide (PreTFSI), demonstrating high electrochemical stability up to  $6.7 \text{ V}$  versus  $\text{Na}^+/\text{Na}$  and enabling the formation of stable interphases on both electrodes. As a result, the  $\text{Na} \parallel \text{SPAN}$  battery with a cathode areal capacity of  $3.3 \text{ mAh cm}^{-2}$ , limited Na (N/P = 1.7) delivered a discharge capacity of  $577 \text{ mAh g}^{-1}$  after 1000 cycles at  $0.2 \text{ A g}^{-1}$ , corresponding

to a capacity retention of 93% ( $617 \text{ mAh g}^{-1}$  at the 5th cycle). In addition, a  $100 \text{ mAh Na} \parallel \text{SPAN}$  pouch cell was fabricated and delivered a capacity retention of 80% (compared to the second cycle) after 100 cycles at  $0.2 \text{ A g}^{-1}$ .

A “dual-salt” strategy was reported by Paar et al. to regulate the solvation chemistry of  $\text{K}^+$  for  $\text{K} \parallel \text{SPAN}$  batteries [315]. They developed an advanced electrolyte comprising 1 M KFSI + 0.05 M KPF<sub>6</sub> in DME and achieved an enhanced interfacial stability of the K metal anode. The incorporation of 0.05 M KPF<sub>6</sub> reduced the number of solvent molecules surrounding the  $\text{K}^+$  and led to facile  $\text{K}^+$  de-solvation, enabling dense and uniform K deposition during the plating process and the formation of a stable KF-rich SEI layer (Figure 32). The resulting  $\text{K} \parallel \text{SPAN}$  battery delivered an initial capacity of  $800 \text{ mAh g}^{-1}$  and retained 90% capacity after 300 cycles at  $4 \text{ mA cm}^{-2}$ .

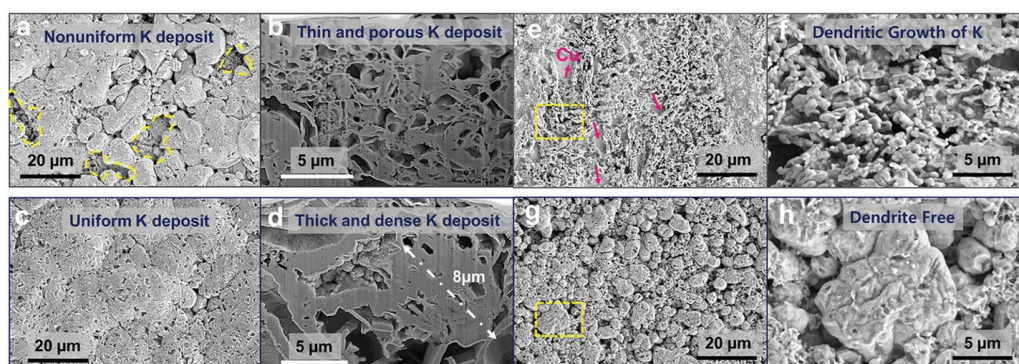


**Figure 32.** Top view and cross-sectional SEM images of K metal anode at a current density of (a–d)  $1 \text{ mA cm}^{-2}$  and (e–h)  $4 \text{ mA cm}^{-2}$ . (a,b,e,f) baseline electrolyte and (c,d,g,h) 0.05 M KPF<sub>6</sub>-containing electrolyte. Reproduced with permission [315]. Copyright © 2023, John Wiley and Sons.

Mg-S batteries face significant challenges due to the rapid formation of passivating layers (comprising oxides, carbonates, and hydroxides) upon exposure to electrolytes and trace oxygen, which severely limits their practical applications [316]. In 2020, Wang et al. reported a Mg || SPAN battery with a halogen-free electrolyte containing Mg(BH<sub>4</sub>)<sub>2</sub> and LiBH<sub>4</sub> in diglyme [317]. The tailored electrolyte featured a low overpotential of 0.04 V and effectively removed the blocking layers on the magnesium metal surface. As a result, the Mg || SPAN battery delivered a reversible capacity of  $1400 \text{ mAh g}^{-1}$  sulfur and maintained stable cycling over 300 cycles at 0.1 C. In the same year, Wang et al. reported another Mg || SPAN battery system with magnesium tetrakis(hexafluoroisopropoxy) borate (Mg[B(hfip)<sub>4</sub>]<sub>2</sub>) as the conductive salt in ether electrolytes and achieved excellent performance [318].

### 9.3. High-Concentration Electrolytes and Localized High-Concentration Electrolytes

As previously discussed, conventional dilute ether-based electrolytes in Li || SPAN batteries suffer from polysulfide dissolution issues. High-concentration electrolytes (HCEs), characterized by elevated salt concentrations, have emerged as an effective solution to mitigate this problem through the common ion effect [319]. In these systems, the high salt concentration essentially transforms the electrolyte into a salt-dominated medium. In 2014, Zhang et al. firstly evaluated the electrochemical performance of the SPAN in DOL/DME or DOL/TEGDME with different concentrations of LiTFSI [320]. Their study revealed that the electrolyte with high concentration of LiTFSI and high viscosity effectively suppressed polysulfides dissolution, therefore improving the electrochemical performance of Li || SPAN batteries (Figure 33a). Inspired by this work, researchers started to explore more HCE systems for high-performance SPAN-based batteries.

In 2018, Zhou et al. developed an innovative ether-based electrolyte composed of 4 M LiFSI in DBE for  $\text{Li} \parallel \text{SPAN}$  batteries [321]. DBE with relatively low dielectric constant (3.06 at 25 °C) effectively suppressed the dissolution of polysulfides and minimized parasitic side reactions at the lithium metal anode. As a result, the  $\text{Li} \parallel \text{SPAN}$  battery exhibited good cycling performance with 80.9% capacity retention after 150 cycles at 1.67 A g<sup>-1</sup>. Furthermore, Xing et al. employed 4 M LiTFSI + 0.5 M LiNO<sub>3</sub> in DOL/DME as the electrolyte for long-cycling  $\text{Li} \parallel \text{SPAN}$  batteries [322].

High-concentration electrolytes can be prepared via a “salt-in” mechanism. Ren et al. demonstrated this approach by incorporating bismuth triflate ( $\text{Bi}(\text{OTf})_3$ ) and 1,3,2-dioxathiolane 2,2-dioxide (DTD) into a 2 M NaOTf in DME electrolyte [323].  $\text{Bi}(\text{OTf})_3$  facilitated the dissolution of NaOTf via a “salt-in” mechanism, which increased the salt concentration and effectively suppressed the decomposition of solvents and additives (Figure 33b). This process also promoted the formation of an anion-derived inorganic SEI. Concurrently, DTD reacted with sodium sulfide to form a thiosulfate-based robust CEI on the SPAN cathode. The resulting  $\text{Na} \parallel \text{SPAN}$  battery delivered an initial capacity of 535 mAh g<sup>-1</sup> and retained 79% of its capacity after 150 cycles at 0.5 C.

Zhang et al. presented a model for understanding the electrolyte decomposition behavior in K-ion batteries by analyzing the reaction pathway for K<sup>+</sup>-solvent pairs on the potassium metal anode and proposed guidelines to design compatible electrolytes [324]. The computational and experimental results revealed that the electrolyte decomposition could be suppressed by tuning the electronegativity through varying solvent chemistry, anion type, and salt concentrations. Following the guidelines, a  $\text{K} \parallel \text{SPAN}$  battery with highly concentrated 5 M KFSI in DME was assembled and displayed high average capacity up to 333.72 mAh g<sup>-1</sup> in the first 300 cycles at 200 mA g<sup>-1</sup>. In 2022, Lee et al. reported a high-performance  $\text{K} \parallel \text{SPAN}$  battery enabled by a HCE composed of 4.34 mol kg<sup>-1</sup> KFSI in DME [325]. With a high concentration of KFSI in DME, the contact ion pairs (CIPs) and aggregates (AGGs) dominated the solvation structure of the HCE by reducing the solvent-separated ion pairs (SSIPs) and free solvent molecules. These features facilitated the formation of a robust KF-rich SEI on the K metal anode and suppressed the K dendrite growth (Figure 33c). As a result, the  $\text{K} \parallel \text{SPAN}$  battery with the HCE delivered an areal capacity of 2.5 mAh cm<sup>-2</sup> and high CE over 700 cycles at 0.5 C.

HCEs suffer from several drawbacks, including high cost, increased viscosity, and reduced ionic conductivity, leading to severe cost and transport limitations [326]. To address these issues, the introduction of an inert diluent with low viscosity and weak coordination ability has been proposed. This approach converts HCEs into localized high-concentration electrolytes (LHCEs), effectively retaining the benefits of HCEs while mitigating their limitations. In 2019, Chen et al. first developed a LHCE system composed of 1.6 M LiFSI in TMP/HFE (1/3) for  $\text{Li} \parallel \text{SPAN}$  batteries [327] (Figure 33d). The LHCE formed localized high-concentration LiFSI/TMP pairs and enabled dendrite-free cycling over 500 cycles. The  $\text{Li} \parallel \text{SPAN}$  battery with this electrolyte delivered an areal capacity of up to 3.41 mAh cm<sup>-2</sup> after 70 cycles at 0.1 C, demonstrating its practical viability.

Yu et al. investigated the effects of sulfur content in SPAN on the performance of  $\text{Li} \parallel \text{SPAN}$  batteries using LHCEs, ether, and carbonate-based electrolytes as platforms [328]. They found that SPAN with 43 wt% of sulfur content exhibited the highest capacity and best compatibility with an LHCE comprising LiFSI in TTE/DME. This LHCE system effectively suppressed polysulfide dissolution and showed superior compatibility with Li metal anode compared to conventional ether and carbonated-based electrolytes.

Following Chen et al.’s pioneering work, numerous LHCE systems have been explored. In 2021, Jiang et al. reported the use of fluorobenzene (FB), an economical hydrocarbon with low density and low viscosity, as a bifunctional diluent to formulate an LHCE composed of

LiFSI in DME/FB for Li<sup>+</sup> | SPAN batteries [204]. FB not only suppresses the decomposition of DME on the lithium metal by strengthening the interactions of DME and FSI<sup>-</sup> around Li<sup>+</sup> but also facilitates the formation of a stable LiF-rich SEI (Figure 34). As a result, the Li<sup>+</sup> | Se<sub>0.05</sub>S<sub>0.95</sub>PAN battery with high-areal-capacity (7.6 mAh cm<sup>-2</sup>) delivered a capacity retention of 82% over 150 cycles at 3 mA cm<sup>-2</sup>. In a later study by Han et al., they adopted a similar FB-based LHCE design for Li<sup>+</sup> | SPAN batteries [329]. Subsequently, other diluents including BTFE [330], TTE [205,223,331–334], monofluorobenzene [335], DIPE [210], 1,1,2,2-tetrafluoroethyl 2,2,3,3-tetrafluoropropyl ether [336,337], 1,2-diethoxyethane [338], anisole [339], 1,1,2,2-tetrafluoroethyl ether [340], DBE [341], and benzotrifluoride [342] have been explored.

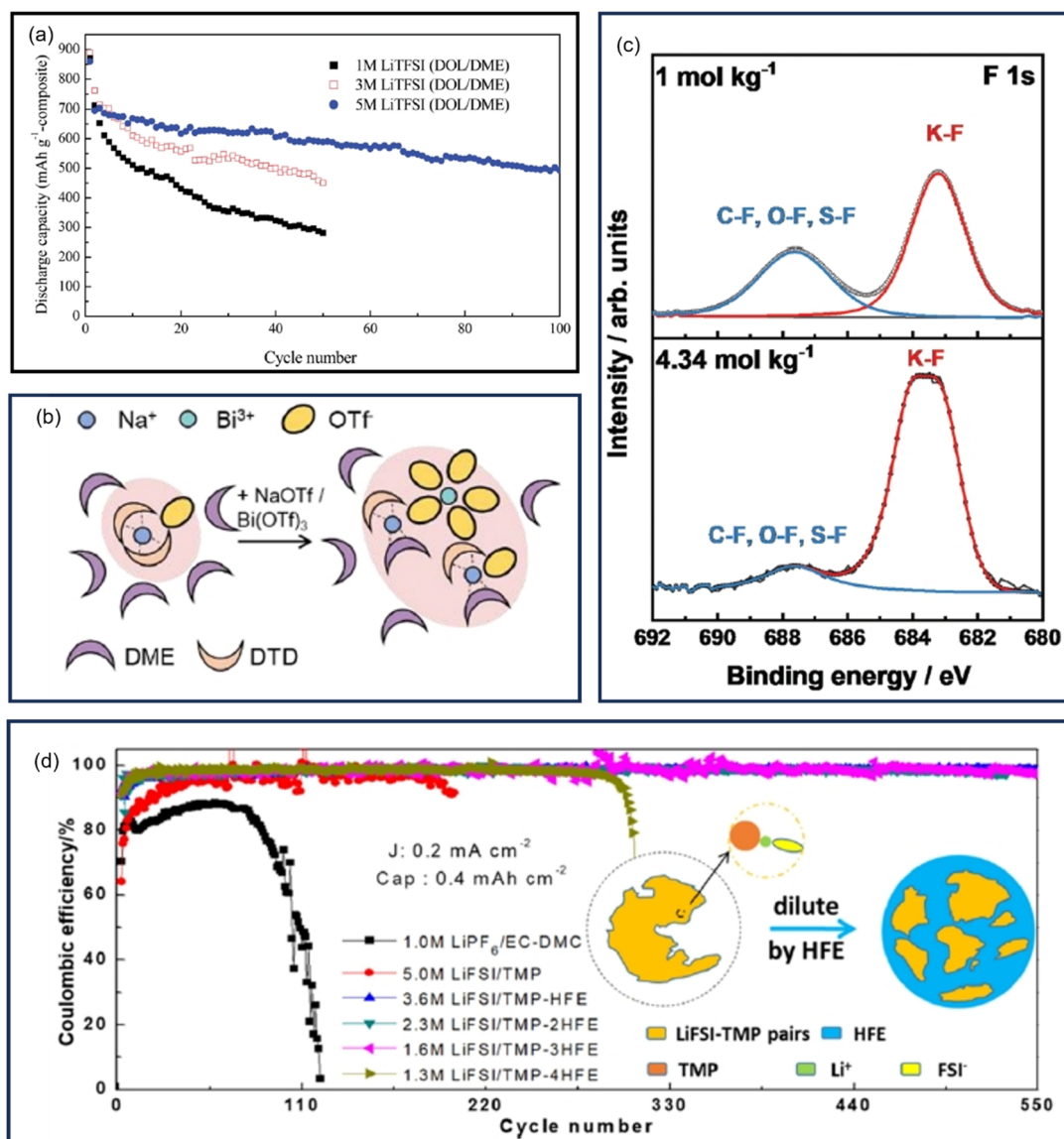


**Figure 33.** (a) Cycling performance of the SPAN cathode in 1 M, 3 M, and 5 M LiTFSI in DOL/DME. Reproduced with permission [320]. Copyright © 2014, Royal Society of Chemistry; (b) Schematic illustration of the change in solvation structure induced by Bi<sup>3+</sup> cation. Reproduced with permission [323]. Copyright © 2023, American Chemical Society; (c) XPS spectra of F 1 s; Comparison of chemical compositions of the SEI layer on the K metal surface between standard electrolyte (**top**) and HCE (**bottom**). Reproduced with permission [325]. Copyright © 2022, John Wiley and Sons; (d) CE of Li deposition/stripping using Cu electrodes in different electrolytes. Reproduced with permission [327]. Copyright © 2019, American Chemical Society.

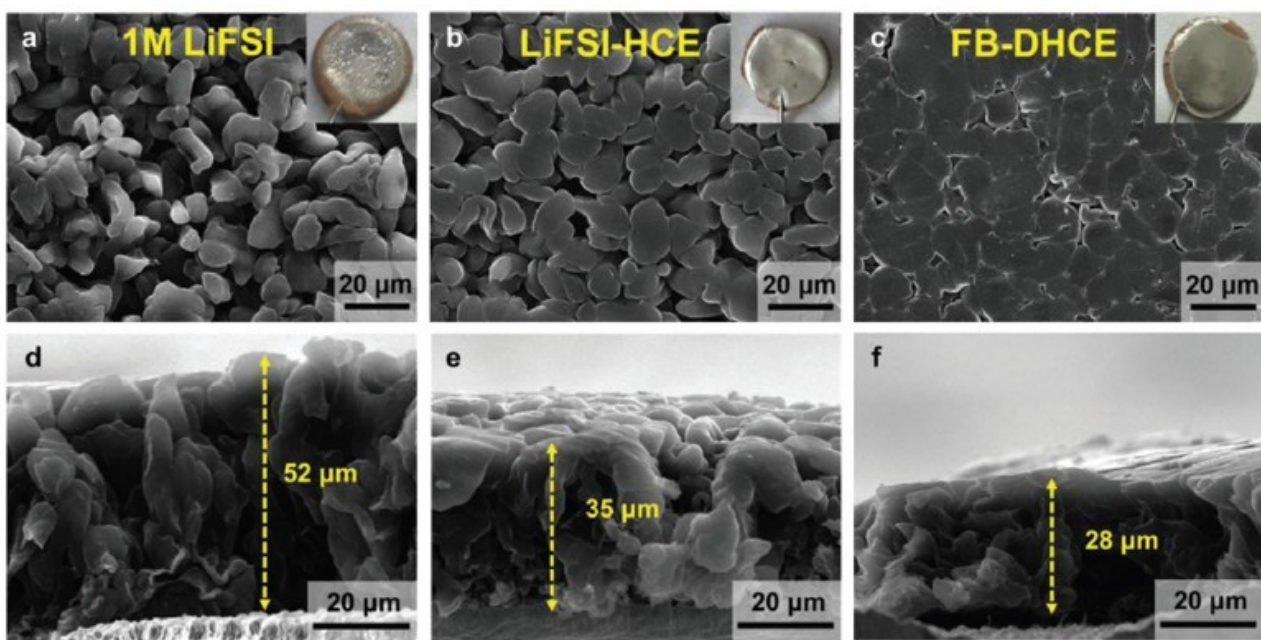


**Figure 34.** (a–c) Top view and (d–f) cross-sectional view SEM images of Li deposition morphology in different electrolytes. Reproduced with permission [204]. Copyright © 2020, John Wiley and Sons.

Wu et al. identified electrolyte transport properties—particularly ionic conductivity and Sand's capacity—as critical factors in preventing short-circuit failures of high-areal-capacity ( $>6 \text{ mAh cm}^{-2}$ )  $\text{Li} \parallel \text{SPAN}$  batteries paired with LHCEs [343]. Operating beyond the transport limit leads to macroscopically heterogeneous Li dendrite growth, triggering short circuits. Guided by this theory, they selected an LHCE (LDME) comprising LiFSI in DME and BTFE, which exhibited a high Sand's capacity, to fabricate  $\text{Li} \parallel \text{SPAN}$  pouch cells. The resulting 2 Ah  $\text{Li} \parallel \text{SPAN}$  pouch cell with a high cathode areal capacity of  $8 \text{ mAh cm}^{-2}$  and lean electrolyte ( $3 \text{ g Ah}^{-1}$ ) achieved over  $260 \text{ Wh kg}^{-1}$  with minimal capacity degradation over 70 cycles at  $0.2 \text{ A}$ .

Several studies have investigated the role of additives in optimizing LHCEs. In 2022, He et al. reported a stable  $\text{Li} \parallel \text{SPAN}$  battery using an LHCE (LiFSI in DME/EC/TTE) with trimethylsilyl azide (TMS-N<sub>3</sub>) as the additive [331]. TMS-N<sub>3</sub> promoted the in situ formation of robust and highly conductive LiF-Li<sub>3</sub>N-rich passivation layers on both the Li metal anode and SPAN cathode (Figure 35a). The passivation layers enhanced the Li<sup>+</sup> transport, improved Li stripping/plating reversibility, suppressed Li dendrite growth, and eliminated polysulfides shuttling. As a result, the  $\text{Li} \parallel \text{SPAN}$  battery delivered a reversible capacity of  $580 \text{ mAh g}^{-1}$  SPAN and stable cycling over 800 cycles at  $0.5 \text{ C}$  with a capacity retention of 99.3%.

In 2024, Qin et al. reported a novel coordinate-anion-enriched LHCE (LDEFE-IL) by incorporating the ionic liquid (Py<sub>13</sub>TFSI) as an additive for high-performance  $\text{Li} \parallel \text{SPAN}$  batteries [340]. The LDEFE-IL, formulated with 1.5 M LiFSI in DEE and 1,1,2,2-tetrafluoroethyl ether (ETFE) with Py<sub>13</sub>TFSI as the additive, exhibited an increased proportion of contact ion pairs (CIPs) by forming Li<sup>+</sup> and TFSI<sup>-</sup> interactions. Both FSI<sup>-</sup> and TFSI<sup>-</sup> interacted with Li<sup>+</sup>, forming a coordinated-anion-enriched solvation structure and facilitating the reduction in anions, yielding a LiF-rich SEI. Consequently, a  $\text{Li} \parallel \text{SPAN}$  pouch cell with a high areal loading of  $6 \text{ mg cm}^{-2}$ , a E/S ratio of  $5 \text{ mL g}^{-1}$  SPAN, and a thin Li foil ( $50 \mu\text{m}$ ) delivered an initial areal capacity of  $4 \text{ mAh cm}^{-2}$  and retained 79.2% of the capacity after 120 cycles at  $0.5 \text{ mA cm}^{-2}$ .

For Na<sup>+</sup> | SPAN batteries, Pai et al. introduced a novel LHCE utilizing cost-effective, low-density nonfluorinated diluent, toluene [344]. DFT calculations and the experimen-

tal results confirmed toluene's superior reduction stability compared to other aromatic solvents with different substitutions. Compared to the conventional TTE diluent, toluene exhibits enhanced compatibility with Na metal. In addition, toluene could modify the solvation structure by favoring anion-dominated species, contributing to the formation of a robust inorganic-rich SEI (Figure 35b). As a result, the Na || SPAN battery achieved a capacity retention of 85% after 200 cycles at 0.5 C. In 2025, the same group reported a novel mixed non-fluorinated ether electrolyte with low density exhibiting localized high-concentration behavior for Na || SPAN batteries [345]. The electrolyte consisted of 2 M NaFSI in 1,2-dimethoxypropane (DMP) and cyclopentyl methyl ether (CPME). CPME, a non-fluorinated weakly solvating cosolvent, tailors the solvation structure to an anion-rich solvation shell while suppressing the shuttle effect. Consequently, the Na || SPAN battery delivered a discharge capacity of  $490 \text{ mAh g}^{-1}$  sulfur after 800 cycles at 0.5 C, corresponding to a capacity decay rate of 0.06% per cycle.

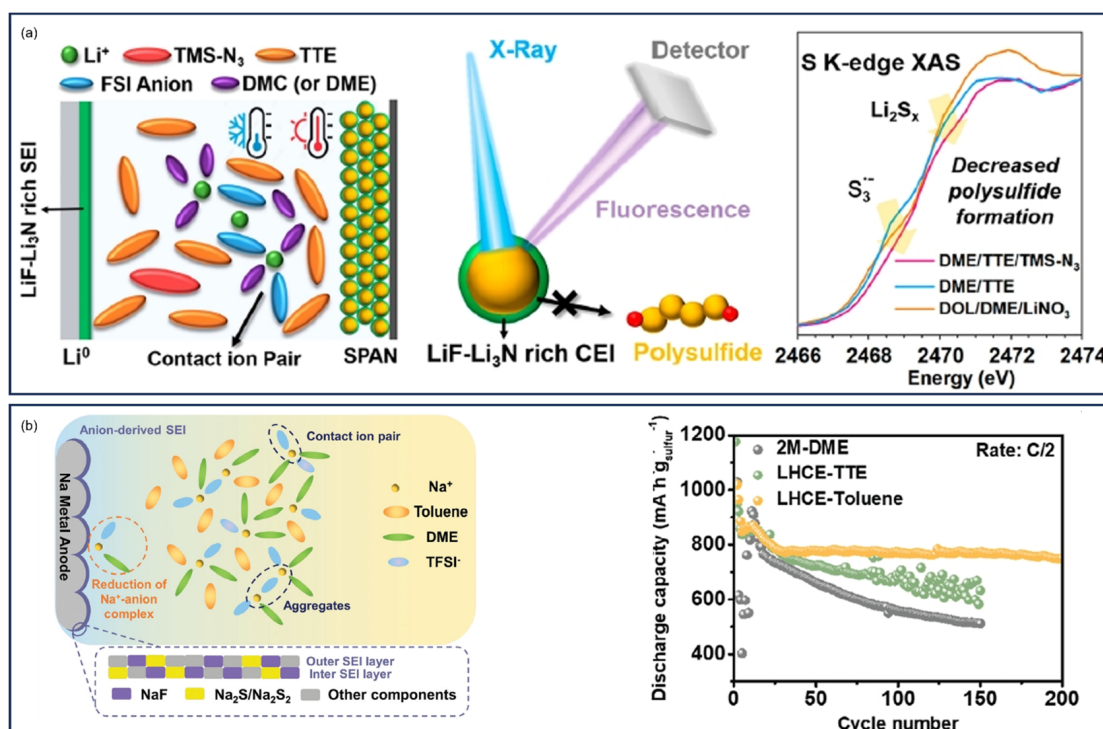


**Figure 35.** (a) Schematic illustration of the proposed “fluorinated LHCE + TMS-N<sub>3</sub> dual additives” strategy. Reproduced with permission [331]. Copyright © 2022, American Chemical Society; (b) left: Schematic illustration of the electrolyte solvation structure with toluene; right: Cycling performance of the Na || SPAN cells in different electrolytes. Reproduced with permission [344]. Copyright © 2024, John Wiley and Sons.

#### 9.4. Other Liquid Electrolytes

Other than conventional carbonate and ether-based electrolytes, several alternative liquid solvents have been explored for high-performance Li || SPAN batteries, offering unique solvation characteristics and improved interfacial stability.

Siloxanes, featuring low toxicity, weakly solvating power, and strong anti-reduction stability, have emerged as promising electrolyte solvents. In 2023, Lu et al. developed a novel carbonate-free, weakly solvating siloxane electrolyte consisting of 2 M LiFSI in (3,3,3-trifluoropropyl) methyldimethoxysilane (FPDMS) for Li || SPAN batteries [346] (Figure 36a). The weakly solvating nature of FPDMS facilitated the formation of a robust anion derived SEI on the Li metal anode, effectively suppressing dendrite growth. In addition, the

electrostatic shielding effect of silicon methyl and trifluoropropyl groups significantly inhibited polysulfide dissolution. As a result, the Li||SPAN battery delivered prolonged cycle life, with a capacity retention of 96.8% after 500 cycles at 0.5 C. A 0.2 Ah pouch cell with a high cathode areal capacity ( $6.5 \text{ mAh cm}^{-2}$ ), limited lithium (N/P = 2), and lean electrolyte (E/S = 5) demonstrated a capacity retention of 92.4% after 20 cycles at 0.1 C.

Li et al. later developed a low-density ( $0.99 \text{ g cm}^{-3}$ ) and weakly solvating siloxane-based electrolyte comprising 1.5 M LiFSI in dimethyldimethoxysilane (DMMS) for Li||SPAN batteries [347]. The weakly solvating power of DMMS solvents resulted in weak  $\text{Li}^+$ -solvent interactions, forming a highly ion-paired solvation structure which promotes the decomposition of  $\text{FSI}^-$  and the formation of a stable inorganic-rich SEI. In addition, DMMS suppressed polysulfides dissolution, enabling long-term cycling for the batteries. Consequently, the Li||SPAN battery delivered a capacity retention of 96.9% after 300 cycles at  $0.2 \text{ A g}^{-1}$ .

In 2024, Ma et al. designed an intrinsic flame-retardant siloxane ether-based electrolyte with 2.5 M LiFSI in tetrapropoxysilane (TPOS) for Li||SPAN batteries operating at high temperature ( $80^\circ\text{C}$ ) [348]. TPOS regulated the solvation structure and participated in the formation of a LiF-rich CEI. The resulting Li||SPAN battery delivered a reversible capacity of  $760 \text{ mAh g}^{-1}$  SPAN after 85 cycles at 1 C and  $80^\circ\text{C}$ , corresponding to a capacity retention of 98.4% (Figure 36b). Tian et al. further expanded the utility of siloxanes by employing a lightweight and eco-friendly diethoxydimethylsilane (DEMS) based electrolyte for Li||SPAN batteries [349]. The low-polar DEMS promoted the “solid–solid” conversion of SPAN during cycling and mitigated the shuttle effect. In addition, DEMS features low melting point ( $-87^\circ\text{C}$ ) and high boiling point ( $113^\circ\text{C}$ ), which enables highly reversible Li plating/stripping behavior over a wide temperature range spanning from  $-20$  to  $60^\circ\text{C}$ . Consequently, the Li||SPAN battery cycled at 0.2 C delivered discharge capacities of 524.4, 598.8,  $318.6 \text{ mAh g}^{-1}$  after 200, 100, and 50 cycles at  $26$ ,  $60$ , and  $-20^\circ\text{C}$ , respectively.

A weakly solvating electrolyte employing tetrahydropyran (THP) as the single solvent for high-performance Li||SPAN batteries was reported by Liao et al. in 2025 [350] (Figure 37a). By modulating the salt concentration in THP, the solvation structure could be effectively optimized to stabilize both the SPAN cathode by mitigating the polysulfide generation and the Li metal anode through the formation of an inorganic-rich SEI. THP’s wide liquid range ( $-45$  to  $88^\circ\text{C}$ ) enabled stable cycling of Li||SPAN batteries across a wide temperature range from  $0$  to  $50^\circ\text{C}$ . A Li||SPAN pouch cell with a high SPAN loading of  $5 \text{ mg cm}^{-2}$  and lean electrolyte ( $E/\text{SPAN} = 3 \mu\text{L mg}^{-1}$ ) exhibited a capacity retention of 79.1% after 40 cycles at 0.1 C.

Ren et al. developed an electrolyte with chlorine-free magnesium bis(diisopropyl)amide (MBA) as the salt and 1-butyl-1-methylpiperidinium bis(trifluoromethyl sulfonyl)imide (PP<sub>14</sub>TFSI) ionic liquid and THF as the solvents for Mg batteries [351]. The MBA-based electrolytes exhibited high ionic conductivity and anodic stability. A Mg||SePAN cell employing this electrolyte delivered an initial capacity of  $447.8 \text{ mAh g}^{-1}$  and a capacity decay rate of 0.66% per cycle for over 70 cycles at 0.2 C with the LiTFSI additive. Wang et al. reported a  $\text{Mg}^{2+}/\text{Li}^+$  hybrid electrolyte composed of  $(\text{CF}_3\text{SO}_3)_2\text{Mg}$ , lithium trifluoromethanesulfonate,  $\text{MgCl}_2$ , and  $\text{AlCl}_3$  in DME for room-temperature Mg||SPAN batteries in 2021 [352]. The addition of the lithium salt effectively reduced the resistance and the overpotential of the battery through the formation of  $\text{MgLiS}_x$  species while facilitating a stable SEI layer on the Mg anode. The resulting Mg||SPAN battery delivered a reversible capacity of  $1100 \text{ mAh g}^{-1}$  sulfur over 100 cycles at 1 C with almost no capacity decay. Zhang et al. also reported a hybrid electrolyte composed of PhMgCl,  $\text{AlCl}_3$ ,  $\text{LiCl}$ , and MBA in THF for Mg||SPAN batteries, which demonstrated stable cycling [353].

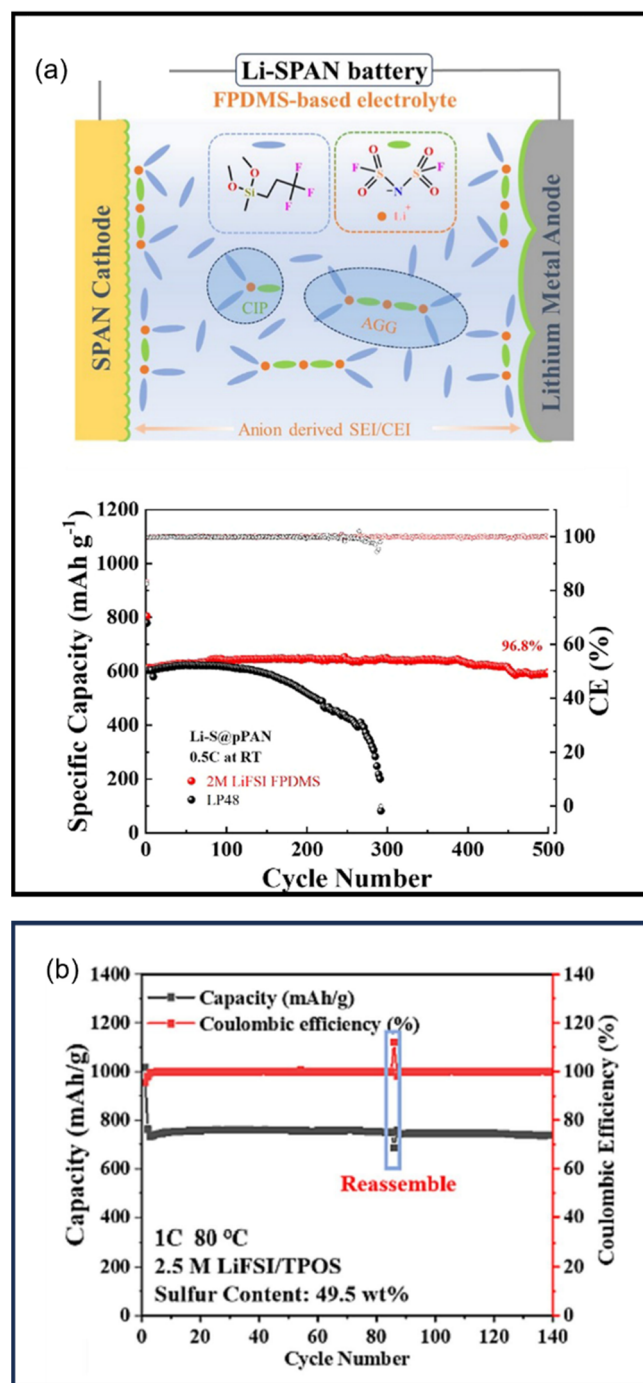


**Figure 36.** (a) **top:** Schematic illustration of the solvation structure of the 2 M LiFSI–PDMS electrolytes; **bottom:** Cycling performance of Li||SPAN batteries in different electrolytes. Reproduced with permission [346]. Copyright © 2023, Elsevier; (b) Cycling performance of Li||SPAN batteries in the 2.5 M LiFSI/TPOS electrolyte. Reproduced with permission [348]. Copyright © 2024, Elsevier.

In 2025, Li et al. developed highly reversible Zn||SPAN batteries using aqueous electrolytes containing tetraglyme (G4) and  $\text{I}_2$  additives [354]. The electron-donating  $-\text{COC}-$  groups in G4 reduced  $\text{I}_2$  to  $\text{I}_3^-/\text{I}^-$  redox couple for tandem catalysis during charge/discharge, thus enhancing the reaction kinetics. An organic-inorganic SEI containing organic fluoride and  $\text{I}_3^-$  was generated on the Zn metal anode, suppressing the dendrite growth. As a result, the Zn||SPAN aqueous battery delivered a high reversible capacity of  $465.8 \text{ mAh g}^{-1}$  and retained 81.8% of the capacity after 800 cycles at  $2 \text{ A g}^{-1}$  (Figure 37b).

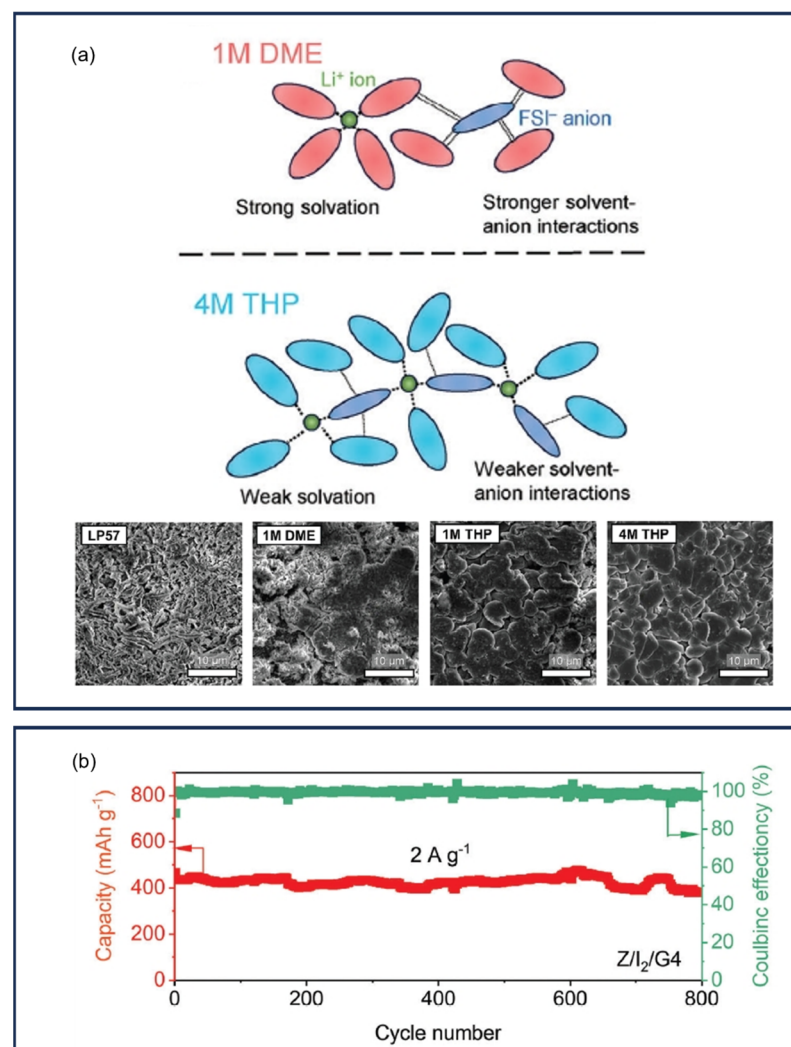


**Figure 37.** (a) **top:** Schematic illustration of the molecular interactions in the DME and THP electrolytes; **bottom:** SEM images of the Li metal after 20 cycles in different electrolytes in Li || SPAN cells. Reproduced with permission [350]. Copyright © 2024, John-Wiley and Sons; (b) Cycling performance of Zn || SPAN batteries in proposed aqueous electrolyte. Reproduced with permission [354]. Copyright © 2024, John-Wiley and Sons.

### 9.5. Gel Polymer Electrolytes

Gel polymer electrolytes (GPEs), consisting of polymer matrices and organic electrolytes, offer an attractive combination of high ionic conductivity and excellent electrode-electrolyte interface compatibility [6,355,356]. In this section, studies that feature the application of GPEs in SPAN-based rechargeable batteries are discussed.

The application of GPEs in SPAN-based rechargeable batteries can be traced back to the pioneering work on Li || SPAN batteries reported by Wang et al. during 2002–2004 [9–11], where PVDF-HFP combined with carbonate electrolytes was applied in Li || SPAN batteries. PVDF has emerged as a highly promising polymer matrix for GPEs in SPAN batteries due to its exceptional mechanical properties, chemical stability, and high ionic conductivity. Subsequent studies by Jeddi et al. further advanced this approach by developing GPEs based on PVDF-HFP blended with functionalized organic polymers or silica, which effectively suppressed polysulfide diffusion during cycling, thereby enhancing battery performance [357–359]. Other variations in composite GPEs based on the PVDF matrix have been developed by different research groups over the years, such as

4-aminophenylsulfonyl(trifluoromethylsulfonyl) imide (LiATFSI) grafted poly(ethylene-alt-maleic anhydride) (PEMA) (PEMA-graft-LiATFSI) polymer and PVDF-HFP composite electrolyte by Li et al. in 2018 [360] and PMMA-PVDF by Liu et al. in 2019 [361]. In 2021, Zhang et al. reported a GPE (KM10@PH-GPE) composed of PVDF-HFP and 250 nm filler KMgF<sub>3</sub> to address the lithium dendrite growth issue in LMBs [362] (Figure 38a). The incorporation of KMgF<sub>3</sub> not only improved the Li<sup>+</sup> transfer number to 0.63 but also promoted the formation of a SEI rich in LiF and flexible polycarbonates, significantly reducing the side reactions on lithium metal surface. As a result, the Li||SPAN battery employing this electrolyte delivered a reversible discharge capacity of 1313.8 mAh g<sup>-1</sup> sulfur after 250 cycles at 1 C, corresponding to a capacity retention of 79% against the second cycle.

A novel strategy involving the direct integration of the SPAN cathode with the PVDF-HFP-cellulose acetate (PCA) electrolyte was proposed by Huang et al. in 2023 [363]. The PCA was coated on the SPAN cathode to accommodate volume changes, suppress the Li<sub>2</sub>SO<sub>4</sub> accumulation, and reduce electrolyte leakage (Figure 38b). As a result, the Li||PCA@ASPA battery delivered a reversible capacity of 891.5 mAh g<sup>-1</sup> after 1000 cycles at 1 C, corresponding to a capacity retention of 62.1%.

Beyond PVDF-based GPEs, researchers have explored alternative polymer matrices to construct GPEs for Li||SPAN batteries. In 2018, Huang et al. developed a novel nano-SiO<sub>2</sub>-embedded poly(propylene carbonate)-based composite gel electrolyte (G-PPC-CPE) with 7.3 wt.% ether-based electrolyte as the plasticizer for Li||SPAN batteries [364]. The incorporation of nano-SiO<sub>2</sub> particles enhanced interfacial stability, improved ionic conductivity, and suppressed polysulfides diffusion. Consequently, the Li||SPAN battery with G-PPC-CPE delivered a high reversible capacity of 700.5 mAh g<sup>-1</sup> SPAN over 100 cycles and retained 85% of capacity after 500 cycles at 100 mA g<sup>-1</sup>. In 2022, Huang et al. introduced an eco-friendly and cellulose gel electrolyte (GE) prepared via UV photopolymerization and phase inversion method for Li||SPAN batteries [365]. Black phosphorous nanosheets (BP-Li) were fabricated and used as the Li<sup>+</sup> conductors in the GE (Figure 38c). The composite GPE exhibited high ionic conductivity up to  $5.21 \times 10^{-3}$  S cm<sup>-1</sup> and lithium transference number of 0.72. The resulting Li||SPAN battery delivered a discharge capacity of 938.8 mAh g<sup>-1</sup> after 500 cycles at 0.5 C, corresponding to a capacity retention of 72.8%.

Gao et al. reported an ionic liquid (IL) gel polymer electrolyte (IL-GPE) with a fibrous structure for Li||SPAN batteries [152]. The IL-GPE was prepared by soaking electro-spun fibrous PAN/PMMA composite film into the IL-based electrolyte containing N-Methyl-N-propylpiperidinium bis(trifluoromethanesulfonyl)imide, LiTFSI, LiNO<sub>3</sub>, DOL, and DME. The IL-GPE demonstrated high ionic conductivity of  $6.25 \times 10^{-4}$  S cm<sup>-1</sup> and promoted uniform Li<sup>+</sup> flux, enabling the Li||SPAN battery to maintain reversible capacity of 1080 mAh g<sup>-1</sup> after 200 cycles at 0.8 A g<sup>-1</sup> without capacity decay.

Zhang et al. developed a flame-retardant functionalized polyimide (PI) which could gelatinize the liquid carbonate electrolyte to form a flame-retardant GPE [366] (Figure 39a). The trifluoromethyl group in PI provided a negative electrical environment which facilitated Li<sup>+</sup> transport (Li transference number = 0.727) while the CH/π interaction between the alkyl group of the solvent and the aromatic benzene ring reduced the parasitic reactions between Li metal and the electrolyte. As a result, the Li||SPAN battery achieved a capacity retention of 92.8% against the second cycle after 200 cycles and retained 1153.4 mAh g<sup>-1</sup> after 450 cycles at 0.2 C. Hao et al. also reported using PI to gelatinize carbonate-based electrolyte to prepare a GPE for Li||SPAN batteries [367].

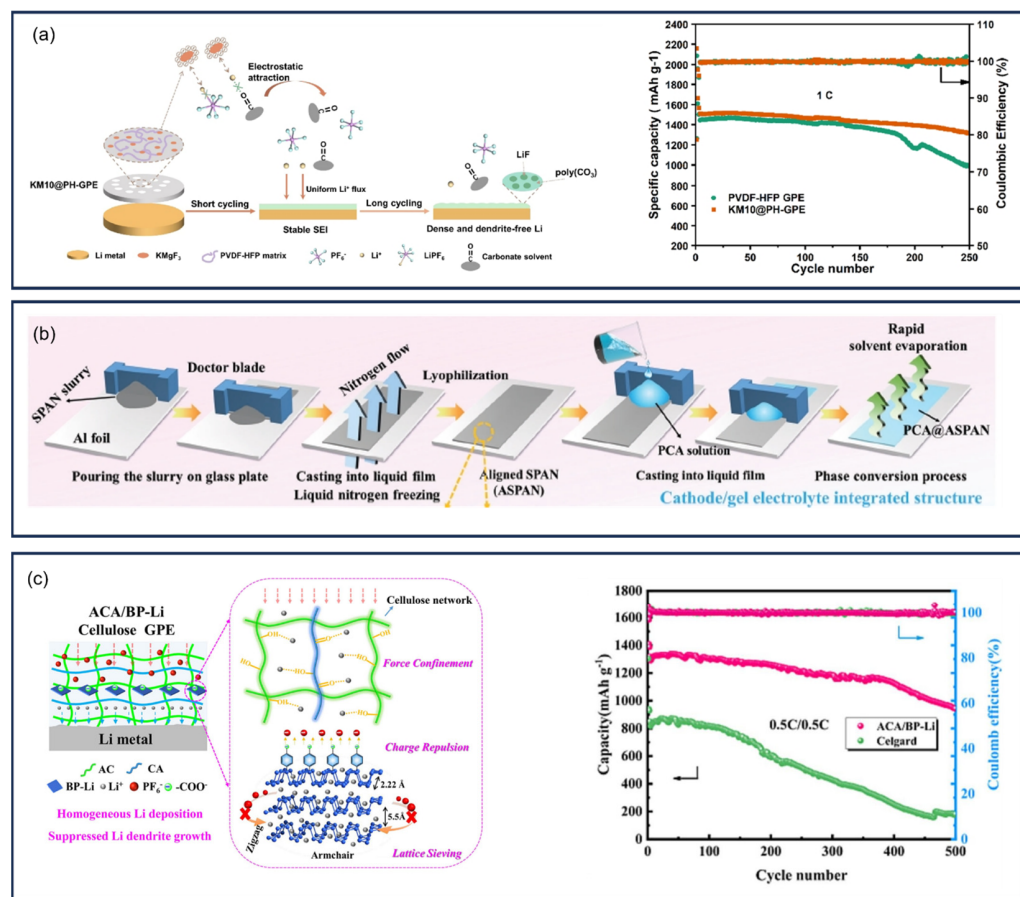


**Figure 38.** (a) Schematic illustration of Li deposition in PVDF-HFP and KM10@PH-GPE and the corresponding cycling performance of Li || SPAN cells. Reproduced with permission [362]. Copyright © 2021, American Chemical Society; (b) Schematic illustration of the fabrication process of PCA@AS PAN electrode. Reproduced with permission [363]. Copyright © 2023, John-Wiley and Sons; (c) left: Proposed mechanism of stabilizing Li metal anode by ACA/BP-Li GPE; right: Cycling performance of Li || SPAN cells with Celgard and ACA/BP-Li GPE at 50 °C. Reproduced with permission [365]. Copyright © 2023, John-Wiley and Sons.

In 2024, Zhang et al. reported a GPE prepared via *in situ* copolymerization of hexafluorobutyl acrylate (HFBA) and pentaerythritol tetraacrylate (PETEA) for high-performance Li || SPAN batteries [368] (Figure 39b). The as-prepared GPE possessed a cross-linked structure and abundant polar groups, exhibiting high ionic conductivity of  $1.61 \text{ mS cm}^{-1}$ . In addition, a C-O- and LiF-rich CEI on the SPAN cathode and favorable SEI on the Li metal anode could be constructed, allowing uniform distribution of Li<sup>+</sup> and reduced parasitic reactions. As a result, Li || PFGPE || SPAN batteries in both carbonate and ether-based electrolytes with the PFGPE achieved excellent electrochemical performances. The carbonate-based Li || PFGPE || SPAN battery delivered a discharge capacity of  $624.9 \text{ mAh g}^{-1}$  after 900 cycles at 1 C, corresponding to a capacity decay rate of 0.0003% per cycle. The ether-based Li || PFGPE || SPAN battery delivered a discharge capacity of  $725.1 \text{ mAh g}^{-1}$  after 600 cycles at 0.2 C, corresponding to a capacity retention of 58.5%. Guo et al. reported an *in situ* polymerized gel electrolyte based on VC, LiTFSI, and LiDFOB for high-performance Li || SPAN batteries [369]. The *in situ* formed GPE could regulate the plating/stripping of Li<sup>+</sup> on the electrode and exhibited a high Li transference number of 0.73. Consequently, a Li || SPAN battery with a high cathode loading of  $14.1 \text{ mg cm}^{-2}$  and a E/S ratio of  $5.0 \mu\text{L mg}^{-1}$  delivered a high reversible capacity of  $556.5 \text{ mAh g}^{-1}$  and retained 76.3% of the capacity after 90 cycles at 0.1 C. A Li || SPAN

pouch cell with a cathode loading of  $3.2 \text{ mg cm}^{-2}$  exhibited a capacity retention of 87.3% after 40 cycles at 0.1 C.

In 2024, Zhang et al. designed a GPE based on poly(ethylene glycol) diacrylate (PEGDA) for Li || SPAN batteries [370] (Figure 39c). The PEGDA-based GPE exhibited a high ionic conductivity of up to  $6.87 \times 10^{-3} \text{ S cm}^{-1}$  at 30 °C, suppressed the dissolution of polysulfides and facilitated the formation of flexible and stable passivation layers among the separator, SPAN cathode, and lithium anode. The resulting Li || SPAN battery delivered a discharge capacity of  $1217.3 \text{ mAh g}^{-1}$  sulfur after 250 cycles at 0.2 C, corresponding to a capacity retention of 89.9%.

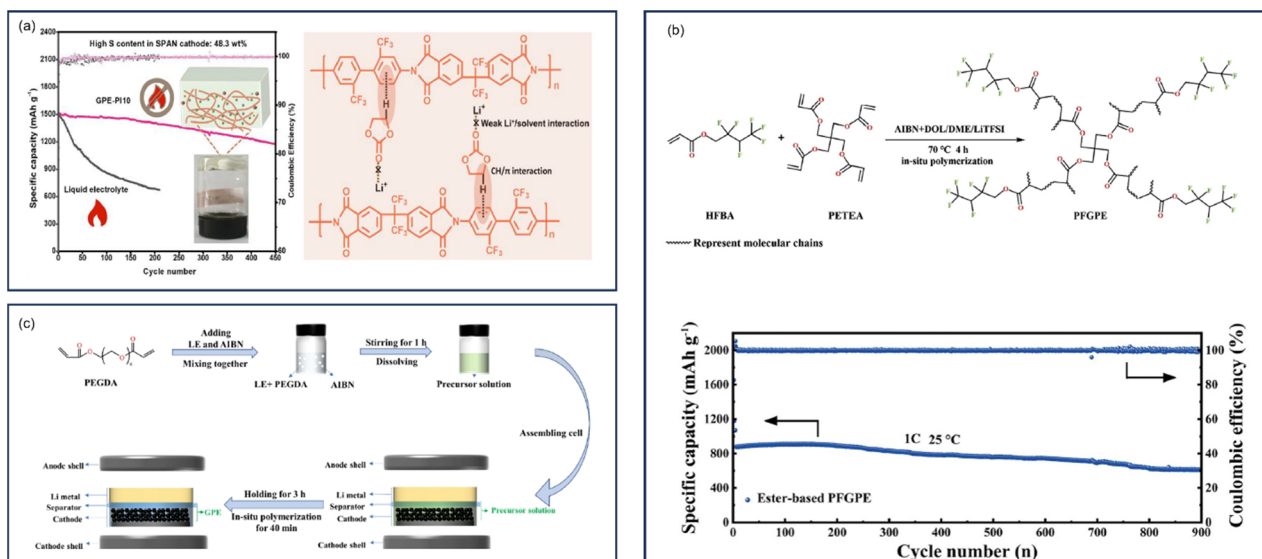


**Figure 39.** (a) Schematic illustration of the formation mechanism for GPE and the cycling performance of the corresponding GPE. Orange: GPE; yellow: Li ion; green: solvent; brown: anion. Reproduced with permission [366]. Copyright © 2023, Elsevier; (b) top: Schematic illustration of the synthesis of PFGPE; bottom: Cycling performance of the Li | PFGPE | SPAN battery. Reproduced with permission [368]. Copyright © 2024, Royal Society of Chemistry; (c) Schematic illustration of the fabrication process of the Li | GPE | SPAN cell. Reproduced with permission [370]. Copyright © 2024, American Chemical Society.

For sodium-based batteries, Murugan et al. developed a high-performance GPE for room temperature Na || SPAN batteries in 2022 [371]. The GPE was prepared by the in situ free radical polymerization of pentaerythritol triacrylate (PETE) in the presence of sodium tetraphenylborate (NaTPB), PC, and FEC on both the Na anode and the SPAN cathode. The as-prepared GPE exhibited high ionic conductivity, excellent electrode-electrolyte interfacial contact, and effective confinement of discharge products. Consequently, the room temperature Na || SPAN battery demonstrated stable cycling with a discharge capacity of over  $600 \text{ mAh g}^{-1}$  sulfur over 2500 cycles at 2 C. Further advancements were made by She et al., who introduced a zeolitic imidazole framework-8 (ZIF-8) enhanced PVDF/PEO blending polymer gel electrolyte (PPZ-GPE) for long-cycling Na || SPAN batteries [372]. The PPZ-GPE facilitated rapid Na<sup>+</sup> transport, exhibited excellent mechanical property, and promoted uniform Na plating. These attributes enabled the Na | PPZ-GPE | SPAN battery to achieve a discharge capacity of  $1150 \text{ mAh g}^{-1}$  after 465 cycles, corresponding to a capacity retention of 97%.

A halogen-free dual-salts GPE prepared via the in situ reaction between lithium/magnesium borohydrides and poly(tetrahydrofuran) for Mg || SPAN batteries was reported by Wang et al. [373]. The GPE demonstrated high ionic conductivities across a broad temperature range, superior polarization behavior, and good compatibility with

sulfur-based cathodes. As a result, the  $\text{Mg} \parallel \text{SPAN}$  battery delivered  $580 \text{ mAh g}^{-1}_{\text{sulfur}}$  after 140 cycles at 0.2 C and room temperature, while retaining about  $300 \text{ mAh g}^{-1}_{\text{sulfur}}$  at 0.2 C and 0 °C.

### 9.6. Solid-State Electrolytes

Currently, commercial batteries predominantly employ liquid electrolytes consisting of lithium salts dissolved in carbonate-based solvents. However, these systems present several safety and performance challenges [374]: (1) the leakage of the liquid electrolyte raises health and environmental concerns; (2) their low boiling points and ignition points create flammability risks; and (3) parasitic reactions between the liquid electrolytes and electrodes significantly degrade battery cycle life. Solid-state batteries, which replace liquid electrolytes with solid-state electrolytes (SSEs), have emerged as a potential technology to mitigate these issues, garnering considerable interests. This section reviews SSE studies for SPAN-based batteries, categorized by SSE type.

#### 9.6.1. Solid-State Polymer Electrolytes

Solid-state polymer electrolytes (SPEs) refer to electrolytes comprising solid polymer matrices and dispersed lithium salts. The first instance of solid-state  $\text{Li} \parallel \text{SPAN}$  batteries was reported by Yu et al. in 2004 [375], utilizing an SPE composed of PEO, LiTFSI, and a ceramic nano-TiO<sub>2</sub> filler. The solid-state  $\text{Li} \parallel \text{SPAN}$  battery exhibited an initial discharge capacity of  $850 \text{ mAh g}^{-1}_{\text{SPAN}}$  and remains  $380 \text{ mAh g}^{-1}_{\text{SPAN}}$  over 40 cycles. In 2019, Zhu et al. designed a solid-state  $\text{Na} \parallel \text{SPAN}$  battery using electrolyte comprising PEO, NaFSI, and nano-TiO<sub>2</sub> fillers and tested its electrochemical performance at 60 °C [376] (Figure 40a). The solid-state  $\text{Na} \parallel \text{SPAN}$  battery delivered a second discharge capacity of  $252 \text{ mAh g}^{-1}_{\text{SPAN}}$  and retained  $251 \text{ mAh g}^{-1}_{\text{SPAN}}$  after 100 cycles at 0.1 A g<sup>-1</sup>. In Fan et al.'s study, a polyethylene (PE) separator was used as the filler in solid-state PEO electrolyte to protect the electrolyte layer by physically blocking the Li dendrites [377].

As discussed earlier, PVDF-HFP has been widely utilized as a polymer matrix for GPEs. Advancing this approach, Li et al. proposed a “polymer-in-salt” strategy, converting PVDF-HFP-in-LiFSI into a solid-state polymer electrolyte by increasing the content of LiFSI to be equal to or greater than 50 wt% of the electrolyte [378]. This formulation enabled fast redox kinetics and small volume change during cycling. As a result, the solid-state  $\text{Li} \parallel \text{SPAN}$  battery delivered a discharge capacity of  $897.4 \text{ mAh g}^{-1}_{\text{sulfur}}$  after 100 cycles at 0.2 C. A solid-state  $\text{Li} \parallel \text{SPAN}$  pouch cell was built and cycled at 0.1 C for 20 cycles with a capacity retention of 91.3%. Further refining this concept, another “polymer-in-salt” solid-state electrolyte was developed by You et al. in 2025 [379]. They prepared elastomeric polymer-in-salt electrolytes (PISEs) by crosslinking poly(ethylene oxide-co-ethylene carbonate) (PEOEC) in LiTFSI in THF solution. The PISE had a LiTFSI content of ~76 wt% and effectively suppressed the dissolution of LiPSs due to the intrinsic saturation of the coordination sites. In addition, LiF-rich electrolyte/electrode interphases could be formed. Consequently, the solid-state  $\text{Li} \parallel \text{PISE} \parallel \text{SPAN}$  battery delivered a 3rd cycle discharge capacity of  $1333.6 \text{ mAh g}^{-1}_{\text{sulfur}}$  and retained  $1258.7 \text{ mAh g}^{-1}_{\text{sulfur}}$  after 100 cycles at 0.1 C, corresponding to a capacity retention of 94.4% (Figure 40b).

Recent advances have focused on facile, sustainable, and cost-effective strategies for developing high-performance SPEs. In 2024, Li et al. engineered an ultrathin yet mechanical robust aramid nanofibers films (ANFs) via a protic solvent penetration strategy and used ANFs to produce a SPE with a thickness of 3.4 μm and a tensile strength of 556.6 MPa for solid-state  $\text{Li} \parallel \text{SPAN}$  batteries [380]. The SPE enabled solid-state  $\text{Li} \parallel \text{SPAN}$  batteries with high cathode loading ( $4 \text{ mg}_{\text{SPAN}} \text{ cm}^{-2}$ ) to cycle stably over 80 cycles at 0.2 C. Nie et al. repurposed *Antheraea pernyi* fibers recycled from waste silk textiles as the

raw materials to construct a porous and strong supporting skeleton for ultrathin SPE [381] (Figure 40c). The incorporation of this skeleton established a 3D continuous pathway for Li<sup>+</sup> conduction and hindered the migration of anions, effectively promoting a uniform Li<sup>+</sup> flux and local current density distribution. The resulting solid-state Li||SPAN battery delivered a capacity retention of 92.3% after 500 cycles at 1 C. Another low-cost and facile approach for creating an SPE was reported by Sapkota et al. in 2025 [382] (Figure 41a). They introduced a Li-rich cellulosic solid-state electrolyte (Paper-Cu-Li SSE) for high-performance solid-state Li||SPAN batteries. The Paper-Cu-Li SSE was prepared by soaking commercial cellulosic paper into Cu<sup>2+</sup> solution followed by soaking in LiTFSI in EC/DME/DOL solution. This process expanded the spacing between cellulosic polymer chains and created channels to facilitate Li<sup>+</sup> transport. As a result, the Paper-Cu-Li SSE exhibited high conductivity ( $24.4 \text{ mS cm}^{-2}$ ) and Li transference number (0.76) at 50 °C. Consequently, the solid-state Li||SPAN battery delivered a capacity retention of 82.2% after 150 cycles at 0.5 C and 50 °C.

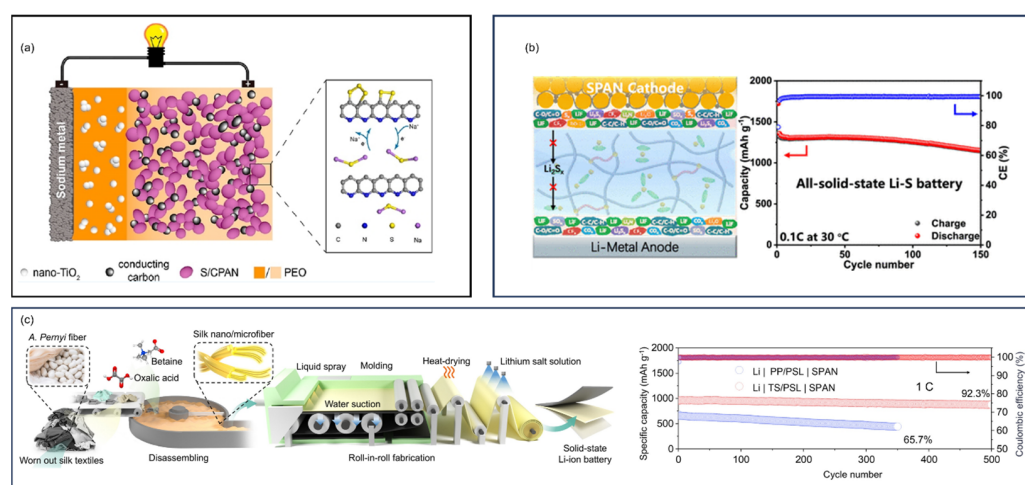


**Figure 40.** (a) Schematic illustration of the configuration of the solid-state Na||SPAN battery. Reproduced with permission [376]. Copyright © 2019, American Chemical Society; (b) Schematic illustration of the suppression of the shuttle effect by the proposed “polymer-in-salt” solid-state electrolyte and the corresponding cycling performance of the Li||SPAN battery. Reproduced with permission [379]. Copyright © 2025, American Chemical Society; (c) Schematic illustration of the fabrication process of the ultrathin SPAN membrane and the cycling performance of the Li||SPAN cells. Reproduced with permission [381]. Copyright © 2025, Elsevier.

An in situ polymerized dual salt-based quasi-solid polymer electrolyte (DS-QSPE) was developed by Huang et al. for high-performance Na||SPAN batteries [383]. The liquid electrolyte consisted of NaTFSI/NaFSI in DOL/FEC mixture, which was polymerized by tin trifluoromethanesulfonate (Sn(OTf)<sub>2</sub>) to obtain DS-QSPE (Figure 41b). DS-QSPE exhibited high ionic conductivity ( $4.8 \times 10^{-4} \text{ S cm}^{-1}$ ) and Na transference number (0.73). In addition, DS-QSPE could form an interconnected network structure in the SPAN cathode and enable seamless electrode/electrolyte interfaces. Consequently, the Na||SPAN battery with DS-QSPE delivered a high capacity of  $327.4 \text{ mAh g}^{-1}$ SPAN after 200 cycles at  $0.2 \text{ A g}^{-1}$ , corresponding to a capacity retention of 81.4%.

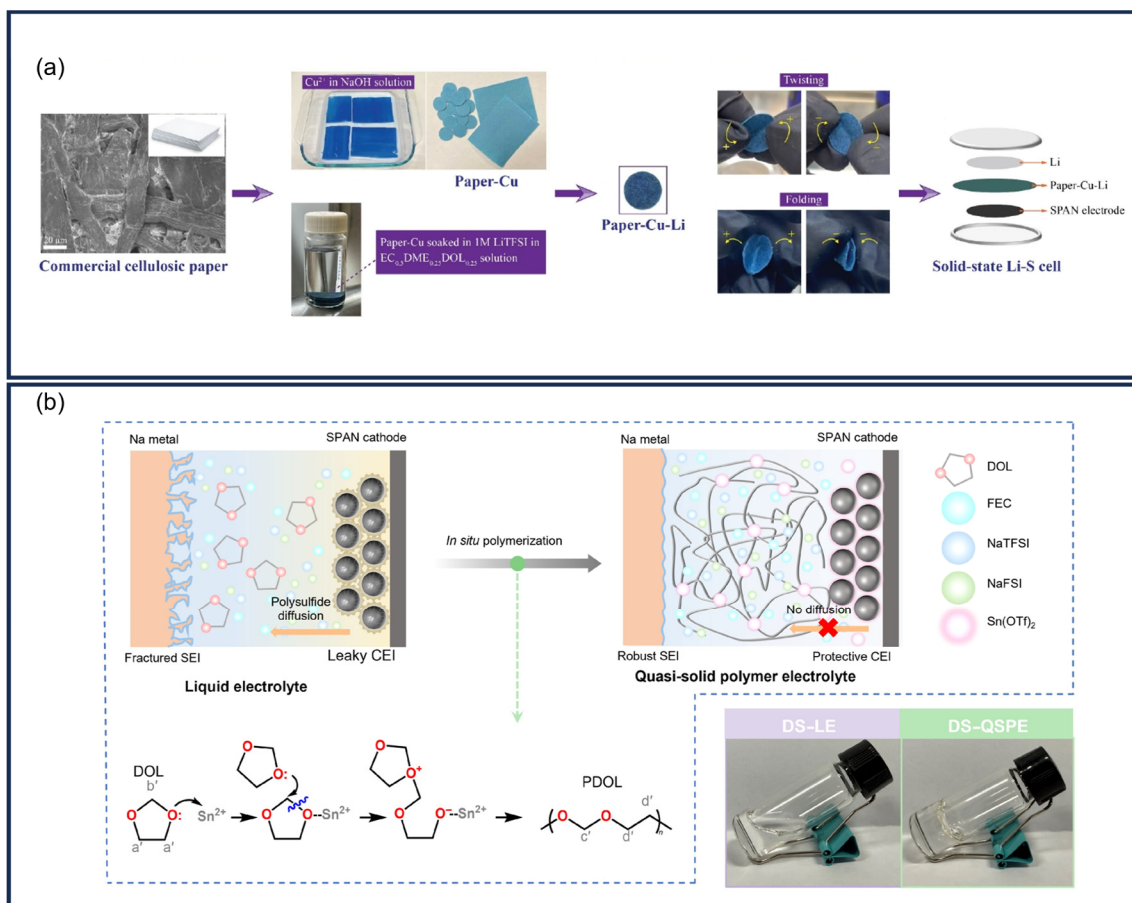


**Figure 41.** (a) Schematic illustration of the preparation and utilization of Paper–Cu–Li SSE from commercial paper. Reproduced with permission [382]. Copyright © 2025, American Chemical Society; (b) Schematic illustration of the in situ ring-opening polymerization of DOL–based electrolytes induced by Sn(OTf)<sub>2</sub> and optical images of DS–LE and DS–QSPE. Reproduced with permission [383]. Copyright © 2024, Tsinghua University Press.

In 2025, Lao et al. employed unsupervised learning and Climbing Image-Nudged Elastic Band (CI-NEB) simulations to screen a series of Hofmann complexes which could potentially offer continuous two-dimensional Li<sup>+</sup> conductive channels for solid-state batteries [384]. The SPE-based cell with Co(DMF)<sub>2</sub>Ni(CN)<sub>4</sub> (Co-Ni) exhibited the optimal electrochemical performance. DFT calculations revealed that the competition between M-O and Li-O bonds could be strategically modulated to optimize the weak coordination environment of Li<sup>+</sup> for rapid conduction kinetics. A 0.6 Ah solid-state Li | Co-Ni | SPAN pouch cell with an areal capacity of 3.8 mAh cm<sup>-2</sup> delivered stable cycling for 20 cycles at 50 mA.

#### 9.6.2. Solid-State Ceramic Electrolytes

Solid-state ceramic electrolytes, as inorganic Li<sup>+</sup> conductors, exhibit high ionic conductivity, excellent electrochemical/chemical/thermal stability, and benign interfacial properties [385]. Early advancements were demonstrated by Trevey et al., who assembled solid-state Li | SPAN batteries with Li<sub>2</sub>S-P<sub>2</sub>S<sub>5</sub> as the electrolyte [386]. The battery maintained a discharge capacity over 605 mAh g<sup>-1</sup>SPAN for 50 cycles. In Zhang et al.'s study, Li<sub>10</sub>GeP<sub>2</sub>S<sub>12</sub> was used as solid electrolyte for Li | Se<sub>0.05</sub>S<sub>0.95</sub>@pPAN batteries which delivered an initial discharge capacity of 840 mAh g<sup>-1</sup>sulfur & selenium and retained 81% of its capacity after 150 cycles at 167.5 mA/g [195] (Figure 42a).

In 2021, Sun et al. reported a dense composite SPAN cathode featuring SPAN supported by a microporous carbon conductive matrix to assemble solid-state Li||SPAN batteries [387]. Li<sub>6</sub>PS<sub>5</sub>Cl (LPSC-SE) was used as the solid electrolyte to suppress the irreversible parasitic reactions with carbonate-based electrolytes. The as-assembled solid-state Li-In||LPSC-SE||SPAN@MaPC battery delivered a high reversible capacity of 1396.2 mAh g<sup>-1</sup><sub>sulfur</sub> and retained 715.5 mAh g<sup>-1</sup><sub>sulfur</sub> after 200 cycles at 0.1 C (Figure 42b). Further electrolyte refinement was achieved by Zhang et al. with an iodine-rich lithium argyrodite Li<sub>5.5</sub>PS<sub>4.5</sub>I<sub>1.5</sub> for solid-state Li||SPAN batteries in 2022 [202].

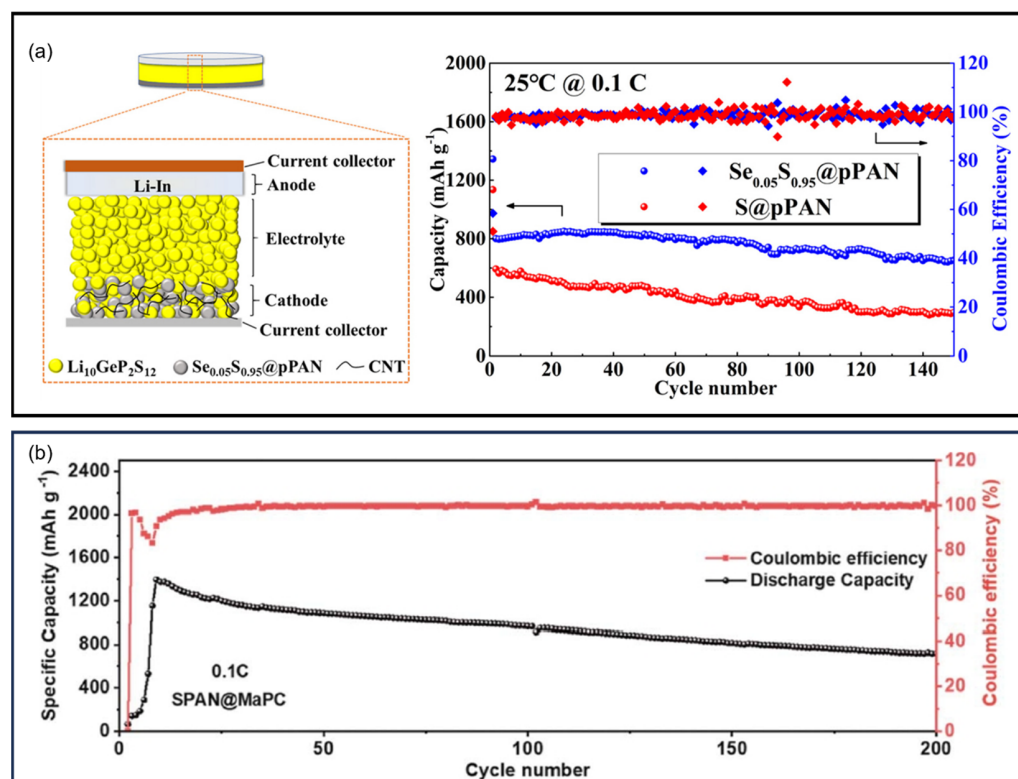


**Figure 42.** (a) left: Schematic illustration of the configuration of the solid-state Li||Li<sub>10</sub>GeP<sub>2</sub>S<sub>12</sub>||SPAN battery; right: Cycling performance comparison of S@pPAN and Se<sub>0.05</sub>S<sub>0.95</sub>@pPAN. Reproduced with permission [195]. Copyright © 2019, Elsevier; (b) Cycling performance of the Li-In||LPSC-SE||SPAN@MaPC battery. Reproduced with permission [387]. Copyright © 2021, Royal Society of Chemistry.

Huang et al. reported a solid-state Li||SPAN battery with Li<sub>4</sub>(BH<sub>4</sub>)<sub>3</sub>I as the solid-state electrolyte, which effectively suppressed the Li dendrite growth and enhanced the cycling performance [388]. Jin et al. developed a composite solid-state electrolyte comprising Li<sub>4</sub>(BH<sub>4</sub>)<sub>3</sub>I and B<sub>2</sub>O<sub>3</sub> prepared by ball-milling for high-performance solid-state Li||SPAN batteries [389] (Figure 43a). The composite solid-state electrolyte exhibited high ionic conductivity ( $1.45 \times 10^{-4}$  S cm<sup>-1</sup>) and high oxidation stability up to 5.0 V. The introduction of boron oxide facilitated the formation of a highly conductive interface and effectively inhibited dendrite formation.

Interlayers and cathode coatings are commonly used techniques to improve the interfacial behavior between the solid-state ceramic electrolytes and the electrodes. Wang et al. introduced a solid-state plastic crystal electrolyte (PCE) as an interlayer in Li<sub>10</sub>GeP<sub>2</sub>S<sub>12</sub>-based solid-state Li||SPAN batteries [390]. The PCE interlayer effectively suppressed the interfacial reactions between Li<sub>10</sub>GeP<sub>2</sub>S<sub>12</sub> and the lithium metal anode (Figure 43b). The resulting solid-state Li||SPAN battery employing the PCE interlayer delivered an

initial discharge capacity of  $1682 \text{ mAh g}^{-1}$  sulfur and retained  $775 \text{ mAh g}^{-1}$  sulfur of its capacity after 100 cycles at  $0.13 \text{ mA cm}^{-2}$ . In 2020, Zhang et al. reported a tellurium-doped SPAN ( $\text{Te}_{0.05}\text{S}_{0.95}\text{PAN}$ ) cathode coated with solid electrolyte ( $\text{Li}_7\text{P}_3\text{S}_{11}$ ) for solid-state batteries [230]. Benefiting from the  $\text{Li}_7\text{P}_3\text{S}_{11}$  and Te doping, the composite cathode exhibited enhanced reaction kinetics and excellent interfacial compatibility with the solid electrolyte  $\text{Li}_{10}\text{GeP}_2\text{S}_{12}$ . The as-assembled  $\text{Li} \parallel \text{Te}_{0.05}\text{S}_{0.95}\text{PAN}$  battery achieved a second discharge capacity of  $1173.1 \text{ mAh g}^{-1}$  composite and retained  $665.3 \text{ mAh g}^{-1}$  composite after 500 cycles at  $0.3 \text{ C}$ .

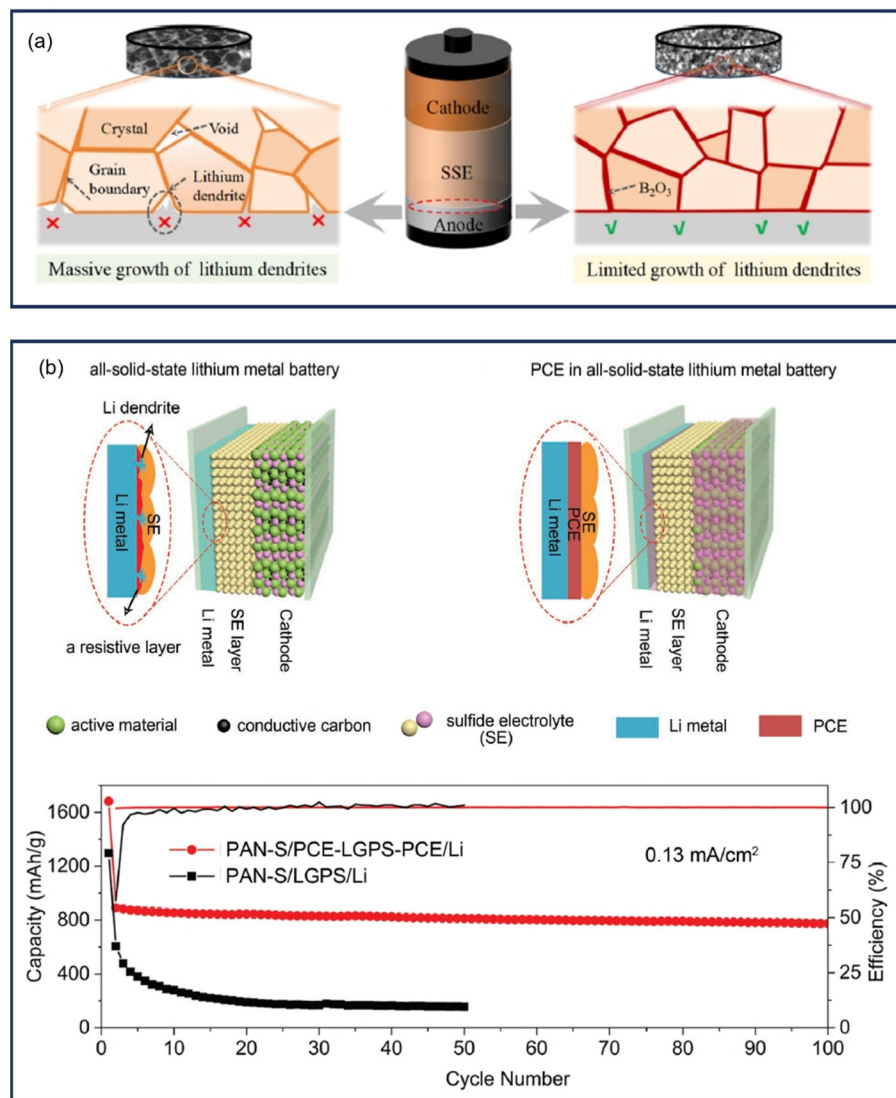


**Figure 43.** (a) Schematic illustration of the  $\text{B}_2\text{O}_3$ -modified layer suppressing the growth of Li dendrites. Reproduced with permission [389]. Copyright © 2025, American Chemical Society; (b) Schematic illustration of the all-solid-state lithium metal batteries with and without the PCE interlayer and the corresponding cycling performance. Reproduced with permission [390]. Copyright © 2019, John Wiley and Sons.

A sandwich structured NASICON-type  $\text{Li}_{1.3}\text{Al}_{0.3}\text{Ti}_{1.7}(\text{PO}_4)_3$  (LATP) solid-state electrolyte coated by a polymer electrolyte (SPE, PEO:LiTFSI = 8:1) for high-performance  $\text{Li} \parallel \text{SPAN}$  batteries was reported by Wang et al. in 2020 [391] (Figure 44a). Due to the unique hierarchical structure of the SPE-coated LATP, the direct contact between the lithium metal anode and LATP was avoided and improved interfacial property could be achieved. As a result, the solid-state  $\text{Li} \parallel \text{SPAN}$  battery delivered a reversible capacity of about

976 mAh g<sup>-1</sup> sulfur and retained 784 mAh g<sup>-1</sup> sulfur after 120 cycles at 0.1 C. A facile powder-polishing strategy to reduce the polarization of Na super ionic conductor (NASICON) structured  $\text{Na}_3\text{Zr}_2\text{Si}_2\text{PO}_{12}$  electrolyte and ameliorate the interfacial contact between the Na anode and the electrolyte by employing isotropic SPAN as the interlayer was proposed by Miao et al. in 2021 [392]. The SPAN interlayer redistributed the interfacial electric field and homogenized the  $\text{Na}^+$  flux, suppressing Na dendrite growth. As a result, the solid-state  $\text{Na} \parallel \text{SPAN}$  battery with the SPAN-modified NASICON electrolyte maintained a discharge capacity of 357.1 mAh g<sup>-1</sup> after 100 cycles.

In 2023, Shi et al. reported a solid-state  $\text{Li} \parallel \text{SPAN}$  cell with a composite cathode (SPAN/LiFSI/nano graphene wire (NGW)) to improve interfacial contact and ionic and electronic conductivity in the cathode [393] (Figure 44b). The SPAN/LiFSI/NGW cathode was deposited on a dense/porous bilayer garnet  $\text{Li}_7\text{La}_3\text{Zr}_2\text{O}_{12}$  (LLZO) solid-state electrolyte impregnated on the porous anode side with Li metal to assemble to solid-state  $\text{Li} \parallel \text{SPAN}$  cell, which demonstrated stable cycling at 60 °C with a high average discharge capacity of 1400 mAh g<sup>-1</sup> sulfur at 0.1 C for over 40 cycles and of 437 mAh g<sup>-1</sup> sulfur at 0.5 C for over 200 cycles. Following their previous work, Shi et al. developed an innovative GPE as a catholyte to replace conventional PEO as a stabilizing interlayer between the cathode and the thin Ta-LLZO bilayer solid-state electrolyte [394]. The GPE interlayer was in situ formed on the dense side of the bilayer LLZO enabled by the polymerization of DOL. In particular, the preferred  $\text{FSI}^-$  decomposition over solvents decomposition facilitated the formation of a completely intimate and conformal CEI coating layer which protected the interface and mitigated the volume expansion of the cathode during cycling. With a high sulfur loading of 5.2 mg cm<sup>-2</sup>, the solid-state  $\text{Li} \parallel \text{SPAN}$  battery delivered an average discharge capacity of 1218 mAh g<sup>-1</sup> over 265 cycles at 1.74 mA cm<sup>-2</sup>, room temperature, and no applied pressure, with a capacity retention of 80%.

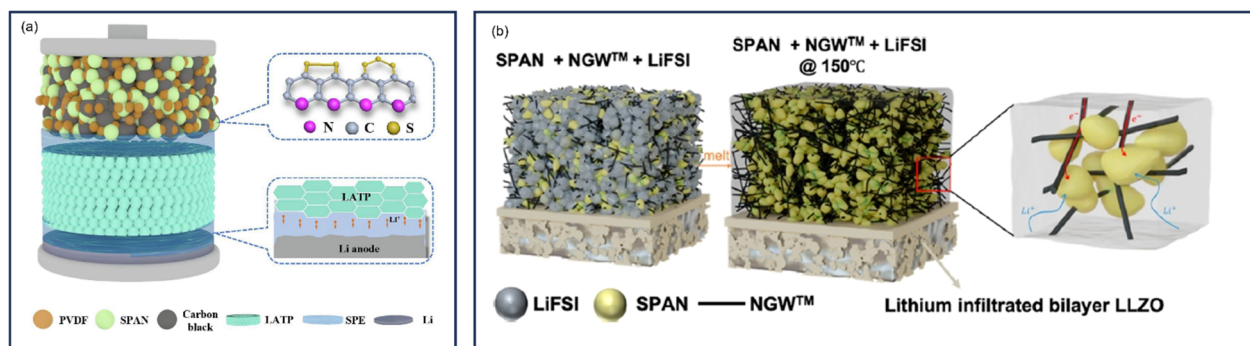


**Figure 44.** (a) Schematic illustration of the NASICON-type solid-state SPAN battery. Reproduced with permission [391]. Copyright © 2020, Elsevier; (b) Schematic illustration of the all-solid-state garnet type  $\text{Li} \parallel \text{SPAN}$  batteries enabled by the novel three-phase cathode and the bilayer-LLZO electrolyte architecture. Reproduced with permission [393]. Copyright © 2023, American Chemical Society.

In Zhao et al.'s study, a graphitic carbon nitride ( $\text{g-C}_3\text{N}_4$ )-dominated artificial interlayer was introduced between the Li metal anode and the solid-state electrolyte  $\text{Li}_6\text{PS}_5\text{Cl}$  (LPSC) to enhance the interfacial stability [395] (Figure 45). The nitrogen-rich GCN layer regulated  $\text{Li}^+$  flux, enabling uniform Li deposition and suppressing Li dendrite growth.

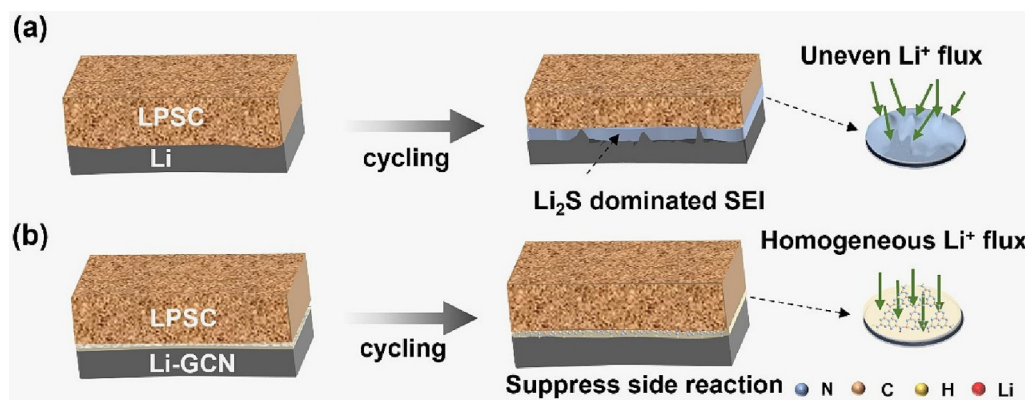


**Figure 45.** Schematic illustration of the comparison of the interface evolution of the (a) Li or (b) Li-GCN and LPSC. Reproduced with permission [395]. Copyright © 2024, Elsevier.

For solid-state sodium batteries, various ceramic electrolytes have been explored.  $\text{Na}_3\text{PS}_4$  was reported as the solid-state electrolyte for  $\text{Na} \parallel \text{Se}_{0.05}\text{S}_{0.95}\text{PAN}$  batteries by An et al. in 2020, delivering 607.6 and 372  $\text{mAh g}^{-1}$  at 10th and 50th cycles at  $0.3 \text{ A g}^{-1}$ , respectively [200].  $\text{Na}_3\text{SbS}_4$  was used as the solid-state electrolyte for room temperature solid-state  $\text{Na}_{15}\text{Sn}_4 \parallel \text{SeSPAN}$  batteries by Zhang et al., delivering a reversible capacity of  $504 \text{ mAh g}^{-1}$  sulfur & selenium and a capacity retention of 98.9% after 100 cycles at  $437.4 \text{ mA g}^{-1}$  [201]. In 2020, Jia et al. employed the halogen doping strategy on a novel solid-state electrolyte  $\text{Na}_{3.57}[\text{Sn}_{0.67}\text{Si}_{0.33}]_{0.67}\text{P}_{0.33}\text{S}_{3.9} \times 0.1$  ( $X = \text{Cl}, \text{Br}, \text{and I}$ ) to achieve higher ionic conductivities and lower activation energies than the pristine sample [198]. The solid-state  $\text{Na} \parallel \text{Se}_{0.05}\text{S}_{0.95}\text{PAN}$  battery with  $\text{Na}_{3.57}[\text{Sn}_{0.67}\text{Si}_{0.33}]_{0.67}\text{P}_{0.33}\text{S}_{3.9}\text{I}_{0.1}$  as the solid-state electrolyte, and  $\text{Na}_3\text{Sn}$  alloy as the anode delivered  $657.4 \text{ mAh g}^{-1}$  sulfur & selenium at the second cycle and maintained 76% after 40 cycles at  $0.15 \text{ A g}^{-1}$ . In the same year, Jia et al. reported another quinary Na fast-conductive electrolyte,  $\text{Na}_{3.8}[\text{Sn}_{0.67}\text{Si}_{0.33}]_{0.8}\text{Sb}_{0.2}\text{S}_4$ , as solid electrolytes for room temperature solid-state  $\text{Na}_3\text{Sn} \parallel \text{Se}_{0.05}\text{S}_{0.95}\text{PAN}$  batteries [199].

### 9.6.3. Solid-State Composite Electrolytes and Hybrid Electrolytes

Solid-state composite electrolytes, which combine the solid-state inorganic and organic electrolytes, have emerged as promising candidates for high-performance SPAN-based batteries. In 2020, Li et al. developed a solid-state  $\text{Li} \parallel \text{SPAN}$  battery using thio-LiSICON/polymer composite electrolyte (LCE) composed of  $\text{Li}_{3.25}\text{Ge}_{0.25}\text{P}_{0.75}\text{S}_4$  and plasticized PEO [396] (Figure 46a). The composite electrolyte exhibited high ionic conductivity and  $\text{Li}^+$  transfer number, which facilitated good interfacial wetting and stable lithium stripping/plating. The resulting solid-state  $\text{Li} \parallel \text{SPAN}$  battery delivered a discharge capacity of  $588 \text{ mAh g}^{-1}$  after 50 cycles at  $0.1 \text{ C}$  and  $60^\circ\text{C}$ . Another LGPS-based solid-state composite electrolyte comprising  $\text{Li}_{10}\text{GeP}_2\text{S}_{12}$  and PTFE with a polymeric ionic liquid-based solid polymer coating was developed by Chen et al. in 2023 [397]. High room temperature ionic conductivity up to  $0.91 \text{ mS cm}^{-1}$  could be achieved (Figure 46b). The  $\text{Li} \parallel \text{LGPS-PTFE} \parallel \text{SPAN}$  battery delivered an initial capacity of  $824.7 \text{ mAh g}^{-1}$  and retained 52.49% of its initial capacity after 120 cycles at  $0.1 \text{ C}$ .

Temeche et al. reported the synthesis of a solid-state composite electrolyte with superior ionic conductivities at room temperature for  $\text{Li} \parallel \text{SPAN}$  batteries [398]. By co-dissolving PEO with  $\text{Li}_x\text{PON}$  or  $\text{Li}_x\text{SiPON}$  followed by casting, PEO solid-solution films were yielded and exhibited enhanced ionic conductivities and lower activation energies for cation transport. The optimized electrolyte enabled the solid-state  $\text{Li} \parallel \text{SPAN}$  battery to deliver discharge capacities of  $1000 \text{ mAh g}^{-1}$  sulfur at  $0.25 \text{ C}$  and  $800 \text{ mAh g}^{-1}$  sulfur at  $1 \text{ C}$ , with high capacity retention rate over 100 cycles. In a later study by Temeche

et al., they investigated the electrochemical performance of  $\text{Li}_x\text{SiON}$  ( $x = 2, 4$ , and  $6$ ) polymer electrolytes [399]. The results revealed that  $\text{Li}_6\text{SiON}$  electrolyte exhibited high ionic conductivity ( $6.5 \times 10^{-6} \text{ S cm}^{-1}$ ) and high  $\text{Li}^+$  transference number (0.75–1) at ambient temperature.

A novel solid-state composite electrolyte composed of PEO and lithium borohydrides with nano- $\text{SiO}_2$  as an inorganic filler ( $\text{PEO}_{10}\text{-Li}_4(\text{BH}_4)_3\text{I-SiO}_2$  (5 wt.%)) was developed by Zhang et al. in 2021 [400].  $\text{LiBH}_4$  exhibited high ionic conductivity and acted as a lithium salt, while  $\text{SiO}_2$  inhibited the Li dendrite growth. The resulting solid-state  $\text{Li} \parallel \text{SPAN}$  battery delivered a reversible capacity of  $967 \text{ mAh g}^{-1}$  sulfur after 75 cycles at  $50 \text{ mA g}^{-1}$ .

In 2022, Luo et al. designed a high-performance  $\text{Li}_{6.75}\text{La}_3\text{Zr}_{1.75}\text{Ta}_{0.25}\text{O}_{12}$  (LLZTO)-based solid-state composite electrolyte for  $\text{Li} \parallel \text{SPAN}$  batteries [401] (Figure 46c). The composite electrolyte was composed of an electrospun polyimide film, LLZTO ionically conducting filler, and a PAN matrix, exhibiting high ionic conductivity ( $2.75 \times 10^{-4} \text{ S cm}^{-1}$ ), high  $\text{Li}^+$  transference number of 0.67, and excellent interfacial wettability. As a result, the solid-state  $\text{Li} \parallel \text{SPAN}$  battery delivered a reversible capacity of  $254 \text{ mAh g}^{-1}$  and retained  $219.7 \text{ mAh g}^{-1}$  after 1000 cycles at 1 C. LLZTO-based solid-state composite electrolytes were further studied by Ma et al. in 2024 ( $\text{PEO/Li}_7\text{La}_3\text{Zr}_{1.4}\text{Ta}_{0.6}\text{O}_{12}$ ) [225] and Nie et al. in 2024 ( $\text{PVDF/polyurethane/Li}_{6.4}\text{La}_3\text{Zr}_{1.4}\text{Ta}_{0.6}\text{O}_{12}$ ) [402], underscoring their potential in solid-state SPAN-based batteries.

The wide-used polymer matrix, PVDF-HFP, can also be applied to construct a solid-state composite electrolyte. In 2024, Zhu et al. developed a solid-state composite polymer electrolyte (CPE) using PVDF-HFP as the matrix, LiFSI as the salt, and a rationally designed Hofmann-DMF coordination complex ( $\text{Ni}(\text{DMF})_2\text{Ni}[\text{CN}]_4$ , denoted as Ni-DMF) to address the degradation issue of DMF [403]. The incorporation of Ni-DMF effectively confined and reduced DMF consumption, facilitating the formation of a stable inorganic-rich SEI. The optimized CPE exhibited high ionic conductivity of  $6.5 \times 10^{-4} \text{ S cm}^{-1}$  at room temperature due to the incorporation of DMF. As a result, the solid-state  $\text{Li} \parallel \text{SPAN}$  pouch cell delivered a capacity of  $47 \text{ mAh}$  after 35 cycles at 0.1 C.

Hybrid electrolytes refer to solid-state electrolytes incorporating a certain amount of liquid electrolytes. In 2014, Unemoto et al. assembled a solid-state  $\text{Li} \parallel \text{SPAN}$  battery with electrolytes consisting of tetraethylene glycol dimethyl ether–lithium bis(trifluoromethanesulfonyl) amide ( $[\text{Li}(\text{G4})_1]\text{TFSAs}$ ) and fumed silica nanoparticles [404]. The battery exhibited high and stable charge–discharge performance, with 2nd and 50th discharge capacity of 450 and  $390 \text{ mAg g}^{-1}$  SPAN, respectively, and nearly 100% Coulombic efficiency.

Further advancements were made by Yang et al., who developed a cation-solvent fully coordinated metal–organic frameworks (MOFs)-ether hybrid electrolyte to address the issues of both Li anode and SPAN cathode [405]. By constraining the ether electrolyte into a MOF structure, the solvent activity was suppressed in terms of solvent conformers, flammability, and anti-oxidation capability. Raman spectroscopy revealed a unique electrolyte solvation sheath and a highly aggressive ion-pair interaction between  $\text{Li}^+$  and  $\text{TFSI}^-$ . Consequently, the Li plating/stripping showed enhanced reversibility. The assembled 0.2 Ah solid-state  $\text{Li} \parallel \text{SPAN}$  pouch cell with high cathode loading (sulfur loading =  $6.0 \text{ mg cm}^{-2}$ ), limited lithium ( $\text{N/P} = 1.4$ ), and lean electrolyte ( $1 \mu\text{L mg}^{-1}$  sulfur) delivered a capacity retention of 69.7% after 100 cycles at 0.15 C and  $60^\circ\text{C}$ .

The hybridization of PVDF-HFP as the polymer matrix and  $\text{LiTa}_2\text{PO}_8$  (LTPO) as the filler to construct a solid-state electrolyte membrane (LTPO-HSE) for  $\text{Li} \parallel \text{SPAN}$  batteries was reported by Anbunathan et al. in 2024 [406] (Figure 46d). The incorporation of LTPO ceramic fillers reduced the crystallinity of PVDF-HFP, facilitated smooth ionic conduction, and enhanced the mechanical strength of the membrane. The solid-state  $\text{Li} \parallel \text{SPAN}$  battery exhibited high  $\text{Li}^+$  transference number (0.78), high onset potential (5.25 V), and excellent

compatibility with the SPAN cathode. As a result, the battery delivered capacity retention rates of 96% and 81% after 200 and 350 cycles at 0.2 C and 0.5 C, respectively.

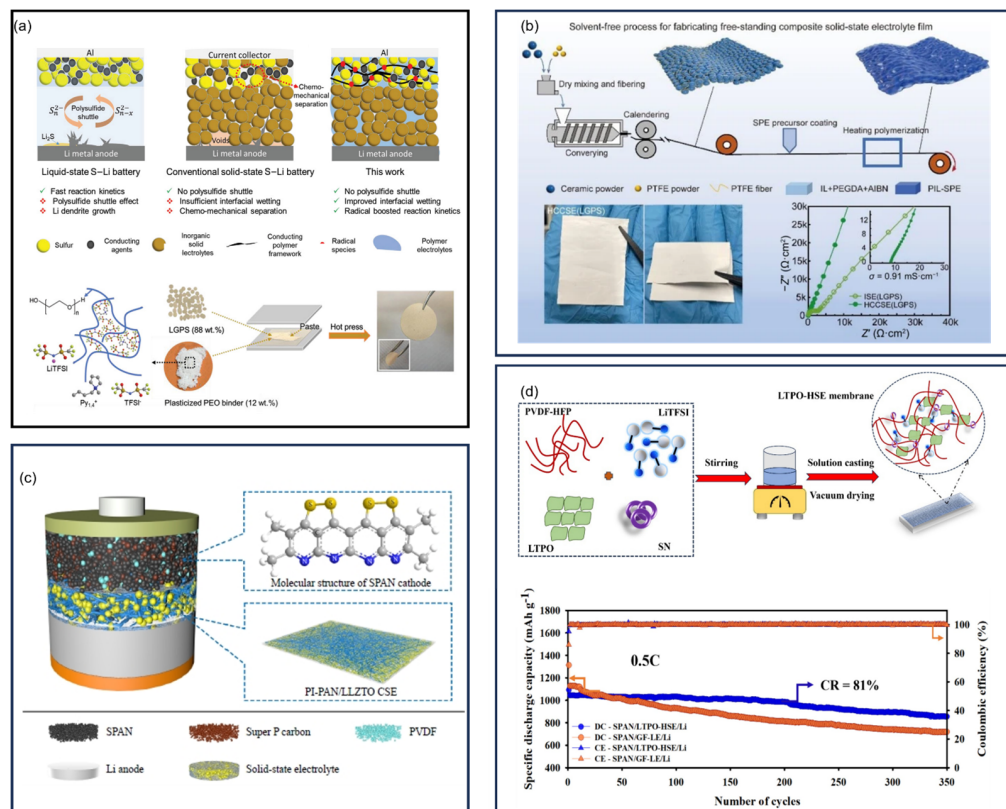


**Figure 46.** (a) top: Schematic illustration of comparison of liquid–state LSBs, conventional solid–state LSBs, and the solid–state LSBs with LCE; bottom: Schematic illustration of the fabrication process of LCE. Reproduced with permission [396]. Copyright © 2020, John Wiley and Sons; (b) Schematic illustration of the fabrication process of the composite solid-state electrolyte films. Reproduced with permission [397]. Copyright © 2023, Springer Nature; (c) Diagram of the configuration of the solid–state battery, molecular structure of SPAN and schematic structure of LLZTO–based solid-state composite electrolyte. Reproduced with permission [401]. Copyright © 2021, Springer Nature; (d) top: Schematic illustration of the preparation of LTPO–HSE composite membranes; bottom: Cycling performance at 0.5 C for 350 cycles. Reproduced with permission [406]. Copyright © 2024, Elsevier.

## 10. Binders

In most cases, binders are indispensable components in SPAN electrodes. An ideal binder should possess several critical properties: (1) strong interfacial adhesive forces to maintain electrical contact among components, and (2) robust mechanical strength to preserve structural integrity [407,408]. In this section, studies feature the development of binders for SPAN-based rechargeable batteries are discussed.

In early stages of SPAN research, polytetrafluoroethylene (PTFE) paired with organic solvent was the predominant binder system for SPAN cathodes [9–11,14]. Later, PVDF, a standard binder in commercial LIB cathodes, paired with N-methyl-2-pyrrolidone (NMP), was adopted in the preparation of SPAN cathodes [66,409]. Compared to PTFE and PVDF, aqueous binders have garnered significant interest due to their low cost, environmental friendliness, and improved safety. In 2013, Wang et al. introduced an aqueous binder, carbonyl- $\beta$ -cyclodextrin (C- $\beta$ -CD) for SPAN cathodes [410]. The SPAN cathode with the C- $\beta$ -CD binder exhibited a high reversible capacity of  $1542.7 \text{ mAh g}^{-1}$  sulfur and remained

1456  $\text{mAh g}^{-1}$  sulfur after 50 cycles, demonstrating its superior electrochemical properties (Figure 47a).

In 2017, Li et al. improved the electrochemical performance of  $\text{Li} \parallel \text{SPAN}$  batteries by employing sodium carboxymethyl cellulose (NaCMC) as the binder [411]. The NaCMC binder formed a continuous conductive network and mitigated the loss of active species upon cycling. Compared to the conventional PVDF binder, The SPAN cathode fabricated with the NaCMC binder delivered superior cycling performance, with a reversible capacity of 938  $\text{mAg g}^{-1}$  sulfur after 450 cycles at 0.9 C in both carbonate and ether electrolytes (Figure 47b). This work demonstrated the potential of water-soluble and oxygen containing binders to improve the electrochemical performance of SPAN cathodes.

PAA was firstly used as the binder to improve the integrity of the SPAN cathode by Kim et al. In 2017 [266]. The resulting  $\text{Li} \parallel \text{SPAN}$  coin cell achieved a high initial discharge capacity of 1500  $\text{mAh g}^{-1}$  sulfur and retained 98.5% of capacity after 100 cycles at 0.5 C. Later, Eng et al. demonstrated the effectiveness of the PAA binder in  $\text{Na} \parallel \text{SPAN}$  batteries [412]. The carboxyl groups in PAA not only anchored polysulfide intermediates and enhanced reaction kinetics but also formed strong binder-cathode interaction to allow the cathode to tolerate huge volume changes during cycling. As a result, the  $\text{Na} \parallel \text{SPAN}$  battery utilizing a PAA binder delivered an initial discharge capacity of 1195  $\text{mAh g}^{-1}$  sulfur and retained 1000  $\text{mAh g}^{-1}$  sulfur after 1000 cycles at 0.5 C, corresponding to a capacity decay rate of 0.016% per cycle (Figure 47c). The exceptional performance of the PAA binder was further demonstrated by Hwang et al. in  $\text{K} \parallel \text{SPAN}$  batteries [413].

In 2020, Zhang et al. systematically investigated the effects of different binders on the electrochemical performance of  $\text{Mg} \parallel \text{SPAN}$  batteries [414]. PVDF, PEO, sodium polyacrylate (PAAS), locust beam gum (LBG), guar gum (GG), carboxymethyl cellulose (SCMC), and  $\beta$ -cyclodextrin ( $\beta$ -CD) were tested. Among these, the SPAN cathode with the amorphous PAAS binder demonstrated optimal mechanical and adhesion properties, cycle stability, and rate performance (Figure 47d). Wong et al. explored the interactions between  $\text{Ti}_3\text{C}_2\text{T}_x$  MXenes and SPAN with traditional binders such as PVDF, PAA, CMC in  $\text{Na} \parallel \text{SPAN}$  batteries [415]. Their findings suggested that the linearity and polarity of the binder significantly influence the dispersion of SPAN over  $\text{Ti}_3\text{C}_2\text{T}_x$ . The three-dimensional polar CMC provided superior contact surface area with both SPAN and  $\text{Ti}_3\text{C}_2\text{T}_x$  and effectively trapped discharge products. As a result, the  $\text{Na} \parallel \text{SPAN}$  battery using the CMC binder delivered an initial discharge capacity of 1282  $\text{mAh g}^{-1}$  sulfur and stable cycling over 300 cycles at 0.2 C with a capacity decay rate of 0.092% per cycle.

Chen et al. developed an artificial multifunctional flexible binder (AFB) to enable high-areal-capacity and high-density SPAN cathodes via traditional blade-casting method [416]. AFB was synthesized by dissolving carboxylated styrene butadiene rubber (SCR) and GG in DI water, followed by vigorous stirring. GG provided complexation sites for  $\text{Li}^+$  transport, while SCR contributed excellent elasticity and flexibility (Figure 47e). With the AFB, the SPAN cathode exhibited an areal capacity of  $5.55 \text{ mAh cm}^{-2}$  and remarkable sulfur utilization of 91% after 100 cycles at 0.1 C. Notably, an ultra-thick SPAN cathode with an areal capacity up to  $8.31 \text{ mAh cm}^{-2}$  could be achieved. Another network dual-binder system composed of GG and PAA for high-loading SPAN cathodes was reported by Yang et al. in 2020 [417]. The GG-PAA binder was prepared by dissolving PAA powder into GG binder aqueous solutions and stirred overnight. The intermolecular interactions and the ester bond formation between hydroxyl groups in GG and carboxyl groups in PAA ensured the network binder system. After calendaring, the SPAN cathode reached a density of  $1.15 \text{ g cm}^{-3}$  and delivered a high areal capacity of  $6 \text{ mAh cm}^{-2}$  after 120 cycles.

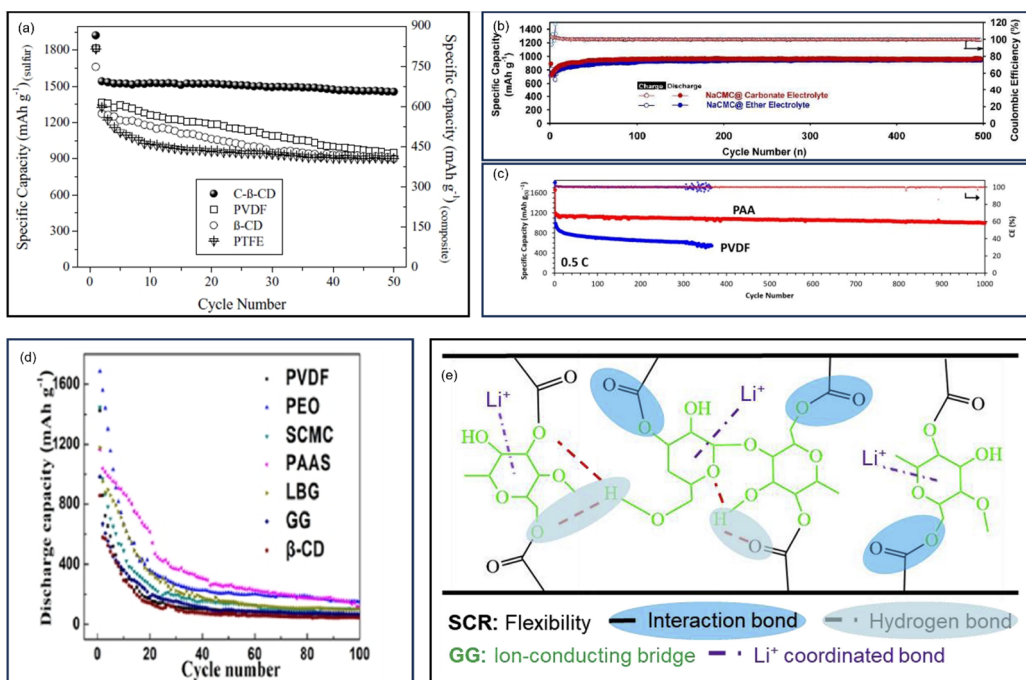


**Figure 47.** (a) Cycling performance of SPAN cathodes with different binders. Reproduced with permission [410]. Copyright © 2012, John Wiley and Sons; (b) Cycling performance of SPAN cathodes with the NaCMC binder in carbonate and ether electrolytes. Reproduced with permission [411]. Copyright © 2017, Royal Society of Chemistry; (c) Cycling performance of Na||SPAN batteries with the PAA and PVDF binders. Reproduced with permission [412]. Copyright © 2020, Royal Society of Chemistry; (d) Cycling performance of SPAN cathodes with different binders. Reproduced with permission [414]. Copyright © 2020, American Chemical Society; (e) Schematic illustration of interactions within the crosslinking network. Reproduced with permission [416]. Copyright © 2020, Elsevier.

Niesen et al. studied the influence of the drying temperature on the performance and binder distribution of SPAN cathodes [418]. Their study revealed contrasting behavior between PVDF- and PAA-based electrodes: at elevated drying temperatures, PVDF migrated to the electrode surface, increasing charge transfer resistance, and reducing cathode rate capability, while PAA-based electrodes maintained more uniform binder distribution. Wu et al. examined the binder effects on cycling performance of SPAN cathodes with high areal capacity ( $>6 \text{ mAh cm}^{-2}$ ) [419]. Thick SPAN cathodes with PVDF binder only maintained 66.7% capacity at 60th cycle due to the mechanical failure. In contrast, CMC remarkably improved the corresponding capacity retention to 94.5%, demonstrating its superior properties in high-loading SPAN cathodes. In 2024, Miao et al. systematically studied the strain evolution of SPAN cathodes with four water-based binders including PAA, GG, CMC-styrene butadiene rubber (SBR), and polyacrylic latex (LA133) [420]. By implanting optical fiber Bragg grating (FBG) sensors, they demonstrated that PAA-based cathodes exhibited the largest strain evolution due to exceptional adhesion properties, correlating with superior electrochemical performance under high loading conditions (Figure 48a). This work established a new methodology for binder evaluation in SPAN systems.

Yuan et al. reported a novel hydrogel binder prepared by introducing Cu<sup>2+</sup> into sodium alginate binders (SA-Cu) for high-performance Li||SPAN batteries [421] (Figure 48b). Cu<sup>2+</sup> served as a crosslinker to construct a stable binder network and as catalysts for sulfide intermediates conversion. This binder enabled Li||SPAN batteries with a high sulfur-content SPAN cathode (52.6%) to deliver a reversible discharge capacity of  $1051.5 \text{ mAh g}^{-1}$  sulfur after 1000 cycles at 1 C, corresponding to a capacity retention of

85.3%. In 2022, Lin et al. also explored the metal-doped binder for SPAN/PDA composite cathode [422]. The metalized polyacrylate (MPAA) binder formed strong polar interactions with cathode components, creating mechanically robust interfaces to accommodate volume changes. Among various metal ions tested,  $\text{Ti}^{4+}$ -MPAA yielded optimal performance, enabling  $\text{Na} \parallel \text{SPAN}$  batteries to maintain  $1271 \text{ mAh g}^{-1}$  after 300 cycles at 1 C.

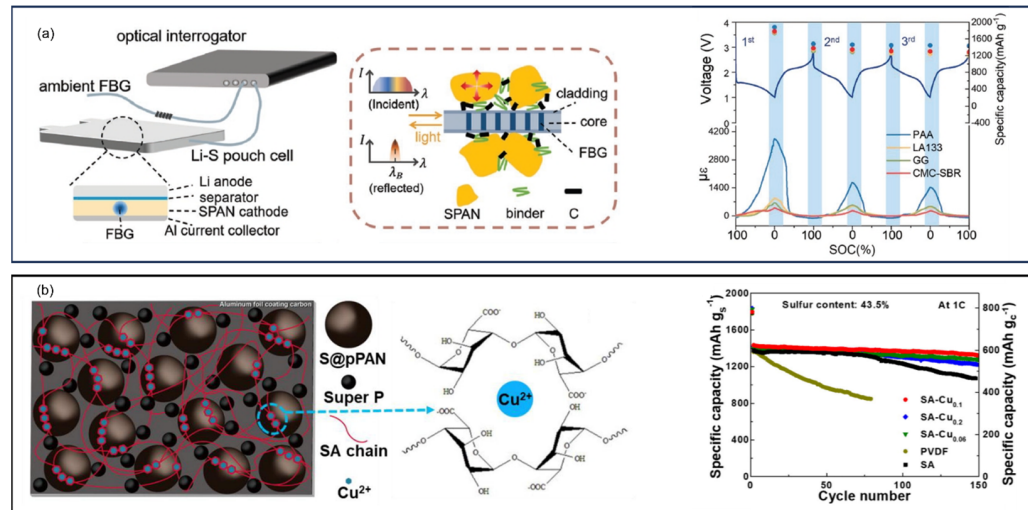


**Figure 48.** (a) left: Schematic illustration of the pouch cell consisting of cathode embedded with FBG sensor, separator, and Li anode; right: The internal strain curves of SPAN cathodes using different binders. Reproduced with permission [420]. Copyright © 2023, John Wiley and Sons; (b) left: Schematic illustration of the SA–Cu binder formation; right: Cycling performance of the SPAN cathodes with different binders. Reproduced with permission [421]. Copyright © 2021, Elsevier.

A multifunctional binder for SPAN cathodes was reported by Syn et al. in 2024 [423].  $\text{Ti}_3\text{C}_2\text{T}_x$  MXene nanosheets as both a conductive and a catalytic binder was used for SPAN cathode fabrication, where MXene could construct a conductive framework for fast charge transport and provide catalytic effect to accelerate the redox kinetics. The as-prepared SPAN electrode exhibited a high electronic conductivity of  $5.05 \text{ S cm}^{-1}$ , four orders of magnitude higher than the conventional polymer binders, and low activation energy and resistance. As a result, the  $\text{Li} \parallel \text{SPAN}$  battery delivered an excellent high-rate cycling performance (a capacity decay rate of ~0.04% per cycle over 1000 cycles at  $5 \text{ A g}^{-1}$ ) and unparalleled rate capability ( $189.0 \text{ mAh g}^{-1}$  SPAN at  $20 \text{ A g}^{-1}$ ).

## 11. Current Collectors

In conventional lithium-ion and lithium–metal batteries, current collectors serve as the substrate for electrode deposition while ensuring efficient electrical conduction. For typical  $\text{Li} \parallel \text{SPAN}$  batteries, aluminum (Al) foil is commonly used as the cathode current collector, while lithium (Li) foil functions as both the anode and current collector. However, with the growing demand for high-energy-density and high-performance SPAN-based batteries, research has shifted toward developing lightweight, durable, low-cost, and chemically stable current collectors. In this section, studies on the current collectors for SPAN-based rechargeable batteries are discussed.

In 2013, Wang et al. introduced a novel lightweight graphene-coated polyethylene terephthalate (G-PET) film as the current collector for  $\text{Li} \parallel \text{SPAN}$  batteries, aiming at achieving low-cost and high-energy-density batteries [409]. A 110 mAh prototype cell was assembled, with energy density of  $452 \text{ Wh kg}^{-1}$  (excluding the package weight), exhibiting capacity retention of 96.8% after 30 cycles.

Kim et al. reported a high-loading SPAN cathode ( $17 \text{ mg}_{\text{SPAN}} \text{ cm}^{-2}$ , areal capacity =  $9 \text{ mAh cm}^{-2}$ ) with decent cyclability (73.3% capacity retention after 90 cycles) [424]. The authors employed multiple strategies to address Li dendrite growth and sulfur cathode high loading issues, including the use of the polydopamine-coated polyethylene separator and  $\text{CsNO}_3$  as an electrolyte additive to inhibit dendrite growth, and the replacement of the traditional aluminum foil with a Ni-coated polyester textile as the current collector to avoid crack formation and film delamination at high loading.

In 2017, Cho et al. introduced micro carbon fibers (CFs) as a lightweight alternative to conventional aluminum current collector for  $\text{Li} \parallel \text{SPAN}$  batteries [425]. The CFs were coated on SPAN electrodes by the electrostatic flocking method, resulting in a current collect with both reduced weight and enhanced electrochemical performance (Figure 49a). The resulting  $\text{Li} \parallel \text{SPAN}$  battery with the CFs current collector delivered better electrochemical performance than that with the conventional Al current collector, exhibiting an initial discharge capacity of  $1373 \text{ mAh g}^{-1}_{\text{sulfur}}$  and a capacity retention of 76% after 100 cycles at 0.2 C. Furthermore, Hara et al. and Baikalov et al. reported high-loading SPAN cathodes with carbon fiber papers as the current collector [426,427]. Zhang et al. extended this approach by incorporating a potassium-sodium liquid alloy anode with carbon paper current collectors [428]. The K-Na  $\parallel$  SPAN battery delivered a high reversible capacity of  $490 \text{ mAh g}^{-1}$  after 100 cycles at  $35 \text{ mA g}^{-1}$ . Kalybekkyzy et al. developed a novel lightweight 3D current collector composed of carbon nanofibers (CNF) fabricated by electrospinning for SPAN cathodes [429] (Figure 49b). The  $\text{Li} \parallel \text{SPAN}$  battery employing this current collector maintained a reversible capacity of  $1104 \text{ mAh g}^{-1}$  after 100 cycles.

Liu et al. demonstrated the use of graphene foams (GFs) as a three-dimensional lightweight current collector for high-performance  $\text{Li} \parallel \text{SPAN}$  batteries [430] (Figure 49c). The open framework structure of GFs enabled high loading of SPAN, with minimal deterioration in capacity. A  $\text{Li} \parallel \text{SPAN}$  cell with high cathode loading ( $26.5 \text{ mg cm}^{-2}$  of sulfur,  $\sim 20 \text{ mAh cm}^{-2}$ ) delivered stable cycling up to 50 cycles at  $3 \text{ mA cm}^{-2}$ .

In 2022, Teng et al. reported a strategy to regulate Li deposition on the commercial Cu current collector by introducing  $\text{ZnF}_x(\text{OH})_y$  coating layers on the Cu surface via an in situ hydrolysis reaction [209].  $\text{ZnF}_x(\text{OH})_y$  could react with lithium to form Li-Zn alloy and LiF, which lowered the Li nucleation energy barrier and accelerated the  $\text{Li}^+$  diffusion rate. In addition,  $\text{ZnF}_x(\text{OH})_y$ -modified layers also improved the interfacial stability and suppressed parasitic reactions between the Li metal anode and the electrolyte. To fabricate the anode, lithium was electrochemically deposited on  $\text{ZnF}_x(\text{OH})_y @ \text{Cu}$  current collector to form the  $\text{Li/ZnF}_x(\text{OH})_y @ \text{Cu}$  anode, and the  $\text{Li/ZnF}_x(\text{OH})_y @ \text{Cu} \parallel \text{SeSPAN}$  battery with high cathode mass loading ( $7 \text{ mg cm}^{-2}$ ), lean electrolyte ( $20 \mu\text{L}$ ), and limited lithium (N/P = 1.5) achieved a capacity retention of 95% after 60 cycles at  $0.1 \text{ A g}^{-1}$  (Figure 49d).

An “active” CNT bucky sandwich (BS) current collector for high-loading SPAN cathodes was developed by Sapkota et al. in 2023 [431]. The BS SPAN cathode (35 wt% S) with  $\approx 5.5 \text{ mg cm}^{-2}$  of S loading delivered an areal capacity of  $\approx 7.8 \text{ mAh cm}^{-2}$  at 0.1 C over 100 cycles with a E/S ratio =  $7 \mu\text{L mg}^{-1}$ . In addition, the pouch cell using BS SPAN cathode with  $\approx 5 \text{ mg cm}^{-2}$  delivered a discharge capacity of  $\approx 1300 \text{ mAh g}^{-1}_{\text{sulfur}}$  at 0.1 C.

In 2023, Shuai et al. reported the use of fluorinated aluminum foam as the current collector to compound with Na metal to yield sodiophilic aluminum foam@Na electrode ( $\text{NaHFAl}$ ) [432].  $\text{NaHFAl}$  enabled a non-dendritic Na deposition morphology and reduced voltage hysteresis due to its sodiophilic surface. As a result, the  $\text{NaHFAl} \parallel \text{SPAN}$  battery exhibited stable cycling with a capacity retention of 68% after 800 cycles at 0.5 C. In the same year, Lou et al. reported the utilization of fluorinated aluminum foam as the current collector for NaK liquid alloy anode in SPAN-based batteries [433].

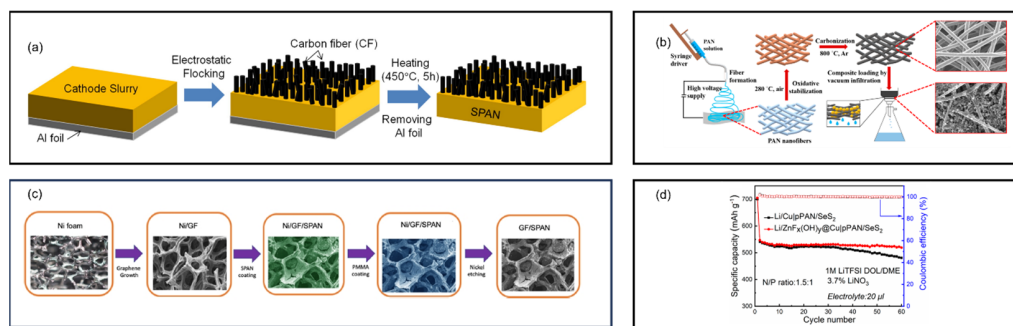


**Figure 49.** (a) Schematic illustration of the fabrication process of SPAN electrode with carbon fiber current collector. Reproduced with permission [425]. Copyright © 2017, Elsevier; (b) Schematic illustration of the carbon nanofiber fabrication and SPAN cathode preparation. Reproduced with permission [429]. Copyright © 2020, MDPI; (c) Schematic illustration of the fabrication process of a GF/SPAN cathode. Reproduced with permission [430]. Copyright © 2021, American Chemical Society; (d) Cycling performance of a Li/Cu||SeSPAN battery and Li/ZnFx(OH)y@Cu||SeSPAN battery. Reproduced with permission [209]. Copyright © 2022, MDPI.

## 12. Separators

As one of the core components in batteries, separators ensure the electrical isolation between the cathode and the anode while facilitating ion transport. The most widely commercialized separators for LMBs and LIBs are polypropylene separator (PP) and polyethylene separator (PE). However, their low electrolyte wettability, narrow working temperature window, poor barrier properties, and nonconductivity characteristics limit their suitability for long-life SPAN-based batteries [434,435]. In this section, studies that feature the development of novel separators or modification strategies on separators for SPAN-based rechargeable batteries are discussed.

The properties of PP and PE separators can be enhanced by functional coatings. Several research groups have demonstrated significant improvements using this approach. Kim et al. employed a polydopamine-coated polyethylene separator to enable high-loading SPAN cathode [424]. In 2019, Zhang et al. developed a simple and effective method to enhance the interfacial stability of the lithium metal anode by coating a conventional PP separator with a composite layer containing nano-Si and PAA [436] (Figure 50a). Nano-Si and PAA reacted with lithium upon adding electrolytes, forming a highly ion-conductive protective layer containing robust Li-Si alloy and organic LiPAA on the lithium metal surface. The resulting Li||SPAN battery assembled with this coated PP separator exhibited better electrochemical performance than that of the uncoated one, delivering an initial capacity of over 1850 mAh g<sup>-1</sup> sulfur and retaining over 1150 mAh g<sup>-1</sup> sulfur of its capacity after 1000 cycles at 1 C.

Huang et al. developed a novel thermal-stable composite separator (M-Celgard-p) prepared by coating a layer of silicon dioxide-poly(propylene carbonate) based electrolyte on the commercial Celgard-p separator via simple dripping [437] (Figure 50b). The M-Celgard-p separator exhibited high flame retardancy, thermal stability, and minimal polysulfides shuttling. The Li||SPAN battery employing M-Celgard-p separator delivered a high specific capacity of 724.7 mAh g<sup>-1</sup> sulfur after 200 cycles at 1 A g<sup>-1</sup>. Zhang et al. presented a wet coating strategy to fabricate a functional PE separator to suppress lithium dendrite growth [438]. A protective SPAN layer was coated on the PE separator with PAA as a binder followed by lithiation via the direct contact with the lithium metal. The lithiated SPAN and LiPAA served as lithium-ion conductors and Li<sup>+</sup> flux regulator, promoting uniform lithium deposition. The resulting Li||SPAN battery with the SPAN-coated PE separator

and a high initial areal capacity ( $\sim 9 \text{ mAh cm}^{-2}$ ) maintained  $8.65 \text{ mAh cm}^{-2}$  after 50 cycles at  $0.1 \text{ C}$  (Figure 50c).

In 2023, Anbunathan et al. reported a novel separator, ZIF67@glass fiber (GF), fabricated by the in situ growth of ZIF-67 nanoparticles onto a high-density GF for high-performance Li || SPAN batteries [439] (Figure 50d). GF possessed excellent wettability and good electrolyte uptake, while ZIF67 provided open metal sites which effectively trapped anions and enabled fast  $\text{Li}^+$  transport. As a result, the Li || SPAN battery employing the ZIF67@GF separator delivered an initial capacity of  $821.6 \text{ mAh g}^{-1}$  and retained  $567.6 \text{ mAh g}^{-1}$  after 600 cycles at  $2 \text{ C}$ , corresponding to a capacity decay rate of  $0.05\%$  per cycle.

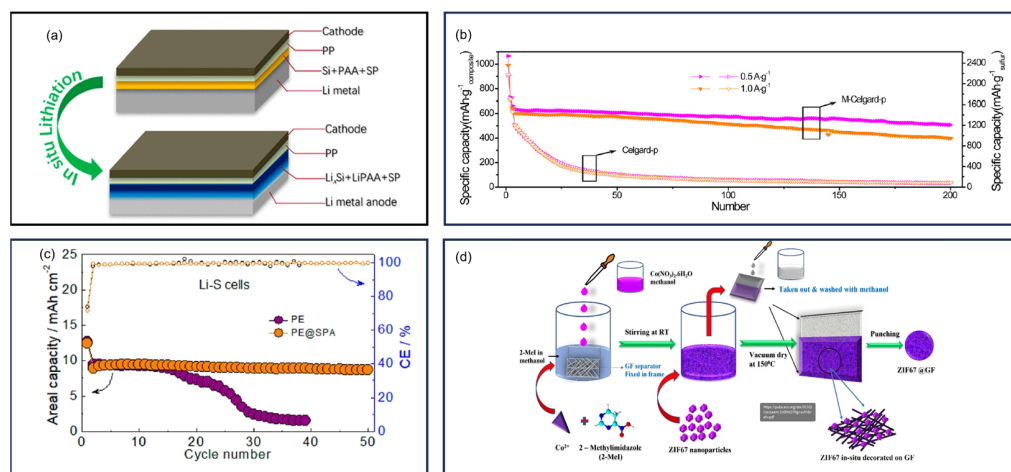


**Figure 50.** (a) Schematic illustration of the in situ lithiation process of the ion-conductive protective layer. Reproduced with permission [436]. Copyright © 2020, American Chemical Society; (b) Cycling performance of the Li || SPAN batteries with different separators. Reproduced with permission [437]. Copyright © 2020, John Wiley and Sons; (c) Cycling performance of the Li || SPAN batteries the conventional PE separator and the SPAN-coated PE separator. Reproduced with permission [438]. Copyright © 2022, American Chemical Society; (d) Schematic illustration of the preparation process of in situ growth of ZIF67 on GF separators. Reproduced with permission [439]. Copyright © 2023, American Chemical Society.

Beyond surface modifications, researchers have also developed new separator architectures. In 2015, Kim et al. developed a novel poreless urea-urethane (spandex) separator to address the polysulfide shuttling and the Li dendrite growth issues in Li || SPAN batteries [293]. The poreless spandex exhibited excellent wet adhesion on the Li metal surface and superior electrolyte uptake capability, therefore effectively blocking the polysulfide shuttling, facilitating  $\text{Li}^+$  diffusion, and suppressing Li dendrite growth. The Li || SPAN batteries with a high cathode areal loading of  $4 \text{ mAh cm}^{-2}$  exhibited superior cycling performance, with  $79.2\%$  capacity retention after 200 cycles and average CE in 2–200 cycles of  $99.8\%$  at  $1 \text{ mA cm}^{-2}$ .

### 13. Anodes

One of the major obstacles to the practical application of Li || SPAN batteries lies in the lithium anode. Unless pre-lithiating the SPAN cathode or harvesting Li from the electrolyte [282], a lithium-containing anode, typically a Li metal anode, must be employed to assemble the battery. However, the high reactivity of the Li metal with the electrolyte results in low CE. In addition, the formation and growth of Li dendrites on the Li metal surface lead to uneven plating/stripping behavior of Li and potential piercing of the separator [440]. To address these challenges, researchers have focused on improving

lithium anode stability. While strategies such as electrolyte engineering and separator modifications have been discussed in earlier sections, this section specifically examines anode engineering approaches for SPAN-based rechargeable batteries.

Applying coatings or interlayers onto the Li or Na metal anode is a simple method to fabricate artificial SEIs and improve the interfacial stability. In 2015, Kim et al. developed a multilayered graphene (MLG) coating on the Li metal anode for  $\text{Li} \parallel \text{SPAN}$  batteries [292]. The MLG physically isolated SEI layers from while applying pressure onto the Li surface, effectively suppressing the Li dendrite growth (Figure 51a). As a result, the  $\text{Li} \parallel \text{SPAN}$  battery delivered high areal capacity of  $4.0 \text{ mAh cm}^{-2}$  and retained 81.0% of capacity after 200 cycles at  $1 \text{ mA cm}^{-2}$ . Shuai et al. reported a facile synthesis of an artificial hybrid SEI on the lithium metal anode [441]. By immersing the pristine lithium foil into a concentrated  $\text{SnCl}_2/\text{THF}$  solution, a multiphasic layer composed of  $\text{Li}_x\text{Sn}_y$  and  $\text{LiCl}$  was fabricated, which not only suppressed the lithium dendrite growth but also provided fast interfacial transport channels. The modified  $\text{Li} \parallel \text{SPAN}$  battery delivered a reversible capacity of  $450 \text{ mAh g}^{-1}$  SPAN at  $10 \text{ A g}^{-1}$ . With an areal capacity of  $4 \text{ mAh cm}^{-2}$  and limited electrolyte ( $7 \mu\text{L mg}^{-1}$  SPAN), a discharge capacity above  $640 \text{ mAh g}^{-1}$  SPAN and 80% after 100 cycles at  $0.1 \text{ A g}^{-1}$  was achieved.

In 2018, Guo et al. developed a versatile interlayer composed of  $\text{AlF}_3$  embedded in CNF to address the dendrite growth issue with the Li metal anode [442].  $\text{AlF}_3$  reduced Li nucleation overpotential and the CNF provided high Young's moduli up to 47 GPa. The  $\text{Li} \parallel \text{SPAN}$  battery with this interlayer delivered excellent cycling performance with almost no decay for 500 cycles at 1 C. Li et al. designed a hybrid functional interphase for the lithium metal anode to improve the low-temperature electrochemical reaction kinetics of LMBs [443] (Figure 51b). The hybrid polymer-alloy-fluoride (PAF) interphase was prepared by dropping  $\text{AgBF}_4$ -DOL solution on the Li metal surface. The PAF layer, comprising polymerized DOL (PDOL),  $\text{LiF}$ , and Li-Ag alloy, exhibited high Li absorbing ability to facilitate  $\text{Li}^+$  desolvation and acted as a fast ionic conductor for  $\text{Li}^+$  transport. In addition, the Li-Ag alloy nanoparticles provided numerous transportation pathways and afforded minor phase transformation during repeated Li plating/stripping.  $\text{LiF}$  exhibited low Li diffusion barriers and high interfacial energy which was beneficial for promoting interfacial  $\text{Li}^+$  transport and suppressing Li dendrite formation. Consequently, at  $-20^\circ\text{C}$ , the PAF- $\text{Li} \parallel \text{SPAN}$  battery delivered an areal capacity of  $2.37 \text{ mAh cm}^{-2}$  after 150 cycles at  $100 \text{ mA g}^{-1}$ , corresponding to a capacity retention of 74.7%. Furthermore, at  $-40^\circ\text{C}$ , the PAF- $\text{Li} \parallel \text{SPAN}$  battery retained 82.1% capacity after 50 cycles at  $50 \text{ mA g}^{-1}$ .

For sodium batteries, Wei et al. developed in situ electro-polymerized ionic liquid membranes to stabilize deposition and block parasitic reactions [444]. The resulting  $\text{Na} \parallel \text{SPAN}$  battery achieved almost 100% Coulombic efficiency and maintained a reversible capacity of above  $400 \text{ mAh g}^{-1}$  over 175 cycles at 0.2 C. Tian et al. developed a heterogeneous Na-based alloys (GaInSn) interfacial protective layer on the Na foil (HAIP Na) constructed via the in situ self-diffusion of liquid metal to improve the interfacial behavior of Na metal anode [445] (Figure 51c). The interfacial Na-based alloys layer facilitated the formation of a  $\text{NaF}$ -rich SEI, enabling uniform  $\text{Na}^+$  flux and dendrite growth suppression. The HAIP  $\text{Na} \parallel \text{SPAN}$  battery delivered a reversible capacity of  $912.2 \text{ mAh g}^{-1}$  sulfur after 1000 cycles at 3 C, corresponding to a capacity retention of 87.4%.

Li alloy anodes in  $\text{Li} \parallel \text{SPAN}$  batteries have attracted significant interests due to their excellent properties, including fast charge-discharge kinetics, ease of processing, and the ability to regulate Li deposition behavior [440]. In 2018, Zhang et al. reported Li-Si alloy anode supported by a free-standing CNF matrix for  $\text{Li} \parallel \text{SPAN}$  batteries [446]. The alloy anode was fabricated by simple pressing and heat treatment of stable lithium metal powder (SLMP), silicon powder, and CNF (Figure 52a). Unlike conventional lithium metal

anode, this design exhibited no pulverization or no dendrite formation during cycling. The resulting Li-Si || SPAN battery demonstrated excellent cycling performance, with a negligible capacity decay rate of 0.03% per cycle over 3000 cycles at 3 C.

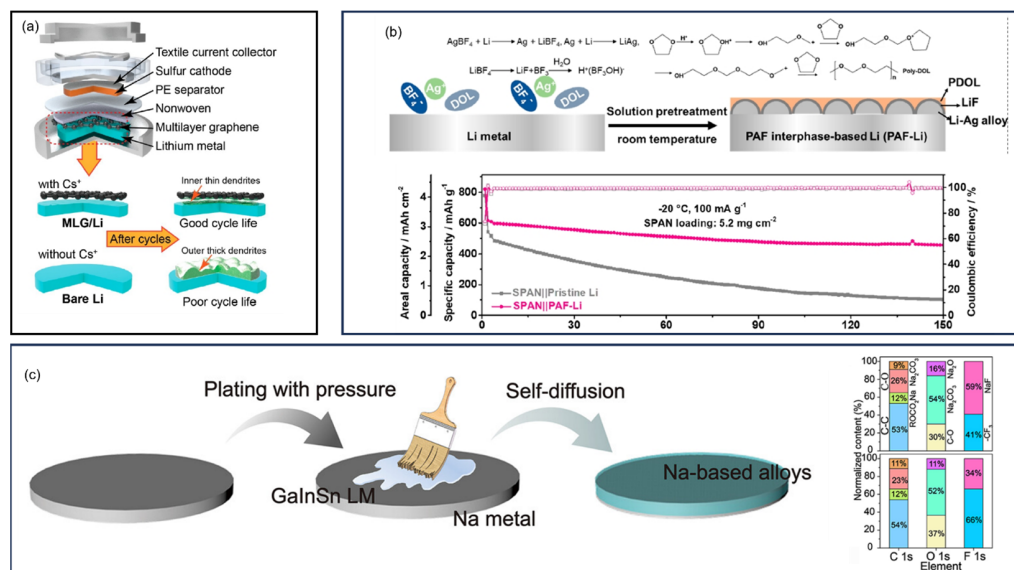


**Figure 51.** (a) Schematic illustration of the cell configuration containing MLG and different Li dendrite growth with or without Cs<sup>+</sup> and MLG. Reproduced with permission [292]. Copyright © 2015, American Chemical Society; (b) **top:** Schematic illustration of the preparation of PAF–Li electrode; **bottom:** Cycling performance of the SPAN batteries with pristine Li or PAF–Li anode. Reproduced with permission [443]. Copyright © 2023, American Chemical Society; (c) Schematic illustration of the fabrication of HAIP Na alloy and the relative percentage of different species in the SEI of Na (**below**) and HAIP Na (**above**) after cycling for 10 cycles. Reproduced with permission [445]. Copyright © 2024, John Wiley and Sons.

A Li-Al alloy anode was employed to suppress the dendrite growth for Li || SPAN batteries by Sun et al. in 2018 [447]. The Li-Al alloy was prepared electrochemically in a half-cell configuration. The Li-Al || SPAN battery with a voltage of 1.5 V delivered a reversible capacity of 550 mAh g<sup>-1</sup>SPAN and retained 83% capacity after 200 cycles at 200 mAh g<sup>-1</sup>. Further advancing this approach, Zhang et al. designed a three-dimensional highly stable Li metal composite anode (LAN) comprising Li-Al, Li<sub>3</sub>N, AlN, and CNT [448] (Figure 52b). The LAN anode was prepared by heating AlN, lithium metal powder, and CNT at 150 °C, while Li<sub>3</sub>N and Li-Al alloy form on the lithium metal surface. Li<sub>3</sub>N facilitated high Li<sup>+</sup> conductivity and LiAl provided abundant lithiophilic sites, leading to a dendrite-free lithium deposition in the anode. In addition, the 3D composite structure could accommodate the volume change in the anode during cycling. As a result, the LAN || SPAN battery with a cathode areal capacity of 4 mAh cm<sup>-2</sup> achieved the capacity retention of 97.4% after 200 cycles at 0.2 C.

In 2020, Chen et al. engineered a 3D Li alloy anode (PS-Li-AuLi<sub>3</sub>@CF) by the infusion of molten lithium into carbon fiber (CF) modified with nanoporous gold [449] (Figure 52c). The as-designed PS-Li-AuLi<sub>3</sub>@CF electrode accommodated huge volume change during lithium plating/stripping process and provided a highly lithiophilic AuLi<sub>3</sub>@CF interface to guide uniform lithium nucleation and suppress lithium dendrite growth. The PS-Li-AuLi<sub>3</sub>@CF || SPAN battery delivered a capacity retention of 70.6% with a CE of 99.8% after 1000 cycles at 2 C.

A protective Li-Sb/Li<sub>3</sub>N double-layer coating for lithium metal was developed by Wang et al. to address the low CE and dendrite growth issues with lithium anode [450].

The Li-Sb layer optimized the electric field distribution and reduced the  $\text{Li}^+$  nucleation overpotential, while the  $\text{Li}_3\text{N}$  layer enabled high  $\text{Li}^+$  conductivity and fast  $\text{Li}^+$  transport. The combined mechanical strength of both layers minimized volume changes during cycling. As a result, the  $\text{Li} \parallel \text{SPAN}$  battery delivered a prolonger lifespan over 1000 cycles at 3 C.

In 2024, Wang et al. reported a synergistic strategy of utilizing a Li-Na alloy and FEC for the in situ construction of a  $\text{LiF}/\text{NaF}$ -rich SEI [451]. During cycling,  $\text{Na}^+$  preferentially deposited on the surface of active Li crystals, forcing  $\text{Li}^+$  to deposit in the inactive regions around Na, thus inhibiting the growth of Li dendrites (Figure 52d). In addition, FEC facilitated the formation of a  $\text{LiF}/\text{NaF}$ -rich SEI on the Li-Na alloy surface. The resulting  $\text{Li-Na} \parallel \text{SPAN}$  battery delivered an initial capacity of  $630 \text{ mAh g}^{-1}$  and retained 84% of the capacity after 150 cycles at  $1 \text{ A g}^{-1}$ .

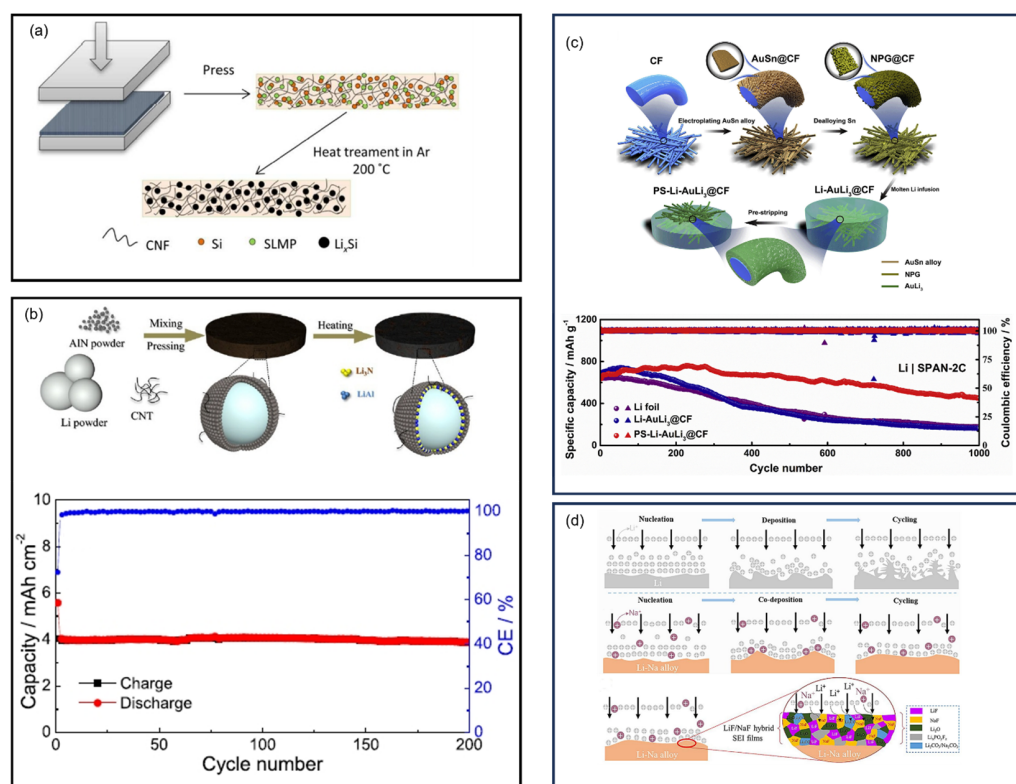


**Figure 52.** (a) Schematic illustration of the preparation process of carbon supported  $\text{Li-Si}$  alloy electrodes. Reproduced with permission [446]. Copyright © 2018, Royal Society of Chemistry; (b) top: Schematic illustration of the fabrication process of the LAN electrode; bottom: Cycling performance of the  $\text{LAN} \parallel \text{SPAN}$  battery. Reproduced with permission [448]. Copyright © 2020, American Chemical Society; (c) top: Schematic illustration of the fabrication process of the  $\text{PS-Li-AuLi}_3@\text{CF}$  electrode; bottom: Cycling performance of SPAN batteries with different anodes. Reproduced with permission [449]. Copyright © 2020, Elsevier; (d) Schematic illustration of the proposed co-deposition mechanism of  $\text{Li-Na}$  alloy anodes and the formation of the SEI. Reproduced with permission [451]. Copyright © 2024, Elsevier.

Among all types of Li alloys explored as alternatives to Li metal anodes, Li-Sn alloys have received significant attention due to their stable electrode structure. In 2023, Duan et al. investigated the electrochemical Li plating/stripping behavior of pristine Li metal electrode and Li/Li-Sn alloy electrode in Ah-level laminated pouch cells, focusing on their fast lithium transport capability across different electrode regions [452]. Porous and dendritic Li deposition with loose structures was observed in pristine Li metal electrode after cycling, where the near-tap and the central regions with close connection with the

current collector showed more severe corrosion than the edge region due to the locally amplified current density. In sharp contrast, uniform Li deposits with a dense structure were observed across different regions of Li/Li-Sn alloy composite anode, along with suppressed parasitic reactions and gas evolution. As a demonstration, a 1.2 Ah Li/Li-Sn || SPAN pouch cell with a cathode areal capacity of  $3.4 \text{ mAh cm}^{-2}$  was assembled, achieving a capacity retention of 87% after 100 cycles at 600 mA, far outperforming the Li || SPAN pouch cells which lost all capacity after 40 cycles (Figure 53a). Du et al. developed a novel composite lithium anode, p-20Li/Li<sub>13</sub>Sn<sub>5</sub>, by incorporating metallic lithium and tin powder via a “roll and fold” technique [453] (Figure 53b). The lithiophilic Li<sub>13</sub>Sn<sub>5</sub> phase was uniformly distributed within the lithium matrix and served as the active site for regulating lithium plating/stripping. When paired with a SPAN cathode (areal capacity:  $5.6 \text{ mAh cm}^{-2}$ ), the p-20Li/Li<sub>13</sub>Sn<sub>5</sub> || SPAN battery exhibited a capacity retention of 91.5% after 150 cycles at  $0.5 \text{ mA cm}^{-2}$ .

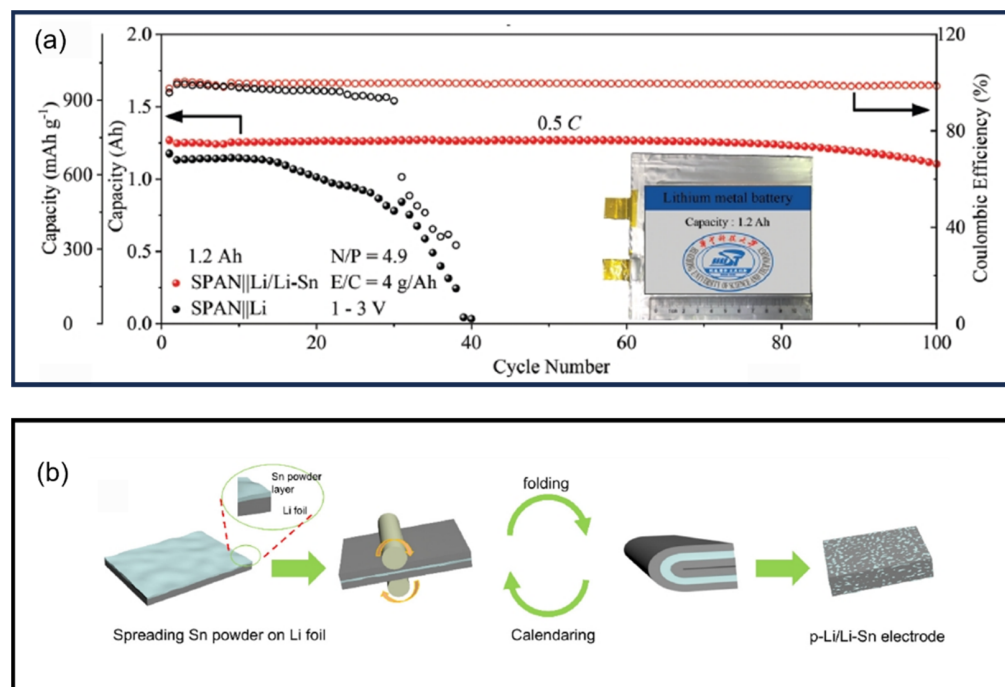


**Figure 53.** (a) Cycling performance of 1.2 Ah Li || SPAN and Li/Li-Sn || SPAN pouch cells. Reproduced with permission [452]. Copyright © 2022, John Wiley and Sons; (b) Schematic illustration of the fabrication process of the p-xLi/Li<sub>13</sub>Sn<sub>5</sub> composite electrode. Reproduced with permission [453]. Copyright © 2025, Royal Society of Chemistry.

The employment of a host material is an effective strategy to mitigate the detrimental performance of the metal anodes. Among these host materials, carbon-based structures have been widely employed. In 2007, Sun et al. reported the use of hard carbon/lithium composite prepared via the direct contact as anode in lithium batteries to reduce the initial irreversible capacity loss of hard carbon [454]. In their study, a SPAN cathode was paired with the hard carbon/lithium composite anode and exhibited good discharge capacity and cyclability. Similarly, Uzakbaiuly et al.’s reported lithiated graphite anode for SPAN batteries, which delivered a discharge capacity of above  $1100 \text{ mAh g}^{-1}$  sulfur after 150 cycles at 0.2 C [455]. Wang et al. also developed a lithiated graphite anode prepared via a novel co-assembly strategy where an ultrathin lithium was assembled on top of the Gr or Si/C anode [456] (Figure 54a). The newly conceptualized configuration effectively prevented over-lithiation and ensured excellent stability. As a result, the pre-lithiated Gr || SPAN and pre-lithiated SiC || SPAN cells exhibited stable cycling, with capacity retention of 97.0% and

69.0% compared to their 100th-cycle capacity after 1800 cycles at 2 C, respectively. In 2023, Mao et al. developed an ultra-thin reduced graphene oxide/Li metal (rGO/Li) composite foil as the anode for high-performance Li || SPAN batteries [457]. The three-dimensional network of the rGO/Li composite facilitated reversible Li plating/stripping behavior. As a result, the rGO/Li || SPAN battery delivered an initial discharge capacity of  $\sim 740 \text{ mAh g}^{-1}$  and retained  $\sim 675 \text{ mAh g}^{-1}$  after 220 cycles at 0.2 C.

Dai et al. investigated the functions of polyacrylonitrile (PAN) on both the sulfur cathode and the lithium anode in Li || SPAN batteries in 2020 [458]. For the cathode, PAN was sulfurized to produce SPAN and integrated into a conductive 3D CNTs-wrapped carbon foam to prepare a self-supporting cathode exhibiting improved ionic and electronic conductivity and mitigated volume expansion. For the lithium metal anode, PAN was carbonized into microporous N-doped cross-linked carbon nanofiber as a lithophilic host to regulate lithium plating and suppress lithium dendrite growth. The as-assembled Li || SPAN battery realized an initial discharge capacity of  $1007 \text{ mAh g}^{-1}$  sulfur and a remarkable cycling performance with  $765 \text{ mAh g}^{-1}$  sulfur after 300 cycles at 0.5 C.

Yu et al. proposed a carbon particle infused lithium metal composite (C-Li) which was able to intercept pit propagation during lithium stripping [459] (Figure 54b). This mechanism was corroborated by a continuum electrochemical model. The pulverization rate of C-Li is 26 times slower than that of commercial lithium, enabling the C-Li || SPAN battery with a cathode areal loading of  $8 \text{ mAh cm}^{-2}$  and mildly lean electrolyte condition ( $5 \text{ g Ah}^{-1}$ ) to sustain stable cycling over an extended lifespan of 277 cycles (77 cycles with commercial Li) at 0.2 C.

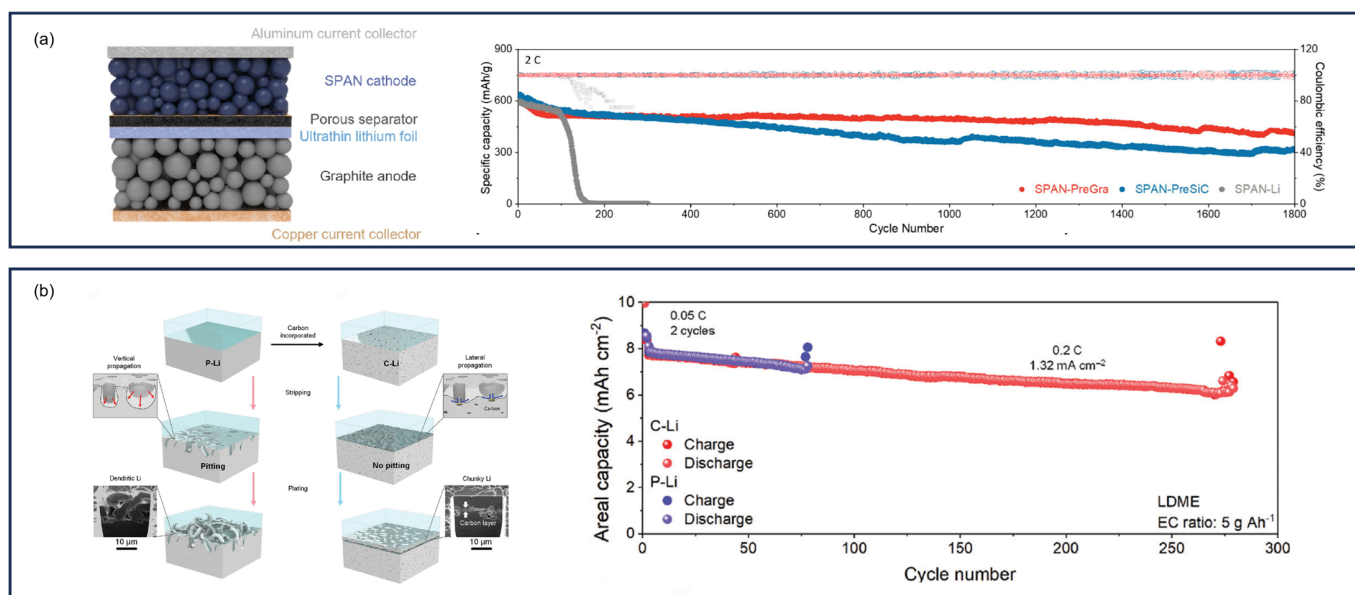


**Figure 54.** (a) Schematic illustration of Gr/Sic || SPAN batteries with ultrathin lithium co-assembly and cycling performance of SPAN batteries with Li or pre-lithiated anodes. Reproduced with permission [456]. Copyright © 2025, American Chemical Society; (b) left: Schematic illustration of the Li stripping/plating behavior of a commercial Li foil (P-Li) and carbon incorporated Li foil (C-Li); right: Cycling performance of SPAN batteries with C-Li and P-Li anodes. Reproduced with permission [459]. Copyright © 2023, John Wiley and Sons.

Beyond lithium anode, Shao et al. designed a flexible and freestanding hollow carbon film (AHCF) as a host for Na-K liquid alloy (Na-K@AHCF) in 2023 [460]. The Na-K@AHCF composite could accommodate the volume expansion of the metal anode during cycling. When paired with a SPAN cathode, the Na-K || SPAN battery exhibited stable cycling over 80 cycles at  $0.5 \text{ A g}^{-1}$ . For potassium batteries, Tang et al. designed a freestanding titanium-

deficient nitrogen-containing MXene/CNT scaffold (DN-MXene/CNT) as the matrix for dendrite-free potassium metal anodes [461]. The porous scaffold enabled high loading of potassium and preserved structure integrity during  $K^+$  plating/stripping. In addition, DN-MXene/CNT scaffold possessed high potassium-philic characteristic and acted as “seed points” to initiate the K nucleation during cycling, effectively inhibiting potassium dendrite growth. When applied to  $K \parallel SPAN$  batteries, the as-assembled battery delivered a reversible discharge capacity of  $331 \text{ mAh g}^{-1}$  sulfur and retained  $230 \text{ mAh g}^{-1}$  sulfur after 500 cycles at 0.5 C.

Silicon-based materials represent another promising class of host materials for Li compounding. In 2017, Shi et al. developed a lithium-ion battery with SPAN cathode and pre-lithiated  $\text{SiO}_x/\text{C}$  anode [462]. The use of pre-lithiated  $\text{SiO}_x/\text{C}$  anode, which was lithiated by the direct contact method, helped avoiding the intrinsic safety issues associated with the lithium metal. Further advancements were made by Huang et al., who developed a high-capacity and cycle-stable  $\text{SiO}_x/\text{C}$  composite anode synthesized from rice husk via an ecofriendly and one-step pyrolysis process [463]. The  $\text{SiO}_x/\text{C}$  composite anode was pre-lithiated electrochemically in a half-cell setup. The resulting pre-lithiated  $\text{SiO}_x/\text{C} \parallel SPAN$  battery delivered an initial discharge capacity of above  $1500 \text{ mAh g}^{-1}$  sulfur and retained over  $700 \text{ mAh g}^{-1}$  sulfur of its capacity after 1000 cycles at  $1600 \text{ mA g}^{-1}$ . In 2019, Zhang et al. introduced a facile lithiation strategy for Si/C anodes by placing the Si/C anode film between the lithium metal foil and the separator during cell assembly [464]. The lithiated Si/C-SPAN cells achieved a capacity retention rate of 88% (compared to the second cycle) after 800 cycles at 1 C. Shuai et al. later developed an air-stable pre-lithiation strategy for silicon/graphite anodes, wherein the lithium foil was sandwiched between two silicon/graphite electrodes with sealed edges to yield the silicon/graphite-lithium-silicon/graphite anode (SLSG) [465]. A SLSG  $\parallel SPAN$  battery with high cathode areal loading ( $8 \text{ mAh cm}^{-2}$ ) was assembled, delivering a specific capacity of  $489 \text{ mAh g}^{-1}$  SPAN and maintaining over  $350 \text{ mAh g}^{-1}$  SPAN after 100 cycles at 0.1 C.

Except for C-Li and Si-Li compounds, several other materials have been developed to compound with Li to improve the interfacial stability of Li metal anodes. In 2021, Ye et al. designed an antipulverizing and high-continuity lithium anode with superior interfacial stability by premixing solid-state electrolyte ( $\text{Li}_6\text{PS}_5\text{Cl}$ ) with molten lithium followed by coating onto a treated copper current collector and calendaring [466] (Figure 55a).  $\text{Li}_6\text{PS}_5\text{Cl}$  facilitated the Li nucleation and contributed to form a micro-sized and dendrite-free electrode during cycling. Simultaneously, the embedded Cu current collector reinforced the mechanical strength and improved charge transfer efficiency, affording good structural integrity and electrical continuity. As a result, the  $\text{Li}_6\text{PS}_5\text{Cl}-\text{Li}@\text{Cu} \parallel SPAN$  battery employing this anode delivered a reversible capacity of  $1452.1 \text{ mAh g}^{-1}$  sulfur after 200 cycles at 0.5 C.

COFs have also emerged as promising compound materials for Li. In 2021, Wei et al. reported a stable and dendrite-free lithium anode fabricated by electrochemically depositing Li on a flexible and freestanding MXene/COF-LZU1 framework (MCFLi) [467]. The lithophilic COF-LZU1 microspheres distributed among the MXene framework as the nucleation seeds promoted uniform Li nucleation by homogenizing the  $\text{Li}^+$  flux and lowering nucleation energy barrier. And the MCFLi  $\parallel SPAN$  battery achieved a discharge capacity of  $850.7 \text{ mAh g}^{-1}$  sulfur after 300 cycles at 1 C, corresponding to a capacity retention of 73.8%.

Liu et al. demonstrated that the Li-ion flux in the electrolyte and current density on the electrode surface were closely related to the dispersity of lithophilic sites based on nonlinear phase-field simulations [468]. ZnO with homogeneously distributed nanodots as

lithiophilic sites achieved uniform Li nucleation and deposition. The lithiated  $ZnO \parallel SPAN$  battery exhibited a reversible discharge capacity of  $1120 \text{ mAh g}^{-1}$  for 800 cycles at 1 C.

In 2022, Li et al. reported nitrogen and zinc co-doped porous carbon nanofibers (MSCNFs) synthesized from MOF crystal (nanoMET-6) and PAN as potassium metal hosts for  $K \parallel SPAN$  batteries [213] (Figure 55b). MSCNFs exhibited high potassiphilicity, abundant pore space to accommodate K metal, and effective induction of a homogeneous electric field, enabling high K loading and smooth plating. The MSCNF-K anode was obtained by thermally infusing K into the MSCNFs and paired a  $Se_{0.05}S_{0.95}\text{PAN}$  cathode to assemble  $K \parallel SPAN$  batteries. The resulting room temperature MSCNF-K ||  $Se_{0.05}S_{0.95}\text{PAN}$  battery delivered a discharge capacity of  $470 \text{ mAh g}^{-1}$  after 600 cycles at  $500 \text{ mA g}^{-1}$ , corresponding to a capacity retention of 60%.

Trück et al. reported a battery system with  $Mg^{2+}$ -doped  $\text{Li}_4\text{Ti}_5\text{O}_{12}$  (LTO) as the anode and SPAN as the cathode [469].  $Mg^{2+}$  was electrochemically inserted into the LTO prior to assembly. The Mg-doped LTO || SPAN battery exhibited a reversible capacity of  $800 \text{ mAh g}^{-1}$  sulfur at 0.3 C and high-rate capability.

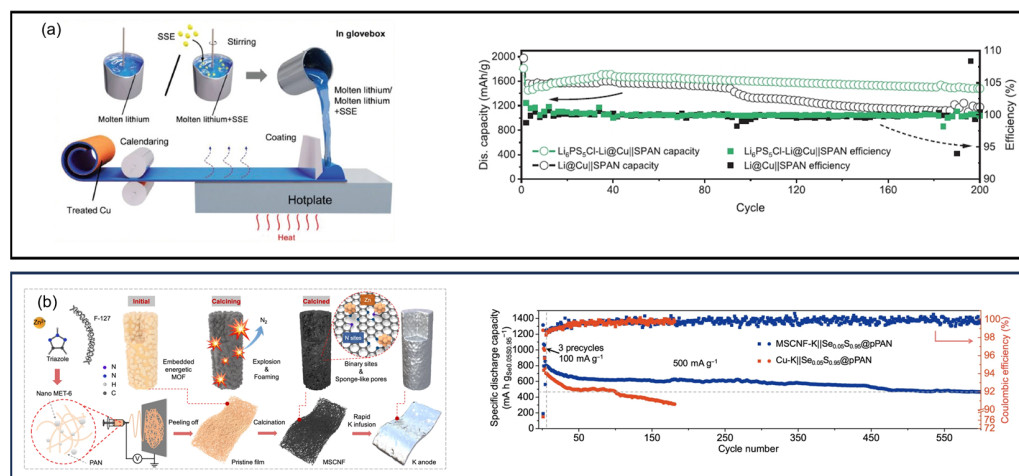


**Figure 55.** (a) left: Schematic illustration of the preparation of the  $\text{Li}_6\text{PS}_5\text{Cl}-\text{Li}@\text{Cu}$  electrode; right: Cycling performance of SPAN batteries with Li and  $\text{Li}_6\text{PS}_5\text{Cl}-\text{Li}@\text{Cu}$  anodes. Reproduced with permission [466]. Copyright © 2021, John Wiley and Sons; (b) left: Schematic illustration of the synthetic route of MSCNFs and the corresponding K composite anode; right: Cycling performance of  $Se_{0.05}S_{0.95}\text{PAN}$  batteries with MSCNF-K and Cu-K anodes. Reproduced with permission [213]. Copyright © 2022, Springer Nature.

#### 14. SPAN as a Cathode Additive

In addition to its role as an active cathode material, SPAN has also been explored as a cathode additive material to enhance the performance of the battery. In 2021, Liu et al. incorporated lithiated SPAN ( $\text{Li}_2\text{SPAN}$ ) as an additional lithium donor into the LFP electrode to obtain a  $\text{LFP}/\text{Li}_2\text{S-PAN}$  composite cathode [245] (Figure 56). When paired with a silicon/graphite/carbon (Si/Gr/C) composite anode, the Si/Gr/C || LFP/ $\text{Li}_2\text{S-PAN}$  full cell delivered a reversible capacity of 123 and  $107 \text{ mAh g}^{-1}$  in the 1st and 10th cycle, which was 15.5% and 24.5% higher than the pristine Si/G/C || LFP full cell, respectively.

In 2023, Takemoto et al. introduced dual additives, SPAN and lithium titanium oxide (LTO), to the sulfur cathode in LSBs [470]. SPAN absorbed polysulfides to inhibit shuttling problem, while LTO provided a fast ion and charge transfer in the cathode. As a result, the  $\text{Li} \parallel \text{S/C}$  battery with the two additives in the cathode delivered a capacity decay rate of 0.776% per cycle over 70 cycles at 0.2 C.

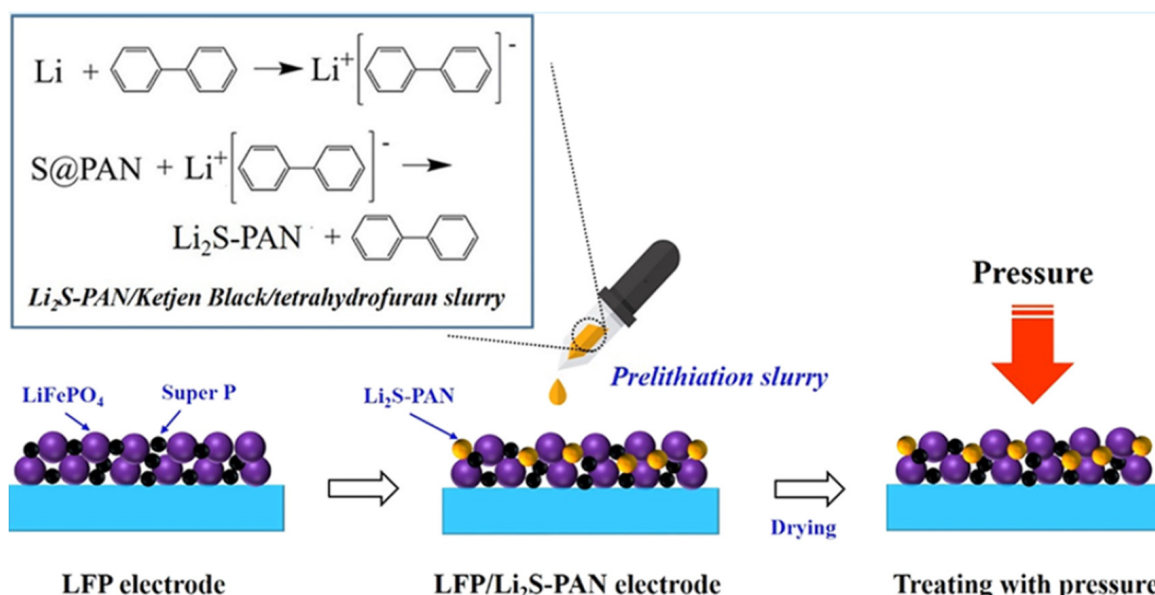


**Figure 56.** Schematic illustration of the fabrication of the LFP/Li<sub>2</sub>S–PAN electrode. Reproduced with permission [245]. Copyright © 2021, American Chemical Society.

## 15. SPAN as Anode

While SPAN has been demonstrated by numerous works as an excellent cathode material for its high capacity, stable cycling, and compatibility with various electrolytes. Researchers started to explore the application of SPAN as an anode material when paired with transition metal-based cathodes.

In 2019, Berhe et al. demonstrated the use of SPAN as the anode and commercial lithium manganese oxide (LMO) LiMn<sub>2</sub>O<sub>4</sub> as the cathode [471] (Figure 57a). The SPAN || LMO cell exhibited 1378 mAh g<sup>-1</sup><sub>sulfur</sub> at 0.1 C and retained 90.8% of its initial capacity after 150 cycles. To further improve cycling stability, the same group later introduced a functional coating composed of PVDF and Li<sub>5.6</sub>Ga<sub>0.26</sub>La<sub>2.9</sub>Zr<sub>1.87</sub>Nb<sub>0.05</sub>O<sub>12</sub> type garnet (PVDF@LGLZNO) on the LMO cathode, serving as an artificial cathode-electrolyte interphase (CEI) [472]. The coated LMO cathode was coupled with a SPAN anode and delivered a capacity retention of 77% after 1000 cycles at 1 C, corresponding to a capacity decay of 0.023% per cycle.

SPAN has also been investigated as an anode in combination with high-voltage LiNi<sub>0.5</sub>Mn<sub>1.5</sub>O<sub>4</sub> (LNMO) cathodes. SPAN || LNMO batteries with SPAN as the anode and LNMO were reported by Yamano et al. [473] and Berhe et al. [474]. In Berhe et al.'s study, 1 M LiPF<sub>6</sub> in FEC/EMC/TTE (3/2/5, E2) was used as the electrolyte (Figure 57b). The fluorine-containing electrolytes facilitated the formation of stable LiF rich CEI and SEI on the cathode and anode surface, respectively. Moreover, the electrolytes showed excellent oxidation resistance, enabling the cell cycling at high voltages. As a result, the SPAN || LNMO battery delivered an initial discharge capacity of 1094 mAh g<sup>-1</sup><sub>SPAN</sub> and retained 73% of its capacity after 100 cycles at 0.4 C.

Wu et al. explored using SPAN as an anode to match with lithium nickel manganese cobalt (NCM) cathode under high voltage conditions [475] (Figure 58a). The SPAN anode demonstrated high capacity and mitigated safety concerns of lithium deposition on the graphite anode due to its high lithiation potential property. The resulting SPAN || NCM-H battery exhibited a good stability with an elevated capacity retention of 89.7% after 100 cycles at 0.5 C and a high voltage of 3.5 V. Jiang et al. used the over-lithiated SPAN as

the anode paired with LFP or NCM622 cathodes to assemble batteries, achieving excellent cycling performance [37].

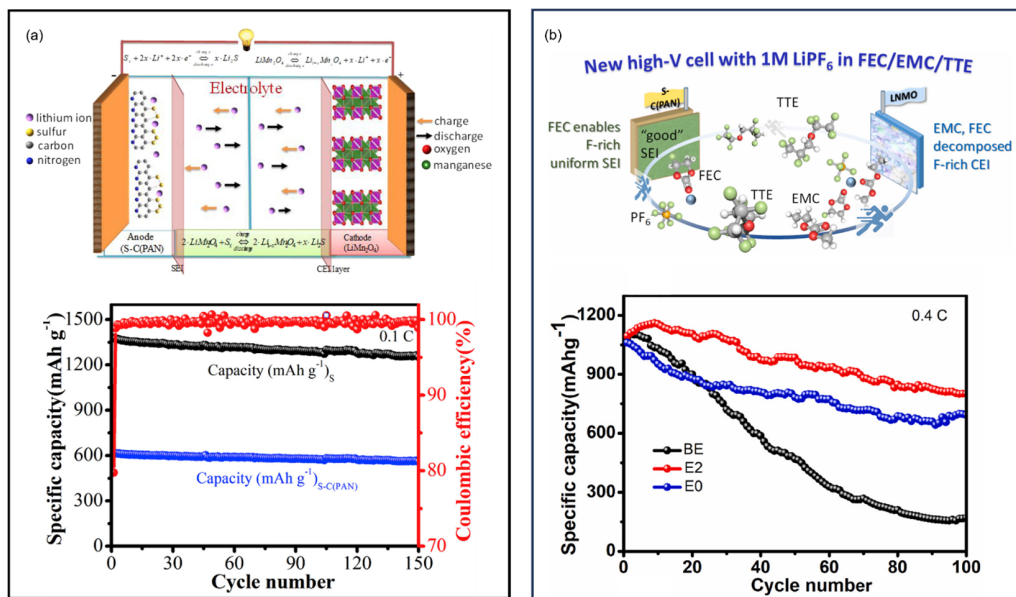


**Figure 57.** (a) Schematic illustration of the charging–discharging process in a SPAN || LMO cell and its cycling performance. Reproduced with permission [471]. Copyright © 2019, Elsevier; (b) Schematic illustration of the SPAN || LNMO cell and its cycling performances in different electrolytes. Reproduced with permission [474]. Copyright © 2023, Elsevier.

In 2019, Shuai et al. developed a SPAN-graphite dual-ion battery, where SPAN served as the anode and graphite was used as cathode with 4 M LiPF<sub>6</sub> in EMC as the electrolyte [476]. During charging, PF<sub>6</sub><sup>-</sup> intercalated into the graphite cathode while Li<sup>+</sup> inserted into the SPAN anode. During discharge, both ions were released. This SPAN-graphite dual-ion battery delivered a specific capacity of 750 mAh g<sup>-1</sup> sulfur over a voltage plateau of about 2 V and retained 93% of its capacity after 50 cycles at 100 mA g<sup>-1</sup>.

Luo et al. developed SPAN/MoS<sub>2</sub> composite materials featuring defective MoS<sub>2</sub> nanocrystals and sulfur nanodots embedded in SPAN fibers via electrospinning [477]. The unique architecture provided multi-entry and short-range channels for Na<sup>+</sup> to enable fast kinetics. In addition, sulfur defects within MoS<sub>2</sub> anchored soluble discharge products by strong interactions. Consequently, the SPAN/MoS<sub>2</sub> electrode exhibited stable cycling (8000 cycles at 5 A g<sup>-1</sup> and 15,000 cycles at 10 A g<sup>-1</sup>) and excellent rate performance (212 mAh g<sup>-1</sup> composite at 25 A g<sup>-1</sup>). In a full-cell configuration with a Na<sub>3</sub>V<sub>2</sub>(PO<sub>4</sub>)<sub>3</sub> cathode, SPAN || MoS<sub>2</sub>-Na<sub>3</sub>V<sub>2</sub>(PO<sub>4</sub>)<sub>3</sub> cell maintained a high capacity of 328 mAh g<sup>-1</sup> composite after 50 cycles at 0.5 A g<sup>-1</sup>.

A potassium-ion battery with K<sub>2</sub>MnFe(CN)<sub>6</sub> as the cathode and SPAN as the anode was reported by Deng et al. in 2021 [478] (Figure 58b). The cell delivered a reversible capacity of 108 mAh g<sup>-1</sup> K<sub>2</sub>MnFe(CN)<sub>6</sub> with a high capacity retention of 95.4% after 1200 cycles at 1 C, highlighting SPAN's versatility beyond lithium-ion systems.

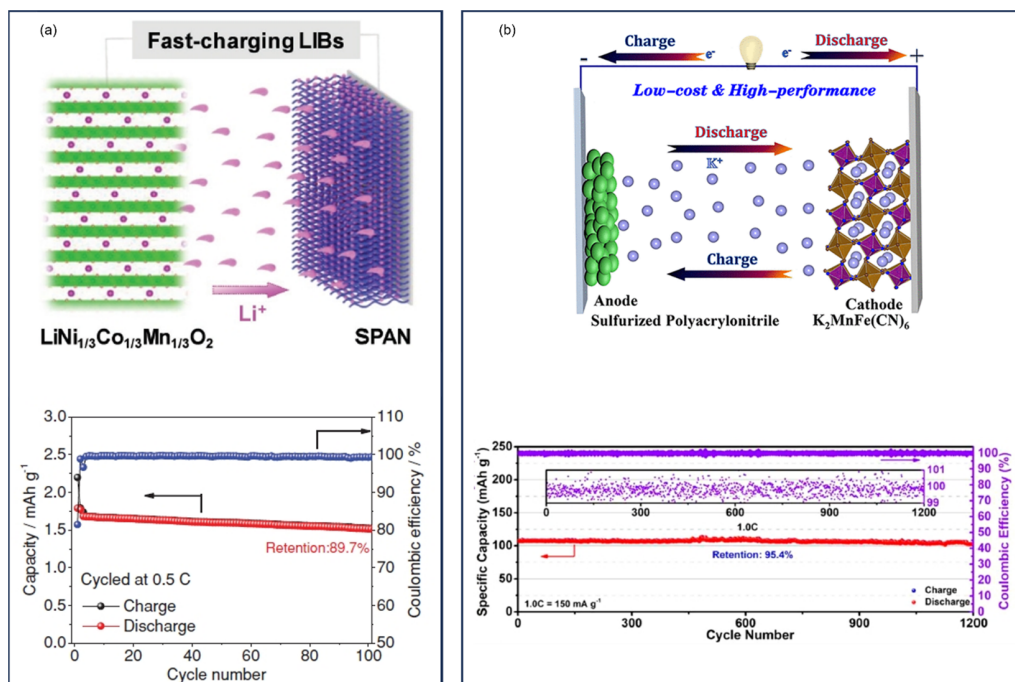


**Figure 58.** (a) Schematic illustration of the SPAN || NCM–H battery and its cycling performance. Reproduced with permission [475]. Copyright © 2019, John Wiley and Sons; (b) Schematic illustration of the SPAN || K<sub>2</sub>MnFe(CN)<sub>6</sub> cell and its cycling performance. Reproduced with permission [478]. Copyright © 2021, American Chemical Society.

## 16. High-Energy Li || SPAN Batteries

Significant efforts have been devoted to enhancing the energy density and cycle life of Li || SPAN batteries through innovations in cathode and anode engineering, electrolyte formulation, binder selection, separator design, and current collector optimization. A comprehensive perspective article by Pham et al. thoroughly discusses the critical challenges and strategies for achieving high-energy, long-life Li || SPAN batteries at both the material and cell levels [3].

Kakiage et al. presented ADEKA's Lithium–Sulfur/Pouch Cell (ALIS-PC), a Li || SPAN pouch cell which achieves record-breaking gravimetric energy densities (713 and 761 Wh kg<sup>-1</sup> cell at 0.1 and 0.05 C rates), the highest reported values for Li || SPAN cells to date [479] (Figure 59). Ten innovative and effective technologies are employed to enable this ultra-lightweight and high-energy ALIS-PS.

1. A lightweight 3D-Al foam sheet, Al-CELMET, was chosen as the current collector for the SPAN cathode. A high areal loading up to 32.4 mg s cm<sup>-2</sup> (68.0 mg<sub>SPAN</sub> cm<sup>-2</sup>) on both sides could be achieved, corresponding to an areal capacity up to 46.6 mAh cm<sup>-2</sup>.
2. The 3D-Al foam was laser-drilled with homogeneous hole of  $\varphi = 1.0$  mm to save the weight by 31%.
3. SWCNT and CNF were used as the conducting agent and the binder to achieve higher SPAN weight ratio in the cathode due to their superior electrical conductivity with high surface area and mechanical strength. A cathode fabricated using these materials achieved up to 98.0 wt% SPAN.
4. SWCNT was dispersed in water using a soft dispersing method, Nihon Spindle Manufacturing's JET PASTER technique. The SPAN cathode fabricated via this method exhibited a low ohmic resistance (Rohm).
5. A unique shape design of the SPAN composite was employed. SPAN particles and fibers were mixed in a blend ratio of 90/10 to obtain the cathode to improve the

electronic and ionic conductivities. As a result, the SPAN cathode exhibited reduced ion diffusion resistance ( $R_{ion}$ ).

6. A porous SPAN fiber prepared via using PAN/PMMA as the electrospinning precursor was applied and exhibited excellent electrolyte absorbency.
7. An expanded charge/discharge window was implemented in a potential range of 3.5–0.3 V to fully utilize the sulfur and the backbone redox capacities in SPAN.
8. A novel ether-based electrolyte solution (Light-Ele) with properties of lightweight ( $0.98 \text{ g cm}^{-3}$ ), high ionic conductivity, and low viscosity was designed. Light-Ele was composed of 0.2 M LiTFSI + 0.2 M LiFSI + 0.1 M LiNO<sub>3</sub> + 0.1 M lithium1,1,2,2,3,3-hexafluoropropene-1,3-disulfonimide (LiHFDF) in DME/DOL/(trifluoromethyl) trimethylsilane (TFMTMS) (75/5/20, v/v/v). However, the activity of SPAN with the Light-Ele was lower than those with the conventional carbonate-based electrolytes, leading to a poorer CEI. Therefore, a two-step charge/discharge method using two different electrolytes was applied. First, a carbonate-based electrolyte with FEC and LiBOB additives was used to form a stable CEI. Second, Light-Ele was used to reduce the cell weight after removing the electrolyte from the first step.
9. To reduce the cell weight, a thin separator, SETELA PE-type separator film, with a thickness of 5  $\mu\text{m}$  and 35% porosity was used. In addition, a thinner pouch of an aluminum laminated film with a thickness under 80  $\mu\text{m}$  (thin-type DNP Battery Pouch) was applied.
10. An anode-free configuration design was implemented to maximize the energy density of the Li || SPAN cells. The SPAN cathode was electrochemically pre-lithiated using the half-cell method in carbonated-based electrolytes with FEC and LiBOB additives (for robust CEI formation). An ultra-thin Li foil ca. 10  $\mu\text{m}$  thickness was used as the negative current collector instead of the conventional Cu foil.

With these ten innovative designs, an 11 Ah ultra-lightweight Li || SPAN pouch cell exhibited 713 and 761 Wh kg<sup>-1</sup><sub>cell</sub> at 0.1 C and 0.05 C, respectively, and cycled stably for at least 15 cycles. The authors also mentioned that pouch cells with less energy densities and longer cycle life could be achieved with applying only some of the ten innovative designs. For example, a 500 Wh kg<sup>-1</sup><sub>cell</sub>-class cell with cycle life over 400 cycles was obtained with the carbon-coated Al foil, carbonate electrolytes, a voltage window of 3.0–1.0 V, and a charge/discharge rate of 0.1 C/0.3 C.

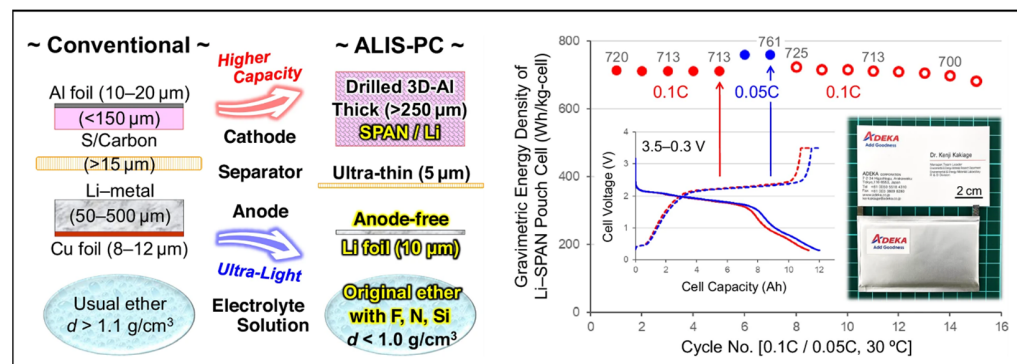


**Figure 59.** Left: Comparison of convention LSBs design and the ADEKA's state-of-the-art Li || SPAN battery (ALIS-PC) design; right: Cycling performance and a photograph of the ALIS-PC pouch cell. Reproduced with permission [479]. Copyright © 2024, Springer Nature.

## 17. Conclusions and Outlook

The past 23 years have witnessed significant progress in research on sulfurized polyacrylonitrile (SPAN)-based rechargeable batteries, from its initial invention to the thriving

scientific community it sustains today. The growing interest in this field is evident from the steadily increasing number of annual publications. This review comprehensively surveys nearly all peer-reviewed studies on SPAN from 2002 to 2025, consolidating advancements across multiple facets: chemical structure, structural evolution during synthesis, redox reaction mechanisms, synthetic conditions, and its roles in battery components—including cathodes, electrolytes, binders, current collectors, separators, and anodes—as well as its applications as an additive, standalone anode, and high-energy cathode material.

Despite the substantial body of original research on SPAN and over 100 secondary publications (reviews, perspectives, etc.) documenting its progress [3,5,6,12,26,247–249,314,478–628], key gaps persist in elucidating SPAN's structural characteristics and redox reaction mechanisms. The practical deployment of SPAN-based rechargeable batteries remains in its early stages, hindered by several critical challenges. First, the high cost of homopolymer PAN underscores the need for scalable synthesis methods capable of producing high-purity PAN with controlled molecular weight and polydispersity. Second, a facile and scale-up synthetic process of SPAN is yet to be established. Third, resolving the limitations of lithium metal anodes—or alternatively, developing lithium compensation strategies (e.g., via cathodes or electrolytes)—is essential for viable cell operation. Furthermore, achieving high-energy, long-cycle-life, and cost-effective SPAN-based batteries demands systematic optimization across all cell components, including cathodes, anodes, electrolytes, separators, current collectors, binders, conductive additives, and cell-level design. Addressing these challenges will require sustained, interdisciplinary collaboration between academia and industry.

**Supplementary Materials:** The following supporting information can be downloaded at: <https://www.mdpi.com/article/10.3390/batteries11080290/s1>, Figure S1: Number of publications of all research articles on SPAN for rechargeable batteries from 2002 to 6 May 2025.

**Funding:** This research received no external funding.

**Data Availability Statement:** The SPAN literature dataset is kept and maintained at <https://github.com/weimufeng/SPAN> (accessed on 6 May 2025).

**Conflicts of Interest:** The author declares no conflicts of interest.

## Abbreviations

The following abbreviations are used in this manuscript:

|                |  |
|----------------|--|
| AB             | acetylene black  |
| AN             | acrylonitrile  |
| ANFs           | aramid nanofibers films  |
| BEAQ           | 1,5-bis(2-(2-(2-methoxyethoxy)ethoxy)ethoxy)anthra-9,10-quinon |
| BME            | butyl methyl ether   |
| BP             | black phosphorus   |
| BTFE           | bis-(2,2,2-trifluorosulfonyl)imide                             |
| CDW            | carbonized delignified wood                                    |
| CE             | Coulombic efficiency   |
| CF             | carbon foam  |
| CFs            | carbon fibers  |
| CNFs           | carbon nanofibers  |
| CNTs           | carbon nanotubes   |
| CPME           | cyclopentyl methyl ether                                       |
| CP-MAS         | cross-polarization/magic angle spinning                        |
| CTAC           | hexadecyl trimethylammonium chloride                           |
| CV             | cyclic voltammetry   |
| C- $\beta$ -CD | carbonyl- $\beta$ -cyclodextrin                                |

|        |   |
|--------|---|
| DBB    | 2,2-dithiobis(benzothiazole)            |
| DBE    | dibutyl ether                           |
| DEC    | diethylene carbonate                    |
| DEE    | diethyl ether                           |
| DEMS   | diethoxydimethylsilane                  |
| DFAQ   | 1,4-difluoroanthraquinone               |
| DFT    | density functional theory               |
| DG     | diphenylguanidine                       |
| DGE    | desolvated gel electrolyte              |
| DIG    | diglyme                                 |
| DIPE   | diisopropyl ether                       |
| DMC    | dimethyl carbonate                      |
| DME    | dimethoxyethane                         |
| DMM    | dimethoxymethane                        |
| DMMP   | dimethyl methylphosphonate              |
| DMMS   | dimethyldimethoxysilane                 |
| DMP    | 1,2-dimethoxypropane                    |
| DMSO   | dimethyl sulfoxide                      |
| DOD    | depth of discharge                      |
| DOL    | 1,3-dioxolane                           |
| DPC    | dipropyl carbonate                      |
| DPE    | dipropyl ether                          |
| DPGDME | dipropylene glycol dimethyl ether       |
| DSC    | differential scanning calorimetric      |
| DTD    | 1,3,2-dioxathiolane 2,2-dioxide         |
| EA     | elemental analysis                      |
| EC     | ethylene carbonate                      |
| EC-AFM | electrochemical atomic force microscopy |
| EGBMC  | ethylene glycol bis(methyl carbonate)   |
| EIS    | electrochemical impedance spectroscopy  |
| EMC    | ethyl methyl carbonate                  |
| EPR    | electron paramagnetic resonance         |
| ET     | ethlenethiourea                         |
| EVs    | electric vehicles                       |
| FB     | fluorobenzene                           |
| FEC    | fluoroethylene carbonate                |
| FT-IR  | Fourier transform infrared              |
| GCN    | graphitic carbon nitride                |
| GE     | gel electrolyte                         |
| GF     | glass fiber                             |
| GFs    | graphene foams                          |
| GG     | guar gum                                |
| GNS    | graphene nanosheet                      |
| GO     | graphene oxide                          |
| GPEs   | gel polymer electrolytes                |
| Gr     | graphite                                |
| G4     | tetraglyme                              |
| HBO    | boric acid                              |
| HC-EM  | half-cell electrochemical method        |
| HCEs   | high-concentration electrolytes         |
| HFBA   | hexafluorobutyl acrylate                |
| HFE    | hexafluoropropylene                     |
| IA     | itaconic acid                           |
| IL     | ionic liquid                            |

|         |   |
|---------|---|
| IL-GPE  | ionic liquid gel polymer electrolyte                    |
| KB      | Ketjen black  |
| LA133   | polyacrylic latex                                       |
| LBG     | locust beam gum   |
| LHCEs   | localized high concentration electrolytes               |
| LiBOB   | lithium bis(oxalate) borate                             |
| LIBs    | lithium-ion batteries                                   |
| LiDFBOP | lithium difluorobis (oxalate) phosphate                 |
| LiDFOB  | lithium difluoro(oxalate)borate                         |
| LiFSI   | lithium bis(Fluorosulfonyl)imide                        |
| LiHFDF  | lithium 1,1,2,2,3,3-hexafluoropropane-1,3-disulfonimide |
| LiODFB  | lithium oxalyldifluoroborate                            |
| LiPSs   | lithium polysulfides                                    |
| LiTFSI  | lithium bis(trifluoromethanesulfonyl)imide              |
| LMA     | lithium metal anode                                     |
| LMO     | lithium manganese oxide                                 |
| LSBs    | lithium–sulfur batteries                                |
| MaPC    | macro-porous carbon                                     |
| MBA     | magnesium bis(diisopropyl)amide                         |
| MBT     | 2-mercaptobenzothiazoles                                |
| MCPs    | microporous carbon polyhedrons                          |
| MD      | molecular dynamics                                      |
| MeIM    | 2-methylimidazole                                       |
| MLG     | multilayered graphene                                   |
| MOFs    | metal–organic frameworks                                |
| MP      | methyl propionate                                       |
| MSBs    | metal–sulfur batteries                                  |
| MTFP    | methyl 3,3,3-trifluoropionate                           |
| MWCNTs  | multi-walled carbon nanotube                            |
| NaCMC   | sodium carboxymethyl cellulose                          |
| NaTPB   | sodium tetraphenylborate                                |
| NaTFSI  | sodium trifluoromethanesulfonimide                      |
| NaPPB   | sodium bis(perfluoropinacol)borate                      |
| NCM     | lithium nickel manganese cobalt                         |
| NER     | nitrogen evolution reaction                             |
| NMP     | N-methyl-2-pyrrolidone                                  |
| NMR     | nuclear magnetic resonance                              |
| PAA     | polyacrylic acid  |
| PAAS    | sodium polyacrylate                                     |
| PAF     | polymer-alloy-fluoride                                  |
| PAN     | polyacrylonitrile                                       |
| PC      | propylene carbonate                                     |
| PCE     | plastic crystal electrolyte                             |
| PDA     | polydopamine  |
| PDF     | pair distribution function                              |
| PDSe    | phenyl diselenide                                       |
| PE      | polyethylene  |
| PEG     | polyethylene glycol                                     |
| PEGDA   | poly(ethylene glycol) diacrylate                        |
| PEO     | polyethylene oxide                                      |
| PEOEC   | poly(ethylene oxide-co-ethylene carbonate)              |
| PETA    | pentaerythritol triacrylate                             |
| PETEA   | pentaerythritol tetraacrylate                           |
| PI      | polyimide   |

|                    |   |
|--------------------|---|
| PIBs               | potassium-ion batteries                                 |
| PMMA               | poly(methyl methacrylate)                               |
| PP                 | polypropylene separator                                 |
| Ppy                | polypyrole  |
| PS                 | polystyrene   |
| PuA                | pulutan-graft-sodium polyacrylic acid                   |
| PVA                | polyvinyl alcohol                                       |
| PVDF               | polyvinylidenefluoride                                  |
| PVP                | polyvinyl pyrrolidone                                   |
| RAFT               | addition-fragmentation chain transfer                   |
| Rsf                | interfacial impedance                                   |
| Rct                | charge transfer resistance                              |
| rGO                | reduced graphene oxide                                  |
| RP                 | red phosphorus  |
| sAXS               | soft X-ray absorption spectroscopy                      |
| SBR                | styrene butadiene rubber                                |
| SCMC               | carboxymethyl cellulose                                 |
| SCR                | carboxylated styrene butadiene rubber                   |
| SC-EM              | short-circuit electrochemical method                    |
| Se                 | selenium  |
| SEI                | solid-electrolyte interface                             |
| SEM                | scanning electron microscopy                            |
| SIPS               | solvent-induced phase separation                        |
| SLMP               | stable lithium metal powder                             |
| SPAN               | sulfurized polyacrylonitrile                            |
| SPEs               | Solid-state polymer electrolytes                        |
| SPVac              | sulfurized poly(vinylacetylene)                         |
| SWCNTs             | single-walled carbon nanotubes                          |
| TD                 | tetrathylthiuruam disulfide                             |
| Te                 | tellurium   |
| TEGDME             | tetraethylene glycol dimethyl ether                     |
| TEM                | transmission electron microscopy                        |
| TEP                | triethyl phosphate                                      |
| TFMTMS             | (trifluoromethyl)trimethylsilane                        |
| TG                 | thermogravimetry  |
| THF                | tetrahydrofuran   |
| THP                | tetrahydropyran   |
| TI                 | triallyl isocyanurate                                   |
| TIPS               | thermally induced phase separation                      |
| TMP                | trimethyl phosphate                                     |
| TMSB               | tris(trimethylsilyl) borate                             |
| TMSP               | tris(trimethylsilyl) phosphite                          |
| TMS-N <sub>3</sub> | trimethylsilyl azide                                    |
| TPA                | terephthalic acid                                       |
| TPOS               | tetrapropoxysilane                                      |
| TOF-SIMS           | time-of flight secondary ion mass spectrometry          |
| TPPi               | triphenyl phosphite                                     |
| TTCA               | trithiocyanuric acid                                    |
| TTE                | 1,1,2,2-tetrafluoroethyl-2,2,3,3-tetrafluoropropylether |
| TTFP               | tris(2,2,2-trifluoroethyl) phosphite                    |
| VAs                | vulcanization accelerators                              |
| VC                 | vinylene carbonate                                      |
| VGCF               | vapor grown carbon fiber                                |
| XAS                | X-ray absorption spectroscopy                           |

|      |                                      |
|------|--------------------------------------|
| XPS  | X-ray photoelectron spectroscopy     |
| XRD  | X-ray diffraction                    |
| ZDB  | zinc N-ethyl-N-phenyldithiocarbamate |
| 2-FP | 2-fluoropyridine                     |

## References

- Chung, S.-H.; Manthiram, A. Current Status and Future Prospects of Metal–Sulfur Batteries. *Adv. Mater.* **2019**, *31*, 1901125. [[CrossRef](#)]
- Yu, X.; Manthiram, A. A Progress Report on Metal–Sulfur Batteries. *Adv. Funct. Mater.* **2020**, *30*, 2004084. [[CrossRef](#)]
- Phan, A.L.; Le, P.M.L.; Wang, C. Realizing High-Energy and Long-Life Li/SPAN Batteries. *Joule* **2024**, *8*, 1601–1618. [[CrossRef](#)]
- Wagenfeld, J.-G.; Al-Ali, K.; Almheiri, S.; Slavens, A.F.; Calvet, N. Sustainable Applications Utilizing Sulfur, a by-Product from Oil and Gas Industry: A State-of-the-Art Review. *Waste Manag.* **2019**, *95*, 78–89. [[CrossRef](#)]
- Zhang, X.; Ma, H.; Liu, J.; Chen, J.; Lu, H.; Huang, Y.; Wang, J. Structure and Reactions Mechanism of Sulfurized Polyacrylonitrile as Cathodes for Rechargeable Li-S Batteries. *Nano Res.* **2023**, *16*, 8159–8172. [[CrossRef](#)]
- Zhao, X.; Wang, C.; Li, Z.; Hu, X.; Razzaq, A.A.; Deng, Z. Sulfurized Polyacrylonitrile for High-Performance Lithium Sulfur Batteries: Advances and Prospects. *J. Mater. Chem. A* **2021**, *9*, 19282–19297. [[CrossRef](#)]
- Shaibani, M.; Mirshekarloo, M.S.; Singh, R.; Easton, C.D.; Cooray, M.C.D.; Eshraghi, N.; Abendroth, T.; Dörfler, S.; Althues, H.; Kaskel, S.; et al. Expansion-Tolerant Architectures for Stable Cycling of Ultrahigh-Loading Sulfur Cathodes in Lithium-Sulfur Batteries. *Sci. Adv.* **2020**, *6*, eaay2757. [[CrossRef](#)]
- Li, J.; Gao, L.; Pan, F.; Gong, C.; Sun, L.; Gao, H.; Zhang, J.; Zhao, Y.; Wang, G.; Liu, H. Engineering Strategies for Suppressing the Shuttle Effect in Lithium–Sulfur Batteries. *Nano-Micro Lett.* **2023**, *16*, 12. [[CrossRef](#)]
- Wang, J.; Yang, J.; Xie, J.; Xu, N. A Novel Conductive Polymer–Sulfur Composite Cathode Material for Rechargeable Lithium Batteries. *Adv. Mater.* **2002**, *14*, 963–965. [[CrossRef](#)]
- Wang, J.; Yang, J.; Wan, C.; Du, K.; Xie, J.; Xu, N. Sulfur Composite Cathode Materials for Rechargeable Lithium Batteries. *Adv. Funct. Mater.* **2003**, *13*, 487–492. [[CrossRef](#)]
- Wang, J.; Wang, Y.; He, X.; Ren, J.; Jiang, C.; Wan, C. Electrochemical Characteristics of Sulfur Composite Cathode Materials in Rechargeable Lithium Batteries. *J. Power Sources* **2004**, *138*, 271–273. [[CrossRef](#)]
- Miao, Q.; Solan, N.; Hyun, G.; Holoubek, J.; Liu, P. Electrolyte Engineering for Long-Life Li-SPAN Batteries. *ACS Energy Lett.* **2023**, *8*, 4818–4830. [[CrossRef](#)]
- Wei, M. SPAN Dataset 2025. Available online: <https://github.com/weimufeng/SPAN> (accessed on 23 July 2025).
- Yu, X.; Xie, J.; Yang, J.; Huang, H.; Wang, K.; Wen, Z. Lithium Storage in Conductive Sulfur-Containing Polymers. *J. Electroanal. Chem.* **2004**, *573*, 121–128. [[CrossRef](#)]
- Fanous, J.; Wegner, M.; Grimminger, J.; Andresen, Å.; Buchmeiser, M.R. Structure-Related Electrochemistry of Sulfur-Poly(Acrylonitrile) Composite Cathode Materials for Rechargeable Lithium Batteries. *Chem. Mater.* **2011**, *23*, 5024–5028. [[CrossRef](#)]
- Fanous, J.; Wegner, M.; Grimminger, J.; Rolff, M.; Spera, M.B.M.; Tenzer, M.; Buchmeiser, M.R. Correlation of the Electrochemistry of Poly(Acrylonitrile)–Sulfur Composite Cathodes with Their Molecular Structure. *J. Mater. Chem.* **2012**, *22*, 23240–23245. [[CrossRef](#)]
- Doan, T.N.L.; Ghaznavi, M.; Zhao, Y.; Zhang, Y.; Konarov, A.; Sadhu, M.; Tangirala, R.; Chen, P. Binding Mechanism of Sulfur and Dehydrogenated Polyacrylonitrile in Sulfur/Polymer Composite Cathode. *J. Power Sources* **2013**, *241*, 61–69. [[CrossRef](#)]
- Zhang, S.S. Understanding of Sulfurized Polyacrylonitrile for Superior Performance Lithium/Sulfur Battery. *Energies* **2014**, *7*, 4588–4600. [[CrossRef](#)]
- Wei, S.; Ma, L.; Hendrickson, K.E.; Tu, Z.; Archer, L.A. Metal–Sulfur Battery Cathodes Based on PAN–Sulfur Composites. *J. Am. Chem. Soc.* **2015**, *137*, 12143–12152. [[CrossRef](#)]
- Wang, W.; Cao, Z.; Elia, G.A.; Wu, Y.; Wahyudi, W.; Abou-Hamad, E.; Emwas, A.-H.; Cavallo, L.; Li, L.-J.; Ming, J. Recognizing the Mechanism of Sulfurized Polyacrylonitrile Cathode Materials for Li–S Batteries and beyond in Al–S Batteries. *ACS Energy Lett.* **2018**, *3*, 2899–2907. [[CrossRef](#)]
- Jin, Z.-Q.; Liu, Y.-G.; Wang, W.-K.; Wang, A.-B.; Hu, B.-W.; Shen, M.; Gao, T.; Zhao, P.-C.; Yang, Y.-S. A New Insight into the Lithium Storage Mechanism of Sulfurized Polyacrylonitrile with No Soluble Intermediates. *Energy Storage Mater.* **2018**, *14*, 272–278. [[CrossRef](#)]
- Weret, M.A.; Jeffrey Kuo, C.-F.; Zeleke, T.S.; Beyene, T.T.; Tsai, M.-C.; Huang, C.-J.; Berhe, G.B.; Su, W.-N.; Hwang, B.-J. Mechanistic Understanding of the Sulfurized-Poly(Acrylonitrile) Cathode for Lithium-Sulfur Batteries. *Energy Storage Mater.* **2020**, *26*, 483–493. [[CrossRef](#)]

23. Huang, C.-J.; Lin, K.-Y.; Hsieh, Y.-C.; Su, W.-N.; Wang, C.-H.; Brunklaus, G.; Winter, M.; Jiang, J.-C.; Hwang, B.J. New Insights into the N–S Bond Formation of a Sulfurized-Polyacrylonitrile Cathode Material for Lithium–Sulfur Batteries. *ACS Appl. Mater. Interfaces* **2021**, *13*, 14230–14238. [[CrossRef](#)]
24. Huang, C.-J.; Cheng, J.-H.; Su, W.-N.; Partovi-Azar, P.; Kuo, L.-Y.; Tsai, M.-C.; Lin, M.-H.; Panahian Jand, S.; Chan, T.-S.; Wu, N.-L.; et al. Origin of Shuttle-Free Sulfurized Polyacrylonitrile in Lithium-Sulfur Batteries. *J. Power Sources* **2021**, *492*, 229508. [[CrossRef](#)]
25. Zhu, T.; Mueller, J.E.; Hanauer, M.; Sauter, U.; Jacob, T. Structural Motifs for Modeling Sulfur-Poly(Acrylonitrile) Composite Materials in Sulfur-Lithium Batteries. *ChemElectroChem* **2017**, *4*, 2494–2499. [[CrossRef](#)]
26. Wu, X.; Zhao, Y.; Li, H.; Zhou, C.; Wang, X.; Du, L. Sulfurized Polyacrylonitrile as Cathodes for Advanced Lithium–Sulfur Batteries: Advances in Modification Strategies. *Nanoscale* **2024**, *16*, 5060–5078. [[CrossRef](#)]
27. He, X.-M.; Wang, L.; Pu, W.-H.; Ren, J.-G.; Wu, W.; Jiang, C.-Y.; Wan, C.-R. Thermal Analysis of Sulfurization of Polyacrylonitrile with Elemental Sulfur. *J. Therm. Anal. Calorim.* **2008**, *94*, 151–155. [[CrossRef](#)]
28. Xie, J.; Chen, J.; Guo, L.; Li, Y.; Wang, Y.; Zheng, S.; Zhang, N.; Meng, J.; Zhang, K.; Li, Q.; et al. Deciphering the Sulfur-Involved Bonding Interactions in Sulfurized Polyacrylonitrile: The Formation Thermodynamics and the Roles in Electrochemical Characteristics. *ACS Nano* **2025**, *19*, 3931–3943. [[CrossRef](#)]
29. He, X.; Pu, W.; Ren, J.; Wang, L.; Wang, J.; Jiang, C.; Wan, C. Charge/Discharge Characteristics of Sulfur Composite Cathode Materials in Rechargeable Lithium Batteries. *Electrochim. Acta* **2007**, *52*, 7372–7376. [[CrossRef](#)]
30. He, X.; Pu, W.; Ren, J.; Wang, L.; Wang, J.; Jiang, C.; Wan, C. Charge/Discharge Characteristics of Sulfur Composite Electrode at Different Temperature and Current Density in Rechargeable Lithium Batteries. *Ionics* **2008**, *14*, 335–337. [[CrossRef](#)]
31. He, X.; Ren, J.; Wang, L.; Pu, W.; Jiang, C.; Wan, C. Expansion and Shrinkage of the Sulfur Composite Electrode in Rechargeable Lithium Batteries. *J. Power Sources* **2009**, *190*, 154–156. [[CrossRef](#)]
32. Wang, L.; He, X.; Ren, J.; Pu, W.; Li, J.; Gao, J. The Electrochemical Characteristics of Sulfur Composite Cathode. *Ionics* **2010**, *16*, 689–695. [[CrossRef](#)]
33. Niesen, S.; Trück, J.; Seidl, C.; Renger, K.; Buchmeiser, M.R. Lithium-Sulfur Batteries Based on Sulfurized Poly(Acrylonitrile) Cathodes: Impact of Electrode Density on Cell Performance. *J. Electrochem. Soc.* **2021**, *168*, 110513. [[CrossRef](#)]
34. Moschner, R.; Gerle, M.; Danner, T.; Simanjuntak, E.K.; Michalowski, P.; Latz, A.; Nojabaei, M.; Kwade, A.; Friedrich, K.A. Impact of the Sulfurized Polyacrylonitrile Cathode Microstructure on the Electrochemical Performance of Lithium–Sulfur Batteries. *Adv. Sci.* **2025**, *12*, 2415436. [[CrossRef](#)]
35. Wang, L.; Zhao, J.; He, X.; Wan, C. Kinetic Investigation of Sulfurized Polyacrylonitrile Cathode Material by Electrochemical Impedance Spectroscopy. *Electrochim. Acta* **2011**, *56*, 5252–5256. [[CrossRef](#)]
36. Wang, L.; He, X.; Sun, W.; Li, J.; Gao, J.; Tian, G.; Wang, J.; Fan, S. Organic Polymer Material with a Multi-Electron Process Redox Reaction: Towards Ultra-High Reversible Lithium Storage Capacity. *RSC Adv.* **2013**, *3*, 3227–3231. [[CrossRef](#)]
37. Jiang, Z.; Guo, H.-J.; Zeng, Z.; Chen, X.; Lei, Y.; Liang, X.; Han, Z.; Hu, W.; Feng, J.; Wen, R.; et al. In Situ Characterization of Over-Lithiation of Organosulfide-Based Lithium Metal Anodes. *ACS Appl. Mater. Interfaces* **2021**, *13*, 41555–41562. [[CrossRef](#)]
38. Dominko, R.; Patel, M.U.M.; Bele, M.; Pejovnik, S. Sulphured Polyacrylonitrile Composite Analysed by in Operando UV-Visible Spectroscopy and 4-Electrode Swagelok Cell. *Acta Chim. Slov.* **2016**, *63*, 569–577. [[CrossRef](#)]
39. Warneke, S.; Eusterholz, M.; Zenn, R.K.; Hintennach, A.; Dinnebier, R.E.; Buchmeiser, M.R. Differences in Electrochemistry between Fibrous SPAN and Fibrous S/C Cathodes Relevant to Cycle Stability and Capacity. *J. Electrochem. Soc.* **2017**, *165*, A6017. [[CrossRef](#)]
40. Kappler, J.; Klostermann, S.V.; Lange, P.L.; Dyballa, M.; Veith, L.; Schleid, T.; Weil, T.; Kästner, J.; Buchmeiser, M.R. Sulfur-Composites Derived from Poly(Acrylonitrile) and Poly(Vinylacetylene)—A Comparative Study on the Role of Pyridinic and Thioamidic Nitrogen. *Batter. Supercaps* **2023**, *6*, e202200522. [[CrossRef](#)]
41. Wang, S.; Lu, B.; Cheng, D.; Wu, Z.; Feng, S.; Zhang, M.; Li, W.; Miao, Q.; Patel, M.; Feng, J.; et al. Structural Transformation in a Sulfurized Polymer Cathode to Enable Long-Life Rechargeable Lithium–Sulfur Batteries. *J. Am. Chem. Soc.* **2023**, *145*, 9624–9633. [[CrossRef](#)]
42. Tan, S.; Rahman, M.M.; Wu, Z.; Liu, H.; Wang, S.; Ghose, S.; Zhong, H.; Waluyo, I.; Hunt, A.; Liu, P.; et al. Structural and Interphasial Stabilities of Sulfurized Polyacrylonitrile (SPAN) Cathode. *ACS Energy Lett.* **2023**, *8*, 2496–2504. [[CrossRef](#)]
43. Pereira, R.; Sarode, K.K.; Rafie, A.; Fafarman, A.; Kalra, V. In-Operando FTIR Study on the Redox Behavior of Sulfurized Polyacrylonitrile as Cathode Material for Li–S Batteries. *J. Phys. Chem. C* **2023**, *127*, 19356–19365. [[CrossRef](#)]
44. Hu, J.; Wang, Z.; Lyu, L.; Qin, N.; Li, Y.; Gu, S.; Wang, Z.; Chen, J.; Yuan, H.; Yang, M.; et al. New Insights into the Reaction Mechanism of Sulfurized Polyacrylonitrile Cathode Material for Li–S Batteries. *Compos. Commun.* **2024**, *49*, 101971. [[CrossRef](#)]
45. Liu, J.; Lu, H.; Wang, Q.; Kong, X.; Hao, C.; Yang, J.; NuLi, Y.; Duan, H.; Wang, J. Roles of the Polymer Backbone for Sulfurized Polyacrylonitrile Cathodes in Rechargeable Lithium Batteries. *J. Am. Chem. Soc.* **2025**, *147*, 426–435. [[CrossRef](#)]
46. Kappler, J.; Tonbul, G.; Schoch, R.; Murugan, S.; Nowakowski, M.; Lange, P.L.; Klostermann, S.V.; Bauer, M.; Schleid, T.; Kästner, J.; et al. Understanding the Redox Mechanism of Sulfurized Poly(Acrylonitrile) as Highly Rate and Cycle Stable Cathode Material for Sodium-Sulfur Batteries. *J. Electrochem. Soc.* **2023**, *170*, 010526. [[CrossRef](#)]

47. Zhu, T.; Mueller, J.E.; Hanauer, M.; Sauter, U.; Jacob, T. Theoretical Studies on the Charging and Discharging of Poly(Acrylonitrile)-Based Lithium-Sulfur Batteries. *ChemElectroChem* **2017**, *4*, 2975–2980. [[CrossRef](#)]
48. Bertolini, S.; Jacob, T. Atomistic Discharge Studies of Sulfurized-Polyacrylonitrile through Ab Initio Molecular Dynamics. *Electrochim. Acta* **2022**, *403*, 139538. [[CrossRef](#)]
49. Beltran, S.P.; Balbuena, P.B. First-Principles Explorations of the Electrochemical Lithiation Dynamics of a Multilayer Graphene Nanosheet-Based Sulfur-Carbon Composite. *J. Mater. Chem. A* **2018**, *6*, 18084–18094. [[CrossRef](#)]
50. Perez Beltran, S.; Balbuena, P.B. Sulfurized Polyacrylonitrile for High-Performance Lithium-Sulfur Batteries: In-Depth Computational Approach Revealing Multiple Sulfur’s Reduction Pathways and Hidden Li<sup>+</sup> Storage Mechanisms for Extra Discharge Capacity. *ACS Appl. Mater. Interfaces* **2021**, *13*, 491–502. [[CrossRef](#)]
51. Perez Beltran, S.; Balbuena, P.B. Sulfurized Polyacrylonitrile (SPAN): Changes in Mechanical Properties during Electrochemical Lithiation. *J. Phys. Chem. C* **2021**, *125*, 13185–13194. [[CrossRef](#)]
52. Bertolini, S.; Jacob, T. Density Functional Theory Studies on Sulfur–Polyacrylonitrile as a Cathode Host Material for Lithium–Sulfur Batteries. *ACS Omega* **2021**, *6*, 9700–9708. [[CrossRef](#)]
53. Bertolini, S.; Jacob, T. Sulfurized-Polyacrylonitrile in Lithium-Sulfur Batteries: Interactions between Undercoordinated Carbons and Polymer Structure under Low Lithiation. *J. Energy Chem.* **2022**, *66*, 587–596. [[CrossRef](#)]
54. Bertolini, S.; Jacob, T. Capturing Polysulfides by Sulfurized-Polyacrylonitrile in Lithium-Sulfur Batteries and the Sulfur-Chain Effects through Density Functional Theory. *Electrochem. Sci. Adv.* **2022**, *2*, e2100129. [[CrossRef](#)]
55. Bertolini, S.; Venezuela, P.; Delcorte, A. The Effect of Lithium Battery Overpotential on Sulfurized-Polyacrylonitrile (SPAN): A Theoretical Approach. *J. Energy Storage* **2024**, *78*, 110049. [[CrossRef](#)]
56. Simanjuntak, E.K.; Danner, T.; Wang, P.; Buchmeiser, M.R.; Latz, A. A Novel Modeling Approach for Sulfurized Polyacrylonitrile (SPAN) Electrodes in Li Metal Batteries. *Electrochim. Acta* **2024**, *497*, 144571. [[CrossRef](#)]
57. Yu, X.; Xie, J.; Li, Y.; Huang, H.; Lai, C.; Wang, K. Stable-Cycle and High-Capacity Conductive Sulfur-Containing Cathode Materials for Rechargeable Lithium Batteries. *J. Power Sources* **2005**, *146*, 335–339. [[CrossRef](#)]
58. Wang, L.; He, X.; Li, J.; Gao, J.; Guo, J.; Jiang, C.; Wan, C. Analysis of the Synthesis Process of Sulphur–Poly(Acrylonitrile)-Based Cathode Materials for Lithium Batteries. *J. Mater. Chem.* **2012**, *22*, 22077–22081. [[CrossRef](#)]
59. Langrud, S.; Razzaq, A.A.; Santhanagopalan, S.; Brow, R.; Xing, W. Comprehensive Characterization of Multi-Phase Sulfurized Polyacrylonitrile Cathodes for Lithium-Sulfur Batteries. *J. Electrochem. Soc.* **2022**, *169*, 070514. [[CrossRef](#)]
60. Pan, J.; Nie, J.; Zeng, B.; Chen, X.; Chen, Z.; Kang, D.; Miao, Y.; Liu, W.; Zhang, W. Optimized Preparation of Polyacrylonitrile/Sulfur Composite as Cathode for Lithium Sulfur Batteries. *Int. J. Electrochem. Sci.* **2022**, *17*, 22021. [[CrossRef](#)]
61. Shi, Z.; Wang, Y.; Liu, M.; Ma, J.; Yue, H.; Hu, Z.; Yang, S.-T.; Yin, Y. Synthesis of Highly Cyclized Polyacrylonitrile via Liquid-Phase Cyclization for Advanced Cathode Materials. *ACS Sustain. Chem. Eng.* **2024**, *12*, 17806–17816. [[CrossRef](#)]
62. Liu, Y.; Wang, W.; Wang, A.; Jin, Z.; Zhao, H.; Yang, Y. Effect of Vapor Pressure on Performance of Sulfurized Polyacrylonitrile Cathodes for Li/S Batteries. *RSC Adv.* **2016**, *6*, 106625–106630. [[CrossRef](#)]
63. Páez Jerez, A.L.; Chemes, D.M.; Sham, E.L.; Davies, L.E.; Tesio, A.Y.; Flexer, V. Low-Temperature Synthesis of a Sulfur–Polyacrylonitrile Composite Cathode for Lithium-Sulfur Batteries. *ChemistrySelect* **2020**, *5*, 5465–5472. [[CrossRef](#)]
64. Fanous, J.; Wegner, M.; Spera, M.B.M.; Buchmeiser, M.R. High Energy Density Poly(Acrylonitrile)-Sulfur Composite-Based Lithium-Sulfur Batteries. *J. Electrochem. Soc.* **2013**, *160*, A1169. [[CrossRef](#)]
65. Cho, G.-B.; Park, H.-B.; Jeong, J.-S.; Chae, M.-R.; Im, Y.-M.; Han-Gyeol, L.; Sang-Hui, P.; Kim, K.-W. Effect of Ball Milling on Electrochemical Properties of Sulfur/Polyacrylonitrile (SPAN) Cathode in Li/S Battery. *J. Nanosci. Nanotechnol.* **2018**, *18*, 6431–6436. [[CrossRef](#)]
66. Konarov, A.; Gosselink, D.; Doan, T.N.L.; Zhang, Y.; Zhao, Y.; Chen, P. Simple, Scalable, and Economical Preparation of Sulfur–PAN Composite Cathodes for Li/S Batteries. *J. Power Sources* **2014**, *259*, 183–187. [[CrossRef](#)]
67. Du, K.; Zhang, Q. Facile Fabrication of Sulfur Entrapped Carbonized Material as a Cathode for High-Performance Lithium Batteries. *RSC Adv.* **2016**, *6*, 87690–87695. [[CrossRef](#)]
68. Sarode, K.; Yim, T.; Pereira, R.; Cardoza, N.; Kalra, V. Solid–Liquid–Solid Mediated Artificial SEI Coated Stable Lithium and High-Sulfur Percentage SPAN for High Performance Li–S Batteries. *Energy Adv.* **2024**, *3*, 584–591. [[CrossRef](#)]
69. Zhu, G. A Novel Suspension Polymerization Process to Prepare Sulfur Composite Cathode Materials for Lithium/Sulfur Batteries. *World Electr. Veh. J.* **2010**, *4*, 332–334. [[CrossRef](#)]
70. Zhang, Y.; Zhao, Y.; Bakenov, Z.; Konarov, A.; Chen, P. Preparation of Novel Network Nanostructured Sulfur Composite Cathode with Enhanced Stable Cycle Performance. *J. Power Sources* **2014**, *270*, 326–331. [[CrossRef](#)]
71. Pu, W.; He, X.; Wang, L.; Tian, Z.; Jiang, C.; Wan, C. Sulfur Composite Cathode Materials: Comparative Characterization of Polyacrylonitrile Precursor. *Ionics* **2007**, *13*, 273–276. [[CrossRef](#)]
72. Lei, J.; Chen, J.; Zhang, H.; Naveed, A.; Yang, J.; Nuli, Y.; Wang, J. High Molecular Weight Polyacrylonitrile Precursor for S@pPAN Composite Cathode Materials with High Specific Capacity for Rechargeable Lithium Batteries. *ACS Appl. Mater. Interfaces* **2020**, *12*, 33702–33709. [[CrossRef](#)]

73. Liu, H.; He, R.; Li, Y.; Jin, Y.; Liu, H.; Zhang, X. Effect of Sulfurized Polyacrylonitrile-g-rGO Composition on the Specific Capacity and Cycling Stability of Lithium Sulfur Batteries. *J. Electroanal. Chem.* **2023**, *939*, 117465. [[CrossRef](#)]
74. Wang, Y.; Chen, Y.; Shi, C.; Shen, Y. Diphenylguanidine Combined with High Molecular Weight Polyacrylonitrile Precursor for High-Conductivity and High-Sulfur-Loading Cathode of Lithium-Sulfur Battery. *Mater. Lett.* **2023**, *336*, 133831. [[CrossRef](#)]
75. Yi, Y.; Hai, F.; Chen, W.; Gao, X.; Guo, J.; Xue, W.; Li, M. A Universal Strategy for the Refined Frameworks and Improved Performance of Distinct Commercial Polyacrylonitriles in Sulfur Cathodes. *Sci. China Mater.* **2024**, *67*, 2915–2924. [[CrossRef](#)]
76. Geller, B.E. Status and Prospects for Development of Polyacrylonitrile Fibre Production. A Review. *Fibre Chem.* **2002**, *34*, 151–161. [[CrossRef](#)]
77. Huang, X. Fabrication and Properties of Carbon Fibers. *Materials* **2009**, *2*, 2369–2403. [[CrossRef](#)]
78. Wei, W.; Wang, J.; Zhou, L.; Yang, J.; Schumann, B.; NuLi, Y. CNT Enhanced Sulfur Composite Cathode Material for High Rate Lithium Battery. *Electrochem. Commun.* **2011**, *13*, 399–402. [[CrossRef](#)]
79. Shi, Z.; Bi, D.; Wang, L.; Xu, H.; Yue, H.; Yin, Y.; Yang, S. Disulfide Dichloride: A High Efficiency Vulcanizing Agent for Sulfurized Polyacrylonitrile. *ACS Appl. Energy Mater.* **2022**, *5*, 8015–8022. [[CrossRef](#)]
80. Liu, X.-M.; Huang, Z.D.; Oh, S.W.; Zhang, B.; Ma, P.-C.; Yuen, M.M.F.; Kim, J.-K. Carbon Nanotube (CNT)-Based Composites as Electrode Material for Rechargeable Li-Ion Batteries: A Review. *Compos. Sci. Technol.* **2012**, *72*, 121–144. [[CrossRef](#)]
81. Tong, Z.; Lv, C.; Bai, G.-D.; Yin, Z.-W.; Zhou, Y.; Li, J.-T. A Review on Applications and Challenges of Carbon Nanotubes in Lithium-Ion Battery. *Carbon Energy* **2025**, *7*, e643. [[CrossRef](#)]
82. Yin, L.; Wang, J.; Yang, J.; Nuli, Y. A Novel Pyrolyzed Polyacrylonitrile-sulfur@MWCNT Composite Cathode Material for High-Rate Rechargeable Lithium/Sulfur Batteries. *J. Mater. Chem.* **2011**, *21*, 6807–6810. [[CrossRef](#)]
83. Electrochemical properties of lithium/sulfur-polyacrylonitrile-carbon nanotube composite cells using ether-based electrolyte at high rate. *J. Ceram. Process. Res.* **2015**, *16*, 199–202. [[CrossRef](#)]
84. Abdul Razzaq, A.; Yao, Y.; Shah, R.; Qi, P.; Miao, L.; Chen, M.; Zhao, X.; Peng, Y.; Deng, Z. High-Performance Lithium Sulfur Batteries Enabled by a Synergy between Sulfur and Carbon Nanotubes. *Energy Storage Mater.* **2019**, *16*, 194–202. [[CrossRef](#)]
85. Razzaq, A.A.; Yuan, X.; Chen, Y.; Hu, J.; Mu, Q.; Ma, Y.; Zhao, X.; Miao, L.; Ahn, J.-H.; Peng, Y.; et al. Anchoring MOF-Derived CoS<sub>2</sub> on Sulfurized Polyacrylonitrile Nanofibers for High Areal Capacity Lithium–Sulfur Batteries. *J. Mater. Chem. A* **2020**, *8*, 1298–1306. [[CrossRef](#)]
86. Abdul Razzaq, A.; Chen, G.; Zhao, X.; Yuan, X.; Hu, J.; Li, Z.; Chen, Y.; Xu, J.; Shah, R.; Zhong, J.; et al. Cobalt Coordination with Pyridines in Sulfurized Polyacrylonitrile Cathodes to Form Conductive Pathways and Catalytic M-N<sub>4</sub>S Sites for Accelerated Li-S Kinetics. *J. Energy Chem.* **2021**, *61*, 170–178. [[CrossRef](#)]
87. Wang, X.; Qian, Y.; Wang, L.; Yang, H.; Li, H.; Zhao, Y.; Liu, T. Sulfurized Polyacrylonitrile Cathodes with High Compatibility in Both Ether and Carbonate Electrolytes for Ultrastable Lithium–Sulfur Batteries. *Adv. Funct. Mater.* **2019**, *29*, 1902929. [[CrossRef](#)]
88. Li, H.; Xue, W.; Xu, W.; Wang, L.; Liu, T. Controllable Synthesis of Sulfurized Polyacrylonitrile Nanofibers for High Performance Lithium–Sulfur Batteries. *Compos. Commun.* **2021**, *24*, 100675. [[CrossRef](#)]
89. Hu, X.; Jiang, H.; Hou, Q.; Yu, M.; Jiang, X.; He, G.; Li, X. Scalable SPAN Membrane Cathode with High Conductivity and Hierarchically Porous Framework for Enhanced Ion Transfer and Cycling Stability in Li–S Batteries. *ACS Mater. Lett.* **2023**, *5*, 2047–2057. [[CrossRef](#)]
90. Shao, J.; Huang, C.; Zhu, Q.; Sun, N.; Zhang, J.; Wang, R.; Chen, Y.; Zhang, Z. Flexible CNT-Interpenetrating Hierarchically Porous Sulfurized Polyacrylonitrile (CIHP-SPAN) Electrodes for High-Rate Lithium-Sulfur (Li-S) Batteries. *Nanomaterials* **2024**, *14*, 1155. [[CrossRef](#)]
91. Zuo, W.; Guo, Y.; Zhang, C.; Zhang, L.; Zhang, S. Mussel and Cobweb Inspired High Areal Capacity SPAN Electrode. *Small* **2024**, *20*, 2309126. [[CrossRef](#)]
92. Liu, H.; Zhang, Y.; Li, Y.; Liu, H.; Han, N.; Zhang, X. Loadings of Functionalized Multiwalled Carbon Nanotubes for Enhancing Sulfurized Polyacrylonitrile Performance in Lithium–Sulfur Batteries. *ACS Appl. Nano Mater.* **2023**, *6*, 21058–21067. [[CrossRef](#)]
93. Geim, A.K.; Novoselov, K.S. The Rise of Graphene. *Nat. Mater.* **2007**, *6*, 183–191. [[CrossRef](#)]
94. Yin, L.; Wang, J.; Lin, F.; Yang, J.; Nuli, Y. Polyacrylonitrile/Graphene Composite as a Precursor to a Sulfur-Based Cathode Material for High-Rate Rechargeable Li-S Batteries. *Energy Environ. Sci.* **2012**, *5*, 6966–6972. [[CrossRef](#)]
95. Yin, L.; Wang, J.; Yu, X.; Monroe, C.W.; NuLi, Y.; Yang, J. Dual-Mode Sulfur-Based Cathode Materials for Rechargeable Li-S Batteries. *Chem. Commun.* **2012**, *48*, 7868–7870. [[CrossRef](#)]
96. Zhang, Y.; Zhao, Y.; Bakenov, Z.; Babaa, M.-R.; Konarov, A.; Ding, C.; Chen, P. Effect of Graphene on Sulfur/Polyacrylonitrile Nanocomposite Cathode in High Performance Lithium/Sulfur Batteries. *J. Electrochem. Soc.* **2013**, *160*, A1194. [[CrossRef](#)]
97. Wang, J.; Yin, L.; Jia, H.; Yu, H.; He, Y.; Yang, J.; Monroe, C.W. Hierarchical Sulfur-Based Cathode Materials with Long Cycle Life for Rechargeable Lithium Batteries. *ChemSusChem* **2014**, *7*, 563–569. [[CrossRef](#)]
98. Konarov, A.; Bakenov, Z.; Yashiro, H.; Sun, Y.-K.; Myung, S.-T. Effect of Carbon-Sulphur Bond in a Sulphur/Dehydrogenated Polyacrylonitrile/Reduced Graphene Oxide Composite Cathode for Lithium-Sulphur Batteries. *J. Power Sources* **2017**, *355*, 140–146. [[CrossRef](#)]

99. Krishnaveni, K.; Subadevi, R.; Sivakumar, M. Graphene Oxide-Crowned Poly(Acrylonitrile)/Sulfur as a Lithium–Sulfur Battery Cathode: Performance and Characterization. *SN Appl. Sci.* **2020**, *2*, 766. [[CrossRef](#)]
100. Wang, T.; Zhang, Q.; Zhong, J.; Chen, M.; Deng, H.; Cao, J.; Wang, L.; Peng, L.; Zhu, J.; Lu, B. 3D Holey Graphene/Polyacrylonitrile Sulfur Composite Architecture for High Loading Lithium Sulfur Batteries. *Adv. Energy Mater.* **2021**, *11*, 2100448. [[CrossRef](#)]
101. Kim, H.; Hwang, J.-Y.; Bang, S.; Jung, H.-G.; Sun, Y.-K. Geometrical Engineering of a SPAN–Graphene Composite Cathode for Practical Li–S Batteries. *J. Mater. Chem. A* **2022**, *10*, 10844–10853. [[CrossRef](#)]
102. Lu, J.; Zhang, Y.; Huang, J.; Jiang, H.; Liang, B.; Wang, B.; He, D.; Chen, H. A Free-Standing Sulfide Polyacrylonitrile/Reduced Graphene Oxide Film Cathode with Nacre-like Architecture for High-Performance Lithium-Sulfur Batteries. *J. Power Sources* **2025**, *629*, 235916. [[CrossRef](#)]
103. Li, Y.; Zeng, Q.; Gentle, I.R.; Wang, D.-W. “Soft” Graphene Oxide-Organopolysulfide Nanocomposites for Superior Pseudocapacitive Lithium Storage. *Chin. Chem. Lett.* **2018**, *29*, 603–605. [[CrossRef](#)]
104. Kumar, A.; Verma, C.J.; Singh, M.K.; Prakash, R. 5—Porous Carbon from Conducting Polymers for Electrochemical Applications. In *Conjugated Polymers for Next-Generation Applications*; Kumar, V., Sharma, K., Sehgal, R., Kalia, S., Eds.; Woodhead Publishing Series in Electronic and Optical Materials; Woodhead Publishing: Sawston, UK, 2022; Volume 1, pp. 147–180, ISBN 978-0-12-823442-6.
105. Wen, Z.; Lu, D. Fabrication and Electrochemical Performance of Polyacrylonitrile-S/Carbon Composite as Cathode for Lithium Ion Batteries. *J. Electrochem. Soc.* **2013**, *160*, A2311. [[CrossRef](#)]
106. Sohn, H.; Gordin, M.L.; Regula, M.; Kim, D.H.; Jung, Y.S.; Song, J.; Wang, D. Porous Spherical Polyacrylonitrile-Carbon Nanocomposite with High Loading of Sulfur for Lithium–Sulfur Batteries. *J. Power Sources* **2016**, *302*, 70–78. [[CrossRef](#)]
107. Xu, A.; Jin, Z.; Wang, B.; Xie, X.; Xiao, X.; Wang, A.; Zhang, J.; Wang, W.; Lu, J.; Zeng, F. Unraveling the Mechanism on Improved Kinetics Performance of Sulfurized Polyacrylonitrile with Defective Conductive Carbon Matrix. *Chem. Eng. J.* **2024**, *484*, 149558. [[CrossRef](#)]
108. Chang, Z.; Dou, H.; Ding, B.; Wang, J.; Wang, Y.; Xu, G.; Li, C. Interconnected Core–Shell Pyrolyzed Polyacrylonitrile@sulfur/Carbon Nanocomposites for Rechargeable Lithium–Sulfur Batteries. *New J. Chem.* **2016**, *40*, 7680–7686. [[CrossRef](#)]
109. Zhang, Y.-Z.; Wu, Z.-Z.; Pan, G.-L.; Liu, S.; Gao, X.-P. Microporous Carbon Polyhedrons Encapsulated Polyacrylonitrile Nanofibers as Sulfur Immobilizer for Lithium–Sulfur Battery. *ACS Appl. Mater. Interfaces* **2017**, *9*, 12436–12444. [[CrossRef](#)]
110. Kuo, C.J.; Weret, M.A.; Hung, H.; Tsai, M.; Huang, C.; Su, W.; Hwang, B. Sulfurized–poly(Acrylonitrile) Wrapped Carbonsulfur Composite Cathode Material for High Performance Rechargeable Lithiumsulfur Batteries. *J. Power Sources* **2019**, *412*, 670–676. [[CrossRef](#)]
111. Zhang, W.; Pan, J.; Liu, P.; Ouyang, Z.; Fang, R.; Zhang, S.; Lian, J. A Li<sup>+</sup>-Conductive Porous Carbon/Polyacrylonitrile/Sulfur Composite for Li–S Batteries. *Int. J. Electrochem. Sci.* **2020**, *15*, 7925–7934. [[CrossRef](#)]
112. Qin, F.; Zhang, K.; Hong, B.; Zhang, L.; Zhang, Z.; Li, J.; Wang, X.; Lai, Y. A New Insight into Capacity Fading of Sulfurized Polyacrylonitrile Composite in Carbonate Electrolyte. *J. Electroanal. Chem.* **2021**, *882*, 114964. [[CrossRef](#)]
113. Insinna, T.; Bassey, E.N.; Märker, K.; Collauto, A.; Barra, A.-L.; Grey, C.P. Graphite Anodes for Li-Ion Batteries: An Electron Paramagnetic Resonance Investigation. *Chem. Mater.* **2023**, *35*, 5497–5511. [[CrossRef](#)]
114. Zhang, W.; Liu, P.; Chen, Z.; Fang, R.; Kang, D.; Ouyang, Z.; Zhang, S. Polyacrylonitile/Sulphur (PAN-S) Cathode with KS6 Graphite as the Conductive Agent for Li–S Battery. *Int. J. Electrochem. Sci.* **2021**, *16*, 210247. [[CrossRef](#)]
115. Liu, Y.; Haridas, A.K.; Lee, Y.; Cho, K.-K.; Ahn, J.-H. Freestanding Porous Sulfurized Polyacrylonitrile Fiber as a Cathode Material for Advanced Lithium Sulfur Batteries. *Appl. Surf. Sci.* **2019**, *472*, 135–142. [[CrossRef](#)]
116. Han, Z.; Li, S.; Xiong, R.; Jiang, Z.; Sun, M.; Hu, W.; Peng, L.; He, R.; Zhou, H.; Yu, C.; et al. Low Tortuosity and Reinforced Concrete Type Ultra-Thick Electrode for Practical Lithium–Sulfur Batteries. *Adv. Funct. Mater.* **2022**, *32*, 2108669. [[CrossRef](#)]
117. Jo, C.-H.; Yu, J.H.; Kim, H.J.; Hwang, J.-Y.; Kim, J.-Y.; Jung, H.-G.; Myung, S.-T. Sulfurized Carbon Composite with Unprecedentedly High Tap Density for Sodium Storage. *Adv. Energy Mater.* **2022**, *12*, 2102836. [[CrossRef](#)]
118. Dogadkin, B.A.; Shershnev, V.A. Vulcanization of Rubber in the Presence of Organic Accelerators. *Rubber Chem. Technol.* **1962**, *35*, 1–56. [[CrossRef](#)]
119. Chen, H.; Wang, C.; Hu, C.; Zhang, J.; Gao, S.; Lu, W.; Chen, L. Vulcanization Accelerator Enabled Sulfurized Carbon Materials for High Capacity and High Stability of Lithium–Sulfur Batteries. *J. Mater. Chem. A* **2014**, *3*, 1392–1395. [[CrossRef](#)]
120. Wang, Y.; Shuai, Y.; Chen, K. Diphenyl Guanidine as Vulcanization Accelerators in Sulfurized Polyacrylonitrile for High Performance Lithium-Sulfur Battery. *Chem. Eng. J.* **2020**, *388*, 124378. [[CrossRef](#)]
121. Wang, Y.; Zhang, Y.; Shuai, Y.; Chen, K. Diphenyl Guanidine Vulcanization Accelerators Enable Sulfurized Polyacrylonitrile Cathode for High Capacity and Ether-Compatible by Fast Kinetic. *Energy* **2021**, *233*, 121160. [[CrossRef](#)]
122. Qin, J.; Lu, Y.; Wang, R.; Li, Z.; Shen, T.; Wang, D. Sulfurization Accelerator Coupled Fe1–xS Electrocatalyst Boosting SPAN Cathode Performance. *Nano Res.* **2023**, *16*, 9231–9239. [[CrossRef](#)]
123. Wu, Q.; Qin, M.; Wu, Y.; Zhu, H.; Cheng, S.; Xie, J. Triallyl Isocyanurate Enabled SPAN-Based Organosulfur Featuring High Sulfur & Selenium Loading for Advanced Li/Na–S Batteries. *J. Mater. Chem. A* **2023**, *11*, 22913–22921. [[CrossRef](#)]

124. Zhang, X.; Lu, H.-C.; Hao, C.-R.; Liu, J.-Q.; Kong, X.-R.; Wang, J.-L. Delaying Cyclization of Polyacrylonitrile by Boric Acid for Sulfurized Poly(Acrylonitrile) Cathode Materials. *Chem. Eng. J.* **2024**, *500*, 156857. [[CrossRef](#)]
125. Ouyang, Q.; Wang, H.; Cheng, L.; Sun, Y. Effect of Boric Acid on the Stabilization of Poly(Acrylonitrile-Co-Itaconic Acid). *J. Polym. Res.* **2007**, *14*, 497–503. [[CrossRef](#)]
126. Ouyang, Q.; Cheng, L.; Wang, H.; Li, K. FTIR Study of the Retardation Effect of Boric Acid on the Cyclization Reaction of Polyacrylonitrile. *e-Polym.* **2009**, *9*, 015. [[CrossRef](#)]
127. Xiang, J.; Guo, Z.; Yi, Z.; Zhang, Y.; Yuan, L.; Cheng, Z.; Shen, Y.; Huang, Y. Facile Synthesis of Sulfurized Polyacrylonitrile Composite as Cathode for High-Rate Lithium-Sulfur Batteries. *J. Energy Chem.* **2020**, *49*, 161–165. [[CrossRef](#)]
128. Li, Y.; Zhang, S.; Liu, H.; Zhang, Y.; Zhang, X. Effects of Fiber Diameter on Sulfur Loading and Lithium–Sulfur Battery Performance of Semicarbonized and Sulfurized Polyacrylonitrile Cathode Materials. *ACS Appl. Energy Mater.* **2023**, *6*, 8511–8520. [[CrossRef](#)]
129. Hwang, T.H.; Jung, D.S.; Kim, J.-S.; Kim, B.G.; Choi, J.W. One-Dimensional Carbon–Sulfur Composite Fibers for Na–S Rechargeable Batteries Operating at Room Temperature. *Nano Lett.* **2013**, *13*, 4532–4538. [[CrossRef](#)]
130. Wang, K.; Zhao, T.; Zhang, N.; Feng, T.; Li, L.; Wu, F.; Chen, R. Powering Lithium–Sulfur Batteries by Ultrathin Sulfurized Polyacrylonitrile Nanosheets. *Nanoscale* **2021**, *13*, 16690–16695. [[CrossRef](#)]
131. Frey, M.; Zenn, R.K.; Warneke, S.; Müller, K.; Hintennach, A.; Dinnebier, R.E.; Buchmeiser, M.R. Easily Accessible, Textile Fiber-Based Sulfurized Poly(Acrylonitrile) as Li/S Cathode Material: Correlating Electrochemical Performance with Morphology and Structure. *ACS Energy Lett.* **2017**, *2*, 595–604. [[CrossRef](#)]
132. Liu, Y.; Haridas, A.K.; Cho, K.-K.; Lee, Y.; Ahn, J.-H. Highly Ordered Mesoporous Sulfurized Polyacrylonitrile Cathode Material for High-Rate Lithium Sulfur Batteries. *J. Phys. Chem. C* **2017**, *121*, 26172–26179. [[CrossRef](#)]
133. Warneke, S.; Zenn, R.K.; Lebherz, T.; Müller, K.; Hintennach, A.; Starke, U.; Dinnebier, R.E.; Buchmeiser, M.R. Hybrid Li/S Battery Based on Dimethyl Trisulfide and Sulfurized Poly(Acrylonitrile). *Adv. Sustain. Syst.* **2018**, *2*, 1700144. [[CrossRef](#)]
134. Wang, K.; Ju, S.; Gao, Q.; Xia, G.; Wang, G.; Yan, H.; Dong, L.; Yang, Z.; Yu, X. Porous Sulfurized Poly(Acrylonitrile) Nanofiber as a Long-Life and High-Capacity Cathode for Lithium–Sulfur Batteries. *J. Alloys Compd.* **2021**, *860*, 158445. [[CrossRef](#)]
135. Li, Z.; Zhang, J.; Lu, Y.; Lou, X.W. (David) A Pyrolyzed Polyacrylonitrile/Selenium Disulfide Composite Cathode with Remarkable Lithium and Sodium Storage Performances. *Sci. Adv.* **2018**, *4*, eaat1687. [[CrossRef](#)] [[PubMed](#)]
136. Zhang, L.; Zhang, W.; Zhu, Z.; Huang, Q.; Liu, X.; Zhang, M.; Pei, W.-B.; Wu, J. Multi-Channel Sulfurized Polyacrylonitrile with Hollow Structure as Cathode for Room Temperature Sodium–Sulfur Batteries. *J. Solid State Chem.* **2021**, *301*, 122359. [[CrossRef](#)]
137. Huang, X.; Liu, J.; Huang, Z.; Ke, X.; Liu, L.; Wang, N.; Liu, J.; Guo, Z.; Yang, Y.; Shi, Z. Flexible Free-Standing Sulfurized Polyacrylonitrile Electrode for Stable Li/Na Storage. *Electrochim. Acta* **2020**, *333*, 135493. [[CrossRef](#)]
138. Song, Y.; Lai, J.; Li, X.; Huo, J.; Zhao, C.; He, C. Steaming Inspired 3D Porous Architecture for Improving the Capability and Stability of Sulfurized Polyacrylonitrile Cathode. *Mater. Lett.* **2021**, *296*, 129933. [[CrossRef](#)]
139. Lebherz, T.; Frey, M.; Hintennach, A.; Buchmeiser, M.R. Influence of Morphology of Monolithic Sulfur–Poly(Acrylonitrile) Composites Used as Cathode Materials in Lithium–Sulfur Batteries on Electrochemical Performance. *RSC Adv.* **2019**, *9*, 7181–7188. [[CrossRef](#)]
140. He, R.; Li, Y.; Mu, Z.; Liu, H.; Zhang, Y.; Zhang, X. Flower-Shaped Sulfurized Polyacrylonitrile Nanostructures as Cathode Materials for High-Performance Lithium–Sulfur Batteries. *ACS Appl. Nano Mater.* **2023**, *6*, 23163–23172. [[CrossRef](#)]
141. Lei, J.; Chen, J.; Naveed, A.; Zhang, H.; Yang, J.; Nuli, Y.; Wang, J. Sulfurized Polyacrylonitrile Cathode Derived from Intermolecular Cross-Linked Polyacrylonitrile for a Rechargeable Lithium Battery. *ACS Appl. Energy Mater.* **2021**, *4*, 5706–5712. [[CrossRef](#)]
142. Lei, J.; Lu, H.; Chen, J.; Yang, J.; Nuli, Y.; Wang, J. Crosslinked Polyacrylonitrile Precursor for S@pPAN Composite Cathode Materials for Rechargeable Lithium Batteries. *J. Energy Chem.* **2022**, *65*, 186–193. [[CrossRef](#)]
143. Moschner, R.; Cavers, H.; Michalowski, P.; Kwade, A. Investigation of an Industrially Scalable Production of Sulfur–Polyacrylonitrile Based Cathodes. *Batter. Supercaps* **2024**, *7*, e202400154. [[CrossRef](#)]
144. Wang, W.; Xu, W.; Xia, S.; Xue, W.; Wang, J.; Wang, X.; Li, H.; Lin, S.; Zhao, Y.; Wang, L.; et al. A New Insight into the Molecular Rearrangement of Sulfurized Polyacrylonitrile Cathode in Ether Electrolyte. *Chem. Eng. J.* **2023**, *470*, 144142. [[CrossRef](#)]
145. Xue, W.; Xu, W.; Wang, W.; Gao, G.; Wang, L. Iodine-Doped Fibrous Sulfurized Polyacrylonitrile with Accelerated Reaction Kinetics. *Compos. Commun.* **2022**, *30*, 101078. [[CrossRef](#)]
146. Li, H.; Xue, W.; Wang, L.; Liu, T. Two Competing Reactions of Sulfurized Polyacrylonitrile Produce High-Performance Lithium–Sulfur Batteries. *ACS Appl. Mater. Interfaces* **2021**, *13*, 25002–25009. [[CrossRef](#)]
147. Yuan, X.; Zhu, B.; Feng, J.; Wang, C.; Cai, X.; Qin, R. Feasible Catalytic-Insoluble Strategy Enabled by Sulfurized Polyacrylonitrile with In Situ Built Electrocatalysts for Ultrastable Lithium–Sulfur Batteries. *ACS Appl. Mater. Interfaces* **2021**, *13*, 50936–50947. [[CrossRef](#)]
148. Haridas, A.K.; Heo, J.; Li, X.; Ahn, H.-J.; Zhao, X.; Deng, Z.; Agostini, M.; Matic, A.; Ahn, J.-H. A Flexible and Free-Standing FeS/Sulfurized Polyacrylonitrile Hybrid Anode Material for High-Rate Sodium-Ion Storage. *Chem. Eng. J.* **2020**, *385*, 123453. [[CrossRef](#)]

149. Weret, M.A.; Kuo, C.-F.J.; Su, W.-N.; Zeleke, T.S.; Huang, C.-J.; Sahalie, N.A.; Zegeye, T.A.; Wondimkun, Z.T.; Fenta, F.W.; Jote, B.A.; et al. Fibrous Organosulfur Cathode Materials with High Bonded Sulfur for High-Performance Lithium-Sulfur Batteries. *J. Power Sources* **2022**, *541*, 231693. [[CrossRef](#)]
150. Yi, Y.; Hai, F.; Guo, J.; Gao, X.; Chen, W.; Tian, X.; Tang, W.; Hua, W.; Li, M. Electrochemical Enhancement of Lithium-Ion Diffusion in Polypyrrole-Modified Sulfurized Polyacrylonitrile Nanotubes for Solid-to-Solid Free-Standing Lithium–Sulfur Cathodes. *Small* **2023**, *19*, 2303781. [[CrossRef](#)]
151. Liu, H.; Zhang, Y.; Li, Y.; Han, N.; Liu, H.; Zhang, X. Solid-State Transformations of Active Materials in the Pores of Sulfurized-Polyacrylonitrile Fiber Membranes via Nucleophilic Reactions for High-Loading and Free-Standing Lithium–Sulfur Battery Cathodes. *Adv. Fiber Mater.* **2024**, *6*, 772–785. [[CrossRef](#)]
152. Gao, G.; Wang, J.; Zhang, X.; Li, H.; Wang, L.; Liu, T. An Ionic Liquid Enhanced Gel Polymer Electrolyte for High Performance Lithium-Metal Batteries Based on Sulfurized Polyacrylonitrile Cathode. *Compos. Commun.* **2022**, *31*, 101100. [[CrossRef](#)]
153. Kim, I.; Kim, C.H.; Choi, S.H.; Ahn, J.-P.; Ahn, J.-H.; Kim, K.-W.; Cairns, E.J.; Ahn, H.-J. A Singular Flexible Cathode for Room Temperature Sodium/Sulfur Battery. *J. Power Sources* **2016**, *307*, 31–37. [[CrossRef](#)]
154. Kim, H.; Sadan, M.K.; Kim, C.; Jo, J.; Seong, M.; Cho, K.-K.; Kim, K.-W.; Ahn, J.-H.; Ahn, H.-J. Enhanced Reversible Capacity of Sulfurized Polyacrylonitrile Cathode for Room-Temperature Na/S Batteries by Electrochemical Activation. *Chem. Eng. J.* **2021**, *426*, 130787. [[CrossRef](#)]
155. Mentbayeva, A.; Belgibayeva, A.; Umurov, N.; Zhang, Y.; Taniguchi, I.; Kurmanbayeva, I.; Bakenov, Z. High Performance Freestanding Composite Cathode for Lithium-Sulfur Batteries. *Electrochim. Acta* **2016**, *217*, 242–248. [[CrossRef](#)]
156. Kim, H.; Kim, C.; Sadan, M.K.; Yeo, H.; Cho, K.-K.; Kim, K.-W.; Ahn, J.-H.; Ahn, H.-J. Binder-Free and High-Loading Sulfurized Polyacrylonitrile Cathode for Lithium/Sulfur Batteries. *RSC Adv.* **2021**, *11*, 16122–16130. [[CrossRef](#)]
157. Yang, K.; Kim, S.; Yang, X.; Cho, M.; Lee, Y. Binder-Free and High-Loading Cathode Realized by Hierarchical Structure for Potassium–Sulfur Batteries. *Small Methods* **2022**, *6*, 2100899. [[CrossRef](#)] [[PubMed](#)]
158. Sabet, S.M.; Sapkota, N.; Chiluwal, S.; Zheng, T.; Clemons, C.M.; Rao, A.M.; Pilla, S. Sulfurized Polyacrylonitrile Impregnated Delignified Wood-Based 3D Carbon Framework for High-Performance Lithium–Sulfur Batteries. *ACS Sustain. Chem. Eng.* **2023**, *11*, 2314–2323. [[CrossRef](#)]
159. Peng, H.; Wang, X.; Zhao, Y.; Tan, T.; Mentbayeva, A.; Bakenov, Z.; Zhang, Y. Enhanced Electrochemical Performance of Sulfur/Polyacrylonitrile Composite by Carbon Coating for Lithium/Sulfur Batteries. *J. Nanopart. Res.* **2017**, *19*, 348. [[CrossRef](#)]
160. Wang, S.-L.; Hong, J.-L. Polydopamine as an Interfacial Layer to Enhance Mechanical and Adhesive Properties of the Active Materials in a Sulfur Cathode of Sodium-Sulfur Batteries. *Chem. Eng. J. Adv.* **2022**, *11*, 100352. [[CrossRef](#)]
161. Zuo, W.; Li, R.; Wu, X.; Guo, Y.; Zhou, S.; Wen, B.; Luo, J.; Zhang, L. SPAN Secondary Particles Enabled High Energy Density Lithium-Sulfur Battery. *Chem. Eng. J.* **2024**, *491*, 151977. [[CrossRef](#)]
162. Holoubek, J.; Yan, Q.; Liu, H.; Wu, Z.; Xing, X.; Zhou, H.; Luo, J.; Chen, Z.; Liu, P. Low-Cost Li||SPAN Batteries Enabled by Sustained Additive Release. *ACS Appl. Energy Mater.* **2021**, *4*, 6422–6429. [[CrossRef](#)]
163. Qin, R.; Wang, Z.; Li, J.; Deng, L. Sulfureted Polyacrylonitrile Derived Carbon Encapsulated Silicon as High-Performance Anode Material for Lithium-Ion Batteries. *J. Alloys Compd.* **2022**, *929*, 167355. [[CrossRef](#)]
164. Liu, Y.; Wang, W.; Wang, A.; Jin, Z.; Zhao, H.; Yang, Y. A Polysulfide Reduction Accelerator—NiS<sub>2</sub>-Modified Sulfurized Polyacrylonitrile as a High Performance Cathode Material for Lithium–Sulfur Batteries. *J. Mater. Chem. A* **2017**, *5*, 22120–22124. [[CrossRef](#)]
165. Haridas, A.K.; Heo, J.; Liu, Y.; Ahn, H.-J.; Zhao, X.; Deng, Z.; Agostini, M.; Matic, A.; Cho, K.-K.; Ahn, J.-H. Boosting High Energy Density Lithium-Ion Storage via the Rational Design of an FeS-Incorporated Sulfurized Polyacrylonitrile Fiber Hybrid Cathode. *ACS Appl. Mater. Interfaces* **2019**, *11*, 29924–29933. [[CrossRef](#)]
166. Li, Y.; He, R.; Liu, H.; Zhang, Y.; Liu, H.; Han, N.; Zhang, X. Construction of CoS<sub>2</sub> Reduction Accelerator-Modified Sulfurized Polyacrylonitrile Nanofibers as High-Performance Cathode Materials for Practical Lithium–Sulfur Batteries. *ACS Appl. Energy Mater.* **2023**, *6*, 8466–8478. [[CrossRef](#)]
167. Xu, Z.-Q.; Zou, R.; Liu, W.-W.; Liu, G.-L.; Cui, Y.-S.; Lei, Y.-X.; Zheng, Y.-W.; Niu, W.-J.; Wu, Y.-Z.; Gu, B.-N.; et al. Design of Atomic Cobalt Selenide-Doped Sulfurized Polyacrylonitrile Cathode with Enhanced Electrochemical Kinetics for High Performance Lithium-SPAN Batteries. *Chem. Eng. J.* **2023**, *471*, 144581. [[CrossRef](#)]
168. Wang, L.; Shi, H.; Xie, Y.; Wu, Z.-S. Boosting Solid–Solid Conversion Kinetics of Sulfurized Polyacrylonitrile via MoS<sub>2</sub> Doping for High-Rate and Long-Life Li-S Batteries. *Carbon Neutralization* **2023**, *2*, 262–270. [[CrossRef](#)]
169. Lei, Z.; Zheng, J.; He, X.; Wang, Y.; Yang, X.; Xiao, F.; Xue, H.; Xiong, P.; Wei, M.; Chen, Q.; et al. Defect-Rich WS<sub>2</sub>–SPAN Nanofibers for Sodium/Potassium-Ion Batteries: Ultralong Lifespans and Wide-Temperature Workability. *Inorg. Chem. Front.* **2023**, *10*, 1187–1196. [[CrossRef](#)]
170. Xiao, F.; Zhang, J.; Zhou, W.; Fang, Y.; He, X.; Lai, W.; Lin, C.; Ge, M.; Fan, H.; Qian, Q.; et al. Defect-Engineered WS<sub>x</sub>Se<sub>2-x</sub> Nanocrystals Anchored on Selenized Polyacrylonitrile Fibers toward High-Performance Sodium/Potassium-Ion Batteries with a Wide Working Temperature Range. *Inorg. Chem. Front.* **2024**, *11*, 2164–2177. [[CrossRef](#)]

171. Li, X.; Liu, Y.; Lin, C.; Wang, Y.; Lei, Z.; Xiong, P.; Luo, Y.; Chen, Q.; Zeng, L.; Wei, M.; et al. Structure Engineering of BiSbS Nanocrystals Embedded within Sulfurized Polyacrylonitrile Fibers for High Performance of Potassium-Ion Batteries. *Chem.—Eur. J.* **2022**, *28*, e202200028. [[CrossRef](#)]
172. Li, R.; Tong, L.; Jiang, Y.; Wang, Y.; Long, J.; Chen, X.; Wu, J.; Li, X.; Chen, Y. SnS<sub>2</sub> Nanoparticles Embedded in Sulfurized Polyacrylonitrile Composite Fibers for High-Performance Potassium-Ion Batteries. *Interdiscip. Mater.* **2024**, *3*, 150–159. [[CrossRef](#)]
173. Wang, Y.; Guan, Z.; Zhang, Y.; Qu, B.; Sa, B.; Zhou, X.; Wang, J.; Peng, D.-L.; Xie, Q.; Pan, F. Li<sup>+</sup>/Mg<sup>2+</sup> Co-Intercalation SnS<sub>2</sub>-SPAN Cathode for Super-Stable Magnesium-Based Batteries. *J. Magnes. Alloys* **2024**, *in press*. [[CrossRef](#)]
174. Zhang, Y.; Zhao, Y.; Yermukhambetova, A.; Bakenov, Z.; Chen, P. Ternary Sulfur/Polyacrylonitrile/Mg<sub>0.6</sub>Ni<sub>0.4</sub>O Composite Cathodes for High Performance Lithium/Sulfur Batteries. *J. Mater. Chem. A* **2012**, *1*, 295–301. [[CrossRef](#)]
175. He, Y.; Shan, Z.; Tan, T.; Chen, Z.; Zhang, Y. Ternary Sulfur/Polyacrylonitrile/SiO<sub>2</sub> Composite Cathodes for High-Performance Sulfur/Lithium Ion Full Batteries. *Polymers* **2018**, *10*, 930. [[CrossRef](#)] [[PubMed](#)]
176. Páez Jerez, A.L.; Davies, L.E.; Tesio, A.Y.; Flexer, V. Synergistic Combination of TiO<sub>2</sub> and S-PAN for Li-S Batteries with Long-Term Cyclability at High C-Rates. *J. Electrochem. Soc.* **2021**, *168*, 120536. [[CrossRef](#)]
177. Fang, L.; Xu, W.; Lyu, X.; Liu, Y.; Reinhart, B.; Nguyen, H.; Li, T. Suppressing the Shuttle Effects with FeCo/SPAN Cathodes and High-Concentration Electrolytes for High-Performance Lithium-Sulfur Batteries. *ACS Appl. Energy Mater.* **2023**, *6*, 795–801. [[CrossRef](#)]
178. Blázquez-Moreno, J.M.; Páez Jerez, A.L.; Tesio, A.Y.; Benítez, A.; Caballero, Á. Stable Long-Term Cycling of Room-Temperature Sodium-Sulfur Batteries Based on Non-Complex Sulfurised Polyacrylonitrile Cathodes. *Batter. Supercaps* **2025**, *8*, e202400640. [[CrossRef](#)]
179. Páez Jerez, A.L.; Vera, M.L.; Sham, E.L.; Tesio, A.Y.; Flexer, V. Novel Multicomponent Composite with TiO<sub>2</sub>/Y<sub>2</sub>O<sub>3</sub> as Cathode Material and Interlayer for Li-SPAN Batteries Cycled at High C-Rates. *Electrochim. Acta* **2023**, *463*, 142876. [[CrossRef](#)]
180. Yuan, X.; Zhu, B.; Feng, J.; Wang, C.; Cai, X.; Qin, R. An In-Situ Catalytic-Insoluble Strategy Enabled by Sulfurized Polyacrylonitrile-Based Composite Cathode for Potassium–Sulfur Batteries. *Funct. Mater. Lett.* **2021**, *14*, 2143003. [[CrossRef](#)]
181. Ma, S.; Zuo, P.; Zhang, H.; Yu, Z.; Cui, C.; He, M.; Yin, G. Iodine-Doped Sulfurized Polyacrylonitrile with Enhanced Electrochemical Performance for Room-Temperature Sodium/Potassium Sulfur Batteries. *Chem. Commun.* **2019**, *55*, 5267–5270. [[CrossRef](#)]
182. Ma, S.; Zhang, Z.; Wang, Y.; Yu, Z.; Cui, C.; He, M.; Huo, H.; Yin, G.; Zuo, P. Iodine-Doped Sulfurized Polyacrylonitrile with Enhanced Electrochemical Performance for Lithium Sulfur Batteries in Carbonate Electrolyte. *Chem. Eng. J.* **2021**, *418*, 129410. [[CrossRef](#)]
183. Ma, S.; Wang, Y.; Fu, C.; Ma, Y.; Gao, Y.; Yin, G.; Zuo, P. Black Phosphorus-Modified Sulfurized Polyacrylonitrile with High C-Rate and Cycling Performance in Ether-Based Electrolyte for Lithium Sulfur Batteries. *Chem. Commun.* **2020**, *56*, 12797–12800. [[CrossRef](#)]
184. Wang, Y.; Zuo, P.; Ma, S.; Xie, B.; Yu, Z.; Yin, G. DFT and Experimental Study of Nano Red Phosphorus Anchoring on Sulfurized Polyacrylonitrile for Lithium-Ion Batteries. *Chem. Commun.* **2020**, *56*, 12857–12860. [[CrossRef](#)] [[PubMed](#)]
185. Rabiei Baboukani, A.; Khakpour, I.; Adelowo, E.; Drozd, V.; Shang, W.; Wang, C. High-Performance Red Phosphorus-Sulfurized Polyacrylonitrile Composite by Electrostatic Spray Deposition for Lithium-Ion Batteries. *Electrochim. Acta* **2020**, *345*, 136227. [[CrossRef](#)]
186. Hu, Y.; Li, B.; Jiao, X.; Zhang, C.; Dai, X.; Song, J. Stable Cycling of Phosphorus Anode for Sodium-Ion Batteries through Chemical Bonding with Sulfurized Polyacrylonitrile. *Adv. Funct. Mater.* **2018**, *28*, 1801010. [[CrossRef](#)]
187. Abouimrane, A.; Dambournet, D.; Chapman, K.W.; Chupas, P.J.; Weng, W.; Amine, K. A New Class of Lithium and Sodium Rechargeable Batteries Based on Selenium and Selenium–Sulfur as a Positive Electrode. *J. Am. Chem. Soc.* **2012**, *134*, 4505–4508. [[CrossRef](#)]
188. Wang, H.; Li, S.; Chen, Z.; Liu, H.K.; Guo, Z. A Novel Type of One-Dimensional Organic Selenium-Containing Fiber with Superior Performance for Lithium–Selenium and Sodium–Selenium Batteries. *RSC Adv.* **2014**, *4*, 61673–61678. [[CrossRef](#)]
189. Guo, J.; Wen, Z.; Wang, Q.; Jin, J.; Ma, G. A Conductive Selenized Polyacrylonitrile Cathode Material for Re-Chargeable Lithium Batteries with Long Cycle Life. *J. Mater. Chem. A* **2015**, *3*, 19815–19821. [[CrossRef](#)]
190. Zhu, T.; Pang, Y.; Wang, Y.; Wang, C.; Xia, Y. S<sub>0.8</sub>7Se<sub>0.13</sub>/CPAN Composites as High Capacity and Stable Cycling Performance Cathode for Lithium Sulfur Battery. *Electrochim. Acta* **2018**, *281*, 789–795. [[CrossRef](#)]
191. Liu, Y.; Tai, Z.; Zhang, Q.; Wang, H.; Pang, W.K.; Liu, H.K.; Konstantinov, K.; Guo, Z. A New Energy Storage System: Rechargeable Potassium-Selenium Battery. *Nano Energy* **2017**, *35*, 36–43. [[CrossRef](#)]
192. Chen, X.; Peng, L.; Wang, L.; Yang, J.; Hao, Z.; Xiang, J.; Yuan, K.; Huang, Y.; Shan, B.; Yuan, L.; et al. Ether-Compatible Sulfurized Polyacrylonitrile Cathode with Excellent Performance Enabled by Fast Kinetics via Selenium Doping. *Nat. Commun.* **2019**, *10*, 1021. [[CrossRef](#)]
193. Jiang, M.; Wang, K.; Gao, S.; Wang, R.; Han, J.; Yan, J.; Cheng, S.; Jiang, K. Selenium as Extra Binding Site for Sulfur Species in Sulfurized Polyacrylonitrile Cathodes for High Capacity Lithium-Sulfur Batteries. *ChemElectroChem* **2019**, *6*, 1365–1370. [[CrossRef](#)]

194. Zhang, W.; Wang, H.; Zhang, N.; Liu, H.; Chen, Z.; Zhang, L.; Guo, S.; Li, D.; Xu, J. One-Step In Situ Preparation of Polymeric Selenium Sulfide Composite as a Cathode Material for Enhanced Sodium/Potassium Storage. *ACS Appl. Mater. Interfaces* **2019**, *11*, 29807–29813. [CrossRef] [PubMed]
195. Zhang, Y.; Sun, Y.; Peng, L.; Yang, J.; Jia, H.; Zhang, Z.; Shan, B.; Xie, J. Se as Eutectic Accelerator in Sulfurized Polyacrylonitrile for High Performance All-Solid-State Lithium-Sulfur Battery. *Energy Storage Mater.* **2019**, *21*, 287–296. [CrossRef]
196. Wang, L.; Chen, X.; Li, S.; Yang, J.; Sun, Y.; Peng, L.; Shan, B.; Xie, J. Effect of Eutectic Accelerator in Selenium-Doped Sulfurized Polyacrylonitrile for High Performance Room Temperature Sodium–Sulfur Batteries. *J. Mater. Chem. A* **2019**, *7*, 12732–12739. [CrossRef]
197. Pham, V.H.; Boscoboinik, J.A.; Stacchiola, D.J.; Self, E.C.; Manikandan, P.; Nagarajan, S.; Wang, Y.; Pol, V.G.; Nanda, J.; Paek, E.; et al. Selenium-Sulfur (SeS) Fast Charging Cathode for Sodium and Lithium Metal Batteries. *Energy Storage Mater.* **2019**, *20*, 71–79. [CrossRef]
198. Jia, H.; Liang, X.; An, T.; Peng, L.; Feng, J.; Xie, J. Effect of Halogen Doping in Sodium Solid Electrolytes Based on the Na–Sn–Si–P–S Quinary System. *Chem. Mater.* **2020**, *32*, 4065–4071. [CrossRef]
199. Jia, H.; Peng, L.; Zhang, Z.; An, T.; Xie, J.  $\text{Na}_{3.8}[\text{Sn}_{0.67}\text{Si}_{0.33}]_{0.8}\text{Sb}_{0.2}\text{S}_4$ : A Quinary Sodium Fast Ionic Conductor for All-Solid-State Sodium Battery. *J. Energy Chem.* **2020**, *48*, 102–106. [CrossRef]
200. An, T.; Jia, H.; Peng, L.; Xie, J. Material and Interfacial Modification toward a Stable Room-Temperature Solid-State Na–S Battery. *ACS Appl. Mater. Interfaces* **2020**, *12*, 20563–20569. [CrossRef]
201. Zhang, Z.; Cao, H.; Yang, M.; Yan, X.; Yu, C.; Liu, D.; Zhang, L. High Performance Room Temperature All-Solid-State Na–SexS Battery with  $\text{Na}_3\text{SbS}_4$ -Coated Cathode via Aqueous Solution. *J. Energy Chem.* **2020**, *48*, 250–258. [CrossRef]
202. Zhang, Z.; Yu, C.; Xu, R.; Peng, L.; Ren, H.; Zhang, J.; Zhang, L.; Cheng, S.; Xie, J. Iodine-Rich Lithium Argyrodite with Enhanced Ionic Conductivity for Solid-State Batteries. *Scr. Mater.* **2022**, *210*, 114475. [CrossRef]
203. Jiang, Z.; Guo, H.-J.; Zeng, Z.; Han, Z.; Hu, W.; Wen, R.; Xie, J. Reconfiguring Organosulfur Cathode by Over-Lithiation to Enable Ultrathick Lithium Metal Anode toward Practical Lithium–Sulfur Batteries. *ACS Nano* **2020**, *14*, 13784–13793. [CrossRef] [PubMed]
204. Jiang, Z.; Zeng, Z.; Liang, X.; Yang, L.; Hu, W.; Zhang, C.; Han, Z.; Feng, J.; Xie, J. Fluorobenzene, A Low-Density, Economical, and Bifunctional Hydrocarbon Cosolvent for Practical Lithium Metal Batteries. *Adv. Funct. Mater.* **2021**, *31*, 2005991. [CrossRef]
205. Jiang, Z.; Zeng, Z.; Hu, W.; Han, Z.; Cheng, S.; Xie, J. Diluted High Concentration Electrolyte with Dual Effects for Practical Lithium–Sulfur Batteries. *Energy Storage Mater.* **2021**, *36*, 333–340. [CrossRef]
206. Zhang, W.; Li, S.; Wang, L.; Wang, X.; Xie, J. Insight into Sulfur-Rich Selenium Sulfide/Pyrolyzed Polyacrylonitrile Cathodes for Li–S Batteries. *Sustain. Energy Fuels* **2020**, *4*, 3588–3596. [CrossRef]
207. Liu, Y.; Yang, D.; Wang, W.; Hu, K.; Huang, Q.; Zhang, Y.; Miao, Y.; Fu, L.; Wu, M.; Wu, Y. Toward Heat-Tolerant Potassium Batteries Based on Pyrolyzed Selenium Disulfide/Polyacrylonitrile Positive Electrode and Gel Polymer Electrolyte. *J. Mater. Chem. A* **2020**, *8*, 4544–4551. [CrossRef]
208. He, B.; Rao, Z.; Cheng, Z.; Liu, D.; He, D.; Chen, J.; Miao, Z.; Yuan, L.; Li, Z.; Huang, Y. Rationally Design a Sulfur Cathode with Solid-Phase Conversion Mechanism for High Cycle-Stable Li–S Batteries. *Adv. Energy Mater.* **2021**, *11*, 2003690. [CrossRef]
209. Teng, W.; Li, Y.; Ma, T.; Ren, X.; Nan, D.; Liu, J.; Wang, X.; Yang, Q.; Deng, J. Uniform Lithium Deposition Induced by  $\text{ZnF}_x(\text{OH})_y$  for High-Performance Sulfurized Polyacrylonitrile-Based Lithium–Sulfur Batteries. *Polymers* **2022**, *14*, 4494. [CrossRef]
210. Kong, X.; Kong, Y.; He, L.; Zhang, W.; Song, Y.; Liu, S.; Zhao, Y. A New Ether-Based Medium-Concentrated Electrolyte for Lithium–Sulfur Battery with Lean Li Anode. *J. Power Sources* **2022**, *551*, 232211. [CrossRef]
211. Kong, X.; Kong, Y.; Liao, X.; Liu, S.; Zhao, Y. A Novel Mixed Ether-Based Electrolyte for Lithium–Sulfur Batteries with Li Anode Protection by Dual Salts. *Sustain. Energy Fuels* **2022**, *6*, 3658–3668. [CrossRef]
212. Han, Z.; Zhang, H.; Wu, Q.; Li, S.; Zhong, W.; He, R.; Cheng, S.; Xie, J. High-Performance Prelithiated Si–S Full Cell Enabled by Trifluorobenzene Modified Diluted High-Concentration Electrolyte. *Mater. Today Energy* **2022**, *28*, 101069. [CrossRef]
213. Li, S.; Zhu, H.; Liu, Y.; Han, Z.; Peng, L.; Li, S.; Yu, C.; Cheng, S.; Xie, J. Codoped Porous Carbon Nanofibres as a Potassium Metal Host for Nonaqueous K-Ion Batteries. *Nat. Commun.* **2022**, *13*, 4911. [CrossRef]
214. Wang, Y.; Chen, X.; Chen, X.; Lin, C.; Wang, H.-E.; Xiong, P.; Chen, Q.; Qian, Q.; Wei, M.; Zeng, L. Stabilizing Intermediate Phases via the Efficient Confinement Effects of the  $\text{SnS}_2$ -SPAN Fibre Composite for Ultra-Stable Half/Full Sodium/Potassium-Ion Batteries. *J. Mater. Chem. A* **2022**, *10*, 11449–11457. [CrossRef]
215. Wang, Y.; Xiao, F.; Chen, X.; Xiong, P.; Lin, C.; Wang, H.-E.; Wei, M.; Qian, Q.; Chen, Q.; Zeng, L. Extraordinarily Stable and Wide-Temperature Range Sodium/Potassium-Ion Batteries Based on 1D SnSe-SePAN Composite Nanofibers. *InfoMat* **2023**, *5*, e12467. [CrossRef]
216. He, R.; Li, Y.; Wei, S.; Liu, H.; Zhang, S.; Han, N.; Liu, H.; Wang, X.; Zhang, X. Construction of High-Performance Sulfurized Poly(Acrylonitrile) Cathodes for Lithium–Sulfur Batteries via Catalytic and Conductive Regulation. *J. Alloys Compd.* **2022**, *919*, 165838. [CrossRef]

217. He, R.; Li, Y.; Yin, Z.; Liu, H.; Jin, Y.; Zhang, Y.; Liu, H.; Zhang, X. Selenium-Doped Sulfurized Poly(Acrylonitrile) Composites as Ultrastable and High-Volumetric-Capacity Cathodes for Lithium–Sulfur Batteries. *ACS Appl. Energy Mater.* **2023**, *6*, 3903–3914. [[CrossRef](#)]
218. Wu, Q.; Zhang, W.; Li, S.; Zhong, W.; Zhu, H.; Zeng, Z.; Yu, C.; Cheng, S.; Xie, J. Electrospun Sulfurized Polyacrylonitrile Nanofibers for Long-Term Cycling Stability and High-Rate Lithium–Sulfur Batteries. *ACS Appl. Energy Mater.* **2022**, *5*, 5212–5218. [[CrossRef](#)]
219. Xu, L.; Ye, J.; Guo, W.; Chen, T.; Chen, X.; Qian, Q.; Zhang, J.; Wei, M.; Peng, X.; Zeng, L. Rational Construction of VSe<sub>2</sub> Encapsulated in Selenized Polyacrylonitrile toward a High-Rate Capacity and Wide Temperature Tolerance for Potassium-Ion Batteries. *Inorg. Chem. Front.* **2023**, *10*, 5053–5063. [[CrossRef](#)]
220. Yuan, Z.; Zheng, J.; Chen, X.; Xiao, F.; Yang, X.; Luo, L.; Xiong, P.; Lai, W.; Lin, C.; Qin, F.; et al. In Situ Encapsulation of MoS<sub>x</sub>Se<sub>2-x</sub> Nanocrystals with the Synergistic Function of Anion Doping and Physical Confinement with Chemical Bonding for High-Performance Sodium/Potassium-Ion Batteries with Wide Temperature Workability. *ACS Sustain. Chem. Eng.* **2023**, *11*, 13050–13061. [[CrossRef](#)]
221. Yang, F.; Yun, Z.; Gao, H.; Gao, S.; Tian, Z.; Huang, J. Se as Eutectic Accelerator SPAN Cathode for K–S Batteries with Improved Specific Capacity and Reaction Kinetics. *ChemistrySelect* **2023**, *8*, e202302227. [[CrossRef](#)]
222. Liu, H.; Yan, T.; Xu, Q.; Zhang, Y.; Li, Y.; Han, N.; Liu, H.; Zhang, X. Enhancing the Performance of a Lithium-Sulfur Battery with Spatially Confined Mesoporous Nanoreactors in Sulfurized Polyacrylonitrile Cathodes. *J. Colloid Interface Sci.* **2025**, *678*, 829–840. [[CrossRef](#)]
223. Ma, T.; Ren, X.; Hu, L.; Teng, W.; Wang, X.; Wu, G.; Liu, J.; Nan, D.; Li, B.; Yu, X. A Diluted Electrolyte for Long-Life Sulfurized Polyacrylonitrile-Based Anode-Free Li-S Batteries. *Polymers* **2022**, *14*, 3312. [[CrossRef](#)] [[PubMed](#)]
224. Ma, T.; Deng, J.; Lin, Y.; Liang, Q.; Hu, L.; Wang, X.; Liu, J.; Zhao, X.; Li, Y.; Nan, D.; et al. Li-Rich Organosulfur Cathode with Boosted Kinetics for High-Energy Lithium-Sulfur Batteries. *Energy Environ. Mater.* **2024**, *7*, e12704. [[CrossRef](#)]
225. Ma, S.; Yu, Z.; Wang, L.; Zuo, P. Selenium-Doped Sulfurized Polyacrylonitrile Hybrid Cathodes with Ultrahigh Sulfur Content for High-Performance Solid-State Lithium Sulfur Batteries. *Langmuir* **2024**, *40*, 9255–9264. [[CrossRef](#)]
226. Wang, K.; Zhao, T.; Liu, Y.; Yu, T.; Chen, G.; Tang, W.; Li, L.; Wu, F.; Chen, R. Accelerating Redox Kinetics of Sulfurized Polyacrylonitrile Nanosheets by Trace Doping of Element. *Chem. Eng. J.* **2024**, *487*, 150300. [[CrossRef](#)]
227. Li, S.; Han, Z.; Hu, W.; Peng, L.; Yang, J.; Wang, L.; Zhang, Y.; Shan, B.; Xie, J. Manipulating Kinetics of Sulfurized Polyacrylonitrile with Tellurium as Eutectic Accelerator to Prevent Polysulfide Dissolution in Lithium-Sulfur Battery under Dissolution-Deposition Mechanism. *Nano Energy* **2019**, *60*, 153–161. [[CrossRef](#)]
228. Li, S.; Zeng, Z.; Yang, J.; Han, Z.; Hu, W.; Wang, L.; Ma, J.; Shan, B.; Xie, J. High Performance Room Temperature Sodium–Sulfur Battery by Eutectic Acceleration in Tellurium-Doped Sulfurized Polyacrylonitrile. *ACS Appl. Energy Mater.* **2019**, *2*, 2956–2964. [[CrossRef](#)]
229. Wang, K.; Guan, Y.; Jin, Z.; Wang, W.; Wang, A. Te<sub>0.045</sub>S<sub>0.955</sub>PAN Composite with High Average Discharge Voltage for Li–S Battery. *J. Energy Chem.* **2019**, *39*, 249–255. [[CrossRef](#)]
230. Zhang, W.; Zhang, Y.; Peng, L.; Li, S.; Wang, X.; Cheng, S.; Xie, J. Elevating Reactivity and Cyclability of All-Solid-State Lithium-Sulfur Batteries by the Combination of Tellurium-Doping and Surface Coating. *Nano Energy* **2020**, *76*, 105083. [[CrossRef](#)]
231. Li, Y.; He, R.; Liu, H.; Zhang, X. Construction of High-Rate Performance Sulfurized Poly(Acrylonitrile) Nanofibers Cathodes for Practical Lithium–Sulfur Batteries via Tellurium Catalytic Regulation. *Mater. Chem. Phys.* **2023**, *308*, 128288. [[CrossRef](#)]
232. Wu, Q.; Zhang, W.; Qin, M.; Zhong, W.; Yan, H.; Zhu, H.; Cheng, S.; Xie, J. Tellurium Doped Sulfurized Polyacrylonitrile Nanoflower for High-Energy-Density, Long-Lifespan Sodium-Sulfur Batteries. *Nano Energy* **2024**, *129*, 110049. [[CrossRef](#)]
233. Fang, C.; Li, J.; Zhang, M.; Zhang, Y.; Yang, F.; Lee, J.Z.; Lee, M.-H.; Alvarado, J.; Schroeder, M.A.; Yang, Y.; et al. Quantifying Inactive Lithium in Lithium Metal Batteries. *Nature* **2019**, *572*, 511–515. [[CrossRef](#)]
234. Liu, J.; Bao, Z.; Cui, Y.; Dufek, E.J.; Goodenough, J.B.; Khalifah, P.; Li, Q.; Liaw, B.Y.; Liu, P.; Manthiram, A.; et al. Pathways for Practical High-Energy Long-Cycling Lithium Metal Batteries. *Nat. Energy* **2019**, *4*, 180–186. [[CrossRef](#)]
235. Zhang, X.; Yang, Y.; Zhou, Z. Towards Practical Lithium-Metal Anodes. *Chem. Soc. Rev.* **2020**, *49*, 3040–3071. [[CrossRef](#)] [[PubMed](#)]
236. Albertus, P.; Babinec, S.; Litzelman, S.; Newman, A. Status and Challenges in Enabling the Lithium Metal Electrode for High-Energy and Low-Cost Rechargeable Batteries. *Nat. Energy* **2018**, *3*, 16–21. [[CrossRef](#)]
237. Ding, J.-F.; Xu, R.; Yan, C.; Li, B.-Q.; Yuan, H.; Huang, J.-Q. A Review on the Failure and Regulation of Solid Electrolyte Interphase in Lithium Batteries. *J. Energy Chem.* **2021**, *59*, 306–319. [[CrossRef](#)]
238. Jin, L.; Shen, C.; Wu, Q.; Shellikeri, A.; Zheng, J.; Zhang, C.; Zheng, J.P. Pre-Lithiation Strategies for Next-Generation Practical Lithium-Ion Batteries. *Adv. Sci.* **2021**, *8*, 2005031. [[CrossRef](#)]
239. He, X.; Ren, J.; Wang, L.; Pu, W.; Wan, C.; Jiang, C. Electrochemical Characteristics of Sulfur Composite Cathode for Reversible Lithium Storage. *Ionics* **2009**, *15*, 477–481. [[CrossRef](#)]
240. Machida, K.; Miyauchi, H.; Ushioda, Y.; Takahashi, K.; Seki, S. Investigation for Charge–Discharge Operations of Li<sub>4</sub>Ti<sub>5</sub>O<sub>12</sub>-Sulfur Batteries by Suitable Choice of Materials and Cell Preparation Processes. *Electrochemistry* **2022**, *90*, 067006. [[CrossRef](#)]

241. Shen, C.; Ye, D.; Jin, L.; Andrei, P.; Zheng, J.P. Communication—A Simple and Scalable Pre-Lithiation Approach for High Energy and Low Cost Lithium Ion Sulfur Batteries. *J. Electrochem. Soc.* **2020**, *167*, 060517. [[CrossRef](#)]
242. Wang, L.; Wang, X.; Zhan, R.; Chen, Z.; Tu, S.; Li, C.; Liu, X.; Seh, Z.W.; Sun, Y. Nanocomposite of Conducting Polymer and Li Metal for Rechargeable High Energy Density Batteries. *ACS Appl. Mater. Interfaces* **2022**, *14*, 37709–37715. [[CrossRef](#)]
243. Zhang, H.; Zhang, Y.; Cao, C.; Zhao, W.; Huang, K.; Zhang, Y.; Shen, Y.; Li, Z.; Huang, Y. Lithium–Sulfur Pouch Cells with 99% Capacity Retention for 1000 Cycles. *Energy Environ. Sci.* **2024**, *17*, 7047–7057. [[CrossRef](#)]
244. Shen, Y.; Zhang, J.; Pu, Y.; Wang, H.; Wang, B.; Qian, J.; Cao, Y.; Zhong, F.; Ai, X.; Yang, H. Effective Chemical Prelithiation Strategy for Building a Silicon/Sulfur Li-Ion Battery. *ACS Energy Lett.* **2019**, *4*, 1717–1724. [[CrossRef](#)]
245. Liu, Z.; Ma, S.; Mu, X.; Li, R.; Yin, G.; Zuo, P. A Scalable Cathode Chemical Prelithiation Strategy for Advanced Silicon-Based Lithium Ion Full Batteries. *ACS Appl. Mater. Interfaces* **2021**, *13*, 11985–11994. [[CrossRef](#)]
246. Lu, H.; Zhang, T.; Kuai, Y.; Yang, J.; Wang, J.; Nuli, Y.; Guo, Y.; Liang, C. A Superb 3D Composite Lithium Metal Anode Prepared by In-Situ Lithiation of Sulfurized Polyacrylonitrile. *Energy Storage Mater.* **2020**, *33*, 452–459. [[CrossRef](#)]
247. Guo, J.; Yang, Z.; Yu, Y.; Abruna, H.D.; Archer, L.A. Lithium–Sulfur Battery Cathode Enabled by Lithium–Nitrile Interaction. *J. Am. Chem. Soc.* **2013**, *135*, 763–767. [[CrossRef](#)]
248. Wang, P.; Xia, C.; Yang, J.; He, X.; Lv, K.; Ren, S.; Song, H.; Wang, J.; He, P.; Zhou, H. High-Energy Silicon-Sulfurized Poly(Acrylonitrile) Battery Based on a Nitrogen Evolution Reaction. *Sci. Bull.* **2022**, *67*, 256–262. [[CrossRef](#)]
249. Chen, W.-J.; Li, B.-Q.; Zhao, C.-X.; Zhao, M.; Yuan, T.-Q.; Sun, R.-C.; Huang, J.-Q.; Zhang, Q. Electrolyte Regulation towards Stable Lithium-Metal Anodes in Lithium–Sulfur Batteries with Sulfurized Polyacrylonitrile Cathodes. *Angew. Chem. Int. Ed.* **2020**, *59*, 10732–10745. [[CrossRef](#)]
250. Ahmed, M.S.; Lee, S.; Agostini, M.; Jeong, M.-G.; Jung, H.-G.; Ming, J.; Sun, Y.-K.; Kim, J.; Hwang, J.-Y. Multiscale Understanding of Covalently Fixed Sulfur–Polyacrylonitrile Composite as Advanced Cathode for Metal–Sulfur Batteries. *Adv. Sci.* **2021**, *8*, 2101123. [[CrossRef](#)]
251. Ma, T.; Tao, Z. Challenges and Prospects of Electrolyte Design for Lithium-Sulfurized Polyacrylonitrile Batteries. *Batter. Supercaps* **2024**, *7*, e202400284. [[CrossRef](#)]
252. Wang, L.; He, X.; Li, J.; Chen, M.; Gao, J.; Jiang, C. Charge/Discharge Characteristics of Sulfurized Polyacrylonitrile Composite with Different Sulfur Content in Carbonate Based Electrolyte for Lithium Batteries. *Electrochim. Acta* **2012**, *72*, 114–119. [[CrossRef](#)]
253. Warneke, S.; Hintennach, A.; Buchmeiser, M.R. Communication—Influence of Carbonate-Based Electrolyte Composition on Cell Performance of SPAN-Based Lithium–Sulfur-Batteries. *J. Electrochem. Soc.* **2018**, *165*, A2093. [[CrossRef](#)]
254. Shen, Z.; Zhang, W.; Mao, S.; Li, S.; Wang, X.; Lu, Y. Tailored Electrolytes Enabling Practical Lithium–Sulfur Full Batteries via Interfacial Protection. *ACS Energy Lett.* **2021**, *6*, 2673–2681. [[CrossRef](#)]
255. Wu, B.; Liu, Q.; Mu, D.; Ren, Y.; Li, Y.; Wang, L.; Xu, H.; Wu, F. New Desolvated Gel Electrolyte for Rechargeable Lithium Metal Sulfurized Polyacrylonitrile (S-PAN) Battery. *J. Phys. Chem. C* **2014**, *118*, 28369–28376. [[CrossRef](#)]
256. Beltran, S.P.; Balbuena, P.B. A Solid Electrolyte Interphase to Protect the Sulfurized Polyacrylonitrile (SPAN) Composite for Li–S Batteries: Computational Approach Addressing the Electrolyte/SPAN Interfacial Reactivity. *J. Mater. Chem. A* **2021**, *9*, 7888–7902. [[CrossRef](#)]
257. Klostermann, S.V.; Kappler, J.; Waigum, A.; Buchmeiser, M.R.; Köhn, A.; Kästner, J. The Reduction Behavior of Sulfurized Polyacrylonitrile (SPAN) in Lithium–Sulfur Batteries Using a Carbonate Electrolyte: A Computational Study. *Phys. Chem. Chem. Phys.* **2024**, *26*, 9998–10007. [[CrossRef](#)]
258. Lin, F.; Wang, J.; Jia, H.; Monroe, C.W.; Yang, J.; NuLi, Y. Nonflammable Electrolyte for Rechargeable Lithium Battery with Sulfur Based Composite Cathode Materials. *J. Power Sources* **2013**, *223*, 18–22. [[CrossRef](#)]
259. Wang, J.; Lin, F.; Jia, H.; Yang, J.; Monroe, C.W.; NuLi, Y. Towards a Safe Lithium–Sulfur Battery with a Flame-Inhibiting Electrolyte and a Sulfur-Based Composite Cathode. *Angew. Chem. Int. Ed.* **2014**, *53*, 10099–10104. [[CrossRef](#)]
260. Jia, H.; Wang, J.; Lin, F.; Monroe, C.W.; Yang, J.; NuLi, Y. TPPi as a Flame Retardant for Rechargeable Lithium Batteries with Sulfur Composite Cathodes. *Chem. Commun.* **2014**, *50*, 7011–7013. [[CrossRef](#)]
261. Yang, H.; Li, Q.; Guo, C.; Naveed, A.; Yang, J.; Nuli, Y.; Wang, J. Safer Lithium–Sulfur Battery Based on Nonflammable Electrolyte with Sulfur Composite Cathode. *Chem. Commun.* **2018**, *54*, 4132–4135. [[CrossRef](#)]
262. Wu, J.; Liu, J.; Lu, Z.; Lin, K.; Lyu, Y.-Q.; Li, B.; Ciucci, F.; Kim, J.-K. Non-Flammable Electrolyte for Dendrite-Free Sodium-Sulfur Battery. *Energy Storage Mater.* **2019**, *23*, 8–16. [[CrossRef](#)]
263. Wu, B.; Chen, F.; Mu, D.; Liao, W.; Wu, F. Cycleability of Sulfurized Polyacrylonitrile Cathode in Carbonate Electrolyte Containing Lithium Metasilicate. *J. Power Sources* **2015**, *278*, 27–31. [[CrossRef](#)]
264. Wang, L.; Li, Q.; Yang, H.; Yang, J.; Nuli, Y.; Wang, J. Superior Rate Capability of a Sulfur Composite Cathode in a Tris(Trimethylsilyl)Borate-Containing Functional Electrolyte. *Chem. Commun.* **2016**, *52*, 14430–14433. [[CrossRef](#)] [[PubMed](#)]
265. Xu, Z.; Wang, J.; Yang, J.; Miao, X.; Chen, R.; Qian, J.; Miao, R. Enhanced Performance of a Lithium–Sulfur Battery Using a Carbonate-Based Electrolyte. *Angew. Chem. Int. Ed.* **2016**, *55*, 10372–10375. [[CrossRef](#)]

266. Kim, H.M.; Hwang, J.-Y.; Aurbach, D.; Sun, Y.-K. Electrochemical Properties of Sulfurized-Polyacrylonitrile Cathode for Lithium-Sulfur Batteries: Effect of Polyacrylic Acid Binder and Fluoroethylene Carbonate Additive. *J. Phys. Chem. Lett.* **2017**, *8*, 5331–5337. [[CrossRef](#)]
267. Yang, H.; Naveed, A.; Li, Q.; Guo, C.; Chen, J.; Lei, J.; Yang, J.; Nuli, Y.; Wang, J. Lithium Sulfur Batteries with Compatible Electrolyte Both for Stable Cathode and Dendrite-Free Anode. *Energy Storage Mater.* **2018**, *15*, 299–307. [[CrossRef](#)]
268. Chen, Z.; Zhou, J.; Guo, Y.; Liang, C.; Yang, J.; Wang, J.; Nuli, Y. A Compatible Carbonate Electrolyte with Lithium Anode for High Performance Lithium Sulfur Battery. *Electrochim. Acta* **2018**, *282*, 555–562. [[CrossRef](#)]
269. Shuai, Y.; Zhang, Z.; Chen, K.; Lou, J.; Wang, Y. Highly Stable Lithium Plating by a Multifunctional Electrolyte Additive in a Lithium-Sulfurized Polyacrylonitrile Battery. *Chem. Commun.* **2019**, *55*, 2376–2379. [[CrossRef](#)]
270. Cai, G.; Holoubek, J.; Xia, D.; Li, M.; Yin, Y.; Xing, X.; Liu, P.; Chen, Z. An Ester Electrolyte for Lithium–Sulfur Batteries Capable of Ultra-Low Temperature Cycling. *Chem. Commun.* **2020**, *56*, 9114–9117. [[CrossRef](#)]
271. Park, H.; Kang, H.; Kim, H.; Kansara, S.; Allen, J.L.; Tran, D.; Sun, H.H.; Hwang, J.-Y. Strategy for High-Energy Li–S Battery Coupling with a Li Metal Anode and a Sulfurized Polyacrylonitrile Cathode. *ACS Appl. Mater. Interfaces* **2023**, *15*, 45876–45885. [[CrossRef](#)]
272. Dai, H.; Xi, K.; Liu, X.; Lai, C.; Zhang, S. Cationic Surfactant-Based Electrolyte Additives for Uniform Lithium Deposition via Lithiophobic Repulsion Mechanisms. *J. Am. Chem. Soc.* **2018**, *140*, 17515–17521. [[CrossRef](#)]
273. Jin, F.; Hu, C.; Liu, C.; Zheng, Y.; Chen, H.; Shen, Y.; Chen, L. Enhancing the Performance of Sulfurized Polyacrylonitrile Cathode by in-Situ Wrapping. *J. Electroanal. Chem.* **2019**, *835*, 156–160. [[CrossRef](#)]
274. Li, Q.; Yang, H.; Naveed, A.; Guo, C.; Yang, J.; Nuli, Y.; Wang, J. Duplex Component Additive of Tris(Trimethylsilyl) Phosphite-Vinylene Carbonate for Lithium Sulfur Batteries. *Energy Storage Mater.* **2018**, *14*, 75–81. [[CrossRef](#)]
275. Zhao, J.; Wan, Z.; Zeng, X.; Tian, M.; Wang, K.; Chen, X.; Ling, M.; Ni, W.; Liang, C. Solubilized LiNO<sub>3</sub> by the Cationic Size Effect of CsF for Lithium Metal Anode Protection and Dendrite Formation Prevention in Carbonate Electrolyte. *Inorg. Chem. Front.* **2023**, *10*, 1809–1817. [[CrossRef](#)]
276. Guo, Z.; Yang, H.; Wei, Q.; Xu, S.; Hu, G.; Bai, S.; Li, F. Dual-Additives Enable Stable Electrode-Electrolyte Interfaces for Long Life Li-SPAN Batteries. *Chin. Chem. Lett.* **2024**, *35*, 108622. [[CrossRef](#)]
277. Lebherz, T.; Weldin, D.L.; Hintennach, A.; Buchmeiser, M.R. Synthesis of Ionic Dendrimers and Their Potential Use as Electrolytes for Lithium–Sulfur Batteries. *Macromol. Chem. Phys.* **2020**, *221*, 1900436. [[CrossRef](#)]
278. Mayer, A.; Buchmeiser, M.R. Communication—Influence of Temperature and Electrolyte Viscosity on the Electrochemical Performance of SPAN-Based Lithium–Sulfur Cells. *J. Electrochem. Soc.* **2018**, *165*, A3943. [[CrossRef](#)]
279. Cai, G.; Gao, H.; Li, M.; Gupta, V.; Holoubek, J.; Pascal, T.A.; Liu, P.; Chen, Z. Partially Ion-Paired Solvation Structure Design for Lithium–Sulfur Batteries under Extreme Operating Conditions. *Angew. Chem. Int. Ed.* **2024**, *63*, e202316786. [[CrossRef](#)]
280. Zhao, C.-X.; Chen, W.-J.; Zhao, M.; Song, Y.-W.; Liu, J.-N.; Li, B.-Q.; Yuan, T.; Chen, C.-M.; Zhang, Q.; Huang, J.-Q. Redox Mediator Assists Electron Transfer in Lithium–Sulfur Batteries with Sulfurized Polyacrylonitrile Cathodes. *EcoMat* **2021**, *3*, e12066. [[CrossRef](#)]
281. Zhang, W.; Wu, Q.; Zeng, Z.; Yu, C.; Cheng, S.; Xie, J. An Organodiselenide Containing Electrolyte Enables Sulfurized Polyacrylonitrile Cathodes with Fast Redox Kinetics in Li–S Batteries. *Chem. Commun.* **2021**, *57*, 9688–9691. [[CrossRef](#)]
282. Chen, S.; Wu, G.; Jiang, H.; Wang, J.; Chen, T.; Han, C.; Wang, W.; Yang, R.; Zhao, J.; Tang, Z.; et al. External Li Supply Reshapes Li Deficiency and Lifetime Limit of Batteries. *Nature* **2025**, *638*, 676–683. [[CrossRef](#)]
283. Wang, J.; Yang, J.; Nuli, Y.; Holze, R. Room Temperature Na/S Batteries with Sulfur Composite Cathode Materials. *Electrochim. Commun.* **2007**, *9*, 31–34. [[CrossRef](#)]
284. Murugan, S.; Niesen, S.; Kappler, J.; Küster, K.; Starke, U.; Buchmeiser, M.R. Ultra-Stable Cycling of High Capacity Room Temperature Sodium–Sulfur Batteries Based on Sulfurated Poly(Acrylonitrile). *Batter. Supercaps* **2021**, *4*, 1636–1646. [[CrossRef](#)]
285. Murugan, S.; Klostermann, S.V.; Frey, W.; Kästner, J.; Buchmeiser, M.R. A Sodium Bis(Perfluoropinacol) Borate-Based Electrolyte for Stable, High-Performance Room Temperature Sodium–Sulfur Batteries Based on Sulfurized Poly(Acrylonitrile). *Electrochim. Commun.* **2021**, *132*, 107137. [[CrossRef](#)]
286. Liu, Y.; Wang, W.; Wang, J.; Zhang, Y.; Zhu, Y.; Chen, Y.; Fu, L.; Wu, Y. Sulfur Nanocomposite as a Positive Electrode Material for Rechargeable Potassium–Sulfur Batteries. *Chem. Commun.* **2018**, *54*, 2288–2291. [[CrossRef](#)] [[PubMed](#)]
287. Lou, J.; Zhang, Y.; Shuai, Y.; Chen, K.; Chen, S. Na<sup>+</sup>/K<sup>+</sup> Hybrid Battery Based on a Sulfurized Polyacrylonitrile Cathode. *Materials* **2019**, *12*, 969. [[CrossRef](#)]
288. Wu, Z.; Bak, S.-M.; Shadike, Z.; Yu, S.; Hu, E.; Xing, X.; Du, Y.; Yang, X.-Q.; Liu, H.; Liu, P. Understanding the Roles of the Electrode/Electrolyte Interface for Enabling Stable Li||Sulfurized Polyacrylonitrile Batteries. *ACS Appl. Mater. Interfaces* **2021**, *13*, 31733–31740. [[CrossRef](#)]
289. Miao, R.; Yang, J.; Feng, X.; Jia, H.; Wang, J.; Nuli, Y. Novel Dual-Salts Electrolyte Solution for Dendrite-Free Lithium-Metal Based Rechargeable Batteries with High Cycle Reversibility. *J. Power Sources* **2014**, *271*, 291–297. [[CrossRef](#)]

290. Kuai, D.; Wang, S.; Perez-Beltran, S.; Yu, S.; Real, G.A.; Liu, P.; Balbuena, P.B. Interfacial Electrochemical Lithiation and Dissolution Mechanisms at a Sulfurized Polyacrylonitrile Cathode Surface. *ACS Energy Lett.* **2024**, *9*, 810–818. [[CrossRef](#)]
291. Shuai, Y.; Wang, D.; Chen, K.; Zhang, Z.; Wang, Y.; Lou, J. Highly Stable Performance of Lithium-Sulfurized Polyacrylonitrile Batteries Using a Lean Ether-Based Electrolyte. *Chem. Commun.* **2019**, *55*, 11271–11274. [[CrossRef](#)]
292. Kim, J.-S.; Kim, D.W.; Jung, H.T.; Choi, J.W. Controlled Lithium Dendrite Growth by a Synergistic Effect of Multilayered Graphene Coating and an Electrolyte Additive. *Chem. Mater.* **2015**, *27*, 2780–2787. [[CrossRef](#)]
293. Kim, J.-S.; Yoo, D.-J.; Min, J.; Shakoor, R.A.; Kahraman, R.; Choi, J.W. Poreless Separator and Electrolyte Additive for Lithium-Sulfur Batteries with High Areal Energy Densities. *ChemNanoMat* **2015**, *1*, 240–245. [[CrossRef](#)]
294. Jia, P.; Wang, J.; Zheng, T.; Tao, C.; Yila, G.; Wang, L.; Wang, Y.; Liu, T. Boosting Cathode Activity and Anode Stability of Lithium–Sulfur Batteries with Vigorous Iodic Species Triggered by Nitrate. *Angew. Chem. Int. Ed.* **2024**, *63*, e202401055. [[CrossRef](#)] [[PubMed](#)]
295. Luo, J.; Chen, Z.; Zhang, R.; Lu, C.; Zhu, J.; Zhuang, X. Realizing Sulfurized Polyacrylonitrile Cathode in Ether-Based Electrolyte. *Electrochim. Acta* **2024**, *474*, 143533. [[CrossRef](#)]
296. Chen, W.-J.; Zhao, C.-X.; Li, B.-Q.; Jin, Q.; Zhang, X.-Q.; Yuan, T.-Q.; Zhang, X.; Jin, Z.; Kaskel, S.; Zhang, Q. A Mixed Ether Electrolyte for Lithium Metal Anode Protection in Working Lithium–Sulfur Batteries. *Energy Environ. Mater.* **2020**, *3*, 160–165. [[CrossRef](#)]
297. Zheng, X.; Zou, F.; Yang, H.; Su, X.; Hu, X.; Liu, X. 4-Aminobenzoic Acid as an Electrolyte Additive for Enhancing the Electrochemical Properties of the Sulfurized Polyacrylonitrile Cathode in Ether Electrolyte. *Ionics* **2023**, *29*, 3663–3671. [[CrossRef](#)]
298. Wu, Q.; Ma, F.; Zhang, W.; Yan, H.; Chen, X.; Cheng, S.; Xie, J. Bifunctional  $\text{Li}_2\text{Se}$  Mediator to Accelerate Sulfur Conversion and Lithium Deposition Kinetics in Lithium–Sulfurized Polyacrylonitrile Batteries. *ACS Appl. Energy Mater.* **2023**, *6*, 7138–7146. [[CrossRef](#)]
299. Zhang, W.; Ma, F.; Wu, Q.; Cai, Z.; Zhong, W.; Zeng, Z.; Cheng, S.; Xie, J. Bifunctional Fluorinated Anthraquinone Additive for Improving Kinetics and Interfacial Chemistry in Rechargeable Li–S Batteries. *ACS Appl. Energy Mater.* **2022**, *5*, 15719–15728. [[CrossRef](#)]
300. Holoubek, J.; Liu, H.; Wu, Z.; Yin, Y.; Xing, X.; Cai, G.; Yu, S.; Zhou, H.; Pascal, T.A.; Chen, Z.; et al. Tailoring Electrolyte Solvation for Li Metal Batteries Cycled at Ultra-Low Temperature. *Nat. Energy* **2021**, *6*, 303–313. [[CrossRef](#)]
301. Ma, T.; Ni, Y.; Wang, Q.; Zhang, W.; Jin, S.; Zheng, S.; Yang, X.; Hou, Y.; Tao, Z.; Chen, J. Optimize Lithium Deposition at Low Temperature by Weakly Solvating Power Solvent. *Angew. Chem.* **2022**, *134*, e202207927. [[CrossRef](#)]
302. Liu, X.; Wu, S.; Hao, Z.; Shang, L.; Guo, M.; Hou, J.; Shao, S.; Li, H.; Li, Y.; Lu, Y.; et al. Regulating Interface Dipole Interaction between Ethers and Active Species Toward Highly Stable Li-SPAN Batteries. *Angew. Chem. Int. Ed.* **2025**, *64*, e202416731. [[CrossRef](#)]
303. Cai, G.; Holoubek, J.; Li, M.; Gao, H.; Yin, Y.; Yu, S.; Liu, H.; Pascal, T.A.; Liu, P.; Chen, Z. Solvent Selection Criteria for Temperature-Resilient Lithium–Sulfur Batteries. *Proc. Natl. Acad. Sci. USA* **2022**, *119*, e2200392119. [[CrossRef](#)] [[PubMed](#)]
304. Wu, J.; Li, M.; Ma, L.; Li, X.; Chen, X.; Long, J.; Wang, Y.; Li, X.; Liu, J.; Guo, Z.; et al. Engineering Densely Packed Ion-Cluster Electrolytes for Wide-Temperature Lithium–Sulfurized Polyacrylonitrile Batteries. *ACS Nano* **2024**, *18*, 32984–32994. [[CrossRef](#)] [[PubMed](#)]
305. Ma, T.; Ni, Y.; Li, D.; Zha, Z.; Jin, S.; Zhang, W.; Jia, L.; Sun, Q.; Xie, W.; Tao, Z.; et al. Reversible Solid–Solid Conversion of Sulfurized Polyacrylonitrile Cathodes in Lithium–Sulfur Batteries by Weakly Solvating Ether Electrolytes. *Angew. Chem. Int. Ed.* **2023**, *62*, e202310761. [[CrossRef](#)]
306. Liu, T.; Feng, J.; Shi, Z.; Li, H.; Zhao, W.; Mao, M.; Zhu, X.; Hu, Y.-S.; Li, H.; Huang, X.; et al. Diminishing Ether-Oxygen Content of Electrolytes Enables Temperature-Immune Lithium Metal Batteries. *Sci. China Chem.* **2023**, *66*, 2700–2710. [[CrossRef](#)]
307. Pham, T.D.; Bin Faheem, A.; Kim, J.; Ma, S.-H.; Kwak, K.; Lee, K.-K. High-Efficiency Lithium Metal Stabilization and Polysulfide Suppression in Li–S Battery Enabled by Weakly Solvating Solvent. *Small* **2024**, *20*, 2307951. [[CrossRef](#)]
308. Yin, Y.; Holoubek, J.; Kim, K.; Liu, A.; Bhamwala, B.; Wang, S.; Lu, B.; Yu, K.; Gao, H.; Li, M.; et al. Coulombic Condensation of Liquefied Gas Electrolytes for Li Metal Batteries at Ambient Pressure. *Angew. Chem. Int. Ed.* **2025**, *64*, e202420411. [[CrossRef](#)]
309. Chen, J.; Lu, H.; Zhang, X.; Zhang, Y.; Yang, J.; Nuli, Y.; Huang, Y.; Wang, J. Electrochemical Polymerization of Nonflammable Electrolyte Enabling Fast-Charging Lithium-Sulfur Battery. *Energy Storage Mater.* **2022**, *50*, 387–394. [[CrossRef](#)]
310. Zhou, L.; Cao, Z.; Zhang, J.; Sun, Q.; Wu, Y.; Wahyudi, W.; Hwang, J.-Y.; Wang, L.; Cavallo, L.; Sun, Y.-K.; et al. Engineering Sodium-Ion Solvation Structure to Stabilize Sodium Anodes: Universal Strategy for Fast-Charging and Safer Sodium-Ion Batteries. *Nano Lett.* **2020**, *20*, 3247–3254. [[CrossRef](#)]
311. Liu, D.; Li, Z.; Li, X.; Chen, X.; Li, Z.; Yuan, L.; Huang, Y. Stable Room-Temperature Sodium–Sulfur Batteries in Ether-Based Electrolytes Enabled by the Fluoroethylene Carbonate Additive. *ACS Appl. Mater. Interfaces* **2022**, *14*, 6658–6666. [[CrossRef](#)]
312. Soni, C.B.; Bera, S.; Sungjemmenla; Chandra, M.; K., V.S.; Kumar, S.; Kumar, H.; Kumar, V. Altering Na-Ion Solvation to Regulate Dendrite Growth for a Reversible and Stable Room-Temperature Sodium–Sulfur Battery. *J. Mater. Chem. A* **2024**, *12*, 21853–21863. [[CrossRef](#)]

313. Basel, J.; Sapkota, N.; Parekh, M.; Rao, A.M. Electrolyte Optimization for Sodium-Sulfur Batteries. *Appl. Phys. Lett.* **2024**, *124*, 123901. [[CrossRef](#)]
314. Li, A.-M.; Zavalij, P.Y.; Omenya, F.; Li, X.; Wang, C. Salt-in-Presalt Electrolyte Solutions for High-Potential Non-Aqueous Sodium Metal Batteries. *Nat. Nanotechnol.* **2025**, *20*, 388–396. [[CrossRef](#)]
315. Park, J.; Oh, G.; Kim, U.-H.; Alfaruqi, M.H.; Xu, X.; Liu, Y.; Xiong, S.; Zikri, A.T.; Sun, Y.-K.; Kim, J.; et al. Regulating the Solvation Structure of Electrolyte via Dual-Salt Combination for Stable Potassium Metal Batteries. *Adv. Sci.* **2023**, *10*, 2301201. [[CrossRef](#)]
316. Wang, P.; Buchmeiser, M.R. Rechargeable Magnesium–Sulfur Battery Technology: State of the Art and Key Challenges. *Adv. Funct. Mater.* **2019**, *29*, 1905248. [[CrossRef](#)]
317. Wang, P.; Trück, J.; Niesen, S.; Kappler, J.; Küster, K.; Starke, U.; Ziegler, F.; Hintennach, A.; Buchmeiser, M.R. High-Performance Magnesium–Sulfur Batteries Based on a Sulfurated Poly(Acrylonitrile) Cathode, a Borohydride Electrolyte, and a High-Surface Area Magnesium Anode. *Batter. Supercaps* **2020**, *3*, 1239–1247. [[CrossRef](#)]
318. Wang, P.; Kappler, J.; Sievert, B.; Häcker, J.; Küster, K.; Starke, U.; Ziegler, F.; Buchmeiser, M.R. Characteristics of Magnesium–Sulfur Batteries Based on a Sulfurized Poly(Acrylonitrile) Composite and a Fluorinated Electrolyte. *Electrochim. Acta* **2020**, *361*, 137024. [[CrossRef](#)]
319. Shin, E.S.; Kim, K.; Oh, S.H.; Cho, W.I. Polysulfide Dissolution Control: The Common Ion Effect. *Chem. Commun.* **2013**, *49*, 2004–2006. [[CrossRef](#)]
320. Zhang, Y.Z.; Liu, S.; Li, G.C.; Li, G.R.; Gao, X.P. Sulfur/Polyacrylonitrile/Carbon Multi-Composites as Cathode Materials for Lithium/Sulfur Battery in the Concentrated Electrolyte. *J. Mater. Chem. A* **2014**, *2*, 4652–4659. [[CrossRef](#)]
321. Zhou, J.; Guo, Y.; Liang, C.; Cao, L.; Pan, H.; Yang, J.; Wang, J. A New Ether-Based Electrolyte for Lithium Sulfur Batteries Using a S@pPAN Cathode. *Chem. Commun.* **2018**, *54*, 5478–5481. [[CrossRef](#)]
322. Xing, X.; Li, Y.; Wang, X.; Petrova, V.; Liu, H.; Liu, P. Cathode Electrolyte Interface Enabling Stable Li–S Batteries. *Energy Storage Mater.* **2019**, *21*, 474–480. [[CrossRef](#)]
323. Ren, Y.; Lai, T.; Manthiram, A. Reversible Sodium–Sulfur Batteries Enabled by a Synergistic Dual-Additive Design. *ACS Energy Lett.* **2023**, *8*, 2746–2752. [[CrossRef](#)]
324. Zhang, J.; Cao, Z.; Zhou, L.; Park, G.-T.; Cavallo, L.; Wang, L.; Alshareef, H.N.; Sun, Y.-K.; Ming, J. Model-Based Design of Stable Electrolytes for Potassium Ion Batteries. *ACS Energy Lett.* **2020**, *5*, 3124–3131. [[CrossRef](#)]
325. Lee, S.; Park, H.; Rizell, J.; Kim, U.-H.; Liu, Y.; Xu, X.; Xiong, S.; Matic, A.; Zikri, A.T.; Kang, H.; et al. High-Energy and Long-Lifespan Potassium–Sulfur Batteries Enabled by Concentrated Electrolyte. *Adv. Funct. Mater.* **2022**, *32*, 2209145. [[CrossRef](#)]
326. Yoo, D.-J.; Yang, S.; Kim, K.J.; Choi, J.W. Fluorinated Aromatic Diluent for High-Performance Lithium Metal Batteries. *Angew. Chem. Int. Ed.* **2020**, *59*, 14869–14876. [[CrossRef](#)] [[PubMed](#)]
327. Chen, J.; Yang, H.; Zhang, X.; Lei, J.; Zhang, H.; Yuan, H.; Yang, J.; Nuli, Y.; Wang, J. Highly Reversible Lithium-Metal Anode and Lithium–Sulfur Batteries Enabled by an Intrinsic Safe Electrolyte. *ACS Appl. Mater. Interfaces* **2019**, *11*, 33419–33427. [[CrossRef](#)]
328. Yu, K.; Cai, G.; Li, M.; Wu, J.; Gupta, V.; Lee, D.J.; Holoubek, J.; Chen, Z. Effect of Electrolyte Chemistry and Sulfur Content in Li<sup>+</sup>Sulfurized Polyacrylonitrile (SPAN) Batteries. *ACS Appl. Mater. Interfaces* **2023**, *15*, 43724–43731. [[CrossRef](#)]
329. Han, Z.; Li, S.; Sun, M.; He, R.; Zhong, W.; Yu, C.; Cheng, S.; Xie, J. Fluorobenzene Diluted Low-Density Electrolyte for High-Energy Density and High-Performance Lithium-Sulfur Batteries. *J. Energy Chem.* **2022**, *68*, 752–761. [[CrossRef](#)]
330. Liu, H.; Holoubek, J.; Zhou, H.; Chen, A.; Chang, N.; Wu, Z.; Yu, S.; Yan, Q.; Xing, X.; Li, Y.; et al. Ultrahigh Coulombic Efficiency Electrolyte Enables Li<sup>+</sup>SPAN Batteries with Superior Cycling Performance. *Mater. Today* **2021**, *42*, 17–28. [[CrossRef](#)]
331. He, Y.; Zou, P.; Bak, S.-M.; Wang, C.; Zhang, R.; Yao, L.; Du, Y.; Hu, E.; Lin, R.; Xin, H.L. Dual Passivation of Cathode and Anode through Electrode–Electrolyte Interface Engineering Enables Long-Lifespan Li Metal–SPAN Batteries. *ACS Energy Lett.* **2022**, *7*, 2866–2875. [[CrossRef](#)]
332. Zhu, S.; Chen, J. Dual Strategy with Li-Ion Solvation and Solid Electrolyte Interphase for High Coulombic Efficiency of Lithium Metal Anode. *Energy Storage Mater.* **2022**, *44*, 48–56. [[CrossRef](#)]
333. Tan, S.; Liu, H.; Wu, Z.; Weiland, C.; Bak, S.-M.; Ronne, A.; Liu, P.; Whittingham, M.S.; Shadike, Z.; Hu, E.; et al. Isoxazole-Based Electrolytes for Lithium Metal Protection and Lithium-Sulfurized Polyacrylonitrile (SPAN) Battery Operating at Low Temperature. *J. Electrochem. Soc.* **2022**, *169*, 030513. [[CrossRef](#)]
334. Zhang, X.; Gao, P.; Wu, Z.; Engelhard, M.H.; Cao, X.; Jia, H.; Xu, Y.; Liu, H.; Wang, C.; Liu, J.; et al. Pinned Electrode/Electrolyte Interphase and Its Formation Origin for Sulfurized Polyacrylonitrile Cathode in Stable Lithium Batteries. *ACS Appl. Mater. Interfaces* **2022**, *14*, 52046–52057. [[CrossRef](#)] [[PubMed](#)]
335. Liu, X.; Diemant, T.; Mariani, A.; Dong, X.; Di Pietro, M.E.; Mele, A.; Passerini, S. Locally Concentrated Ionic Liquid Electrolyte with Partially Solvating Diluent for Lithium/Sulfurized Polyacrylonitrile Batteries. *Adv. Mater.* **2022**, *34*, 2207155. [[CrossRef](#)] [[PubMed](#)]
336. Liang, H.; Ma, Z.; Wang, Y.; Zhao, F.; Cao, Z.; Cavallo, L.; Li, Q.; Ming, J. Solvent–Solvent Interaction Mediated Lithium-Ion (De)Intercalation Chemistry in Propylene Carbonate Based Electrolytes for Lithium–Sulfur Batteries. *ACS Nano* **2023**, *17*, 18062–18073. [[CrossRef](#)] [[PubMed](#)]

337. Li, Y.; Qi, X.; Zhou, H.; Yang, F.; Jin, X.; Jiang, R.; Zhu, Z.; Liang, C.; Li, Z.; Yuan, L.; et al. Stabilizing SPAN in Non-Flammable Acetonitrile Electrolytes for Long-Life Graphite || SPAN Batteries. *Angew. Chem. Int. Ed.* **2025**, *64*, e202419995. [[CrossRef](#)]
338. Kim, J.-M.; Gao, P.; Miao, Q.; Zhao, Q.; Rahman, M.M.; Chen, P.; Zhang, X.; Hu, E.; Liu, P.; Zhang, J.-G.; et al. Tailoring Solvation Solvent in Localized High-Concentration Electrolytes for Lithium || Sulfurized Polyacrylonitrile. *ACS Appl. Mater. Interfaces* **2024**, *16*, 20618–20625. [[CrossRef](#)]
339. Liu, X.; Mariani, A.; Diermant, T.; Di Pietro, M.E.; Dong, X.; Su, P.-H.; Mele, A.; Passerini, S. PFAS-Free Locally Concentrated Ionic Liquid Electrolytes for Lithium Metal Batteries. *ACS Energy Lett.* **2024**, *9*, 3049–3057. [[CrossRef](#)]
340. Qin, K.; Li, S.; Yen, D.; Zhang, W.; Yang, Z.; Kamphaus, E.P.; Kim, E.Y.; Huang, J.; Shea, J.J.; Hu, E.; et al. A Coordinated-Anion-Enriched Electrolyte for Lean-Electrolyte Li-S Batteries. *ACS Energy Lett.* **2024**, *9*, 3869–3876. [[CrossRef](#)]
341. Phan, A.L.; Nan, B.; Le, P.M.L.; Miao, Q.; Wu, Z.; Le, K.; Chen, F.; Engelhard, M.; Dan Nguyen, T.; Han, K.S.; et al. Lightweight Electrolyte Design for Li/Sulfurized Polyacrylonitrile (SPAN) Batteries. *Adv. Mater.* **2024**, *36*, 2406594. [[CrossRef](#)]
342. Chen, L.; Zhang, Q.; Song, C.; Jiang, Y.; Sheng, X.; Pan, H.; Yang, L.; Wu, S.; Zeng, L.; Sun, D.; et al. A “Flexible” Solvent Molecule Enabling High-Performance Lithium Metal Batteries. *Angew. Chem. Int. Ed.* **2025**, *64*, e202422791. [[CrossRef](#)]
343. Wu, Z.; Liu, H.; Holoubek, J.; Anderson, C.; Shi, L.; Khemchandani, H.; Lu, D.; Liu, D.; Niu, C.; Xiao, J.; et al. The Role of Ion Transport in the Failure of High Areal Capacity Li Metal Batteries. *ACS Energy Lett.* **2022**, *7*, 2701–2710. [[CrossRef](#)]
344. Pai, M.-H.; Lai, T.; Manthiram, A. Sodium–Sulfur Cells with a Sulfurized Polyacrylonitrile Cathode and a Localized High Concentration Electrolyte with Toluene as a Nonfluorinated Diluent. *Adv. Funct. Mater.* **2024**, *34*, 2407450. [[CrossRef](#)]
345. Pai, M.-H.; Manthiram, A. Fluorine-Free Cosolvent Chemistry Empowering Sodium-Sulfurized Polyacrylonitrile Batteries. *Adv. Energy Mater.* **2025**, *15*, 2500026. [[CrossRef](#)]
346. Lu, H.; Wang, Q.; Chen, J.; Zhang, H.; Ding, J.; Nuli, Y.; Yang, J.; Wang, J. Electrolyte Solvation Regulation Engineering Promotes Li-SPAN Battery without Esters. *Energy Storage Mater.* **2023**, *63*, 102994. [[CrossRef](#)]
347. Li, M.; Chen, H.; Wang, Y.; Chen, X.; Wu, J.; Su, J.; Wang, M.; Li, X.; Li, C.; Ma, L.; et al. Two Birds with One Stone: Engineering Siloxane-Based Electrolytes for High-Performance Lithium–Sulfur Polyacrylonitrile Batteries. *J. Mater. Chem. A* **2023**, *11*, 11721–11729. [[CrossRef](#)]
348. Ma, H.; Wang, Q.; Lu, H.; Si, Y.; Kong, X.; Wang, J. An Intrinsic Safe Siloxane Ether-Based Electrolyte for Lithium–Sulfur Batteries at High Temperatures. *Chem. Eng. J.* **2024**, *479*, 147557. [[CrossRef](#)]
349. Tian, Y.; Li, M.; Chen, H.; Zhu, K.; Long, J.; Xie, W.; Chen, X.; Li, X.; Wu, J.; Chen, Y. Tailoring Eco-Friendly Siloxane-Based Electrolytes for High-Performance Lithium–Sulfur Batteries. *Mater. Sci. Eng. B* **2024**, *310*, 117773. [[CrossRef](#)]
350. Liao, K.; Pai, M.-H.; Manthiram, A. Tuning the Solvation Structure of a Weakly Solvating Cyclic Ether Electrolyte for Wide-Temperature Cycling of Lithium-Sulfurized Polyacrylonitrile Batteries. *Adv. Energy Mater.* **2025**, *15*, 2403733. [[CrossRef](#)]
351. Ren, W.; Wu, D.; NuLi, Y.; Zhang, X.; Yang, J.; Wang, J. A Chlorine-Free Electrolyte Based on Non-Nucleophilic Magnesium Bis(Diisopropyl)Amide and Ionic Liquid for Rechargeable Magnesium Batteries. *ACS Appl. Mater. Interfaces* **2021**, *13*, 32957–32967. [[CrossRef](#)]
352. Wang, P.; Küster, K.; Starke, U.; Liang, C.; Niewa, R.; Buchmeiser, M.R. Performance Enhancement of Rechargeable Magnesium–Sulfur Batteries Based on a Sulfurized Poly(Acrylonitrile) Composite and a Lithium Salt. *J. Power Sources* **2021**, *515*, 230604. [[CrossRef](#)]
353. Zhang, S.; Ren, W.; NuLi, Y.; Wang, B.; Yang, J.; Wang, J. Sulfurized-Pyrolyzed Polyacrylonitrile Cathode for Magnesium-Sulfur Batteries Containing  $Mg^{2+}/Li^+$  Hybrid Electrolytes. *Chem. Eng. J.* **2022**, *427*, 130902. [[CrossRef](#)]
354. Li, H.; Zhang, M.; Zheng, Z.; Wu, X.; Xiao, X.; Piao, Z.; Li, C.; Jia, Y.; Yang, J.; Zhou, G. High-Capacity and Long-Life Aqueous Zn-SPAN Batteries with Tandem Catalysis. *Adv. Mater.* **2025**, *37*, 2409771. [[CrossRef](#)]
355. Cheng, X.; Pan, J.; Zhao, Y.; Liao, M.; Peng, H. Gel Polymer Electrolytes for Electrochemical Energy Storage. *Adv. Energy Mater.* **2018**, *8*, 1702184. [[CrossRef](#)]
356. Qian, J.; Jin, B.; Li, Y.; Zhan, X.; Hou, Y.; Zhang, Q. Research Progress on Gel Polymer Electrolytes for Lithium-Sulfur Batteries. *J. Energy Chem.* **2021**, *56*, 420–437. [[CrossRef](#)]
357. Jeddi, K.; Ghaznavi, M.; Chen, P. A Novel Polymer Electrolyte to Improve the Cycle Life of High Performance Lithium–Sulfur Batteries. *J. Mater. Chem. A* **2013**, *1*, 2769–2772. [[CrossRef](#)]
358. Jeddi, K.; Zhao, Y.; Zhang, Y.; Konarov, A.; Chen, P. Fabrication and Characterization of an Effective Polymer Nanocomposite Electrolyte Membrane for High Performance Lithium/Sulfur Batteries. *J. Electrochem. Soc.* **2013**, *160*, A1052. [[CrossRef](#)]
359. Jeddi, K.; Sarikhani, K.; Qazvini, N.T.; Chen, P. Stabilizing Lithium/Sulfur Batteries by a Composite Polymer Electrolyte Containing Mesoporous Silica Particles. *J. Power Sources* **2014**, *245*, 656–662. [[CrossRef](#)]
360. Li, Z.; Lu, W.; Zhang, N.; Pan, Q.; Chen, Y.; Xu, G.; Zeng, D.; Zhang, Y.; Cai, W.; Yang, M.; et al. Single Ion Conducting Lithium Sulfur Polymer Batteries with Improved Safety and Stability. *J. Mater. Chem. A* **2018**, *6*, 14330–14338. [[CrossRef](#)]
361. Liu, Y.; Yang, D.; Yan, W.; Huang, Q.; Zhu, Y.; Fu, L.; Wu, Y. Synergy of Sulfur/Polyacrylonitrile Composite and Gel Polymer Electrolyte Promises Heat-Resistant Lithium-Sulfur Batteries. *iScience* **2019**, *19*, 316–325. [[CrossRef](#)]

362. Zhang, H.; Lu, H.; Chen, J.; Nuli, Y.; Wang, J. A Novel Filler for Gel Polymer Electrolyte with a High Lithium-Ion Transference Number toward Stable Cycling for Lithium-Metal Anodes in Lithium–Sulfur Batteries. *ACS Appl. Mater. Interfaces* **2021**, *13*, 48622–48633. [[CrossRef](#)]
363. Huang, Y.; Ji, Y.; Zhang, L.; Cai, C.; Fu, Y. Integrated Configuration Design Strategy Via Cathode-Gel Electrolyte with Forged Solid Electrolyte Interface Toward Advanced Lithium-Sulfurized Polyacrylonitrile Batteries. *Adv. Funct. Mater.* **2023**, *33*, 2306484. [[CrossRef](#)]
364. Huang, H.; Ding, F.; Zhong, H.; Li, H.; Zhang, W.; Liu, X.; Xu, Q. Nano-SiO<sub>2</sub>-Embedded Poly(Propylene Carbonate)-Based Composite Gel Polymer Electrolyte for Lithium–Sulfur Batteries. *J. Mater. Chem. A* **2018**, *6*, 9539–9549. [[CrossRef](#)]
365. Huang, Y.; Wang, Y.; Fu, Y. All-Cellulose Gel Electrolyte with Black Phosphorus Based Lithium Ion Conductors toward Advanced Lithium-Sulfurized Polyacrylonitrile Batteries. *Carbohydr. Polym.* **2022**, *296*, 119950. [[CrossRef](#)] [[PubMed](#)]
366. Zhang, H.; Chen, J.; Liu, J.; Zhang, X.; Yang, J.; Nuli, Y.; Ma, H.; Wang, J. Gel Electrolyte with Flame Retardant Polymer Stabilizing Lithium Metal towards Lithium-Sulfur Battery. *Energy Storage Mater.* **2023**, *61*, 102885. [[CrossRef](#)]
367. Hao, C.; Lu, H.; Liu, J.; Zhang, H.; Kong, X.; Yang, J.; Nuli, Y.; Wang, J. Construction of Ordered and Fast Lithium Ion Channels in Gel Electrolytes for Li-SPAN Batteries. *ACS Appl. Mater. Interfaces* **2024**, *16*, 60288–60297. [[CrossRef](#)]
368. Zhang, Y.; Wang, Z.; Pan, Y.; Yu, H.; Li, Z.; Li, C.; Wang, S.; Ma, Y.; Shi, X.; Zhang, H.; et al. Tailoring a Multi-System Adaptable Gel Polymer Electrolyte for the Realization of Carbonate Ester and Ether-Based Li-SPAN Batteries. *Energy Environ. Sci.* **2024**, *17*, 2576–2587. [[CrossRef](#)]
369. Guo, Y.; Zuo, W.; Wu, X.; Zhang, L. Practical SPAN || Li Cells Enabled by in Situ Polymerized Electrolyte. *Mater. Today Energy* **2024**, *45*, 101662. [[CrossRef](#)]
370. Zhang, M.; Xie, W.; Liu, M.; Liu, S.; Wang, W.; Jin, Z.; Wang, A.; Qiu, J.; Zhao, P.; Shi, Z. New Quasi-Solid-State Li-SPAN Battery Enhanced by In Situ Thermally Polymerized Gel Polymer Electrolytes. *ACS Appl. Mater. Interfaces* **2024**, *16*, 1578–1586. [[CrossRef](#)]
371. Murugan, S.; Klostermann, S.V.; Schützendübe, P.; Richter, G.; Kästner, J.; Buchmeiser, M.R. Stable Cycling of Room-Temperature Sodium-Sulfur Batteries Based on an In Situ Crosslinked Gel Polymer Electrolyte. *Adv. Funct. Mater.* **2022**, *32*, 2201191. [[CrossRef](#)]
372. She, C.; Shi, X.; Zhou, J.; Zhu, Z.; Lu, K.; Zheng, Z.; Zhu, Y. A ZIF-8-Enhanced PVDF/PEO Blending Polymer Gel Membrane for Quasi-Solid-State Na-S Batteries with Long Cycling Lifespan. *Chem. Eng. J.* **2024**, *494*, 153119. [[CrossRef](#)]
373. Wang, P.; Trück, J.; Häcker, J.; Schlosser, A.; Küster, K.; Starke, U.; Reinders, L.; Buchmeiser, M.R. A Design Concept for Halogen-Free Mg<sup>2+</sup>/Li<sup>+</sup>-Dual Salt-Containing Gel-Polymer-Electrolytes for Rechargeable Magnesium Batteries. *Energy Storage Mater.* **2022**, *49*, 509–517. [[CrossRef](#)]
374. Li, C.; Wang, Z.; He, Z.; Li, Y.; Mao, J.; Dai, K.; Yan, C.; Zheng, J. An Advance Review of Solid-State Battery: Challenges, Progress and Prospects. *Sustain. Mater. Technol.* **2021**, *29*, e00297. [[CrossRef](#)]
375. Yu, X.; Xie, J.; Yang, J.; Wang, K. All Solid-State Rechargeable Lithium Cells Based on Nano-Sulfur Composite Cathodes. *J. Power Sources* **2004**, *132*, 181–186. [[CrossRef](#)]
376. Zhu, T.; Dong, X.; Liu, Y.; Wang, Y.-G.; Wang, C.; Xia, Y.-Y. An All-Solid-State Sodium–Sulfur Battery Using a Sulfur/Carbonized Polyacrylonitrile Composite Cathode. *ACS Appl. Energy Mater.* **2019**, *2*, 5263–5271. [[CrossRef](#)]
377. Fan, Z.; Ding, B.; Hu, B.; Li, Z.; Xiao, D.; Xu, C.; Dou, H.; Zhang, X. Failure Mechanisms Investigation of Ultra-Thin Composite Polymer Electrolyte-Based Solid-State Lithium Metal Batteries. *Electrochim. Acta* **2022**, *436*, 141441. [[CrossRef](#)]
378. Li, C.; Zhang, Q.; Sheng, J.; Chen, B.; Gao, R.; Piao, Z.; Zhong, X.; Han, Z.; Zhu, Y.; Wang, J.; et al. A Quasi-Intercalation Reaction for Fast Sulfur Redox Kinetics in Solid-State Lithium–Sulfur Batteries. *Energy Environ. Sci.* **2022**, *15*, 4289–4300. [[CrossRef](#)]
379. You, D.; Wei, W.; Xiong, H. All-Solid-State Lithium–Sulfur Batteries with Robust Interphases by Utilizing Elastomeric Polymer-in-Salt Electrolytes. *ACS Appl. Energy Mater.* **2025**, *8*, 452–460. [[CrossRef](#)]
380. Li, C.; Zhang, M.; Li, P.; Ren, H.-R.; Wu, X.; Piao, Z.; Xiao, X.; Zhang, M.; Liang, X.; Wu, X.; et al. Self-Assembly of Ultrathin, Ultrastrong Layered Membranes by Protic Solvent Penetration. *J. Am. Chem. Soc.* **2024**, *146*, 3553–3563. [[CrossRef](#)]
381. Nie, L.; Li, Y.; Wu, X.; Zhang, M.; Wu, X.; Xiao, X.; Gao, R.; Piao, Z.; Wu, X.; Song, Y.; et al. Scalable Ultrathin Solid Electrolyte from Recycled *Antheraea Pernyi* Silk with Regulated Ion Transport for Solid-State Li–S Batteries. *eScience* **2025**, *5*, 100395. [[CrossRef](#)]
382. Sapkota, N.; Sabet, M.; Parekh, M.; Chen, N.; Basel, J.; Koehler, K.C.; Ding, Y.; Rao, A.M. Commercial Cellulosic Paper-Based Solid Electrolyte for High-Temperature Lithium–Sulfur Batteries. *ACS Appl. Mater. Interfaces* **2025**, *17*, 1234–1243. [[CrossRef](#)]
383. Huang, J.; Song, Z.; Wu, J.; Miao, Y.; Li, M.; Lin, D.; Zhu, K.; Chen, X.; Li, X.; Chen, Y. In Situ Polymerized Quasi-Solid Polymer Electrolytes Enabling Void-Free Interfaces for Room-Temperature Sodium–Sulfur Batteries. *Energy Mater. Devices* **2024**, *2*, 9370051. [[CrossRef](#)]
384. Lao, Z.; Tao, K.; Xiao, X.; Qu, H.; Wu, X.; Han, Z.; Gao, R.; Wang, J.; Wu, X.; Chen, A.; et al. Data-Driven Exploration of Weak Coordination Microenvironment in Solid-State Electrolyte for Safe and Energy-Dense Batteries. *Nat. Commun.* **2025**, *16*, 1075. [[CrossRef](#)]
385. Lei, D.; Shi, K.; Ye, H.; Wan, Z.; Wang, Y.; Shen, L.; Li, B.; Yang, Q.-H.; Kang, F.; He, Y.-B. Progress and Perspective of Solid-State Lithium–Sulfur Batteries. *Adv. Funct. Mater.* **2018**, *28*, 1707570. [[CrossRef](#)]

386. Trevey, J.E.; Gilsdorf, J.R.; Stoldt, C.R.; Lee, S.-H.; Liu, P. Electrochemical Investigation of All-Solid-State Lithium Batteries with a High Capacity Sulfur-Based Electrode. *J. Electrochem. Soc.* **2012**, *159*, A1019. [[CrossRef](#)]
387. Sun, Z.; Hu, Y.; Qin, F.; Lv, N.; Li, B.; Jiang, L.; Zhang, Z.; Liu, F. Sulfurized Polyacrylonitrile Cathodes with Electrochemical and Structural Tuning for High Capacity All-Solid-State Lithium–Sulfur Batteries. *Sustain. Energy Fuels* **2021**, *5*, 5603–5614. [[CrossRef](#)]
388. Huang, J.; Shao, Y.; Liu, Z.; Lv, Y.; Guo, F.; Tu, Y.; Ichikawa, T.; Hu, Z.; Zhang, T. Nano Sulfurized Polyacrylonitrile Cathode for High Performance Solid-State Lithium–Sulfur Batteries. *J. Power Sources* **2023**, *570*, 233045. [[CrossRef](#)]
389. Jin, X.; Fan, W.; Zhu, S.; Zhang, T. Synergistic Effects of Anion Substitution and Interfacial Modification to Enhance Ionic Conductivity in a Hydride Electrolyte. *ACS Sustain. Chem. Eng.* **2025**, *13*, 2924–2932. [[CrossRef](#)]
390. Wang, C.; Adair, K.R.; Liang, J.; Li, X.; Sun, Y.; Li, X.; Wang, J.; Sun, Q.; Zhao, F.; Lin, X.; et al. Solid-State Plastic Crystal Electrolytes: Effective Protection Interlayers for Sulfide-Based All-Solid-State Lithium Metal Batteries. *Adv. Funct. Mater.* **2019**, *29*, 1900392. [[CrossRef](#)]
391. Wang, Y.; Wang, G.; He, P.; Hu, J.; Jiang, J.; Fan, L.-Z. Sandwich Structured NASICON-Type Electrolyte Matched with Sulfurized Polyacrylonitrile Cathode for High Performance Solid-State Lithium–Sulfur Batteries. *Chem. Eng. J.* **2020**, *393*, 124705. [[CrossRef](#)]
392. Miao, X.; Wang, H.; Sun, R.; Ge, X.; Zhao, D.; Wang, P.; Wang, R.; Yin, L. Isotropic Sulfurized Polyacrylonitrile Interlayer with Homogeneous  $\text{Na}^+$  Flux Dynamics for Solid-State Na Metal Batteries. *Adv. Energy Mater.* **2021**, *11*, 2003469. [[CrossRef](#)]
393. Shi, C.; Alexander, G.V.; O'Neill, J.; Duncan, K.; Godbey, G.; Wachsman, E.D. All-Solid-State Garnet Type Sulfurized Polyacrylonitrile/Lithium-Metal Battery Enabled by an Inorganic Lithium Conductive Salt and a Bilayer Electrolyte Architecture. *ACS Energy Lett.* **2023**, *8*, 1803–1810. [[CrossRef](#)]
394. Shi, C.; Takeuchi, S.; Alexander, G.V.; Hamann, T.; O'Neill, J.; Dura, J.A.; Wachsman, E.D. High Sulfur Loading and Capacity Retention in Bilayer Garnet Sulfurized-Polyacrylonitrile/Lithium-Metal Batteries with Gel Polymer Electrolytes. *Adv. Energy Mater.* **2023**, *13*, 2301656. [[CrossRef](#)]
395. Zhao, Y.; Lu, H.; Kong, X.; Yang, J.; Nuli, Y.; Wang, J. Graphitic Carbon Nitride Stabilized the Lithium Anode/Sulfide Electrolyte Interface for All-Solid-State Lithium–Sulfur Battery. *Chem. Eng. J.* **2024**, *489*, 150887. [[CrossRef](#)]
396. Li, M.; Frerichs, J.E.; Kolek, M.; Sun, W.; Zhou, D.; Huang, C.J.; Hwang, B.J.; Hansen, M.R.; Winter, M.; Bieker, P. Solid-State Lithium–Sulfur Battery Enabled by Thio-LiSiCON/Polymer Composite Electrolyte and Sulfurized Polyacrylonitrile Cathode. *Adv. Funct. Mater.* **2020**, *30*, 1910123. [[CrossRef](#)]
397. Chen, D.; Hu, C.; Chen, Q.; Xue, G.; Tang, L.; Dong, Q.; Chen, B.; Zhang, F.; Gao, M.; Xu, J.; et al. High Ceramic Content Composite Solid-State Electrolyte Films Prepared via a Scalable Solvent-Free Process. *Nano Res.* **2023**, *16*, 3847–3854. [[CrossRef](#)]
398. Temeche, E.; Zhang, X.; Laine, R.M. Solid Electrolytes for Li–S Batteries: Solid Solutions of Poly(Ethylene Oxide) with  $\text{Li}_x\text{PON}$ - and  $\text{Li}_x\text{SiPON}$ -Based Polymers. *ACS Appl. Mater. Interfaces* **2020**, *12*, 30353–30364. [[CrossRef](#)] [[PubMed](#)]
399. Temeche, E.; Zhang, X.; Laine, R.M. Electrochemical Performance of  $\text{Li}_x\text{SiON}$  Polymer Electrolytes Derived from an Agriculture Waste Product, Rice Hull Ash. *ACS Appl. Polym. Mater.* **2021**, *3*, 2144–2152. [[CrossRef](#)]
400. Zhang, X.; Zhang, T.; Shao, Y.; Cao, H.; Liu, Z.; Wang, S.; Zhang, X. Composite Electrolytes Based on Poly(Ethylene Oxide) and Lithium Borohydrides for All-Solid-State Lithium–Sulfur Batteries. *ACS Sustain. Chem. Eng.* **2021**, *9*, 5396–5404. [[CrossRef](#)]
401. Luo, S.; Zhao, E.; Gu, Y.; Saito, N.; Zhang, Z.; Yang, L.; Hirano, S. Flexible, Solid-State, Fiber-Network-Reinforced Composite Solid Electrolyte for Long Lifespan Solid Lithium-Sulfurized Polyacrylonitrile Battery. *Nano Res.* **2022**, *15*, 3290–3298. [[CrossRef](#)]
402. Nie, L.; Zhu, J.; Wu, X.; Zhang, M.; Xiao, X.; Gao, R.; Wu, X.; Zhu, Y.; Chen, S.; Han, Z.; et al. A Large-Scale Fabrication of Flexible, Ultrathin, and Robust Solid Electrolyte for Solid-State Lithium–Sulfur Batteries. *Adv. Mater.* **2024**, *36*, 2400115. [[CrossRef](#)]
403. Zhu, Y.; Lao, Z.; Zhang, M.; Hou, T.; Xiao, X.; Piao, Z.; Lu, G.; Han, Z.; Gao, R.; Nie, L.; et al. A Locally Solvent-Tethered Polymer Electrolyte for Long-Life Lithium Metal Batteries. *Nat. Commun.* **2024**, *15*, 3914. [[CrossRef](#)]
404. Unemoto, A.; Gambe, Y.; Komatsu, D.; Honma, I. Development of High Capacity All-Solid-State Lithium Battery Using Quasi-Solid-State Electrolyte Containing Tetraglyme–Li-TFSA Equimolar Complexes. *Solid State Ion.* **2014**, *262*, 765–768. [[CrossRef](#)]
405. Yang, H.; Qiao, Y.; Chang, Z.; He, P.; Zhou, H. Designing Cation–Solvent Fully Coordinated Electrolyte for High-Energy-Density Lithium–Sulfur Full Cell Based on Solid–Solid Conversion. *Angew. Chem. Int. Ed.* **2021**, *60*, 17726–17734. [[CrossRef](#)] [[PubMed](#)]
406. Anbunathan, A.; Walle, K.Z.; Wu, S.-H.; Wu, Y.-S.; Chang, J.-K.; Jose, R.; Yang, C.-C. Advanced Quasi-Solid-State Lithium–Sulfur Batteries: A High-Performance Flexible  $\text{LiTa}_2\text{PO}_8$ -Based Hybrid Solid Electrolyte Membrane with Enhanced Safety and Efficiency. *J. Energy Storage* **2024**, *93*, 112294. [[CrossRef](#)]
407. Shi, Y.; Zhou, X.; Yu, G. Material and Structural Design of Novel Binder Systems for High-Energy, High-Power Lithium-Ion Batteries. *Acc. Chem. Res.* **2017**, *50*, 2642–2652. [[CrossRef](#)]
408. Zou, F.; Manthiram, A. A Review of the Design of Advanced Binders for High-Performance Batteries. *Adv. Energy Mater.* **2020**, *10*, 2002508. [[CrossRef](#)]
409. Wang, L.; He, X.; Li, J.; Gao, J.; Fang, M.; Tian, G.; Wang, J.; Fan, S. Graphene-Coated Plastic Film as Current Collector for Lithium/Sulfur Batteries. *J. Power Sources* **2013**, *239*, 623–627. [[CrossRef](#)]
410. Wang, J.; Yao, Z.; Monroe, C.W.; Yang, J.; Nuli, Y. Carbonyl- $\beta$ -Cyclodextrin as a Novel Binder for Sulfur Composite Cathodes in Rechargeable Lithium Batteries. *Adv. Funct. Mater.* **2013**, *23*, 1194–1201. [[CrossRef](#)]

411. Li, Y.; Zeng, Q.; Gentle, I.R.; Wang, D.-W. Carboxymethyl Cellulose Binders Enable High-Rate Capability of Sulfurized Polyacrylonitrile Cathodes for Li–S Batteries. *J. Mater. Chem. A* **2017**, *5*, 5460–5465. [[CrossRef](#)]
412. Eng, A.Y.S.; Nguyen, D.-T.; Kumar, V.; Subramanian, G.S.; Ng, M.-F.; Seh, Z.W. Tailoring Binder–Cathode Interactions for Long-Life Room-Temperature Sodium–Sulfur Batteries. *J. Mater. Chem. A* **2020**, *8*, 22983–22997. [[CrossRef](#)]
413. Hwang, J.-Y.; Kim, H.M.; Sun, Y.-K. High Performance Potassium–Sulfur Batteries Based on a Sulfurized Polyacrylonitrile Cathode and Polyacrylic Acid Binder. *J. Mater. Chem. A* **2018**, *6*, 14587–14593. [[CrossRef](#)]
414. Zhang, S.; Huang, Y.; NuLi, Y.; Wang, B.; Yang, J.; Wang, J. Sodium Polyacrylate as a Promising Aqueous Binder of S@pPAN Cathodes for Magnesium–Sulfur Batteries. *J. Phys. Chem. C* **2020**, *124*, 20712–20721. [[CrossRef](#)]
415. Wong, A.J.Y.; Lieu, W.Y.; Chinnadurai, D.; Ng, M.-F.; Seh, Z.W. Uncovering the Binder Interactions with S-PAN and MXene for Room Temperature Na–S Batteries. *Nano Lett.* **2023**, *23*, 3592–3598. [[CrossRef](#)]
416. Chen, J.; Zhang, H.; Yang, H.; Lei, J.; Naveed, A.; Yang, J.; Nuli, Y.; Wang, J. Towards Practical Li–S Battery with Dense and Flexible Electrode Containing Lean Electrolyte. *Energy Storage Mater.* **2020**, *27*, 307–315. [[CrossRef](#)]
417. Yang, H.; Chen, J.; Yang, J.; Nuli, Y.; Wang, J. Dense and High Loading Sulfurized Pyrolyzed Poly (Acrylonitrile)(S@pPAN) Cathode for Rechargeable Lithium Batteries. *Energy Storage Mater.* **2020**, *31*, 187–194. [[CrossRef](#)]
418. Niesen, S.; Kappler, J.; Trück, J.; Veith, L.; Weil, T.; Soczka-Guth, T.; Buchmeiser, M.R. Influence of the Drying Temperature on the Performance and Binder Distribution of Sulfurized Poly(Acrylonitrile) Cathodes. *J. Electrochem. Soc.* **2021**, *168*, 050510. [[CrossRef](#)]
419. Wu, Z.; Liu, H.; Yu, S.; Liu, P. Communication—Binder Effects on Cycling Performance of High Areal Capacity SPAN Electrodes. *J. Electrochem. Soc.* **2021**, *168*, 110504. [[CrossRef](#)]
420. Miao, Z.; Xiao, X.; Li, J.; Xu, X.; Chen, W.; Yuan, L.; Sun, Q.; Li, Z.; Huang, Y. Evaluating the Effect of Binder for Sulfurized Polyacrylonitrile Cathode via Optical Fiber Sensors. *Adv. Funct. Mater.* **2024**, *34*, 2301736. [[CrossRef](#)]
421. Yuan, H.; Guo, C.; Chen, J.; Lu, H.; Yang, J.; Nuli, Y.; Wang, J. A Crosslinking Hydrogel Binder for High-Sulfur Content S@pPAN Cathode in Rechargeable Lithium Batteries. *J. Energy Chem.* **2021**, *60*, 360–367. [[CrossRef](#)]
422. Lin, H.-C.; Hong, J.-L. Metalized Polyacrylates as Efficient Binder for a Sulfurized Polyacrylonitrile/Polydopamine Active Material in Sulfur Cathodes for Room Temperature Sodium–Sulfur Batteries. *ACS Appl. Energy Mater.* **2022**, *5*, 11304–11316. [[CrossRef](#)]
423. Sun, T.; Wang, S.; Xu, M.; Qiao, N.; Zhu, Q.; Xu, B. High-Performance Sulfurized Polyacrylonitrile Cathode by Using MXene as a Conductive and Catalytic Binder for Room-Temperature Na/S Batteries. *ACS Appl. Mater. Interfaces* **2024**, *16*, 10093–10103. [[CrossRef](#)] [[PubMed](#)]
424. Kim, J.-S.; Hwang, T.H.; Kim, B.G.; Min, J.; Choi, J.W. A Lithium–Sulfur Battery with a High Areal Energy Density. *Adv. Funct. Mater.* **2014**, *24*, 5359–5367. [[CrossRef](#)]
425. Cho, G.; Jeong, J.; Chae, M.; Noh, J.; Cho, K.; Kim, J.; Ahn, H.; Nam, T.; Kim, K. Electrochemical Properties of Sulfurized Poly-Acrylonitrile (SPAN) Cathode Containing Carbon Fiber Current Collectors. *Surf. Coat. Technol.* **2017**, *326*, 443–449. [[CrossRef](#)]
426. Hara, T.; Konarov, A.; Mentbayeva, A.; Kurmanbayeva, I.; Bakenov, Z. High Mass-Loading of Sulfur-Based Cathode Composites and Polysulfides Stabilization for Rechargeable Lithium/Sulfur Batteries. *Front. Energy Res.* **2015**, *3*, 22. [[CrossRef](#)]
427. Baikalov, N.; Serik, N.; Kalybekkyzy, S.; Kurmanbayeva, I.; Bakenov, Z.; Mentbayeva, A. High Mass-Loading Sulfur-Composite Cathode for Lithium-Sulfur Batteries. *Front. Energy Res.* **2020**, *8*, 207. [[CrossRef](#)]
428. Zhang, Y.; Lou, J.; Shuai, Y.; Chen, K.; He, X.; Wang, Y.; Li, N.; Zhang, Z.; Gan, F. A Novel Rechargeable Potassium–Sulfur Battery Based on Liquid Alloy Anode. *Mater. Lett.* **2019**, *242*, 5–8. [[CrossRef](#)]
429. Kalybekkyzy, S.; Mentbayeva, A.; Yerkinbekova, Y.; Baikalov, N.; Kahraman, M.V.; Bakenov, Z. Electrospun 3D Structured Carbon Current Collector for Li/S Batteries. *Nanomaterials* **2020**, *10*, 745. [[CrossRef](#)]
430. Liu, F.; Chiluwal, S.; Childress, A.S.; Etteh, C.; Miller, K.; Washington, M.; Rao, A.M.; Podila, R. Graphene Foam Current Collector for High-Areal-Capacity Lithium–Sulfur Batteries. *ACS Appl. Nano Mater.* **2021**, *4*, 53–60. [[CrossRef](#)]
431. Sapkota, N.; Chiluwal, S.; Parajuli, P.; Rowland, A.; Podila, R. Insights into the Pseudocapacitive Behavior of Sulfurized Polymer Electrodes for Li–S Batteries. *Adv. Sci.* **2023**, *10*, 2206901. [[CrossRef](#)]
432. Shuai, Y.; Hu, Y.; Lou, J.; Gong, X.; Li, M.; Xu, Z.; Deng, D.; Jiang, F.; Li, M. Fluorinated Aluminum Foam for Dendrite-Free Na Metal Anodes. *J. Electrochem. Soc.* **2023**, *170*, 030519. [[CrossRef](#)]
433. Lou, J.; Zhou, J.; Ma, X.; Chen, K.; Chen, S. A Novel Sodium–Potassium Anode Supported by Fluorinated Aluminum Foam. *Materials* **2023**, *16*, 7269. [[CrossRef](#)]
434. Xiang, Y.; Li, J.; Lei, J.; Liu, D.; Xie, Z.; Qu, D.; Li, K.; Deng, T.; Tang, H. Advanced Separators for Lithium-Ion and Lithium–Sulfur Batteries: A Review of Recent Progress. *ChemSusChem* **2016**, *9*, 3023–3039. [[CrossRef](#)] [[PubMed](#)]
435. Li, C.; Liu, R.; Xiao, Y.; Cao, F.; Zhang, H. Recent Progress of Separators in Lithium-Sulfur Batteries. *Energy Storage Mater.* **2021**, *40*, 439–460. [[CrossRef](#)]
436. Zhang, T.; Yang, J.; Xu, Z.; Li, H.; Guo, Y.; Liang, C.; Wang, J. Suppressing Dendrite Growth of a Lithium Metal Anode by Modifying Conventional Polypropylene Separators with a Composite Layer. *ACS Appl. Energy Mater.* **2020**, *3*, 506–513. [[CrossRef](#)]

437. Huang, H.; Zhao, C.; Ding, F.; Li, H.; Zhang, S.; Liu, X.; Xu, Q. A Thermo-Stable Poly(Propylene Carbonate)-Based Composite Separator for Lithium-Sulfur Batteries under Elevated Temperatures. *Int. J. Energy Res.* **2020**, *44*, 10295–10306. [[CrossRef](#)]
438. Zhang, T.; Li, X.; Miao, X.; Sun, R.; Li, J.; Zhang, Z.; Wang, R.; Wang, C.; Li, Z.; Yin, L. Achieve Stable Lithium Metal Anode by Sulfurized-Polyacrylonitrile Modified Separator for High-Performance Lithium Batteries. *ACS Appl. Mater. Interfaces* **2022**, *14*, 14264–14273. [[CrossRef](#)]
439. Anbunathan, A.; Karuppiah, C.; Chang, J.-K.; Jose, R.; Yang, C.-C. In Situ Grown ZIF67 Particles on a Glass Fiber Separator: The Performance Booster and Anode Defender for Lithium–Sulfurized Polyacrylonitrile (SPAN) Batteries. *ACS Appl. Energy Mater.* **2023**, *6*, 3549–3565. [[CrossRef](#)]
440. Zhao, H.; Deng, N.; Yan, J.; Kang, W.; Ju, J.; Ruan, Y.; Wang, X.; Zhuang, X.; Li, Q.; Cheng, B. A Review on Anode for Lithium-Sulfur Batteries: Progress and Prospects. *Chem. Eng. J.* **2018**, *347*, 343–365. [[CrossRef](#)]
441. Shuai, Y.; Zhang, B.; Ding, X.; Lou, J.; Wang, Y.; Chen, S.; Chen, K. Enhancing Fast Ion Transport at Interfaces of Lithium Metal Anode in Lithium-Sulfurized Polyacrylonitrile Batteries. *Energy Technol.* **2020**, *8*, 1901287. [[CrossRef](#)]
442. Guo, C.; Yang, H.; Naveed, A.; Nuli, Y.; Yang, J.; Cao, Y.; Yang, H.; Wang, J. AlF<sub>3</sub>-Modified Carbon Nanofibers as a Multifunctional 3D Interlayer for Stable Lithium Metal Anodes. *Chem. Commun.* **2018**, *54*, 8347–8350. [[CrossRef](#)]
443. Li, Y.; Mao, E.; Min, Z.; Cai, Z.; Chen, Z.; Fu, L.; Duan, X.; Wang, L.; Zhang, C.; Lu, Z.; et al. Hybrid Polymer-Alloy-Fluoride Interphase Enabling Fast Ion Transport Kinetics for Low-Temperature Lithium Metal Batteries. *ACS Nano* **2023**, *17*, 19459–19469. [[CrossRef](#)]
444. Wei, S.; Choudhury, S.; Xu, J.; Nath, P.; Tu, Z.; Archer, L.A. Highly Stable Sodium Batteries Enabled by Functional Ionic Polymer Membranes. *Adv. Mater.* **2017**, *29*, 1605512. [[CrossRef](#)]
445. Tian, K.; Wei, C.; Wang, Z.; Li, Y.; Xi, B.; Xiong, S.; Feng, J. Stable Sodium Metal Anode Enabled by Interfacial Room-Temperature Liquid Metal Engineering for High-Performance Sodium–Sulfur Batteries with Carbonate-Based Electrolyte. *Interdiscip. Mater.* **2024**, *3*, 425–436. [[CrossRef](#)]
446. Zhang, T.; Hong, M.; Yang, J.; Xu, Z.; Wang, J.; Guo, Y.; Liang, C. A High Performance Lithium-Ion–Sulfur Battery with a Free-Standing Carbon Matrix Supported Li-Rich Alloy Anode. *Chem. Sci.* **2018**, *9*, 8829–8835. [[CrossRef](#)] [[PubMed](#)]
447. Sun, J.; Zeng, Q.; Lv, R.; Lv, W.; Yang, Q.-H.; Amal, R.; Wang, D.-W. A Li-Ion Sulfur Full Cell with Ambient Resistant Al-Li Alloy Anode. *Energy Storage Mater.* **2018**, *15*, 209–217. [[CrossRef](#)]
448. Zhang, T.; Lu, H.; Yang, J.; Xu, Z.; Wang, J.; Hirano, S.; Guo, Y.; Liang, C. Stable Lithium Metal Anode Enabled by a Lithiophilic and Electron/Ion Conductive Framework. *ACS Nano* **2020**, *14*, 5618–5627. [[CrossRef](#)] [[PubMed](#)]
449. Chen, Y.; Ke, X.; Cheng, Y.; Fan, M.; Wu, W.; Huang, X.; Liang, Y.; Zhong, Y.; Ao, Z.; Lai, Y.; et al. Boosting the Electrochemical Performance of 3D Composite Lithium Metal Anodes through Synergistic Structure and Interface Engineering. *Energy Storage Mater.* **2020**, *26*, 56–64. [[CrossRef](#)]
450. Wang, S.; Chen, J.; Lu, H.; Zhang, Y.; Yang, J.; Nuli, Y.; Wang, J. Artificial Alloy/Li<sub>3</sub>N Double-Layer Enabling Stable High-Capacity Lithium Metal Anodes. *ACS Appl. Energy Mater.* **2021**, *4*, 13132–13139. [[CrossRef](#)]
451. Wang, Z.; Zhang, C.; Li, Z.; Teng, Z.; Wang, Y.; Chen, K.; Zhu, C. In-Situ Construction of LiF/NaF-Rich Hybrid Solid Electrolyte Interphase for Dendrite-Free and Stable Li-Na Alloy Anodes. *J. Electroanal. Chem.* **2024**, *968*, 118489. [[CrossRef](#)]
452. Duan, X.; Wang, L.; Li, G.; Liu, X.; Wan, M.; Du, J.; Zhan, R.; Wang, W.; Li, Y.; Tu, S.; et al. Revealing the Intrinsic Uneven Electrochemical Reactions of Li Metal Anode in Ah-Level Laminated Pouch Cells. *Adv. Funct. Mater.* **2023**, *33*, 2210669. [[CrossRef](#)]
453. Du, J.; Li, G.; Tan, Y.; Duan, X.; Fan, T.; Du, C.; Zhou, A.; Wang, Y. Tuning the Li-Sn Alloy Dispersity to Improve the Lithiophilicity of Lithium Metal Anodes towards Stable Lithium Metal Batteries. *Inorg. Chem. Front.* **2025**, *12*, 3137–3146. [[CrossRef](#)]
454. Sun, H.; He, X.; Ren, J.; Li, J.; Jiang, C.; Wan, C. Hard Carbon/Lithium Composite Anode Materials for Li-Ion Batteries. *Electrochim. Acta* **2007**, *52*, 4312–4316. [[CrossRef](#)]
455. Uzakbaiuly, B.; Mentbayeva, A.; Konarov, A.; Kurmanbayeva, I.; Zhang, Y.; Bakenov, Z. Evaluating Sulfur-Composite Cathode Material with Lithiated Graphite Anode in Coin Cell and Pouch Cell Configuration. *Front. Energy Res.* **2020**, *8*, 595481. [[CrossRef](#)]
456. Wang, H.; Ye, Y.; Liu, H.; Li, Q.; Wang, K.; Sun, S.; Wu, F.; Chen, R.; Li, L. Coassembly of Ultrathin Lithium with Dual Lithium-Free Electrodes for Long-Lasting Sulfurized Polyacrylonitrile Batteries. *Nano Lett.* **2025**, *25*, 2266–2274. [[CrossRef](#)] [[PubMed](#)]
457. Mao, E.; Du, J.; Duan, X.; Wang, L.; Wang, X.; Li, G.; Fu, L.; Sun, Y. Preparation and Electrochemical Performance of Ultra-Thin Reduced Graphene Oxide/Lithium Metal Composite Foils. *New Carbon Mater.* **2023**, *38*, 754–763. [[CrossRef](#)]
458. Dai, Z.; Wang, M.; Zhang, Y.; Wang, B.; Luo, H.; Zhang, X.; Wang, Q.; Zhang, Y.; Wu, H. Engineering Bifunctional Host Materials of Sulfur and Lithium-Metal Based on Nitrogen-Enriched Polyacrylonitrile for Li–S Batteries. *Chem.—Eur. J.* **2020**, *26*, 8784–8793. [[CrossRef](#)]
459. Yu, S.; Wang, S.; Miao, Q.; Hui, Z.; Hyun, G.; Holoubek, J.; Yu, X.; Gao, J.; Liu, P. Composite Lithium Metal Structure to Mitigate Pulverization and Enable Long-Life Batteries. *Adv. Energy Mater.* **2023**, *13*, 2302400. [[CrossRef](#)]
460. Shao, M.; Wu, N.; Chen, T.; Han, X.; Shen, Y.; Zhang, W.; Zheng, B.; Li, S.; Huo, F. Amorphous Hollow Carbon Film as a Flexible Host for Liquid Na-K Alloy Anode. *Chin. Chem. Lett.* **2023**, *34*, 107767. [[CrossRef](#)]

461. Tang, X.; Zhou, D.; Li, P.; Guo, X.; Sun, B.; Liu, H.; Yan, K.; Gogotsi, Y.; Wang, G. MXene-Based Dendrite-Free Potassium Metal Batteries. *Adv. Mater.* **2020**, *32*, 1906739. [CrossRef]
462. Shi, L.; Liu, Y.; Wang, W.; Wang, A.; Jin, Z.; Wu, F.; Yang, Y. High-Safety Lithium-Ion Sulfur Battery with Sulfurized Polyacrylonitrile Cathode, Prelithiated  $\text{SiO}_x/\text{C}$  Anode and Carbonate-Based Electrolyte. *J. Alloys Compd.* **2017**, *723*, 974–982. [CrossRef]
463. Huang, S.-S.; Tung, M.T.; Huynh, C.D.; Hwang, B.-J.; Bieker, P.M.; Fang, C.-C.; Wu, N.-L. Engineering Rice Husk into a High-Performance Electrode Material through an Ecofriendly Process and Assessing Its Application for Lithium-Ion Sulfur Batteries. *ACS Sustain. Chem. Eng.* **2019**, *7*, 7851–7861. [CrossRef]
464. Zhang, T.; Xu, Z.; Guo, Y.; Liang, C.; Wang, J.; Yang, J. Building High Performance Silicon–Oxygen and Silicon–Sulfur Battery by In-Situ Lithiation of Fibrous Si/C Anode. *J. Alloys Compd.* **2019**, *806*, 335–342. [CrossRef]
465. Shuai, Y.; Lou, J.; Wang, Y.; Chen, K. An Air-Stable Prelithiation Technology for Lithium Ion-Sulfurized Polyacrylonitrile Battery. *Funct. Mater. Lett.* **2020**, *13*, 1950094. [CrossRef]
466. Ye, Y.; Zhao, Y.; Zhao, T.; Xu, S.; Xu, Z.; Qian, J.; Wang, L.; Xing, Y.; Wei, L.; Li, Y.; et al. An Antipulverization and High-Continuity Lithium Metal Anode for High-Energy Lithium Batteries. *Adv. Mater.* **2021**, *33*, 2105029. [CrossRef] [PubMed]
467. Wei, C.; Wang, Y.; Zhang, Y.; Tan, L.; Qian, Y.; Tao, Y.; Xiong, S.; Feng, J. Flexible and Stable 3D Lithium Metal Anodes Based on Self-Standing MXene/COF Frameworks for High-Performance Lithium-Sulfur Batteries. *Nano Res.* **2021**, *14*, 3576–3584. [CrossRef]
468. Liu, Y.; Sun, J.; Hu, X.; Li, Y.; Du, H.; Wang, K.; Du, Z.; Gong, X.; Ai, W.; Huang, W. Lithophilic Sites Dependency of Lithium Deposition in Li Metal Host Anodes. *Nano Energy* **2022**, *94*, 106883. [CrossRef]
469. Trück, J.; Wang, P.; Buch, E.; Groos, J.; Niesen, S.; Buchmeiser, M.R. Communication—Lithium Titanate as Mg-Ion Insertion Anode for Mg-Ion Sulfur Batteries Based on Sulfurated Poly(Acrylonitrile) Composite. *J. Electrochem. Soc.* **2022**, *169*, 010505. [CrossRef]
470. Takemoto, K.; Wakasugi, J.; Kubota, M.; Kanamura, K.; Abe, H. Dual Additive of Lithium Titanate and Sulfurized Pyrolyzed Polyacrylonitrile in Sulfur Cathode for High Rate Performance in Lithium–Sulfur Battery. *Phys. Chem. Chem. Phys.* **2022**, *25*, 351–358. [CrossRef]
471. Berhe, G.B.; Su, W.-N.; Huang, C.-J.; Hagos, T.M.; Hagos, T.T.; Bezabh, H.K.; Weret, M.A.; Abrha, L.H.; Yang, Y.-W.; Hwang, B.-J. A New Class of Lithium-Ion Battery Using Sulfurized Carbon Anode from Polyacrylonitrile and Lithium Manganese Oxide Cathode. *J. Power Sources* **2019**, *434*, 126641. [CrossRef]
472. Berhe, G.B.; Su, W.-N.; Abrha, L.H.; Bezabh, H.K.; Hagos, T.M.; Hagos, T.T.; Huang, C.-J.; Sahalie, N.A.; Jote, B.A.; Thirumalraj, B.; et al. Garnet–PVDF Composite Film Modified Lithium Manganese Oxide Cathode and Sulfurized Carbon Anode from Polyacrylonitrile for Lithium-Ion Batteries. *J. Mater. Chem. A* **2020**, *8*, 14043–14053. [CrossRef]
473. Yamano, A.; Kubo, T.; Chujo, F.; Yamashita, N.; Morishita, M.; Yanagida, M.; Furusawa, S.; Kikuchi, N.; Sakai, T. Rubber-Derived Sulfur Composite as a High Capacity Anode for Li-Ion Battery Using 5 V-Class  $\text{LiNi}_{0.5}\text{Mn}_{1.5}\text{O}_4$  Cathode. *Electrochemistry* **2022**, *90*, 127004. [CrossRef]
474. Berhe, G.B.; Su, W.-N.; Hagos, T.T.; Bezabh, H.K.; Hagos, T.M.; Hwang, B.J. Partially Fluorinated Electrolyte for High-Voltage Cathode with Sulfurized Carbon Anode from Polyacrylonitrile for Lithium-Ion Battery. *J. Power Sources* **2023**, *558*, 232567. [CrossRef]
475. Wu, Y.; Wang, W.; Ming, J.; Li, M.; Xie, L.; He, X.; Wang, J.; Liang, S.; Wu, Y. An Exploration of New Energy Storage System: High Energy Density, High Safety, and Fast Charging Lithium Ion Battery. *Adv. Funct. Mater.* **2019**, *29*, 1805978. [CrossRef]
476. Shuai, Y.; He, X.; Zhang, Z.; Chen, K.; Lou, J.; Wang, Y.; Li, N. A Highly Reversible and Low-Cost Sulfur-Graphite Dual-Ion Battery. *Energy Technol.* **2019**, *7*, 1800729. [CrossRef]
477. Luo, F.; Feng, X.; Zeng, L.; Lin, L.; Li, X.; Kang, B.; Xiao, L.; Chen, Q.; Wei, M.; Qian, Q. In Situ Simultaneous Encapsulation of Defective MoS<sub>2</sub> Nanolayers and Sulfur Nanodots into SPAN Fibers for High Rate Sodium-Ion Batteries. *Chem. Eng. J.* **2021**, *404*, 126430. [CrossRef]
478. Deng, L.; Hong, Y.; Yang, Y.; Zhang, J.; Niu, X.; Wang, J.; Zeng, L.; Hao, W.; Guo, L.; Zhu, Y. Sulfurized Polyacrylonitrile as a High-Performance and Low-Volume Change Anode for Robust Potassium Storage. *ACS Nano* **2021**, *15*, 18419–18428. [CrossRef]
479. Kakiage, K.; Yano, T.; Uehara, H.; Kakiage, M. Ultra-Lightweight Rechargeable Battery with Enhanced Gravimetric Energy Densities >750 Wh Kg<sup>-1</sup> in Lithium–Sulfur Pouch Cell. *Commun. Eng.* **2024**, *3*, 177. [CrossRef]
480. Wang, Y.; Cao, G. Developments in Nanostructured Cathode Materials for High-Performance Lithium-Ion Batteries. *Adv. Mater.* **2008**, *20*, 2251–2269. [CrossRef]
481. Cai, C.; Wang, Y. Novel Nanocomposite Materials for Advanced Li-Ion Rechargeable Batteries. *Materials* **2009**, *2*, 1205–1238. [CrossRef]
482. Yin, Y.-X.; Xin, S.; Guo, Y.-G.; Wan, L.-J. Lithium–Sulfur Batteries: Electrochemistry, Materials, and Prospects. *Angew. Chem. Int. Ed.* **2013**, *52*, 13186–13200. [CrossRef]
483. Manthiram, A.; Fu, Y.; Su, Y.-S. Challenges and Prospects of Lithium–Sulfur Batteries. *Acc. Chem. Res.* **2013**, *46*, 1125–1134. [CrossRef]
484. Yang, Y.; Zheng, G.; Cui, Y. Nanostructured Sulfur Cathodes. *Chem. Soc. Rev.* **2013**, *42*, 3018–3032. [CrossRef]

485. Wang, D.-W.; Zeng, Q.; Zhou, G.; Yin, L.; Li, F.; Cheng, H.-M.; Gentle, I.R.; Lu, G.Q.M. Carbon–Sulfur Composites for Li–S Batteries: Status and Prospects. *J. Mater. Chem. A* **2013**, *1*, 9382–9394. [[CrossRef](#)]
486. Liu, J.; Zhang, J.-G.; Yang, Z.; Lemmon, J.P.; Imhoff, C.; Graff, G.L.; Li, L.; Hu, J.; Wang, C.; Xiao, J.; et al. Materials Science and Materials Chemistry for Large Scale Electrochemical Energy Storage: From Transportation to Electrical Grid. *Adv. Funct. Mater.* **2013**, *23*, 929–946. [[CrossRef](#)]
487. Bresser, D.; Passerini, S.; Scrosati, B. Recent Progress and Remaining Challenges in Sulfur-Based Lithium Secondary Batteries—A Review. *Chem. Commun.* **2013**, *49*, 10545–10562. [[CrossRef](#)] [[PubMed](#)]
488. Zhang, S.S. Sulfurized Carbon: A Class of Cathode Materials for High Performance Lithium/Sulfur Batteries. *Front. Energy Res.* **2013**, *1*, 10. [[CrossRef](#)]
489. Fedorková, A.; Oriňáková, R.; Čech, O.; Sedláříková, M. New Composite Cathode Materials for Li/S Batteries: A Review. *Int. J. Electrochem. Sci.* **2013**, *8*, 10308–10319. [[CrossRef](#)]
490. Manthiram, A.; Fu, Y.; Chung, S.-H.; Zu, C.; Su, Y.-S. Rechargeable Lithium–Sulfur Batteries. *Chem. Rev.* **2014**, *114*, 11751–11787. [[CrossRef](#)]
491. Chen, L.; Shaw, L.L. Recent Advances in Lithium–Sulfur Batteries. *J. Power Sources* **2014**, *267*, 770–783. [[CrossRef](#)]
492. Zhang, S.; Ueno, K.; Dokko, K.; Watanabe, M. Recent Advances in Electrolytes for Lithium–Sulfur Batteries. *Adv. Energy Mater.* **2015**, *5*, 1500117. [[CrossRef](#)]
493. Adelhelm, P.; Hartmann, P.; Bender, C.L.; Busche, M.; Eufinger, C.; Janek, J. From Lithium to Sodium: Cell Chemistry of Room Temperature Sodium–Air and Sodium–Sulfur Batteries. *Beilstein J. Nanotechnol.* **2015**, *6*, 1016–1055. [[CrossRef](#)] [[PubMed](#)]
494. Pope, M.A.; Aksay, I.A. Structural Design of Cathodes for Li–S Batteries. *Adv. Energy Mater.* **2015**, *5*, 1500124. [[CrossRef](#)]
495. Li, Z.; Huang, Y.; Yuan, L.; Hao, Z.; Huang, Y. Status and Prospects in Sulfur–Carbon Composites as Cathode Materials for Rechargeable Lithium–Sulfur Batteries. *Carbon* **2015**, *92*, 41–63. [[CrossRef](#)]
496. Lin, Z.; Liang, C. Lithium–Sulfur Batteries: From Liquid to Solid Cells. *J. Mater. Chem. A* **2014**, *3*, 936–958. [[CrossRef](#)]
497. Fang, X.; Peng, H. A Revolution in Electrodes: Recent Progress in Rechargeable Lithium–Sulfur Batteries. *Small* **2015**, *11*, 1488–1511. [[CrossRef](#)]
498. Pang, Q.; Liang, X.; Kwok, C.Y.; Nazar, L.F. Review—The Importance of Chemical Interactions between Sulfur Host Materials and Lithium Polysulfides for Advanced Lithium-Sulfur Batteries. *J. Electrochem. Soc.* **2015**, *162*, A2567. [[CrossRef](#)]
499. Zhang, S.S. Heteroatom-Doped Carbons: Synthesis, Chemistry and Application in Lithium/Sulphur Batteries. *Inorg. Chem. Front.* **2015**, *2*, 1059–1069. [[CrossRef](#)]
500. Zhao, Y.; Zhang, Y.; Bakenova, Z.; Bakenov, Z. Carbon/Sulfur Composite Cathodes for Flexible Lithium/Sulfur Batteries: Status and Prospects. *Front. Energy Res.* **2015**, *3*, 2. [[CrossRef](#)]
501. Seh, Z.W.; Sun, Y.; Zhang, Q.; Cui, Y. Designing High-Energy Lithium–Sulfur Batteries. *Chem. Soc. Rev.* **2016**, *45*, 5605–5634. [[CrossRef](#)]
502. Liang, J.; Sun, Z.-H.; Li, F.; Cheng, H.-M. Carbon Materials for Li–S Batteries: Functional Evolution and Performance Improvement. *Energy Storage Mater.* **2016**, *2*, 76–106. [[CrossRef](#)]
503. Sun, Y.; Liu, N.; Cui, Y. Promises and Challenges of Nanomaterials for Lithium-Based Rechargeable Batteries. *Nat. Energy* **2016**, *1*, 16071. [[CrossRef](#)]
504. Griebel, J.J.; Glass, R.S.; Char, K.; Pyun, J. Polymerizations with Elemental Sulfur: A Novel Route to High Sulfur Content Polymers for Sustainability, Energy and Defense. *Prog. Polym. Sci.* **2016**, *58*, 90–125. [[CrossRef](#)]
505. Xie, J.; Zhao, C.; Lin, Z.; Gu, P.; Zhang, Q. Nanostructured Conjugated Polymers for Energy-Related Applications beyond Solar Cells. *Chem.—Asian J.* **2016**, *11*, 1489–1511. [[CrossRef](#)] [[PubMed](#)]
506. Zhao, X.; Cheruvally, G.; Kim, C.; Cho, K.-K.; Ahn, H.-J.; Kim, K.-W.; Ahn, J.-H. Lithium/Sulfur Secondary Batteries: A Review. *J. Electrochem. Sci. Technol.* **2016**, *7*, 97–114. [[CrossRef](#)]
507. Gu, X.; Zhang, S.; Hou, Y. Graphene-Based Sulfur Composites for Energy Storage and Conversion in Li–S Batteries. *Chin. J. Chem.* **2016**, *34*, 13–31. [[CrossRef](#)]
508. Gu, X.; Hencz, L.; Zhang, S. Recent Development of Carbonaceous Materials for Lithium–Sulphur Batteries. *Batteries* **2016**, *2*, 33. [[CrossRef](#)]
509. Peng, H.-J.; Huang, J.-Q.; Cheng, X.-B.; Zhang, Q. Review on High-Loading and High-Energy Lithium–Sulfur Batteries. *Adv. Energy Mater.* **2017**, *7*, 1700260. [[CrossRef](#)]
510. Dirlam, P.T.; Glass, R.S.; Char, K.; Pyun, J. The Use of Polymers in Li–S Batteries: A Review. *J. Polym. Sci. Part Polym. Chem.* **2017**, *55*, 1635–1668. [[CrossRef](#)]
511. Xin, S.; Chang, Z.; Zhang, X.; Guo, Y.-G. Progress of Rechargeable Lithium Metal Batteries Based on Conversion Reactions. *Natl. Sci. Rev.* **2017**, *4*, 54–70. [[CrossRef](#)]
512. Zhang, X.; Xie, H.; Kim, C.-S.; Zaghib, K.; Mauger, A.; Julien, C.M. Advances in Lithium—Sulfur Batteries. *Mater. Sci. Eng. R Rep.* **2017**, *121*, 1–29. [[CrossRef](#)]
513. Zeng, L.-C.; Li, W.-H.; Jiang, Y.; Yu, Y. Recent Progress in Li–S and Li–Se Batteries. *Rare Met.* **2017**, *36*, 339–364. [[CrossRef](#)]

514. Wang, T.; Kretschmer, K.; Choi, S.; Pang, H.; Xue, H.; Wang, G. Fabrication Methods of Porous Carbon Materials and Separator Membranes for Lithium–Sulfur Batteries: Development and Future Perspectives. *Small Methods* **2017**, *1*, 1700089. [[CrossRef](#)]
515. Li, G.; Wang, S.; Zhang, Y.; Li, M.; Chen, Z.; Lu, J. Revisiting the Role of Polysulfides in Lithium–Sulfur Batteries. *Adv. Mater.* **2018**, *30*, 1705590. [[CrossRef](#)] [[PubMed](#)]
516. Yuan, H.; Huang, J.-Q.; Peng, H.-J.; Titirici, M.-M.; Xiang, R.; Chen, R.; Liu, Q.; Zhang, Q. A Review of Functional Binders in Lithium–Sulfur Batteries. *Adv. Energy Mater.* **2018**, *8*, 1802107. [[CrossRef](#)]
517. Yang, X.; Li, X.; Adair, K.; Zhang, H.; Sun, X. Structural Design of Lithium–Sulfur Batteries: From Fundamental Research to Practical Application. *Electrochem. Energy Rev.* **2018**, *1*, 239–293. [[CrossRef](#)]
518. Kumar, R.; Liu, J.; Hwang, J.-Y.; Sun, Y.-K. Recent Research Trends in Li–S Batteries. *J. Mater. Chem. A* **2018**, *6*, 11582–11605. [[CrossRef](#)]
519. Zhang, J.; Huang, H.; Bae, J.; Chung, S.-H.; Zhang, W.; Manthiram, A.; Yu, G. Nanostructured Host Materials for Trapping Sulfur in Rechargeable Li–S Batteries: Structure Design and Interfacial Chemistry. *Small Methods* **2018**, *2*, 1700279. [[CrossRef](#)]
520. Wang, Y.; Huang, X.; Zhang, S.; Hou, Y. Sulfur Hosts against the Shuttle Effect. *Small Methods* **2018**, *2*, 1700345. [[CrossRef](#)]
521. Ould Ely, T.; Kamzabek, D.; Chakraborty, D.; Doherty, M.F. Lithium–Sulfur Batteries: State of the Art and Future Directions. *ACS Appl. Energy Mater.* **2018**, *1*, 1783–1814. [[CrossRef](#)]
522. Liu, J.; Wang, M.; Xu, N.; Qian, T.; Yan, C. Progress and Perspective of Organosulfur Polymers as Cathode Materials for Advanced Lithium–Sulfur Batteries. *Energy Storage Mater.* **2018**, *15*, 53–64. [[CrossRef](#)]
523. Guo, W.; Fu, Y. A Perspective on Energy Densities of Rechargeable Li–S Batteries and Alternative Sulfur-Based Cathode Materials. *Energy Environ. Mater.* **2018**, *1*, 20–27. [[CrossRef](#)]
524. Li, S.-Y.; Wang, W.-P.; Duan, H.; Guo, Y.-G. Recent Progress on Confinement of Polysulfides through Physical and Chemical Methods. *J. Energy Chem.* **2018**, *27*, 1555–1565. [[CrossRef](#)]
525. Zhao, F.; Li, Y.; Feng, W. Recent Advances in Applying Vulcanization/Inverse Vulcanization Methods to Achieve High-Performance Sulfur-Containing Polymer Cathode Materials for Li–S Batteries. *Small Methods* **2018**, *2*, 1800156. [[CrossRef](#)]
526. Zeng, Z.; Liu, X. Sulfur Immobilization by “Chemical Anchor” to Suppress the Diffusion of Polysulfides in Lithium–Sulfur Batteries. *Adv. Mater. Interfaces* **2018**, *5*, 1701274. [[CrossRef](#)]
527. Conder, J.; Marino, C.; Novák, P.; Villevieille, C. Do Imaging Techniques Add Real Value to the Development of Better Post-Li-Ion Batteries? *J. Mater. Chem. A* **2018**, *6*, 3304–3327. [[CrossRef](#)]
528. Arias, A.N.; Tesio, A.Y.; Flexer, V. Review—Non-Carbonaceous Materials as Cathodes for Lithium–Sulfur Batteries. *J. Electrochem. Soc.* **2018**, *165*, A6119. [[CrossRef](#)]
529. Wang, D.-Y.; Guo, W.; Fu, Y. Organosulfides: An Emerging Class of Cathode Materials for Rechargeable Lithium Batteries. *Acc. Chem. Res.* **2019**, *52*, 2290–2300. [[CrossRef](#)]
530. Lu, Y.; Rong, X.; Hu, Y.-S.; Chen, L.; Li, H. Research and Development of Advanced Battery Materials in China. *Energy Storage Mater.* **2019**, *23*, 144–153. [[CrossRef](#)]
531. Hong, X.; Mei, J.; Wen, L.; Tong, Y.; Vasileff, A.J.; Wang, L.; Liang, J.; Sun, Z.; Dou, S.X. Nonlithium Metal–Sulfur Batteries: Steps Toward a Leap. *Adv. Mater.* **2019**, *31*, 1802822. [[CrossRef](#)]
532. Kopeć, M.; Lamson, M.; Yuan, R.; Tang, C.; Kruk, M.; Zhong, M.; Matyjaszewski, K.; Kowalewski, T. Polyacrylonitrile-Derived Nanostructured Carbon Materials. *Prog. Polym. Sci.* **2019**, *92*, 89–134. [[CrossRef](#)]
533. Huang, S.; Guan, R.; Wang, S.; Xiao, M.; Han, D.; Sun, L.; Meng, Y. Polymers for High Performance Li–S Batteries: Material Selection and Structure Design. *Prog. Polym. Sci.* **2019**, *89*, 19–60. [[CrossRef](#)]
534. Yan, C.; Zhang, X.-Q.; Huang, J.-Q.; Liu, Q.; Zhang, Q. Lithium-Anode Protection in Lithium–Sulfur Batteries. *Trends Chem.* **2019**, *1*, 693–704. [[CrossRef](#)]
535. Gu, X.; Tang, T.; Liu, X.; Hou, Y. Rechargeable Metal Batteries Based on Selenium Cathodes: Progress, Challenges and Perspectives. *J. Mater. Chem. A* **2019**, *7*, 11566–11583. [[CrossRef](#)]
536. Teng, Y.; Zhou, Q.; Gao, P. Applications and Challenges of Elemental Sulfur, Nanosulfur, Polymeric Sulfur, Sulfur Composites, and Plasmonic Nanostructures. *Crit. Rev. Environ. Sci. Technol.* **2019**, *49*, 2314–2358. [[CrossRef](#)]
537. Liu, D.; Li, Z.; Li, X.; Cheng, Z.; Yuan, L.; Huang, Y. Recent Advances in Cathode Materials for Room-Temperature Sodium–Sulfur Batteries. *ChemPhysChem* **2019**, *20*, 3164–3176. [[CrossRef](#)] [[PubMed](#)]
538. Gupta, A.; Sivaram, S. Separator Membranes for Lithium–Sulfur Batteries: Design Principles, Structure, and Performance. *Energy Technol.* **2019**, *7*, 1800819. [[CrossRef](#)]
539. Pan, Y.; Li, S.; Yin, M.; Li, J. Electrolyte Evolution Propelling the Development of Nonlithium Metal–Sulfur Batteries. *Energy Technol.* **2019**, *7*, 1900164. [[CrossRef](#)]
540. Poizot, P.; Gaubicher, J.; Renault, S.; Dubois, L.; Liang, Y.; Yao, Y. Opportunities and Challenges for Organic Electrodes in Electrochemical Energy Storage. *Chem. Rev.* **2020**, *120*, 6490–6557. [[CrossRef](#)]
541. Zhao, M.; Li, B.-Q.; Peng, H.-J.; Yuan, H.; Wei, J.-Y.; Huang, J.-Q. Lithium–Sulfur Batteries under Lean Electrolyte Conditions: Challenges and Opportunities. *Angew. Chem. Int. Ed.* **2020**, *59*, 12636–12652. [[CrossRef](#)]

542. Liu, T.; Hu, H.; Ding, X.; Yuan, H.; Jin, C.; Nai, J.; Liu, Y.; Wang, Y.; Wan, Y.; Tao, X. 12 Years Roadmap of the Sulfur Cathode for Lithium Sulfur Batteries (2009–2020). *Energy Storage Mater.* **2020**, *30*, 346–366. [[CrossRef](#)]
543. Zhang, X.; Chen, K.; Sun, Z.; Hu, G.; Xiao, R.; Cheng, H.-M.; Li, F. Structure-Related Electrochemical Performance of Organosulfur Compounds for Lithium–Sulfur Batteries. *Energy Environ. Sci.* **2020**, *13*, 1076–1095. [[CrossRef](#)]
544. Fang, R.; Xu, J.; Wang, D.-W. Covalent Fixing of Sulfur in Metal–Sulfur Batteries. *Energy Environ. Sci.* **2020**, *13*, 432–471. [[CrossRef](#)]
545. Chen, Y.; Zhuo, S.; Li, Z.; Wang, C. Redox Polymers for Rechargeable Metal-Ion Batteries. *EnergyChem* **2020**, *2*, 100030. [[CrossRef](#)]
546. Ding, J.; Zhang, H.; Fan, W.; Zhong, C.; Hu, W.; Mitlin, D. Review of Emerging Potassium–Sulfur Batteries. *Adv. Mater.* **2020**, *32*, 1908007. [[CrossRef](#)] [[PubMed](#)]
547. Chen, J.; Naveed, A.; Nuli, Y.; Yang, J.; Wang, J. Designing an Intrinsically Safe Organic Electrolyte for Rechargeable Batteries. *Energy Storage Mater.* **2020**, *31*, 382–400. [[CrossRef](#)]
548. Yang, H.; Chen, J.; Yang, J.; Wang, J. Prospect of Sulfurized Pyrolyzed Poly(Acrylonitrile) (S@pPAN) Cathode Materials for Rechargeable Lithium Batteries. *Angew. Chem.* **2020**, *132*, 7374–7386. [[CrossRef](#)]
549. Li, S.; Zhang, W.; Zeng, Z.; Cheng, S.; Xie, J. Selenium or Tellurium as Eutectic Accelerators for High-Performance Lithium/Sodium–Sulfur Batteries. *Electrochem. Energy Rev.* **2020**, *3*, 613–642. [[CrossRef](#)]
550. Zhao, X.; Lu, Y.; Qian, Z.; Wang, R.; Guo, Z. Potassium-Sulfur Batteries: Status and Perspectives. *EcoMat* **2020**, *2*, e12038. [[CrossRef](#)]
551. Mukkabla, R.; Buchmeiser, M.R. Cathode Materials for Lithium–Sulfur Batteries Based on Sulfur Covalently Bound to a Polymeric Backbone. *J. Mater. Chem. A* **2020**, *8*, 5379–5394. [[CrossRef](#)]
552. Huang, X.; Luo, B.; Chen, P.; Searles, D.J.; Wang, D.; Wang, L. Sulfur-Based Redox Chemistry for Electrochemical Energy Storage. *Coord. Chem. Rev.* **2020**, *422*, 213445. [[CrossRef](#)]
553. Siczek, K. The Toxicity of Secondary Lithium-Sulfur Batteries Components. *Batteries* **2020**, *6*, 45. [[CrossRef](#)]
554. Dias, J.A.; Santagneli, S.H.; Messaddeq, Y. Methods for Lithium Ion NASICON Preparation: From Solid-State Synthesis to Highly Conductive Glass-Ceramics. *J. Phys. Chem. C* **2020**, *124*, 26518–26539. [[CrossRef](#)]
555. Chen, Y.; Wang, T.; Tian, H.; Su, D.; Zhang, Q.; Wang, G. Advances in Lithium–Sulfur Batteries: From Academic Research to Commercial Viability. *Adv. Mater.* **2021**, *33*, 2003666. [[CrossRef](#)]
556. Liu, Y.-T.; Liu, S.; Li, G.-R.; Gao, X.-P. Strategy of Enhancing the Volumetric Energy Density for Lithium–Sulfur Batteries. *Adv. Mater.* **2021**, *33*, 2003955. [[CrossRef](#)] [[PubMed](#)]
557. Hou, L.-P.; Zhang, X.-Q.; Li, B.-Q.; Zhang, Q. Challenges and Promises of Lithium Metal Anode by Soluble Polysulfides in Practical Lithium–Sulfur Batteries. *Mater. Today* **2021**, *45*, 62–76. [[CrossRef](#)]
558. Li, Y.; Guo, S. Material Design and Structure Optimization for Rechargeable Lithium-Sulfur Batteries. *Matter* **2021**, *4*, 1142–1188. [[CrossRef](#)]
559. Eng, A.Y.S.; Kumar, V.; Zhang, Y.; Luo, J.; Wang, W.; Sun, Y.; Li, W.; Seh, Z.W. Room-Temperature Sodium–Sulfur Batteries and Beyond: Realizing Practical High Energy Systems through Anode, Cathode, and Electrolyte Engineering. *Adv. Energy Mater.* **2021**, *11*, 2003493. [[CrossRef](#)]
560. Sun, J.; Du, Z.; Liu, Y.; Ai, W.; Wang, K.; Wang, T.; Du, H.; Liu, L.; Huang, W. State-Of-The-Art and Future Challenges in High Energy Lithium–Selenium Batteries. *Adv. Mater.* **2021**, *33*, 2003845. [[CrossRef](#)]
561. Shadike, Z.; Tan, S.; Wang, Q.-C.; Lin, R.; Hu, E.; Qu, D.; Yang, X.-Q. Review on Organosulfur Materials for Rechargeable Lithium Batteries. *Mater. Horiz.* **2021**, *8*, 471–500. [[CrossRef](#)]
562. Liu, G.; Sun, Q.; Li, Q.; Zhang, J.; Ming, J. Electrolyte Issues in Lithium–Sulfur Batteries: Development, Prospect, and Challenges. *Energy Fuels* **2021**, *35*, 10405–10427. [[CrossRef](#)]
563. Han, Z.; Li, S.; Wu, Y.; Yu, C.; Cheng, S.; Xie, J. Challenges and Key Parameters in Exploring the Cyclability Limitation of Practical Lithium–Sulfur Batteries. *J. Mater. Chem. A* **2021**, *9*, 24215–24240. [[CrossRef](#)]
564. Lyu, H.; Sun, X.-G.; Dai, S. Organic Cathode Materials for Lithium-Ion Batteries: Past, Present, and Future. *Adv. Energy Sustain. Res.* **2021**, *2*, 2000044. [[CrossRef](#)]
565. Tan, J.; Matz, J.; Dong, P.; Ye, M.; Shen, J. Appreciating the Role of Polysulfides in Lithium-Sulfur Batteries and Regulation Strategies by Electrolytes Engineering. *Energy Storage Mater.* **2021**, *42*, 645–678. [[CrossRef](#)]
566. Chai, J.; Du, J.; Li, Q.; Han, N.; Zhang, W.; Tang, B. Recent Breakthroughs in the Bottleneck of Cathode Materials for Li–S Batteries. *Energy Fuels* **2021**, *35*, 15455–15471. [[CrossRef](#)]
567. Li, S.; Lorandi, F.; Wang, H.; Liu, T.; Whitacre, J.F.; Matyjaszewski, K. Functional Polymers for Lithium Metal Batteries. *Prog. Polym. Sci.* **2021**, *122*, 101453. [[CrossRef](#)]
568. Angulakshmi, N.; Dhanalakshmi, R.B.; Sathya, S.; Ahn, J.-H.; Stephan, A.M. Understanding the Electrolytes of Lithium–Sulfur Batteries. *Batter. Supercaps* **2021**, *4*, 1064–1095. [[CrossRef](#)]
569. Jin, F.; Wang, B.; Wang, J.; Wang, Y.; Ning, Y.; Yang, J.; Zhang, Z.; Liu, P.; Zhou, Y.; Wang, D.; et al. Boosting Electrochemical Kinetics of S Cathodes for Room Temperature Na/S Batteries. *Matter* **2021**, *4*, 1768–1800. [[CrossRef](#)]

570. Chiluwal, S.; Rao, A.M.; Podila, R. Strategies for Improving Rechargeable Lithium-Ion Batteries: From Active Materials to CO<sub>2</sub> Emissions. *Nanotechnol. Rev.* **2021**, *10*, 1993–2026. [[CrossRef](#)]
571. Huang, Y.; Lin, L.; Zhang, C.; Liu, L.; Li, Y.; Qiao, Z.; Lin, J.; Wei, Q.; Wang, L.; Xie, Q.; et al. Recent Advances and Strategies toward Polysulfides Shuttle Inhibition for High-Performance Li–S Batteries. *Adv. Sci.* **2022**, *9*, 2106004. [[CrossRef](#)]
572. Deng, R.; Wang, M.; Yu, H.; Luo, S.; Li, J.; Chu, F.; Liu, B.; Wu, F. Recent Advances and Applications Toward Emerging Lithium–Sulfur Batteries: Working Principles and Opportunities. *Energy Environ. Mater.* **2022**, *5*, 777–799. [[CrossRef](#)]
573. Pan, Z.; Brett, D.J.L.; He, G.; Parkin, I.P. Progress and Perspectives of Organosulfur for Lithium–Sulfur Batteries. *Adv. Energy Mater.* **2022**, *12*, 2103483. [[CrossRef](#)]
574. Li, H.; Li, Y.; Zhang, L. Designing Principles of Advanced Sulfur Cathodes toward Practical Lithium–Sulfur Batteries. *SusMat* **2022**, *2*, 34–64. [[CrossRef](#)]
575. Xing, C.; Chen, H.; Qian, S.; Wu, Z.; Nizami, A.; Li, X.; Zhang, S.; Lai, C. Regulating Liquid and Solid-State Electrolytes for Solid-Phase Conversion in Li–S Batteries. *Chem* **2022**, *8*, 1201–1230. [[CrossRef](#)]
576. Zhang, Q.; Huang, Q.; Hao, S.-M.; Deng, S.; He, Q.; Lin, Z.; Yang, Y. Polymers in Lithium–Sulfur Batteries. *Adv. Sci.* **2022**, *9*, 2103798. [[CrossRef](#)]
577. Zou, R.; Liu, W.; Ran, F. Sulfur-Containing Polymer Cathode Materials: From Energy Storage Mechanism to Energy Density. *InfoMat* **2022**, *4*, e12319. [[CrossRef](#)]
578. Rafie, A.; Kim, J.W.; Sarode, K.K.; Kalra, V. A Review on the Use of Carbonate-Based Electrolytes in Li–S Batteries: A Comprehensive Approach Enabling Solid–Solid Direct Conversion Reaction. *Energy Storage Mater.* **2022**, *50*, 197–224. [[CrossRef](#)]
579. Weret, M.A.; Su, W.-N.; Hwang, B.J. Strategies towards High Performance Lithium–Sulfur Batteries. *Batter. Supercaps* **2022**, *5*, e20220059. [[CrossRef](#)]
580. Zhang, S.; Andreas, N.S.; Li, R.; Zhang, N.; Sun, C.; Lu, D.; Gao, T.; Chen, L.; Fan, X. Mitigating Irreversible Capacity Loss for Higher-Energy Lithium Batteries. *Energy Storage Mater.* **2022**, *48*, 44–73. [[CrossRef](#)]
581. Li, X.; Yuan, L.; Liu, D.; Xiang, J.; Li, Z.; Huang, Y. Solid/Quasi-Solid Phase Conversion of Sulfur in Lithium–Sulfur Battery. *Small* **2022**, *18*, 2106970. [[CrossRef](#)]
582. Xu, J.; Liu, K.; Khan, M.A.; Wang, H.; He, T.; Zhao, H.; Ye, D.; Tang, Y.; Zhang, J. Sub-Zero Temperature Electrolytes for Lithium–Sulfur Batteries: Functional Mechanisms, Challenges and Perspectives. *Chem. Eng. J.* **2022**, *443*, 136637. [[CrossRef](#)]
583. Luo, J.; Guan, K.; Lei, W.; Zhang, S.; Jia, Q.; Zhang, H. One Dimensional Carbon-Based Composites as Cathodes for Lithium–Sulfur Battery. *J. Mater. Sci. Technol.* **2022**, *122*, 101–120. [[CrossRef](#)]
584. Lim, C.Y.J.; Seh, Z.W. Quasi-Solid-State Conversion Cathode Materials for Room-Temperature Sodium–Sulfur Batteries. *Battery Energy* **2022**, *1*, 20220008. [[CrossRef](#)]
585. Jiao, L.; Li, H.; Zhang, C.; Jiang, H.; Yang, S.; Shu, D.; Li, C.; Cheng, B.; Yang, Q.; Zhang, W. Molecular Engineering of Sulfur-Providing Materials for Optimized Sulfur Conversion in Li–S Chemistry. *EcoMat* **2022**, *4*, e12262. [[CrossRef](#)]
586. Ren, S.; Sang, P.; Guo, W.; Fu, Y. Organosulfur Polymer-Based Cathode Materials for Rechargeable Batteries. *Polym. Chem.* **2022**, *13*, 5676–5690. [[CrossRef](#)]
587. Yi, Y.; Hai, F.; Guo, J.; Tian, X.; Zheng, S.; Wu, Z.; Wang, T.; Li, M. Progress and Prospect of Practical Lithium–Sulfur Batteries Based on Solid-Phase Conversion. *Batteries* **2023**, *9*, 27. [[CrossRef](#)]
588. Li, X.-Y.; Zhao, C.-X.; Li, B.-Q.; Huang, J.-Q.; Zhang, Q. Advances on Composite Cathodes for Lithium–Sulfur Batteries. *J. Electrochem.* **2022**, *28*, 28–40+4–5. [[CrossRef](#)]
589. Sang, P.; Chen, Q.; Wang, D.-Y.; Guo, W.; Fu, Y. Organosulfur Materials for Rechargeable Batteries: Structure, Mechanism, and Application. *Chem. Rev.* **2023**, *123*, 1262–1326. [[CrossRef](#)] [[PubMed](#)]
590. Raza, H.; Bai, S.; Cheng, J.; Majumder, S.; Zhu, H.; Liu, Q.; Zheng, G.; Li, X.; Chen, G. Li–S Batteries: Challenges, Achievements and Opportunities. *Electrochem. Energy Rev.* **2023**, *6*, 29. [[CrossRef](#)]
591. Sun, J.; Liu, Y.; Liu, L.; Bi, J.; Wang, S.; Du, Z.; Du, H.; Wang, K.; Ai, W.; Huang, W. Interface Engineering Toward Expedited Li<sub>2</sub>S Deposition in Lithium–Sulfur Batteries: A Critical Review. *Adv. Mater.* **2023**, *35*, 2211168. [[CrossRef](#)]
592. Bi, C.-X.; Hou, L.-P.; Li, Z.; Zhao, M.; Zhang, X.-Q.; Li, B.-Q.; Zhang, Q.; Huang, J.-Q. Protecting Lithium Metal Anodes in Lithium–Sulfur Batteries: A Review. *Energy Mater. Adv.* **2023**, *4*, 0010. [[CrossRef](#)]
593. Liu, X.; Mariani, A.; Adenusi, H.; Passerini, S. Locally Concentrated Ionic Liquid Electrolytes for Lithium-Metal Batteries. *Angew. Chem. Int. Ed.* **2023**, *62*, e202219318. [[CrossRef](#)]
594. Lv, Z.-C.; Wang, P.-F.; Wang, J.-C.; Tian, S.-H.; Yi, T.-F. Key Challenges, Recent Advances and Future Perspectives of Rechargeable Lithium–Sulfur Batteries. *J. Ind. Eng. Chem.* **2023**, *124*, 68–88. [[CrossRef](#)]
595. Kim, J.T.; Hao, X.; Wang, C.; Sun, X. Cathode Materials for Single-Phase Solid–Solid Conversion Li–S Batteries. *Matter* **2023**, *6*, 316–343. [[CrossRef](#)]
596. Zhang, Q.; Ma, Q.; Wang, R.; Liu, Z.; Zhai, Y.; Pang, Y.; Tang, Y.; Wang, Q.; Wu, K.; Wu, H.; et al. Recent Progress in Advanced Organosulfur Cathode Materials for Rechargeable Lithium Batteries. *Mater. Today* **2023**, *65*, 100–121. [[CrossRef](#)]

597. Zhang, M.; Mao, H.; Liang, Y.; Yu, X. Recent Progress in Zeolitic Imidazolate Frameworks (ZIFs)-Derived Nanomaterials for Effective Lithium Polysulfide Management in Lithium–Sulfur Batteries. *J. Mater. Chem. A* **2023**, *11*, 17892–17919. [[CrossRef](#)]
598. Yang, S.; Wang, B.; Lv, Q.; Zhang, N.; Zhang, Z.; Jing, Y.; Li, J.; Chen, R.; Wu, B.; Xu, P.; et al. Recent Advances in Cathodes for All-Solid-State Lithium-Sulfur Batteries. *Chin. Chem. Lett.* **2023**, *34*, 107783. [[CrossRef](#)]
599. Pang, Z.; Zhang, H.; Wang, L.; Song, D.; Shi, X.; Ma, Y.; Kong, L.; Zhang, L. Towards Safe Lithium-Sulfur Batteries from Liquid-State Electrolyte to Solid-State Electrolyte. *Front. Mater. Sci.* **2023**, *17*, 230630. [[CrossRef](#)]
600. Xin, S.; Zhang, X.; Wang, L.; Yu, H.; Chang, X.; Zhao, Y.-M.; Meng, Q.; Xu, P.; Zhao, C.-Z.; Chen, J.; et al. Roadmap for Rechargeable Batteries: Present and Beyond. *Sci. China Chem.* **2024**, *67*, 13–42. [[CrossRef](#)]
601. Fei, Y.; Li, G. Unveiling the Pivotal Parameters for Advancing High Energy Density in Lithium-Sulfur Batteries: A Comprehensive Review. *Adv. Funct. Mater.* **2024**, *34*, 2312550. [[CrossRef](#)]
602. Song, X.; Liang, X.; Eko, J.; Sun, H.H.; Kim, J.-M.; Kim, H.; Sun, Y.-K. Toward Practical Li–S Batteries: On the Road to a New Electrolyte. *Adv. Energy Mater.* **2024**, *14*, 2402506. [[CrossRef](#)]
603. Liang, F.; Wang, S.; Liang, Q.; Zhong, A.; Yang, C.; Qian, J.; Song, H.; Chen, R. Insight into All-Solid-State Li–S Batteries: Challenges, Advances, and Engineering Design. *Adv. Energy Mater.* **2024**, *14*, 2401959. [[CrossRef](#)]
604. Rao, X.-Y.; Xiang, S.-F.; Zhou, J.; Zhang, Z.; Xu, X.-Y.; Xu, Y.-Y.; Zhou, X.-C.; Pan, Z.-D.; Tan, S.-C.; Dong, S.-X.; et al. Recent Progress and Strategies of Cathodes toward Polysulfides Shuttle Restriction for Lithium-Sulfur Batteries. *Rare Met.* **2024**, *43*, 4132–4161. [[CrossRef](#)]
605. Qian, W.; Guo, Y.; Zuo, W.; Wu, X.; Zhang, L. Toward Practical Lithium–Sulfur Batteries. *Mater. Chem. Front.* **2024**, *8*, 2556–2577. [[CrossRef](#)]
606. Tan, J.; Ma, L.; Wang, Y.; Yi, P.; Ye, C.; Fang, Z.; Li, Z.; Ye, M.; Shen, J. Lithium Sulfur Batteries: Insights from Solvation Chemistry to Feasibility Designing Strategies for Practical Applications. *Energy Environ. Mater.* **2024**, *7*, e12688. [[CrossRef](#)]
607. Zhang, X.; Yu, T.; Yang, S.; Qu, Z.; Xiao, R.; Wang, G.; Sun, Z.; Li, F. Organosulfur Cathodes in Lithium Metal Batteries: Bridging the Gap between Fundamentals and Practical Applications. *Adv. Funct. Mater.* **2024**, *34*, 2405122. [[CrossRef](#)]
608. Chen, J.; Zhang, Y.; Yang, J.; Nuli, Y.; Wang, J. Post Lithium-Sulfur Battery Era: Challenges and Opportunities towards Practical Application. *Sci. China Chem.* **2024**, *67*, 106–121. [[CrossRef](#)]
609. Zhang, Y.; Wang, S.; Li, C.; Wang, Z.; Ma, Y.; Shi, X.; Zhang, H.; Song, D.; Zhang, L. Review on Polymer Electrolytes for Lithium-Sulfurized Polyacrylonitrile Batteries. *EcoEnergy* **2025**, *3*, 56–76. [[CrossRef](#)]
610. Feng, Y.; Liu, H.; Lu, Q. From Non-Carbon Host toward Carbon-Free Lithium-Sulfur Batteries. *Nano Res.* **2024**, *17*, 1337–1365. [[CrossRef](#)]
611. Cai, D.; Zheng, F.; Li, Y.; Zhang, C.; Qin, Z.; Li, W.; Liu, Y.; Li, A.; Zhang, J. Design of Coatings for Sulfur-Based Cathode Materials in Lithium-Sulfur Batteries: A Review. *Chem.—Asian J.* **2024**, *19*, e202400099. [[CrossRef](#)]
612. Huang, Z.; Cai, Y.; Zhang, S.; Wang, R.; Li, X.; Liu, Z. 3D Aligned Architectures for Lithium Batteries: Mechanism, Design, and Manufacture. *Energy Storage Mater.* **2025**, *75*, 103999. [[CrossRef](#)]
613. Zhang, Y.; Qin, F.; Baek, J.; Lee, D.H.; Kim, M.; Song, H.-W.; Lee, S. From Non-Aqueous Liquid to Solid-State Li–S Batteries: Design Protocols, Challenges and Solutions. *Mater. Adv.* **2024**, *5*, 8772–8786. [[CrossRef](#)]
614. Feng, J.; Yu, S.; Shi, C.; Tang, X.; Zhao, X.; Chen, S.; Song, J. Advanced Cathode Designs for High-Energy Lithium/Sodium–Selenium Battery. *Adv. Funct. Mater.* **2025**, *35*, 2422013. [[CrossRef](#)]
615. Liu, X.; Xu, C.; Adenusi, H.; Wu, Y.; Passerini, S. Development of PFAS-Free Locally Concentrated Ionic Liquid Electrolytes for High-Energy Lithium and Aluminum Metal Batteries. *Acc. Chem. Res.* **2025**, *58*, 354–365. [[CrossRef](#)] [[PubMed](#)]
616. Ma, T.; Yue, H.; Xiao, Y.; Huang, Y.; Li, X.; Gao, X.; He, N.; Zhan, C.; Nan, D. A Review of Organic Sulfur Applications in Lithium-Sulfur Batteries. *J. Power Sources* **2025**, *625*, 235717. [[CrossRef](#)]
617. Cao, Z.; Wei, B. A Perspective: Carbon Nanotube Macro-Films for Energy Storage. *Energy Environ. Sci.* **2013**, *6*, 3183–3201. [[CrossRef](#)]
618. Holze, R.; Wu, Y.P. Intrinsically Conducting Polymers in Electrochemical Energy Technology: Trends and Progress. *Electrochim. Acta* **2014**, *122*, 93–107. [[CrossRef](#)]
619. Huang, J.-Q.; Zhang, Q.; Wei, F. Multi-Functional Separator/Interlayer System for High-Stable Lithium-Sulfur Batteries: Progress and Prospects. *Energy Storage Mater.* **2015**, *1*, 127–145. [[CrossRef](#)]
620. Liang, Y.; Yao, Y. Positioning Organic Electrode Materials in the Battery Landscape. *Joule* **2018**, *2*, 1690–1706. [[CrossRef](#)]
621. Yuan, H.; Peng, H.-J.; Huang, J.-Q.; Zhang, Q. Sulfur Redox Reactions at Working Interfaces in Lithium–Sulfur Batteries: A Perspective. *Adv. Mater. Interfaces* **2019**, *6*, 1802046. [[CrossRef](#)]
622. Yang, X.; Luo, J.; Sun, X. Towards High-Performance Solid-State Li–S Batteries: From Fundamental Understanding to Engineering Design. *Chem. Soc. Rev.* **2020**, *49*, 2140–2195. [[CrossRef](#)]
623. Li, H.; Yang, H.; Ai, X. Routes to Electrochemically Stable Sulfur Cathodes for Practical Li–S Batteries. *Adv. Mater.* **2023**, *2305038*. [[CrossRef](#)]

624. Wang, Y.; Chai, J.; Li, Y.; Li, Q.; Du, J.; Chen, Z.; Wang, L.; Tang, B. Strategies to Mitigate the Shuttle Effect in Room Temperature Sodium–Sulfur Batteries: Improving Cathode Materials. *Dalton Trans.* **2023**, *52*, 2548–2560. [[CrossRef](#)]
625. Tan, S.-J.; Feng, X.-X.; Wang, Y.-H.; Guo, Y.-G.; Xin, S. Nonconventional Electrochemical Reactions in Rechargeable Lithium–Sulfur Batteries. *ACS Appl. Mater. Interfaces* **2024**, *16*, 67002–67009. [[CrossRef](#)]
626. Manthiram, A.; Chung, S.-H.; Zu, C. Lithium–Sulfur Batteries: Progress and Prospects. *Adv. Mater.* **2015**, *27*, 1980–2006. [[CrossRef](#)] [[PubMed](#)]
627. Wang, J.; He, Y.-S.; Yang, J. Sulfur-Based Composite Cathode Materials for High-Energy Rechargeable Lithium Batteries. *Adv. Mater.* **2015**, *27*, 569–575. [[CrossRef](#)]
628. Ma, J.; Li, Y.; Grundish, N.S.; Goodenough, J.B.; Chen, Y.; Guo, L.; Peng, Z.; Qi, X.; Yang, F.; Qie, L.; et al. The 2021 Battery Technology Roadmap. *J. Phys. Appl. Phys.* **2021**, *54*, 183001. [[CrossRef](#)]

**Disclaimer/Publisher’s Note:** The statements, opinions and data contained in all publications are solely those of the individual author(s) and contributor(s) and not of MDPI and/or the editor(s). MDPI and/or the editor(s) disclaim responsibility for any injury to people or property resulting from any ideas, methods, instructions or products referred to in the content.